Investigations on the relevance of Onsager's conjecture in real incompressible turbulence

Denis Kuzzay

Thèse de Doctorat
de
l'Université Paris-Saclay

Spécialité Physique

Ecole Doctorale n°564: Physique en Île-de-France

par

Denis Kuzzay

Investigations on the relevance of Onsager's conjecture in real incompressible turbulence

Soutenue à Saclay, le 5 Octobre 2016, devant le jury composé de:

M.	Frédéric	Moisy	Président
M.	Laurent	Chevillard	Rapporteur
M.	Jean-Luc	Guermond	Rapporteur
M.	Jean-François	Pinton	Examinateur
Mme.	Bérengère	Dubrulle	Directrice de thèse
M.	François	Daviaud	Invité

Service de Physique de l'État Condensé

CEA Saclay

À tout ceux qui m'ont permis d'en arriver là.

Contents

List of Figures

List of Tables

Préface

La dynamique des écoulements fluides qualifiés de “turbulents” est aujourd'hui encore mal comprise. Pourtant, les équations de leurs mouvements sont connues depuis plus d'un siècle et demi, mais l'on peine à en extraire toutes les informations nécessaires à une compréhension profonde du phénomène. En effet, l'incompressibilité, mélangé à l'advection du champ de vitesse par lui même, rend la résolution de ces équations très difficile, aussi bien analytiquement que numériquement. Pour en venir à bout, le “turbulencier” doit donc mettre en œuvre toute son ingéniosité, et trouver d'autres angles d'attaque pour démonter cette édifice pierre par pierre, et en comprendre l'agencement. Cette thèse présente ma modeste contribution.

Il me serait difficile, aujourd'hui, de faire la liste de tous les facteurs qui, au cours de ma vie, m'ont conduit à rédiger ces lignes. Ces facteurs sont nombreux, aussi bien sur le plan scientifique qu'humain. Ils sont parfois évidents, parfois subtiles, parfois dignes d'intérêt, et parfois triviaux. Quoi qu'il en soit, une telle liste n'apporterait rien ici, et si je ne peux énumérer toutes les circonstances qui m'ont conduit là où j'en suis, je sais en revanche quelles sont les personnes qui m'ont soutenues tout au long de mon parcours.

Lyon, le 4 Novembre 2016

Remerciements

Pour débuter cette longue série de remerciements, j'aimerais commencer les examinateurs et rapporteurs qui ont constitué le jury de ma soutenance, et sans qui celle-ci n'aurait pas eu lieu. Merci à Frédéric d'avoir (sans vraiment avoir eu le choix) présidé. Merci à Laurent et Jean-Luc d'avoir lu ma thèse, rédigé leur rapport, apporté nombres de commentaires et remarques utiles, et tout ça pendant leurs vacances d'été. Enfin, merci à Jean-François Pinton d'avoir su trouver le temps de donner son avis sur mon travail, malgré son emploi du temps plus que surchargé.

Ma thèse s'est déroulé au SPEC dans les meilleures conditions possibles, et ceci en partie dû à la compétence et la gentillesse des secrétaires. Je les remercie donc, en particulier pour avoir fait preuve de patience à mon égard, et pour avoir su supporter mon incompétence et ma flemme administratives. J'en profite aussi pour remercier tous les travailleurs de l'ombre, membres de la direction, de l'administration, de l'école doctorale, ou autre, avec qui je n'ai eu que peu ou pas d'intéractions, et qui ont contribué à ce que ma thèse se passe au mieux. Je ne sais pas exactement quel a été votre rôle, mais je sais que nombres de problèmes ont été interceptés en amont grâce à vous, me permettant ainsi de me concentrer au maximum sur la Science.

Parmi les membres du SPHYNX, qui m'ont accueilli pendant 3 ans, tous sont à remercier, qu'ils soient permanents ou non. La raison première étant que la quasi-totalité d'entre eux, à un moment ou à un autre de ma thèse, a contribué à mon alimentation. Mais j'aimerais aussi souligner la facilité avec laquelle s'est faite mon intégration au groupe, et l'ambiance légère et familiale qui règne au deuxième étage du SPEC. Mes remerciements vont donc:

À Basile, Caroline, Ivan, Saco, Samuel, Sébastien, Simon et Thomas H. pour leur humour et leur bonne humeur.

À Marco, une personne vraie, toujours prêt à charrier et à rigoler, qui colore le quotidien du SPHYNX.

À Roland, qui participe activement à ce que tout le monde puisse rentrer chez lui sain et sauf le soir venu.

À Daniel, pour les discussions scientifiques, sa bonne humeur et son soutien lors des soirées passées au bureau à rédiger.

À Thomas S., de loin la personne la plus gentille que je connaisse, pour son soutien dans les moments difficiles.

À Cécile, dont les contributions à ma thèse ont été si nombreuses que j'en oublie.

Cependant, son sacrifice consistant à m'offrir son petit pain de la cantine pour me fournir les glucides nécessaires au maintient de ma concentration jusqu'en fin journée, lui, ne sera pas oublié.

À Vincent, dont la patience, l'écoute, et la générosité m'ont été d'une grande aide lors de ces trois années, en particulier lors de mes un peu trop nombreuses mésaventures automobiles.

À Alizée, l'hyperactive du groupe, partagée entre les sciences, l'équitation, la grimpe, les raids, les marathons, le violoncelle, la littérature, et j'en passe. Merci pour les discussions, les débats, et surtout pour m'avoir nourrit les samedis midi quand je passais ma journée seul au SPEC à finir ma rédaction.

À Hervé, dont l'esprit aiguisé et les remarques pertinentes m'ont permis à plusieurs reprises d'aborder mon sujet de thèse sous un angle nouveau, et d'en comprendre plus profondément la problématique. De plus, son humour et sa bonne humeur n'ont rendu les pauses café et les séances de grimpe que plus agréables.

À François L., chef parmi les chefs qui, tel Arthur, a toujours essayé d'apporter la lumière à chacun des membres de la table elliptique du SPHYNX. Il a su trouver la force de persévérer dans les moments difficiles, avec gentillesse et bienveillance. Les viennoiseries pendant les réunions furent un vrai régal.

Il est temps maintenant de remercier les personnes avec qui j'ai eu la chance de pouvoir collaborer, du SPHYNX et d'ailleurs. En écrivant ces lignes, mes pensées vont vers:

Caroline et Jean-Luc, qui m'ont fait découvrir la campagne texane.

Frédérique et Jacques, avec qui j'ai pu faire mon monitorat.

Ewe-Wei, qui a rejoint le groupe au cours de ma deuxième année de thèse, et qui a grandement contribué à l'avancée de nos travaux.

Davide, dont la pertinence scientifique et la bonne humeur m'ont accompagné pendant trois ans.

Martin, un co-bureau et ami exceptionnel dont le récit des aventures de sa vie égayent les longues heures passées assis devant un écran.

François D., complémentaire scientifique parfait de Bérengère, qui a su me faire profiter de son approche et de sa perspective sur les questions qui furent au centre de ma thèse. Mon parrain pendant trois ans, et un directeur idéal pour le SPEC, merci d'avoir accepté l'invitation à faire partie du jury, et d'avoir fait fonctionner ta magie lors de la soutenance.

Dans un cadre un plus privé, j'aimerais maintenant remercier toutes les personnes plus ou moins proches, rencontrées récemment ou amis de plus longues dates, qui se sont intéressées de près ou de loin à ma thèse. Merci à ceux qui m'ont accompagné pendant mon parcours, qui sont venus ou pas à ma soutenance, et qui m'ont permis de décompresser en dehors du labo. Je pense notamment à Basile, Cynthia, Cédric, Clément J., Lise, Cambyse, Miko, Jean-Baptiste, Clément M., Clément S., Clémence, Bastien, Flora, Marion, Pierre, Julie, Antoine, Héloise, Romain, Laura, Matthieu, Lucile, Benjamin, Sonny, Mélody, et Miguel.

Je n'oublie pas non plus le rôle qui a été joué par mon professeur de physique de prépa, Philippe Borel, dans l'intérêt que je porte aujourd'hui aux sciences physiques et dans l'orientation de mes études.

Merci aussi à tous les potes d'escrime du club de Rueil-Malmaison, en particulier Gwen, Vincent A., Antoine, Hamid, Xav, Juju, Antho, Vincent S., Alessandro, Thomas, Toussaint, Damien, et Laurélien, pour tous les bons moments. Et bien sûr, merci aux maîtres d'armes, si jeunes et si vigoureux: Philippe et Yvan.

Durant ces quatre dernières années, il m'a fallu surmonter plusieurs épreuves. Heureusement pour moi, je n'ai pas eu à les affronter seul, et la chance m'a été donnée d'avoir à mes côtés quelqu'un d'exceptionnel. Je remercie donc du fond du cœur Sophie pour tous ces moments partagés, et tout ce que tu m'as apporté. Je suis fier du chemin que l'on a parcouru, nous y sommes arrivés ensemble, et je te suis très reconnaissant d'avoir accepté d'avancer avec ma main dans la tienne.

Bien sûr, je ne peux remercier Sophie sans remercier aussi sa famille pour son accueil et sa gentillesse. Merci donc à Michelle, Dominique, Frédérique et Matthieu pour leurs pensées positives et leur soutien.

Merci à tous les membres de ma famille qui m'ont soutenu lors de ma thèse et, plus généralement, lors des vingt-sept dernières années. Merci à ma tante, à Philippe, et à mes grands-parents qui ont fait le déplacement jusque sur le plateau de Saclay, ont affronté la jungle parisienne et le RER B, tout ça pour venir assister à ma soutenance. Merci à mon oncle François pour ses encouragements et, bien évidemment, un grand merci à mes parents qui ont vu en moi la capacité de pousser mes études aussi loin, et qui m'ont soutenu, motivé, et secoué lorsque j'en avais besoin. Ils m'ont aidé à me construire, me reconstruire, m'ont servit de modèles, et d'ouvertures sur le monde. Il n'y a aucun doute que je n'aurais pas parcouru autant de chemin s'ils n'avaient pas été à mes côtés.

Pour mettre un point final à ces remerciements, j'aimerais maintenant dédier quelques lignes à la personne la plus importante de ma thèse. Pendant trois ans elle m'a guidé, accompagné, encouragé, motivé, le tout avec une bonne humeur intarissable. Toutes les étapes de ma thèse se sont déroulées de la meilleure des façons grâce à elle. Un véritable geyser à idées, aussi brillante scientifiquement qu'humainement, à ma directrice, Bérengère, je dis un énorme merci.

Notations

Before entering the heart of the matter, let us first define some notations. These notations will hold throughout this manuscript, unless otherwise specified.

- Vectors are denoted using bold characters, the components of vector $\boldsymbol{v}$ being denoted v_i where $i = 1, 2, 3, \ldots$ or $i = x, y, z, \ldots$.

- The unit tensor is $\delta_{ij} = 1$ if $i = j$ and 0 otherwise. The fully antisymmetric Levi-Civita tensor is $\epsilon_{ijk} = (-1)^s$, where s denotes the sign of the permutation of (i, j, k).

- The operations of symmetrization and antisymmetrization will respectively be denoted by parentheses and square brackets: $T_{(ij)} = (T_{ij}+T_{ji})/2$ and $T_{[ij]} = (T_{ij}-T_{ji})/2$.

- $(x_i, t) \in \mathbb{R}^d \times \mathbb{R}^+$ denotes a point in the $d+1$ dimensional Galilean spacetime.

- $\mathcal{V}$, $\partial\mathcal{V} \subset \mathbb{R}^d$ denote an open connected space and its boundary: $\mathcal{V} \bigcup \partial\mathcal{V}$ is a closed connected space.

- (∂_i, ∂_t), denotes the partial derivatives in spacetime, and $\partial_{ij} = \partial_i \partial_j$.

- The Einstein summation convention over repeated latin indices is used, except on index ℓ denoting scales. Therefore, for two tensors S_{ij} and T_{ij}, $S_{ij}T_{kj} = \sum_j S_{ij}T_{kj}$.

- If the velocity field is denoted u_i, velocity increments are defined as

$$\delta u_i(\boldsymbol{x}, \boldsymbol{r}, t) \stackrel{def}{=} u_i(\boldsymbol{x} + \boldsymbol{r}, t) - u_i(\boldsymbol{x}, t).$$

  The dependence of δu_i on $\boldsymbol{x}$ and t will usually be kept implicit.

- $\overline{Q}$ denotes the time or ensemble average of Q. $< Q >$ denotes its space average.

- S_p denotes the p^{th} order structure function

$$S_p \stackrel{def}{=} \overline{\delta u^p}.$$

If we decompose the velocity increments into two orthogonal components $\delta \boldsymbol{u} = \delta \boldsymbol{u}_{\parallel} + \delta \boldsymbol{u}_{\perp}$, where $\delta u_{\parallel}(\boldsymbol{r}) = \delta \boldsymbol{u}(\boldsymbol{r}) \cdot \boldsymbol{r}/r$, we can define the p^{th} order orthogonal and longitudinal structure functions as

$$S_p^{\perp} \stackrel{def}{=} \overline{\delta u_{\perp}^p},$$

and

$$S_p^{\parallel} \stackrel{def}{=} \overline{\delta u_{\parallel}^p},$$

Causality in Natural Laws

You know my methods. Apply them.

Sir Arthur Conan Doyle

During the year 2011/2012, before the London Summer Olympics[1], I was an Erasmus student at Imperial College, London. One of my many occupations there was to pace up and down the physics section of the library, looking for some interesting readings. Some day, I found a book titled *Causality & Chance in Modern Physics*, written by [Bohm, 1961]. I took it back to my 10 m^2 room, and read through the first chapter. In this chapter, Bohm discusses causal laws, contingencies and describes in details the scientific method which allows to discover new laws. I was very impressed with the clarity of the ideas and, since then, I believe that every student in science should read through the first pages of this book.

To me, the purpose of teaching science to students, besides stimulating their curiosity or providing general knowledge, is to teach them a method for reasoning, *i.e.* to provide them with tools to make logical connections by themselves in everyday life. The typical situation that each one of us experience on a daily basis is the following. Starting from some observations of the world around us, plenty of data are gathered. From all these data, those which are crucial must be separated from those which are merely incidental. Then, causes must be inferred from *inductive* reasoning and consequences from *deductions*. However, during physics and maths lectures, teachers always use fundamental principles as a starting point (according to my own experience) and then *deduce* everything that can be. While this presents a pedagogical interest because it places the students in some rigid reasoning structure which allows most of them to keep up, it also has the drawback of never teaching inductive reasoning, which is the hardest. Moreover, most of breakthroughs in science are made when causal laws are understood. As a consequence, I cannot conceive beginning my thesis without spending a little time writing about the scientific method, which has driven my work during the last three years.

In the physical world, nothing remains constant. Everything undergoes changes of some sort which arise from something else (causes) and will in turn give rise to some other things (consequences). Bohm sums this principle up by saying that "everything comes

[1] Which would turn out to be a major disappointment for French fencing.

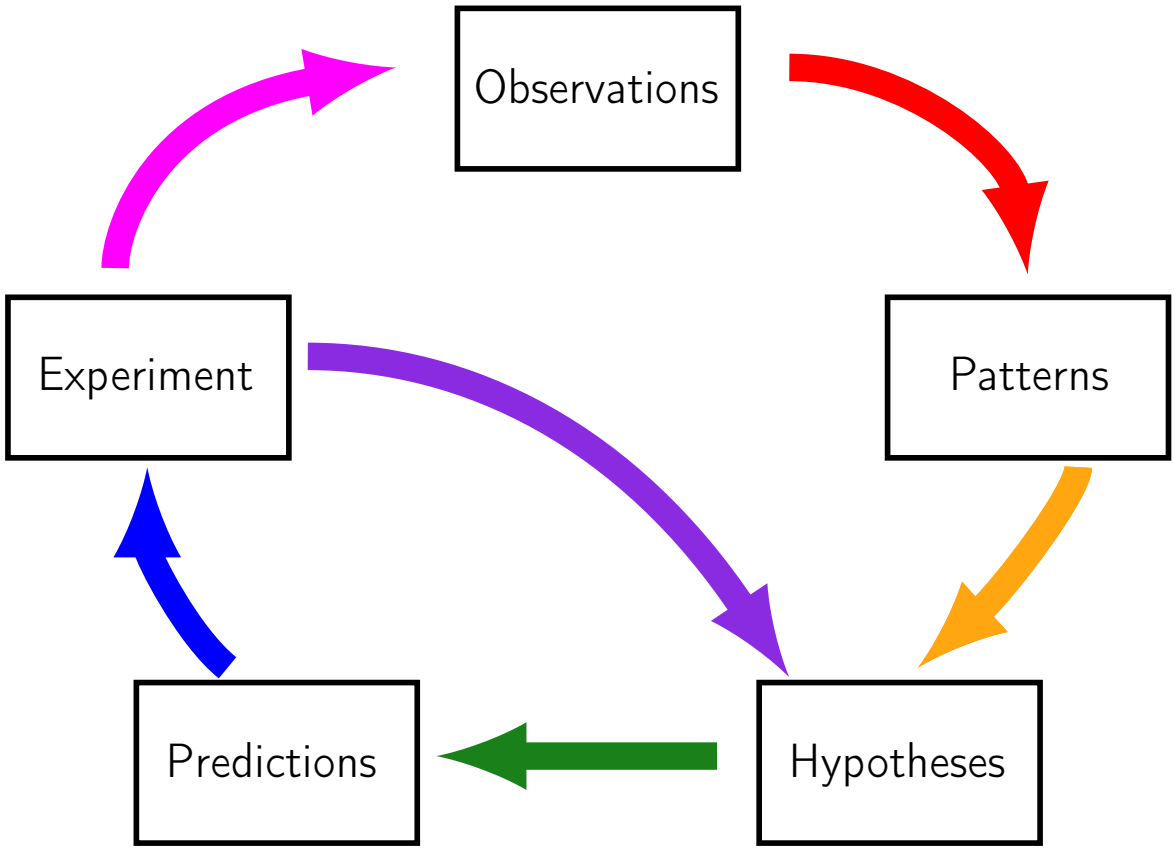

Figure 1: Seeking new laws: the scientific method as an ongoing process.

from other things and gives rise to other things". This means that it is not possible for anything in nature to come out of nothing or disappear without without leaving any trace, however small. This statement is fundamental and, without it, it would be impossible to understand nature in a rational way. Up to now, it has never been disproved. However, this statement alone does not ensure that nature can be understood. For that, causal laws in physical processes must exist. That is, inside of all of the complexity of change and transformation, there are regular relationships that hold within a wide range of conditions. However, causal laws cannot be known *a priori*, they must be found in nature. To discover these laws, the scientific method dictates to proceed as illustrated on Fig. 1. Starting from some observations, we look for patterns, and we provisionally assume these regularities to arise from causal laws. The next step is to make hypotheses on these laws following the most probable explanation of the facts, and allowing for a rational understanding of what is observed. These hypotheses usually provide additional input and make it possible to derive new informations not contained (or not found) in the first set of data. These constitute predictions which can then be tested, either by simple observations or by the more active process of making an experiment. If needed, the hypotheses are modified or refined according to the results of the experiment until all the predictions which can be derived from them are found to hold. When this state is reached, the hypotheses are temporarily considered as true statements until a wider range of observations are made which may challenge them.

As a consequence, we can only prove a theory wrong, and we can never prove it right.

Part I

What is known

Chapter 1

Basics of Fluid Dynamics

> . . . time and space are modes by which we think and not conditions in which we live.
>
> *Einstein as quoted in [Forsee, 1963]*

Contents

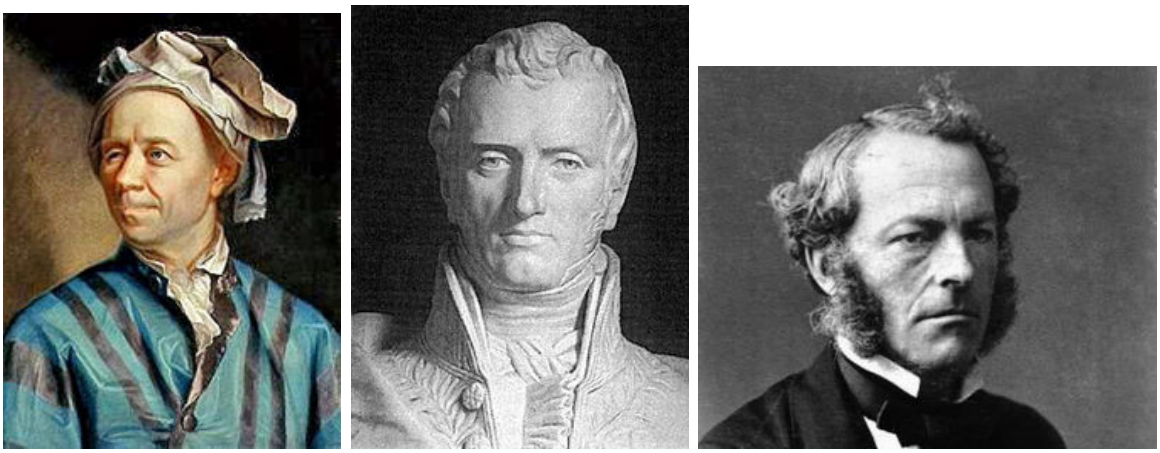

Figure 1.1: Leonhard Euler (left), Claude Louis Marie Henri Navier (middle), George Gabriel Stokes (right).

1.1 The equations of motion

The subject of fluid dynamics aims at describing the motion of fluids at macroscopic scales under various conditions. In this framework, the microscopic nature of fluids is believed to be irrelevant, and matter is considered to be a continuous medium. This means that any small volume is always assumed large enough so that it contains a great number of particles. In this context, *fluid particles* are the *smallest* elements to be considered. They are infinitely small with respect to the whole volume of the flow, but extremely large compared to the distance between molecules. In addition, their mass δm is assumed to be conserved as they move throughout the flow.

Like all macroscopic theories, fluid dynamics involves physical quantities which are *averages* over infinitely small volumes, neglecting the fluctuations due to the molecular nature of matter. Therefore, when we speak of the velocity of a fluid particle, we actually mean the average velocity of all the molecules which are contained in this infinitely small volume. The validity of these assumptions will hold as long as the mean free path between molecules is negligible compared to the smallest characteristic length scale of the flow under study. The physical quantities of interest are then fields, defined at every points in the Galilean spacetime.

In pure hydrodynamics, the state of a fluid is completely described by the velocity field $\boldsymbol{u}$ plus any two thermodynamic quantities like the pressure field p and the mass density ρ. In our study, we will consider fluids which are incompressible, *i.e.* the volume δV of a fluid particle remains always the same so that $\rho = \delta m/\delta V$ is conserved. It can be shown from the mass continuity equation

$$\partial_t \rho + \partial_j (\rho u_j) = 0, \tag{1.1}$$

that incompressibility can be written as a divergence free condition $\partial_j u_j$. As a consequence, throughout this manuscript, we will consider ρ as known and, for simplicity, set

$\rho = 1$. This condition of incompressibility is equivalent to saying that the speed of sound C_s in the medium is infinite, so that incompressibility is valid as long as $\|\boldsymbol{u}\| \ll C_s$ everywhere in the flow. Therefore, only four independent equations are needed to build a full mathematical description of fluids in motion. In addition to mass conservation, Newton's second law applied to a fluid particle, gives the following set of equations, known as the incompressible Navier-Stokes equations (INSE)

$$\underbrace{\partial_t u_i}_{\text{local time variation of } u_i} + \underbrace{u_j \partial_j u_i}_{\text{inertial forces}} = \underbrace{-\partial_i p}_{\text{pressure forces}} + \underbrace{\nu \partial_{jj} u_i}_{\text{viscous forces}}, \tag{1.2}$$

$$\partial_j u_j = 0, \tag{1.3}$$

$$u_i(\boldsymbol{x}, 0) = u_i^0(\boldsymbol{x}), \tag{1.4}$$

where ν is the kinematic viscosity of the fluid, and $\boldsymbol{u}^0$ is a divergence free vector field [Landau and Lifshitz, 1987]. In the absence of viscosity, these equations are known as the incompressible Euler equations. Eq. (1.2) expresses momentum conservation while Eq. (1.3) and Eq. (1.4) respectively are the incompressibility and initial conditions. In order to be considered as physically reasonable, solutions to the INSE must further satisfy some regularity conditions [Fefferman, 2006] on the whole physical domain of interest $\mathcal{V} \subset \mathbb{R}^3$. We require that

$$u_i, p \in C^\infty(\mathcal{V} \times \mathbb{R}^+), \ i = 1, 2, 3, \tag{1.5}$$

along with $\boldsymbol{u} \in L^2(\mathcal{V})$. In other words, the total kinetic energy must remain finite at all times

$$\int_{\mathcal{V}} d\boldsymbol{r} \ E(\boldsymbol{r}, t) < \infty, \forall t \in \mathbb{R}^+, \tag{1.6}$$

where $E(\boldsymbol{r}, t) = \frac{1}{2}\boldsymbol{u}^2(\boldsymbol{r}, t)$. In order to avoid discussing boundary effects, it is common to take $\mathcal{V} = \mathbb{R}^3$ or work on the three dimensional torus $\mathbb{T}^3$ [Fefferman, 2006]. In practice, such domains do not exist and experiments are always confined by some finite smooth boundaries $\partial\mathcal{V}$. Therefore, the INSE must be supplemented with appropriate boundary conditions.

An interesting remark is that even though it would seem at first glance that the INSE are local because only local derivatives are involved, the dynamics of incompressible flows is actually *non-local*. Indeed, incompressibility implies that the velocity at any point in a flow is coupled to the velocity at every other points. This can be seen by taking the divergence of Eq. (1.2), which leads to a Poisson equation for p

$$\partial_{jj} p = -\partial_{ij}(u_i u_j), \tag{1.7}$$

which can then be plugged back into Eq. (1.2) in order to express it solely in terms of the velocity field

$$\partial_t u_i + \left(\delta_{ik} - \partial_{ik}\Delta^{-1}\right)\partial_j(u_j u_k) = \nu \partial_{jj} u_i. \tag{1.8}$$

The operator Δ^{-1} is the inverse Laplacian which is non-local in the physical space (see *e.g.* [Chorin, 1994]).

From vector calculus, we know that under conditions less restrictive than the one required by Eq. (1.5) and Eq. (1.6), a vector field on $\mathcal{V} \subset \mathbb{R}^3$ is uniquely defined by its divergence and its curl[1]. As a consequence, since for incompressible flows we have $\nabla \cdot \boldsymbol{u} = 0$, the INSE actually only need to be solved for the vorticity field $\boldsymbol{\omega} = \nabla \times \boldsymbol{u}$. The equations for the dynamics of $\boldsymbol{\omega}$ are obtained by taking the curl of Eq. (1.2) and take the form

$$\partial_t \omega_i + u_j \partial_j \omega_i = \omega_j \partial_j u_i + \nu \partial_{jj} \omega_i, \tag{1.9}$$

$$\omega_i = \epsilon_{ijk} \partial_j u_k, \tag{1.10}$$

$$\omega_i (\boldsymbol{x}, 0) = \omega_i^0 (\boldsymbol{x}) . \tag{1.11}$$

Eq.(1.9) can be solely expressed in terms of the vorticity field by taking the curl of Eq. (1.10), solving the resulting Poisson equation for $\boldsymbol{u}$, and then plugging back the expression into Eq.(1.9). Therefore, as for Eq. (1.8), the non-local operator Δ^{-1} is still involved in the dynamics of the vorticity field.

1.2 Symmetries and conservation laws

The concept of symmetry plays a central role in the formulation of modern physics, especially since the development of the theory of compact groups in relation to quantum mechanics, largely due to Hermann Weyl [Weyl, 1950]. Weyl's definition of a symmetry is the following

An object is said to be symmetrical if there exists a transformation which preserves the features of this object. The transformation is called a symmetry, and the object is said to be invariant under such symmetry.

The most important symmetry in Newtonian physics is the invariance of physical laws in any inertial frame, the associated symmetry group being the Galilean group. The INSE are widely believed to contain all the informations about the dynamics of fluids in nature. As such, the first property this set of equations must satisfy is invariance under Galilean transformations, and it can be checked that they indeed do [Frisch, 1995]. However, these transformations are not the only symmetries of the INSE and one can also check that parity $(\boldsymbol{x}, t, \boldsymbol{u}, \to -\boldsymbol{x}, t, -\boldsymbol{u})$ leaves these equations invariant. The symmetries of scaling $(\boldsymbol{x}, t, \boldsymbol{u}, \to \lambda \boldsymbol{x}, \lambda^{1-h} t, \lambda^h \boldsymbol{u})$, where $(\lambda, h) \in \mathbb{R}^+ \times \mathbb{R}$, and time reversal $(\boldsymbol{x}, t, \boldsymbol{u}, \to \boldsymbol{x}, -t, -\boldsymbol{u})$, hold for the Euler equations but are explicitly broken by viscous forces. If $\nu \neq 0$, the

[1] This theorem, also known as Helmholtz theorem, plays a central role in electromagnetism. Indeed, it explains why Maxwell's equations are solely written in terms of curls and divergences of the electromagnetic field.

Figure 1.2: Amalie Emmy Noether.

scaling symmetry only holds for $h = -1$.

In 1915, the German mathematician Amalie E. Noether (Fig. 1.2) established a deep relation between symmetries and conservation laws. In the case of continuous media, Noether's theorem states that every differentiable symmetry of the action of a non-dissipative system leads to a local conserved current. This theorem offers a very elegant and natural way of discussing conservation laws, which is not commonly used in fluid dynamics[2]. A mathematical article on the subject can be found at [Tao, 2014]. In the case where there is not any internal frictions, Euler equations describe a non-dissipative system. It is a well known result of Noether's theorem that homogeneity in space and time respectively lead to conservation of momentum and energy, while isotropy leads to the conservation of angular momentum.

- Local momentum conservation (Euler equations):

$$\partial_t u_i + \partial_j \mathscr{U}^{ij} = 0, \tag{1.12}$$

  where $\mathscr{U}^{ij} = u^i u^j + p\delta^{ij}$. An equivalent statement of the local momentum conservation is Kelvin theorem which states that the circulation of velocity $\Gamma = \oint_{\mathscr{C}} \boldsymbol{u} \cdot d\boldsymbol{s}$

[2]We do not attempt to make an exhaustive list of all the invariants of the Euler and Navier-Stokes equations. Here, we only discuss the usual ones.

around any closed contour $\mathscr{C}$ advected by the fluid is a *material invariant i.e.* is conserved along any fluid particle trajectory

$$\partial_t \Gamma + \partial_j \mathscr{G}^j = 0, \tag{1.13}$$

where $\mathscr{G}^j = u^j \Gamma$. As we saw in Sec. 1.1, conservation of momentum is also equivalent to the conservation of vorticity

$$\partial_t \omega_i + \partial_j \mathscr{W}^{ij} = 0, \tag{1.14}$$

where $\mathscr{W}^{ij} = 2\omega^{[i} u^{j]}$.

- Local kinetic energy conservation

$$\partial_t E + \partial_j \mathscr{E}^j = 0, \tag{1.15}$$

where $\mathscr{E}^j = u^j (E + p)$.

- Local angular momentum conservation

$$\partial_t L_i + \partial_j \mathscr{L}^{ij} = 0, \tag{1.16}$$

where $L_i = \epsilon_{ijk} r_j u_k$ is the angular momentum and $\mathscr{L}^{ij} = u^j L^i - \epsilon^{ijk} r^k p$.

Finally, Moreau showed [Moreau, 1961] that the helicity $H(\boldsymbol{r}, t) = \frac{1}{2} u_i \omega_i$ is also a conserved quantity. Later, the conservation of helicity was discovered to be generated by an enlarged Arnold symmetry group of fluid element labeling [Moreau, 1977].

- Local helicity conservation

$$\partial_t H + \partial_j \mathscr{H}^j = 0, \tag{1.17}$$

where $\mathscr{H}^j = u^j H + \omega^j \left(\frac{1}{2} E + p \right)$.

Like kinetic energy, helicity is a quadratic invariant, however, it not sign definite. According to a theorem by Arnold [Arnold, 1986; Arnold and Keshin, 1998], helicity can be topologically interpreted as the average self-linking number of vortex lines in a flow [Betchov, 1961; Moffatt, 1969].

In the presence of internal frictions, the story is a little bit different. Indeed, as we said before, Noether's theorem holds for non-dissipative systems only. In most experiments, flows are studied using fluids with $\nu \neq 0$, *i.e.* are dissipative systems. In this case, the differentiable symmetries that we discussed above such as Galilean transformations do not have to lead to a local conserved current. In the case of nonzero viscosity, it can actually be checked that the conservation laws given above become

- Local momentum conservation (Navier-Stokes equations):

$$\partial_t u_i + \partial_j \mathscr{U}_\nu^{ij} = 0, \tag{1.18}$$

where $\mathscr{U}_\nu^{ij} = \mathscr{U}^{ij} - \nu\partial^j u^i$. Kelvin theorem becomes

$$\partial_t \Gamma + \partial_j \mathscr{G}_\nu^j = 0, \tag{1.19}$$

where $\mathscr{G}_\nu^j = \mathscr{G}^j - \nu\partial^j\Gamma$. Therefore, Γ is not a material invariant anymore but still has an associated conserved current. The conservation of vorticity becomes

$$\partial_t \omega_i + \partial_j \mathscr{W}_\nu^{ij} = 0, \tag{1.20}$$

where $\mathscr{W}_\nu^{ij} = \mathscr{W}^{ij} - \nu\partial^j\omega^i$.

- Local balance of kinetic energy

$$\partial_t E + \partial_j \mathscr{E}_\nu^j = -\mathscr{D}_\nu, \tag{1.21}$$

where $\mathscr{E}_\nu^j = \mathscr{E}^j - \nu\left(\partial^j E + \partial^i\left(u^i u^j\right)\right)$, $\mathscr{D}_\nu = 2\nu S_{ij}S_{ij}$ and $S_{ij} = \partial_{(i}u_{j)}$ is the local strain rate tensor.

- Local angular momentum conservation

$$\partial_t L_i + \partial_j \mathscr{L}_\nu^{ij} = 0, \tag{1.22}$$

where $\mathscr{L}_\nu^{ij} = \mathscr{L}^{ij} - \nu\left(\partial^j L^i - \epsilon^{ijk}\partial^m\left(r^k u^m\right) + \epsilon^{ijk}u^k\right)$

- Local balance of helicity

$$\partial_t H + \partial_j \mathscr{H}_\nu^j = -\mathscr{D}_\nu^\omega, \tag{1.23}$$

where $\mathscr{H}_\nu^j = \mathscr{H}^j - \nu\left(u^i\partial^j\omega^i + \partial^i\left(\omega^i u^j\right)\right)$, $\mathscr{D}_\nu^\omega = 2\nu S_{ij}S_{ij}^\omega$ and $S_{ij}^\omega = \partial_{(i}\omega_{j)}$.

We conclude from this discussion that viscous forces are responsible for the local non-conservation of quadratic invariants of Euler equations.

1.3 The Reynolds number

The fact that for all $\lambda \in \mathbb{R}^+$ the INSE are invariant under $(\boldsymbol{x}, t, \boldsymbol{u}, \to \lambda\boldsymbol{x}, \lambda^2 t, \lambda^{-1}\boldsymbol{u})$, means that the dynamics of fluids has the same properties when spacetime variables are appropriately rescaled. Let us now consider some fluid in motion where there exist a characteristic length scale L and a characteristic velocity U. Making all the quantities dimensionless, we can write the INSE as

$$\partial_t u_i + u_j \partial_j u_i = -\partial_i p + \frac{1}{Re}\partial_{jj} u_i, \tag{1.24}$$

$$\partial_j u_j = 0, \tag{1.25}$$

$$u_i(\boldsymbol{x}, 0) = u_i^0(\boldsymbol{x}), \tag{1.26}$$

where

$$Re = \frac{UL}{\nu}, \tag{1.27}$$

is a dimensionless number called the Reynolds number. The Reynolds number plays a very important role in fluid dynamics as it appears to be the only control parameter that we may act upon in order to change the properties of the dynamics. Indeed, what equation (1.24) tells us is that if two different flows are generated in two different experiments with only a change in the values of U, L and ν (boundary and forcing conditions do not change), the properties of the two flows will be the same as long as the Reynolds numbers are the same. This is known as the similarity principle. As a consequence, any symmetry of the INSE must leave the Reynolds number invariant, and this explains why the scaling symmetry of the Euler equations breaks down to $h = -1$ for finite values of Re. Indeed, $h = -1$ is the only value of the scaling exponent compatible with the similarity principle.

Re bears the name the Irish engineer Osborne Reynolds who, at the end of the XIX^{th} century, understood the importance of this quantity by studying various pipe flows in a systematic fashion [Reynolds, 1883]. Reynolds was able to show that when $Re \ll Re_c$ the flow is laminar, whereas when $Re \gg Re_c$ the flow becomes turbulent. The critical value of Re for which this transition happens is not universal and depends on the way turbulence is generated. In general, $Re_c \approx 10 - 100$. On the other hand, it is easy to see that Re measures the relative effects of inertial forces compared to viscous forces. Turbulence therefore appears as an inertial, non-linear effect.

1.4 The turbulent regime

Instability of steady flows at very high Re

Like all physical systems, the evolution of the state of any fluid is governed by a set of fundamental equations, which we have seen to be the INSE. However, not all solutions

Figure 1.3: Transition to turbulence of the plume of smoke rising from a candle generated by Kelvin-Helmholtz instability.

to the INSE are observed in nature. In the stationary regime, these solutions must also be stable with respect to infinitely small disturbances. If small perturbations, which inevitably occur, do not decrease with time, the solution is unstable and the state of the fluid is bound change. For sufficiently high Re, it is an experimental fact that all steady flows are unstable and undergo a transition to an unsteady solution (see [Chandrasekhar, 1961; Landau and Lifshitz, 1987] for a discussion about the stability of the INSE). This property, which is due to nonlinear effects, is responsible for the onset of turbulence, and in general, high Re steady flows are unstable with respect to various mechanisms. For instance, Fig. 1.3 displays an example in which the transition to a turbulent state is due to Kelvin-Helmholtz instability.

Sensitivity to initial conditions

Turbulent motions are characterized by a highly disorganized and unpredictable space-time behaviour. The velocity continuously fluctuates around some mean value $\overline{\boldsymbol{u}}$ in a random fashion, and it is therefore convenient to decompose the velocity field as $\boldsymbol{u} = \overline{\boldsymbol{u}} + \boldsymbol{v}$, where $\boldsymbol{v}$ is called the turbulent component. Measurements of $\boldsymbol{u}$ using recent velocimetry techniques make it possible to visualize the turbulent component at one time as a function of space, or at one point as a function of time. These kind of measurements show wild fluctuations *over a wide range of space and time scales*. Therefore, one could adopt a deterministic approach and study the dynamics of $\boldsymbol{v}$ by solving the INSE considering a geometry with enough symmetries to allow for their resolution[3], given the initial condi-

[3]Because it is still not known how to solve them in the general 3D case. A high enough degree of symmetry leads to enough simplifications to allow for an analytical resolution.

Figure 1.4: Edward Norton Lorenz.

tion $\boldsymbol{u}^0$ and the forcing details. Then, if $\boldsymbol{u}^0$ can be prepared in a real set-up, the predicted evolution of the turbulent component may be experimentally tested. Now the problem is that very high Re flows exhibit a strong sensitivity to initial conditions. This is a problem because initial conditions and forcing details can only be known and imposed *approximately* in real experiments. Therefore, discrepancies between the predicted and observed flow field will eventually become much larger than the resolution of measurements and, in the end, the measured $\boldsymbol{v}$ will be completely different in its details from what was predicted theoretically.

A reasonable idea is, then, to turn to DNS. In DNS, initial conditions and forcing details can be better controlled. However, the precision of computers is inevitably finite, and this is known to be the source of rounding errors which magnify more or less quickly depending on the nature of the computations. Nonlinearities, which are the cause of the sensitivity to initial conditions, will amplify the computational errors very quickly so that the deterministic approach cannot be saved by turning to DNS. Therefore, this method of investigation has to be dropped[4].

Turbulent fluids as dynamical systems

A possible approach to turbulence is to consider high Re flows as dynamical systems. The theory of dynamical systems was brought into being by the work of the meteorologist Edward N. Lorenz who studied the coupling of the atmosphere with the ocean, described by a coupled system of INSE, through a simplified model for Rayleigh-Bénard convection.

[4]I am not saying that deriving an analytical solution from the INSE for a turbulent flow would be useless. On the contrary, as we shall see later, the statistical properties of such solution could be studied and would bring a deep insight on the physics of turbulence.

This model involves a system of three nonlinear coupled equations which were discovered to exhibit sensitivity to initial conditions [Lorenz, 1963]. Actually, this sensitivity was first studied by Poincaré, and the unpredictable nature of weather was discussed in [Poincaré, 1912]. Discussing the definition of chance, Poincaré said:

> Le premier exemple que nous allons choisir est celui de l'équilibre instable; si un cône repose sur sa pointe, nous savons bien qu'il va tomber, mais nous ne savons pas de quel côté [...]. Si le cône était parfaitement symétrique, si son axe était parfaitement vertical, s'il n'était soumis à aucune autre force que la pesanteur, il ne tomberait pas du tout. Mais le moindre défaut de symétrie va le faire pencher légèrement d'un côté ou de l'autre, et dès qu'il penchera, si peu que ce soit, il tombera tout à fait de ce côté. Si même la symétrie est parfaite, une trépidation très légère, un souffle d'air pourra le faire incliner de quelques secondes d'arc ; ce sera assez pour déterminer sa chute et même le sens de sa chute qui sera celui de l'inclinaison initiale.
>
> Si nous connaissions exactement les lois de la nature et la situation de l'univers à l'instant initial, nous pourrions prédire exactement la situation de ce même univers à un instant ultérieur. Mais, lors même que les lois naturelles n'auraient plus de secret pour nous, nous ne pourrions connaître la situation qu'*approximativement*. Si cela nous permet de prévoir la situation ultérieure *avec la même approximation*, c'est tout ce qu'il nous faut [...] ; mais il n'en est pas toujours ainsi, il peut arriver que de petites différences dans les conditions initiales en engendrent de très grandes dans les phénomènes finaux ; une petite erreur sur les premières produirait une erreur énorme sur les derniers. La prédiction devient impossible [...].

Sensitivity to initial conditions is a well known phenomenon which often occurs when the dynamics of a system is nonlinear, as for *e.g.* the INSE at high Re. When infinitely small perturbations magnify exponentially quickly in time, the system is said to be chaotic. Let us consider the initial state of a flow, in which the velocity field is denoted $\boldsymbol{u}^0$. Let us further assume that this initial state is known within some infinitely small uncertainty $\delta\boldsymbol{u}^0$. If we call T_p the time during which the velocity field can be predicted within a small tolerance $\delta\boldsymbol{u}$, then we have

$$T_p \sim \frac{1}{\lambda_{max}} \ln\left(\frac{\delta\boldsymbol{u}}{\delta\boldsymbol{u}^0}\right), \tag{1.28}$$

where T_p is called the predictability time, and λ_{max} is the leading Lyapunov exponent [Eckmann and Ruelle, 1985]. As pointed out in *e.g.* [Boffetta et al., 1998], this means that T_p has a weak dependence on $\delta\boldsymbol{u}^0$ and, like λ_{max}, is an intrinsic property of the system. However, this description raises some issues [Paladin and Vulpiani, 1987a; Crisanti et al., 1993]. In particular Eq. (1.28) only holds for infinitely small $\delta\boldsymbol{u}^0$ and $\delta\boldsymbol{u}$ whereas in practice, initial errors and the resolution of measurement systems are finite quantities. To remedy this problem, a generalized notion of Lyapunov exponents was introduced in [Aurell et al., 1996] to study the predictability of turbulent motion. By introducing

$T_r(\Delta \boldsymbol{u}^0)$ as the time it takes for a *finite* perturbation $\Delta \boldsymbol{u}^0$ to grow to $r\Delta \boldsymbol{u}^0$, one can define

$$\lambda\left(\Delta \boldsymbol{u}^0\right) = \frac{\ln\ r}{\overline{T_r}\left(\Delta \boldsymbol{u}^0\right)}. \tag{1.29}$$

The interesting feature of Eq. (1.29) is that the Lyapunov exponent λ now depends on $\Delta \boldsymbol{u}^0$ and the predictability time therefore takes the form

$$T_p\left(\Delta \boldsymbol{u}^0, r\right) = \int_{\Delta \boldsymbol{u}^0}^{r\Delta \boldsymbol{u}^0} \frac{d\left(\ln\ \Delta\right)}{\lambda\left(\Delta\right)}. \tag{1.30}$$

It can be expected that λ is a decreasing function of $\Delta \boldsymbol{u}^0$, so that Eq. (1.30) gives longer predictability times than Eq. (1.28). In particular, for Kolmogorov's theory of turbulence (see Sec. 1.7), $\lambda\left(\Delta \boldsymbol{u}^0\right) \sim \left(\Delta \boldsymbol{u}^0\right)^{-2}$ [Aurell et al., 1996]. For more discussions and reviews, see [Aurell et al., 1997; Cencini and Vulpiani, 2013].

Turbulent fluids as stochastic systems

All these considerations about the unpredictability of turbulent flows do not mean that we should give up on making predictions. Another important aspect of high Re flows is that their statistical properties are found to be quite reproducible and even predictable. This points towards a statistical description of turbulence, in which the quantities of interest are obtained from appropriate averages. The question of how these averages should be taken is treated in *e.g.* [Batchelor, 1982; Orszag, 1973; Frisch, 1995].

Equilibrium statistical mechanics is built upon universal fundamental principles which allow to develop a clear framework. The partition function $\mathcal{Z}$ is the central object of the theory as it allows to obtain macroscopic quantities from a microscopic description. Therefore, once the system has been defined and the microstates identified, the thermodynamic state of the system is known through the computation of $\mathcal{Z}$. The problem is that turbulent flows are out-of-equilibrium systems and there does not exist a complete, systematic framework in statistical physics in which they could be studied. There exists various approaches (Langevin, Fokker-Planck, master equations,...), but these lack universality.

The current situation of turbulence theory is such that we do not know (yet) how to extract all the informations we want about turbulence from the INSE, and there does not exist (yet) a general framework for out-of-equilibrium systems we could work in. The strategy which must be adopted is therefore to go back to experiments in order to get some additional input. Patterns in empirical data should be looked for, and reasonable hypotheses will be made and considered as basic assumptions in a first time, their explanations or modifications being brought later if needed. This will lead us to the famous Kolmogorov's theory of homogeneous isotropic turbulence described in Sec. 1.7.

1.5 Symmetry breakings

In Sec. 1.2, we reviewed various symmetries of the INSE and their associated conservation laws. It is an experimental fact that these symmetries are *spontaneously broken* by the mechanisms through which turbulence is generated. In [Frisch, 1995], considering a fluid flow past a cylinder, the author highlights the successive breakings of the symmetries allowed by the equations of motion. However, the author also emphasizes the fact that these symmetries appear to be restored in a statistical sense at sufficiently high Reynolds numbers, and away from boundaries. This is actually a general observation and it will be at the heart of our presentation of Kolmogorov's theory in Sec. 1.7. The regime in which symmetries are statistically restored is known as *fully developed turbulence*, and will be our main focus throughout this thesis.

A particular symmetry which will be of great interest to us, is the *time reversal symmetry* $(\boldsymbol{x}, t, \boldsymbol{u}, \rightarrow \boldsymbol{x}, -t, -\boldsymbol{u})$. As we said in Sec. 1.2, this symmetry holds for the Euler equations but is *explicitly broken* for the Navier-Stokes equations by viscous forces. This symmetry breaking is deeply related to the concepts of energy cascade, energy dissipation and entropy production. Getting a little bit ahead of ourselves, fully turbulent 3D flows are characterized by a cascade of energy from large to small scales (see Sec. 1.6), where kinetic energy is converted into heat by viscous frictions. From thermodynamics, we know that production of heat inside the system leads to an entropy production $\dot{S} > 0$. The *specific direction of the energy cascade*, plus the *increase of the entropy* of the system are direct consequences of the time reversal symmetry breaking. Their effects can be directly measured in experiments via calorimetric measurements.

A central experimental fact of fully turbulent flows is the law of finite energy dissipation. This fact is so important in turbulence that it is also called the *zeroth law of turbulence*.

> **Zeroth law of turbulence** *For high enough but not infinite Re, the time averaged dimensionless energy dissipation rate per unit mass ϵ is a nonzero constant independent of Re.*

This observation was first reported by [Taylor, 1935], in a paper discussing turbulent pipe flows. Since Taylor, the zeroth law of turbulence has found many confirmations in several other experiments [Comte-Bellot and Corrsin, 1971; Williams and Paulson, 1977; Lathrop et al., 1992; Cadot et al., 1997] and DNS [Jimenez et al., 1993; Wang et al., 1996; Yeung and Zhou, 1997; Cao et al., 1999; Gotoh et al., 2002; Kaneda et al., 2003] in various geometries, but a derivation from the INSE has yet to be found. The zeroth law is a surprising statement for at least two reasons. First of all, the scaling of ϵ does not depend on viscosity, which is the property through which fluids dissipate energy. Second, these observations show that the time reversal symmetry of the Euler equations does not appear to be restored as viscosity vanishes, as one might have naively expected. When Kolmogorov developed his theory of homogeneous, isotropic turbulence, this led him to assume that energy dissipation remains nonzero even after taking the limit $Re \rightarrow \infty$, *i.e.*


Figure 1.5: Leonardo di ser Piero da Vinci and his drawing of a turbulent flow generated by water falling into a pool.

$$\lim_{Re\to\infty} \dot{S} > 0. \tag{1.31}$$

This hypothesis is at the heart of Kolmogorov's theory and is termed *anomalous dissipation* by analogy with conservation law anomalies which occur in quantum field theory [Polyakov, 1993].

1.6 Energy cascade and energy dissipation

The turbulent regime of fluids in motion was first described by Leonardo da Vinci who produced the well known drawing displayed on Fig. 1.5. The property of turbulent motion highlighted by this drawing, and which can also be observed on Fig. 1.3, is the existence of eddies of various sizes, down to very small scales compared to the larger ones. This observation reflects what we said in Sec. 1.4 about turbulence occurring on a wide range of space and time scales.

Richardson's energy cascade

Lewis F. Richardson was an English mathematician and physicist who got interested in turbulence. Richardson, as many others, had noticed that turbulent flows are composed of a great number of eddies of different sizes. In order to illustrate this observation in wind patterns, Richardson adapted a nursery rhyme called "The Siphonaptera":

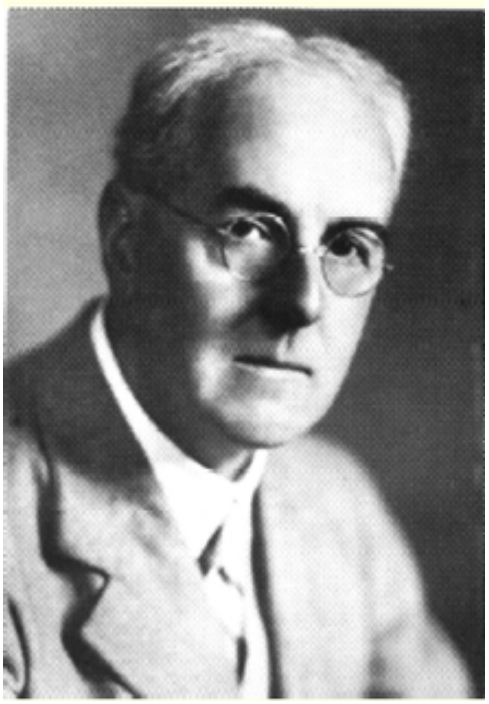

Figure 1.6: Lewis Fry Richardson

Big whorls have little whorls
That feed on their velocity ;
And little whorls have lesser whorls
And so on to viscosity.

In the Richardson's picture of turbulence [Richardson, 1920], kinetic energy is injected at a certain scale L by some forcing system. Therefore, the first eddies which are created have typical size L. When energy is injected efficiently enough inside the flow, turbulence sets in, and these eddies become unstable. They break down into smaller eddies, the energy of the "mother" eddy being divided between the "daughter" eddies. Then, these smaller eddies undergo the same process and create even smaller eddies, and so on. In this way, a continuous set of eddies is created. The dynamics of each of these eddies is governed by the INSE at a Reynolds number Re_ℓ which depends on their size ℓ and their characteristic velocity u_ℓ: $Re_\ell = u_\ell \ell / \nu$. For large eddies, Re_ℓ is small and their dynamics is governed by inertial forces. The range of scales for which this is true is thus called the inertial range. Viscous forces on the other hand only act at small scales, where they destroy the smallest eddies as they are created. This process, by which each mode is excited by smaller modes and in turn excite larger ones, allows energy to be transferred towards the scales where viscous forces can efficiently dissipate energy into heat. We say that energy "cascades" from large to small scales, which appears from this discussion as a non-linear effect. Fig. 1.7 shows a representation of the cascade as pictured by Richardson. Of course, this is just a cartoon and, as described in Richardson's poem,

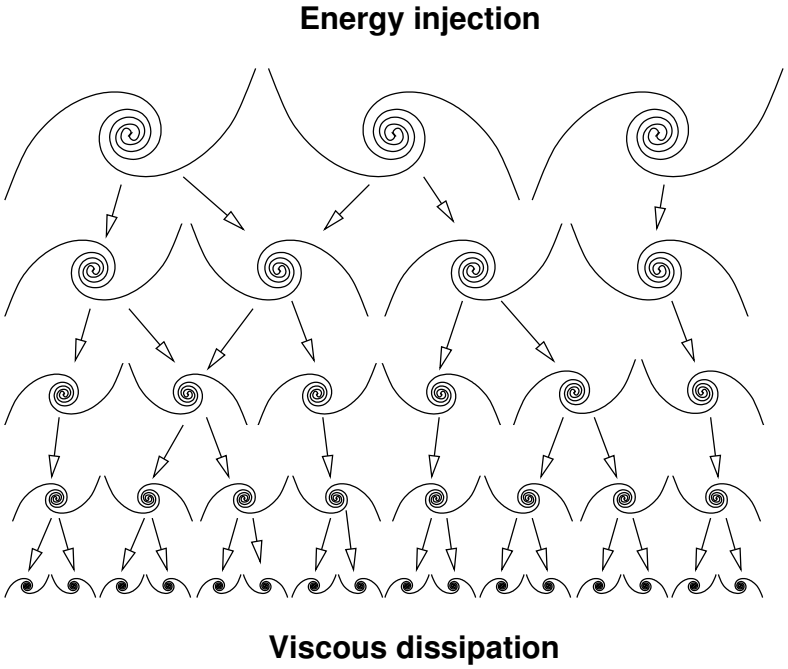

Figure 1.7: Richardson's cascade picture in physical space. Kinetic energy injection is limited to the largest scales and unstable eddies break down creating a local cascade in scale space. When small scales are reached, energy is dissipated into heat. This figure is taken from [Nazarenko, 2014]. Courtesy of S. Nazarenko.

small eddies are contained into larger ones, are advected by them, and span a continuous range of scales. The assumption which is made in the Richardson's picture is the *locality of interactions in scale space*. This means that when an eddy breaks down, the daughter eddies have a size similar to the mother eddy: only modes close to each other can interact. The arrows in Fig. 1.7 represent such local interactions, and transfers of energy between well separated scales do not occur (there are not any arrows from *e.g.* the first line of eddies to the third one).

Taylor's mechanism for energy dissipation in turbulent flows

When [Taylor, 1935] discovered the zeroth law of turbulence, the Richardson's picture was known to him. Discussing the process in which energy is dissipated in turbulent flows he wrote [Taylor and Green, 1937]

> *To explain this process is, perhaps, the fundamental problem in turbulent motion.*

Therefore, Taylor did not stop at simply reporting an experimental fact. He knew that a physical mechanism was missing, and proposed his own [Taylor and Green, 1937; Taylor, 1938]. In this work, Taylor realized the importance of vortex line stretching in the

process of energy dissipation. Indeed, it can be shown that viscous dissipation is related to vorticity and pressure by

$$\mathscr{D}_\nu = \nu\boldsymbol{\omega}^2 - 2\nu\Delta p. \tag{1.32}$$

Therefore, if we take the space average of Eq. (1.32) on *i.e.* $\mathbb{T}^3$ we get

$$\langle\mathscr{D}_\nu\rangle = \nu\left\langle\boldsymbol{\omega}^2\right\rangle. \tag{1.33}$$

Now the dynamics of large eddies is governed by Euler equations which can be written in vorticity form as (see Eq. (1.9))

$$\partial_t\omega_i + u_j\partial_j\omega_i = \omega_j\partial_j u_i. \tag{1.34}$$

The l.h.s of Eq. (1.34) simply describes the convection of vorticity while the r.h.s describes the production of vorticity by vortex line stretching. Indeed, as we discussed in Sec. 1.4, turbulence is a diffusive process and any two fluid particles which are initially infinitely close to each other will quickly separate as time evolves. Therefore, if these two particles initially lie on a vortex line, and since vortex lines are material, they will stretch. By incompressibility, this stretching will be accompanied by a reduction of the cross section of any vortex tube in which they are contained, thus increasing $\boldsymbol{\omega}^2$ through Kelvin's theorem. At some point, when $\langle\boldsymbol{\omega}^2\rangle$ reaches some viscosity dependent value, the effects of viscosity cannot be neglected anymore and kinetic energy dissipation occurs. This process is the widely accepted mechanism from which the zeroth law is believed to arise.

1.7 Kolmogorov's 1941 phenomenology of turbulence

In 1941, the Russian mathematician Andreï N. Kolmogorov (see Fig. 1.8) published four papers [Kolmogorov, 1941a;b;c;d] and paved the way towards a statistical theory of turbulence. His theory, which aims at describing *homogeneous, isotropic* turbulence and referred to as K41, was based on two universality assumptions.

Kolmogorov's first universality assumption *For finite, large enough values of the Reynolds number, all the small scale statistical properties of turbulent flows are uniquely and universally determined by the scale ℓ, the mean energy dissipation rate ϵ and the viscosity ν.*

Kolmogorov's second universality assumption *For the subrange of these scales which are much larger than the smallest scale in the flow, the statistical properties are uniquely and universally determined by ℓ and ϵ.*

The idea at the root of these assumptions is that as eddies break down in the process of energy cascade, there is a point at which the details of the forcing generating turbulence

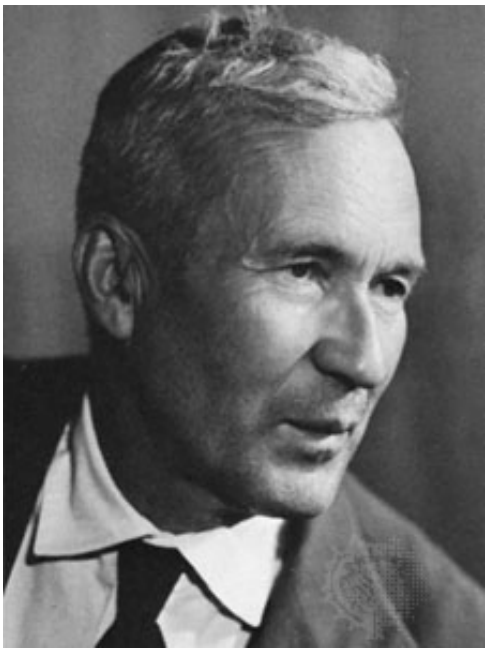

Figure 1.8: Andreï Nikolaïevitch Kolmogorov.

at large scales should become irrelevant. In particular, the anisotropy induced by the forcing disappears locally at small scales, so that all eddies lose their structures and become similar. In [Kolmogorov, 1941b], Kolmogorov actually called these assumptions "similarity assumptions". A reformulation of K41 can be found in [Frisch, 1995], where the emphasis is put on symmetries rather than universality. In this section, we follow this reformulation.

As we said in Sec. 1.2 and 1.5, the INSE have several symmetry groups which are broken at the onset of turbulence, and restored in a statistical sense at very high Re. The first assumption of K41 is that

$\boldsymbol{H_1}$ *In the limit of infinite Re, all the symmetries of the INSE, which are spontaneously broken at the transition to turbulence, are restored statistically at small scales and away from boundaries.*

Small scales are defined as the scales much smaller than the energy injection scale L introduced in Sec. 1.6. In particular, $\boldsymbol{H_1}$ states that local statistical properties of turbulent flows are homogeneous and isotropic. However, for scale invariance in the limit of infinite Re, there are infinitely many symmetry groups labelled by a scaling exponent $h \in \mathbb{R}$ (Sec. 1.2). The next hypothesis is made in order to consider the simplest case, *i.e.* only one value of h is allowed.

$\boldsymbol{H_2}$ *In the limit of infinite Re, turbulent flows are globally self-similar at small scales, i.e. have a unique exponent h.*

Figure 1.9: Lev Davidovitch Landau and his fabulous hairstyle.

The value of h will be specified later, and we will see that it is a direct consequence of the dissipation anomaly.

$\boldsymbol{H_3}$ *In the limit of infinite Re, the mean dimensionless rate of energy dissipation per unit mass* ϵ *remains nonzero.*

These hypotheses, added to the INSE, will allow us to study the physics of turbulence in the inertial range. As we will see, they allow to recover some known results and also lead to new predictions. They are the starting point for the description of turbulence in the sense of Kolmogorov. Actually, as we said in the beginning of this section, Kolmogorov did not exactly formulate his work in this manner. The emphasis was put on the assumed universality of turbulent flows rather than on their symmetries. The problem is that Lev D. Landau (see Fig. 1.9 for an epic hairstyle) argued against universality. The interested reader can find a detailed discussion on this subject in [Frisch, 1995], where it is explained how a reformulation of K41 (which Kolmogorov was aware of) based on symmetries helps reconcile Kolmogorov's work and Landau's objections. Let us now investigate what additional informations can be extracted from $\boldsymbol{H_1}$, $\boldsymbol{H_2}$ and $\boldsymbol{H_3}$.

The Kolmogorov energy density spectrum

If we consider a turbulent flow in the stationary regime, the mean rate of energy injection and dissipation ϵ are equal and constant on time average. The picture which we have drawn up to now is that energy is injected at scale L, cascades locally through the inertial range where there is not any direct energy injection or dissipation, and is finally transformed into heat at small scales. Moreover, statistical stationarity means that there is not any accumulation of energy at any ℓ, on average. As a consequence, the mean rate at which energy cascades does not depend on ℓ or time and is therefore equal to ϵ. Furthermore, locality implies that ϵ can only depend on the characteristic quantities of the flow at scale ℓ. Let us, then, denote as u_ℓ the characteristic velocity of an eddy of size ℓ. Since ϵ does not vanish in the limit of infinite Re ($\boldsymbol{H_3}$), dimensional analysis tells us that the only scaling we can write is

$$\epsilon \sim \frac{u_\ell^3}{\ell}. \tag{1.35}$$

Therefore, we get that

$$u_\ell^2 \sim (\epsilon \ell)^{2/3}, \tag{1.36}$$

where u_ℓ^2 represents the characteristic kinetic energy at scale ℓ. Let us now define the energy density spectrum over the whole three dimensional space $E^{(3D)}(\boldsymbol{k})$ as

$$E^{(3D)}(\boldsymbol{k}) = \frac{1}{2}\int_{\mathbb{R}^3} \frac{d\boldsymbol{r}}{(2\pi)^3}\, \overline{u_i(\boldsymbol{x})\, u_i(\boldsymbol{x}+\boldsymbol{r})}\, e^{-ik_j r_j}. \tag{1.37}$$

Mathematically, $E^{(3D)}(\boldsymbol{k})$ is the Fourier transform of the two-point autocorrelation function of the velocity field. Physically, $E^{(3D)}(\boldsymbol{k})$ represents the amount of energy stored at a wavenumber $k \sim \ell^{-1}$ per unit wavenumber. We then deduce from (1.36) and (1.37) that $E^{(3D)}$ scales as[5]

$$E^{(3D)}(k) \sim \epsilon^{2/3} k^{-11/3}. \tag{1.38}$$

In the case of homogeneous, isotropic turbulence (recovered at small scales through $\boldsymbol{H_1}$), the same amount of information is contained in $E^{(1D)}(k) = 4\pi k^2 E^{(3D)}(k)$. It then follows

$$E^{(1D)}(k) \sim \epsilon^{2/3} k^{-5/3}. \tag{1.39}$$

Therefore, the hypotheses of locality of the energy cascade and $\boldsymbol{H_3}$ lead to the conclusion that $E^{(1D)}$ scales as $k^{-5/3}$. This result was derived independently by several physicists during the 1940s [Kolmogorov, 1941a;b;c; Obukhov, 1941a;b; von Weizsäcker, 1948; Heisenberg, 1948; Onsager, 1949], and is known as the Kolmogorov energy spectrum

[5] In a formulation of K41 based on universality, one directly arrives at Eq. (1.38) from the second assumption.

for homogeneous, isotropic turbulence[6]. It can be shown that this scaling is equivalent to $S_2(r) \sim r^{2/3}$ [Frisch, 1995].

Kolmogorov's 4/5 law

An important result derived in [Kolmogorov, 1941a] is the 4/5 law of turbulence which can be stated as

4/5 law *In the limit of infinite Reynolds number, when homogeneity and isotropy are recovered at small scales, the third order longitudinal structure function is related to ϵ via*

$$S_3^{\parallel}(r) = -\frac{4}{5}\epsilon r. \tag{1.40}$$

As stressed in [Frisch, 1995]

> This is one of the most important results in fully developed turbulence because it is both exact and nontrivial. It thus constitutes a kind of "boundary condition" on theories of turbulence: such theories, to be acceptable, must either satisfy the four-fifths law, or explicitly violate the assumptions made in deriving it.

The derivation of the 4/5 law by Kolmogorov is based on a cornerstone in turbulence known as the Kármán-Howarth equation. This equation, derived for the first time in [von Kármán and Howarth, 1938] from the INSE in homogeneous isotropic turbulence, provides a relation between the second and third order correlations of the velocity field (a derivation can also be found in [Hinze, 1959]). A more systematic derivation of the 4/5 law than Kolmogorov's can be found in [Frisch, 1995] starting from an anisotropic generalization of the Kármán-Howarth equation, largely attributed to Monin [Monin, 1959; Monin and Yaglom, 1975].

Let us define

$$\Pi(\boldsymbol{r}) \stackrel{def}{=} -\partial_t^{NL} \frac{\overline{\boldsymbol{u}(\boldsymbol{x}) \cdot \boldsymbol{u}(\boldsymbol{x}+\boldsymbol{r})}}{2}, \tag{1.41}$$

where the operator ∂_t^{NL} only acts on nonlinear terms of the INSE, *i.e.* inertial forces and pressure. $\Pi(\boldsymbol{r})$ is called the physical space energy flux, and can be linked to the scale space energy transfers through its Fourier transform. Assuming that turbulence is maintained in the statistically stationary regime by a large scale, statistically homogeneous forcing $\boldsymbol{f}$, it can be shown that

[6] It is interesting to note that the equipartition of energy, which would be expressed as $E^{(1D)}(k) \sim k^2$, does not hold in K41. However, since turbulent flows are out-of-equilibrium systems, this is not surprising.

Kármán-Howarth-Monin (KHM) relation *In homogeneous (but not necessarily isotropic) turbulence*

$$\Pi(\boldsymbol{r}) = -\frac{1}{4}\nabla\cdot\overline{|\delta\boldsymbol{u}|^2\delta\boldsymbol{u}(\boldsymbol{r})}, \tag{1.42}$$

$$= -\partial_t\overline{\frac{\boldsymbol{u}(\boldsymbol{x})\cdot\boldsymbol{u}(\boldsymbol{x}+\boldsymbol{r})}{2}} + \overline{\boldsymbol{u}(\boldsymbol{x})\cdot\frac{\boldsymbol{f}(\boldsymbol{x}+\boldsymbol{r})+\boldsymbol{f}(\boldsymbol{x}-\boldsymbol{r})}{2}} + \nu\Delta\overline{\boldsymbol{u}(\boldsymbol{x})\cdot\boldsymbol{u}(\boldsymbol{x}+\boldsymbol{r})}. \tag{1.43}$$

Using the KHM relation, and after a few pages of calculations, Kolmogorov's 4/5 law is derived. The successive assumptions made in these computations are

- First of all, the stationary regime exists and the limit $t\to\infty$ has been taken. In this limit, the mean energy per unit mass remains finite.
- Then, $Re\to\infty$ and homogeneity and isotropy are assumed ($\boldsymbol{H_1}$).
- If there is an external forcing which aims at maintaining turbulence in a stationary regime, the energy injection is confined to large scales as discussed in Sec. 1.6.
- Hypothesis $\boldsymbol{H_3}$ is used.
- $S_3^{\parallel}(r)$ is assumed to vanish as $r\to 0$.

In the end, the anomalous dissipation can be written as

$$-\frac{4}{5}\epsilon = \lim_{r\to 0}\lim_{Re\to\infty}\lim_{t\to\infty}\frac{S_3^{\parallel}(r)}{r}. \tag{1.44}$$

It is interesting to note that the approach used in [Frisch, 1995] to arrive at this result is reminiscent of the point-splitting regularization method used by [Schwinger, 1951] in the first derivation of the axial anomaly in quantum electrodynamics. Indeed, in quantum field theory, products of field operators at different points in spacetime are usually more regular than local products at the same point. The idea of point-splitting regularization is therefore to replace local products by separated products and take the limit of zero separation at the end. This is exactly what we have done here. The analogy was noted by Eyink in a private communication with Frisch (see footnote 5 on page 77 in [Frisch, 1995]).

Finally, dropping isotropy and leaving all other assumptions unchanged, a generalization of the 4/5 law can still be derived

$$\epsilon = -\frac{1}{4}\nabla\cdot\overline{|\delta\boldsymbol{u}|^2\delta\boldsymbol{u}(\boldsymbol{r})}\Big|_{r=0}. \tag{1.45}$$

The value of h

The transformation $(\boldsymbol{x}, t, \boldsymbol{u}, \to \lambda\boldsymbol{x}, \lambda^{1-h}t, \lambda^h\boldsymbol{u})$ leaves the dynamics of turbulent flows invariant in the limit $Re \to \infty$. However, K41 allows for only one particular value of h, which can be determined by rescaling the 4/5 law. We obtain

$$\epsilon = -\frac{5}{4r}\, S_3^{\parallel}\, \lambda^{3h-1}. \tag{1.46}$$

Now since ϵ remains nonzero in the limit $Re \to \infty$, we can conclude that

$$h = \frac{1}{3}. \tag{1.47}$$

As a consequence, the value of h is a direct consequence of $\boldsymbol{H_3}$. In addition, from this result and hypothesis $\boldsymbol{H_2}$, we also obtain the additional prediction that

$$S_p^{\parallel}(r) \sim (\epsilon r)^{p/3}. \tag{1.48}$$

Kolmogorov microscales and degrees of freedom

All the results we have derived up to now have been obtained starting from an initial flow with $Re < \infty$, then the limit $t \to \infty$ is taken first, then $Re \to \infty$, and finally $\ell \to 0$. Taking these limits allow us to always work in the inertial range where energy is neither directly injected nor dissipated, but only cascades from large to small scales. However, if we do not let the viscosity vanish, there appears a range of scales called the dissipation range where entropy is created by kinetic energy dissipation due to viscous forces. This dissipation range contains the scales close to the Kolmogorov length scale which is defined as

$$\eta = \left(\frac{\nu^3}{\epsilon}\right)^{1/4}. \tag{1.49}$$

η is a quantity which is once again built assuming locality in scale space[7]. Nothing much is believed to happen at smaller scales so that η represents the smallest length scale in a flow. In addition to the Kolmogorov length scale, a time scale τ_η can be associated to η

$$\tau_\eta = \sqrt{\frac{\nu}{\epsilon}}, \tag{1.50}$$

which is called the eddy turnover time. Therefore, in order to fully resolve a flow in space and time, velocity must be probed in volumes of size at most η^3 over the whole volume of the flow, every τ_η. A nice reasoning taken from [Saint-Michel, 2013] (and which resembles the introduction of [Diu et al., 1997]) is the following: if we compare the ratio of the energy injection scale L to η we find

[7] Or assuming universality.

$$\frac{L}{\eta} \sim Re^{3/4}. \tag{1.51}$$

In the case of the von Kármán flow studied in Saclay, and given the characteristics of the experimental set-up (see Chap. 2), we get that for $Re = 10^6$, $\eta \sim 1$ µm and $\tau_\eta \sim 10$ µs. Therefore, having a full knowledge of such a flow requires to know 10^{15} numbers every 10 µs. This is a huge amount of data, even for modern storage systems. For instance, an external hard drive needs approximately 20 octets to store the components of a 3D vector. This means that recording the flow for one minute in the whole tank requires around 10^{10} modern external hard drives. This huge number tells us that it is impossible to monitor all the scales of high Reynolds number flows. It also explains why DNS are limited to much smaller Re than what is achieved in experiments. Indeed, the number of grid points N needed in order to be able to follow the dynamics of the smallest structures grows as the cube of Eq. (1.51), *i.e.* $N \sim Re^{9/4}$. This number typically represents the number of degrees of freedom of a flow. In the example of the von Kármán flow at $Re = 10^6$, $N \approx 10^{13}$. This is an additional justification for the statistical approach to turbulence we have adopted so far. We give up keeping track of the variations of physical quantities such as the energy dissipation rate, the structure functions, etc..., and focus our attention on statistical averages.

At this point, it is interesting to make a small remark. As we discussed in Sec. 1.4, there still does not exist any general framework in which out-of-equilibrium systems such as turbulent flows can be studied in a systematic fashion. However, surprisingly, some features of turbulent flows can be understood from equilibrium statistical physics [Chorin, 1994; Thalabard et al., 2015]. In this framework, similitudes have been found between K41 and mean field theory (MFT) [Nelkin, 1974]. The aim of MFT is to gain some insight into the physics of large systems at equilibrium, by approximating the interactions between each components by an average or effective interaction. In field theory, the Hamiltonian associated to the system under consideration can be expanded in the magnitude of the fluctuations around the MFT. MFT then represents the zeroth order of this expansion, and it trivially follows that fluctuations are left aside. In K41, the only relevant dynamical parameter to characterize the properties of turbulent flows is the mean rate of energy dissipation ϵ. K41 therefore appears as a MFT. Of course, MFT is an approximation valid only when fluctuations can be neglected compared to the value of ϵ. Therefore, when these fluctuations are strong, we should expect experimental deviations from K41. Interestingly enough, Landau's argument against Kolmogorov's universality assumption at the root of K41 was based on the role played by these fluctuations. As a matter of fact, discrepancies from K41 do exist in nature, and their manifestations constitute what is called intermittency [Frisch, 1995].

1.8 Conclusion and outlooks

The K41 theory has had many successes for the last seventy five years, and most of the predictions we have deduced from $\boldsymbol{H_1}$, $\boldsymbol{H_2}$ and $\boldsymbol{H_3}$ in Sec. 1.7 have had many ex-

perimental confirmations. On the other hand, some experimental results also disprove K41. For instance, the existence of intermittency, *i.e.* the fact that velocity measurements show periods/areas of strong turbulent intensity separated by periods/areas of weaker fluctuations indicates that, if turbulence is self-similar, this symmetry cannot be global as assumed in $\boldsymbol{H_2}$. Moreover, K41 considers homogeneous isotropic turbulence, and there is *a priori* not any reason why its predictions should apply beyond this case. Building a general consistent framework in which turbulent flows could be studied in a systematic fashion therefore requires to go back to the assumptions underlying our understanding of turbulent flows. Kolmogorov himself made an attempt in this direction by modifying K41 in order to take Landau's comments into considerations [Kolmogorov, 1962]. This thesis attempts at making another step, however small, in the same direction.

In this thesis, we investigate the possibility for turbulent flows not to remain smooth as assumed in Eq. (1.5). This study is rooted in a conjecture by Onsager which provides an alternative explanation to Taylor's in order to account for the existence a dissipation anomaly in turbulence. This conjecture can be found in the last sentences of [Onsager, 1949]:

> It is of some interest to note that in principle, turbulent dissipation as described could take place just as readily without the final assistance by viscosity. In the absence of viscosity, the standard proof of the conservation of energy does not apply, because the velocity field does not remain differentiable! In fact it is possible to show that the velocity field in such "ideal" turbulence cannot obey any Lipschitz condition of the form
>
> $$|\boldsymbol{u}(\boldsymbol{r'}+\boldsymbol{r}) - \boldsymbol{u}(\boldsymbol{r'})| < (const.)\, r^n, \tag{1.52}$$
>
> for any order n greater than 1/3 ; otherwise the energy is conserved. Of course, under the circumstances, the ordinary formulation of the laws of motion in terms of differential equations becomes inadequate and must be replaced by a more general description ; [...].

A lot of work has been performed trying to prove Onsager's conjecture. Following Onsager's idea, Jean Duchon and Raoul Robert have been able to derive an analytical expression for Onsager's dissipation anomaly, along with the corresponding local energy balance [Duchon and Robert, 2000]. In this thesis, we are going to test the predictions of Onsager's theory from experimental data, mostly based on Duchon and Robert's results. In Chap. 2, we will introduce the experimental set-up we used for our study, known as von Kármán (VK) set-up, and review the basic physics of VK flows in the light of the notions introduced in this chapter. In Chap. 3, we will come back on Onsager's assertion, explain its origin by considering a sequence of coarse-grained INSE, connect these ideas to finite time singularities, and introduce the "more general description" mentioned by Onsager. Moreover, as the results obtained in [Duchon and Robert, 2000] are central to our work, we will explain how they have been derived and will comment them in

details. Chap. 4 presents new data analyses of Onsager's dissipation anomaly based on Duchon and Robert's results. These analyses are done using measurements specially performed for our study by Ewe-Wei Saw, who implemented a zoom procedure on well chosen areas of fully developed turbulent VK flows, allowing to resolve the Kolmogorov scale. To our knowledge, these analyses are the first attempt at studying Onsager's theory from experimental data obtained in the inertial range as well as in the dissipative range. In Chap. 5, we make use of the results obtained in Chap. 4 and introduce a new criterion in order to track potential finite time singularities through scales in turbulent incompressible flows, and we apply it to VK flows at Kolmogorov scale. We show that we detect four main types of potential singularities, therefore providing strong evidences that the topology of turbulent incompressible flows at sub-Kolmogorov scales is non-trivial. In Chap. 6, we discuss the possible consequences of our experimental results for computational fluid dynamics. In particular, we provide a promising alternative to large-eddy-simulation models which is more accurate in estimating ϵ in the case of a VK flow, and does not introduce any eddy viscosity. Finally, Chap. 7 presents the conclusions of our studies and the perspectives for future works.

Chapter 2

Illustration on a Concrete Example: The von Kármán Experiment

> Scientists study the world as it is, engineers create the world that never has been.
>
> *Theodore von Kármán*

Contents

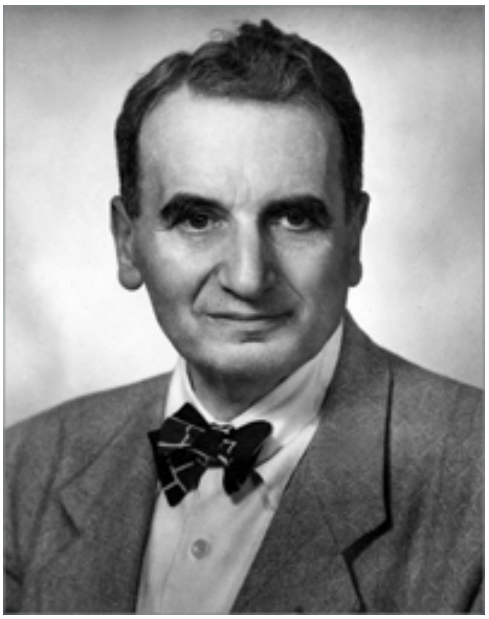

Figure 2.1: Theodore von Kármán.

In Chap. 1, we have reviewed the basic notions for the study of fluids in motion. We have adopted an approach which emphasizes the role of symmetries, and we now propose to illustrate these concepts on a concrete example. In this chapter, we enter the framework of von Kármán (VK) flows generated in the so-called "VK2" experimental set-up located in Saclay. We are going to review the basic properties of such flows in the light of Chap. 1, and we will see that this framework offers an interesting gateway to the study of inhomogeneous, anisotropic turbulence.

2.1 Introduction

VK flows are a particular class of hydrodynamic flows which are generated inside a cylindrical tank by two impellers located at both ends of the tank. This class of flows is named after Theodore von Kármán (see Fig. 2.1), which first investigated the problem of a viscous fluid set into motion by an infinite rotating flat disk (see [Ravelet, 2005] for a concise historical review). The physics of VK flows is very rich and has both practical and fundamental interests. In Saclay, their study began with the "von Kármán sodium" (VKS) project which was built as a model for the study of turbulent geodynamo [Bourgoin et al., 2000; Marié, 2003; Ravelet et al., 2005; Berhanu et al., 2007; Monchaux et al., 2007]. However, VK flows are also a framework of choice for the study of non-homogeneous, non-isotropic hydrodynamic turbulence [Moisy et al., 1999; 2001; Cortet et al., 2009; Herbert et al., 2012]. In the recent years, the emphasis has been put onto the investigation of the statistical properties of time-averaged large scale structures, and has revealed interesting phenomena such as multistability [Ravelet et al., 2004; Ravelet, 2005; de La Torre and Burguete, 2007; Cortet et al., 2010; 2011], spontaneous symmetry break-

ings [Thalabard, 2013; Saint-Michel et al., 2014a; Thalabard et al., 2015] and hysteresis cycles [Ravelet, 2005; Monchaux, 2007]. Therefore, VK flows appear as an interesting paradigm for the study of out-of-equilibrium statistical mechanics [Saint-Michel, 2013], which surprisingly also exhibit features of equilibrium statistical mechanics. Finally, VK flows provide interesting insights in quantum turbulence. The set-up located in Grenoble as part of the SHREK project benefits from a high power cooling system which allows for the study of both classical and quantum turbulence using normal liquid or superfluid helium [Rousset et al., 2014; Saint-Michel et al., 2014b].

2.2 The VK set-up at SPEC

Over the years, the von Kármán set-up located in the basement of SPEC has undergone many changes. The first version, built as part of the VKS project, has been studied during Louis Marié's and Florent Ravelet's Ph.D theses [Marié, 2003; Ravelet, 2005], under the supervision of François Daviaud. Here, we describe the VK2 set-up[1] built during Romain Monchaux's Ph.D thesis [Monchaux, 2007] with the help of Vincent Padilla, and which has been further studied in [Saint-Michel, 2013; Thalabard, 2013].

The tanks

The VK2 set-up, displayed on Fig. 2.2, is constituted of a vertical Plexiglas cylinder of axis (Oz). Its radius is $R = 10$ cm, its height is 47 cm, its thickness is 1 cm, and it can be filled with glycerol, water or a mixing of both, without (theoretically) any leakage. This cylindrical tank is placed inside another cubic Plexiglas tank of square cross section 26×26 cm^2, and thickness 1 cm, filled with the same fluid as the cylindrical tank. The addition of this cubic tank aims at decreasing chromatic aberrations which occur at the interface air-plexiglas when using optical measurement systems.

Impellers geometry

The fluid contained into the cylindrical tank is mechanically stirred by two coaxial impellers, driven by two independent motors. The impellers are $H = 18$ cm apart, which gives the experiment an aspect ratio of $H/R = 1.8$. There exist many different available geometries of impellers, some of them being displayed in Fig. 2.3. Most of the studies performed in this thesis focus on two particular impellers called TM60 and TM87 (see Fig. 2.3) in the counter rotating regime. Their characteristics are summarized in Tab. 2.1. These two types of impellers are essentially the same: they are flat disks, fitted with curved blades, the curvature of which being characterized by the angle α defined on Fig. 2.3. For impellers with $\alpha \neq 0$, there are two non-equivalent ways of forcing the flow, labelled (+) and (-). The rotation frequencies f_1 and f_2 of both impellers can be

[1] Better known among Bérengère Dubrulle's group as "Denis' set-up".

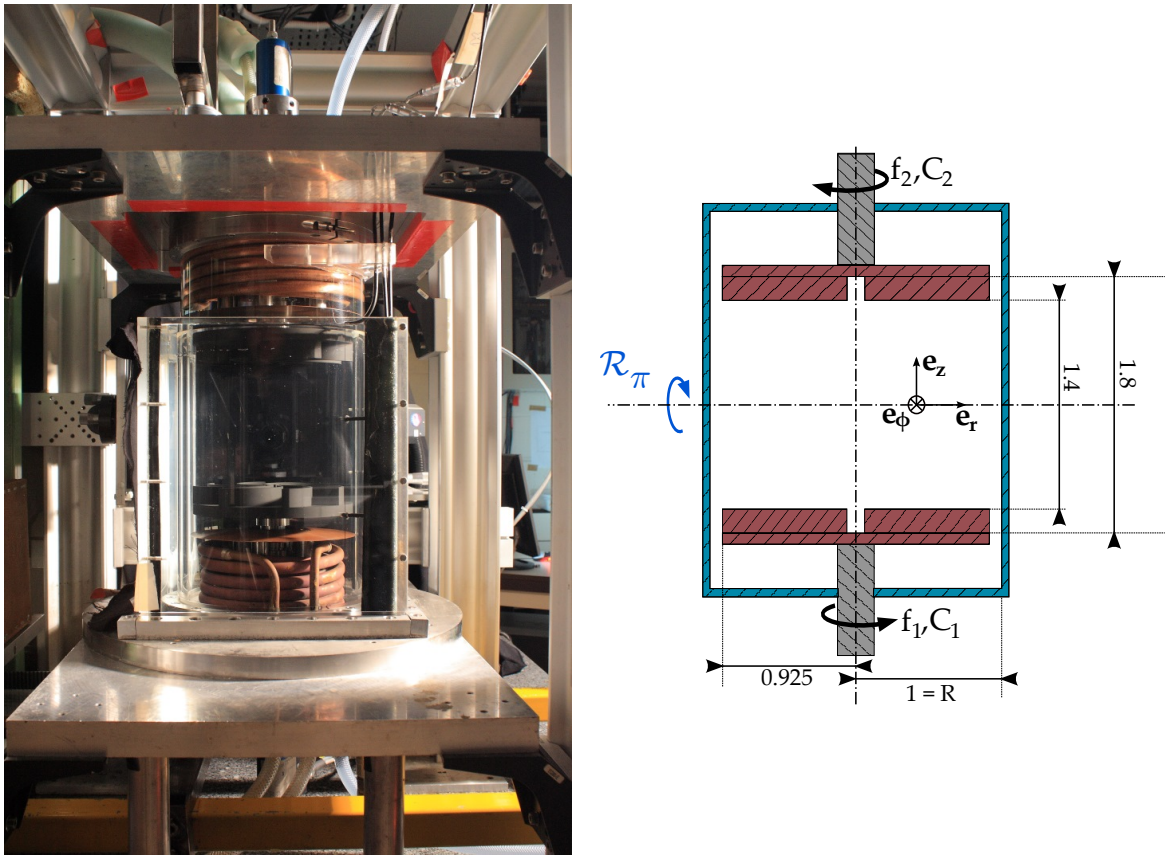

Figure 2.2: The VK2 set-up.

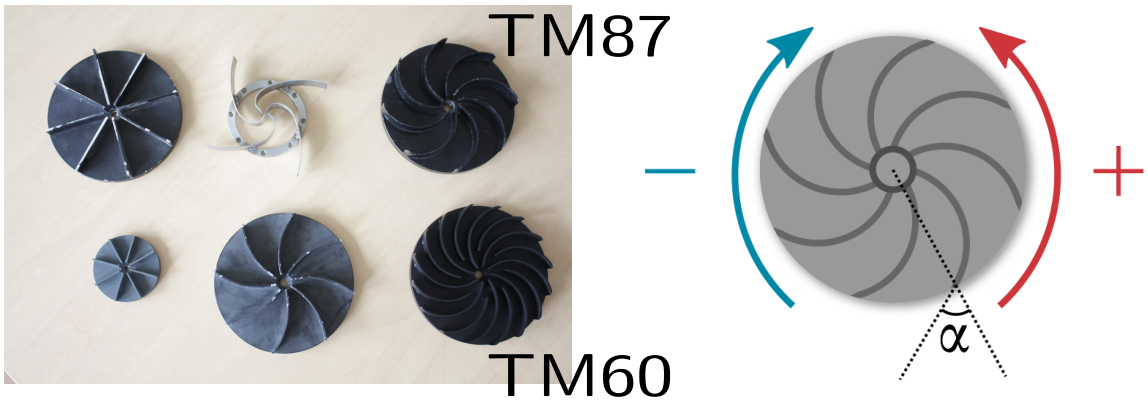

Figure 2.3: Picture of different types of impellers, definition of the angle of curvature α and convention used for the sense of rotation.

impellers	material	radius (cm)	blade number	α (°)	blade thickness (cm)
TM60	stainless steel	9.25	16	72	2
TM87	stainless steel	9.25	8	72	2

Table 2.1: Characteristics of the impellers used in this thesis.

imposed in a range from 1Hz up to typically 10Hz, speed servo loop control ensuring a precision of 2‰ for the mean frequency $f = (f_1 + f_2)/2$.

Relevant parameters

Describing the hydrodynamical properties of a VK flow requires to specify some relevant parameters.

Forcing conditions

The VK set-up located at SPEC allows to set the impellers in corotation or counter rotation and to either impose their rotation frequency or the torque applied by the motors. Throughout this thesis, we will only study flows generated by counter rotating impellers, the frequency of which are imposed.

There exist different types of forcing conditions for generating flows inside a VK set-up. The two main categories are viscous and inertial forcing. Viscous forcing is achieved by using flat disks (*i.e.* without any blades), in which case the fluid is set into motion through momentum diffusion. Inertial forcing, on the other hand, is achieved by fitting blades on these disks, which allow for the generation of a flow through advection[2]. As we said, our study is going to focus on flows generated by TM60 and TM87 impellers. We are thus going to consider inertial forcing only, and the reader is referred to [Ravelet, 2005] for more informations on viscous forcing.

As we noted, the fact that TM60 and TM87 are fitted with curved blades implies that there exist two non-equivalent ways of inertially forcing a VK flow, which are labelled (+) and (-) on Fig. 2.3. As we shall see later, a forcing in the (-) sense is more efficient at creating turbulent fluctuations for the same rotation frequency. Finally, along with the "sign" of the forcing, the curvature of the blades also changes the hydrodynamical properties of the flows and the reader is referred to [Ravelet, 2005] for more discussions on the subject.

Control parameters

The conventional choice made in Saclay for making quantities dimensionless are the radius R of the cylindrical tank for unit length, Ω^{-1} where $\Omega = 2\pi f$ for unit time, and ρR^3 where

[2]In this case, the VK set-up is also called the "french washing machine".

ρ is the mass density of the working fluid for unit mass. In what follows, all the quantities are made dimensionless in this way.

Two control parameters can be defined in our experiment. The first one is the Reynolds number introduced in Sec. 1.3, and the choices of unit length and time naturally lead to a Reynolds number built from R, Ω, and the viscosity ν of the working fluid

$$Re = \frac{R^2\Omega}{\nu}. \tag{2.1}$$

One could actually argue that building a Reynolds number based on the radius of the impellers would have been a better choice. In our case, the difference between the two choices is not important since the radius of the impellers is $R_{imp} = 0.925R$. Since the radius of the cylinder is fixed, the Reynolds number can only be varied by changing either Ω or ν. As we said, f_1 and f_2 can take values from 1Hz up to 10Hz and viscosity can be changed by using different mixings of water and glycerol. Varying these two parameters, it is possible to span range of Reynolds numbers from 10^2 up to more than 10^6. Higher values of Re are reached in the SHREK experiment in Grenoble [Saint-Michel et al., 2014b] where the radius of the tank is 39 cm for the same aspect ratio of 1.8, and superfluid helium is used.

The second control parameter, defined as

$$\theta = \frac{f_1 - f_2}{f_1 + f_2}, \tag{2.2}$$

measures the relative effects of global rotation over a turbulent shear frequency. Indeed, it was shown in [Marié, 2003] that a VK set-up at $\theta \neq 0$ is equivalent within boundary conditions to the same VK set-up at $\theta' = 0$ where $f_1' = f_2' = f$, the whole set-up globally rotating at $(f_1 - f_2)/2$. Our set-up allows to fix the value of θ with an absolute precision of 10^{-3}, and a stability along time better than 0.5×10^{-3}. In the following, we are mainly going to study flows generated with symmetric forcing conditions $(\theta = 0)$.

Measurement systems

The experimental set-up allows for both global and local flow diagnostics.

Torque measurements

Torque (global) measurements at each impeller are performed using SCAIME technology and provide values over the kHz range for K_{p1} and K_{p2}, being respectively the dimensionless torque applied to the bottom and the top shafts (in units of $\rho R^5\Omega^2$). Following the procedure described in [Marié, 2003], they are calibrated using measurements at different mean frequencies, so as to remove spurious contributions from genuine offsets or mechanical frictions. For more details see *e.g.* [Marié, 2003; Saint-Michel, 2013].

In the statistically stationary regime, energy input must balance energy dissipation (heat production) on average. It has been checked that this is true within less than 10% in the SHREK experiment using calorimetric measurements and liquid helium [Rousset

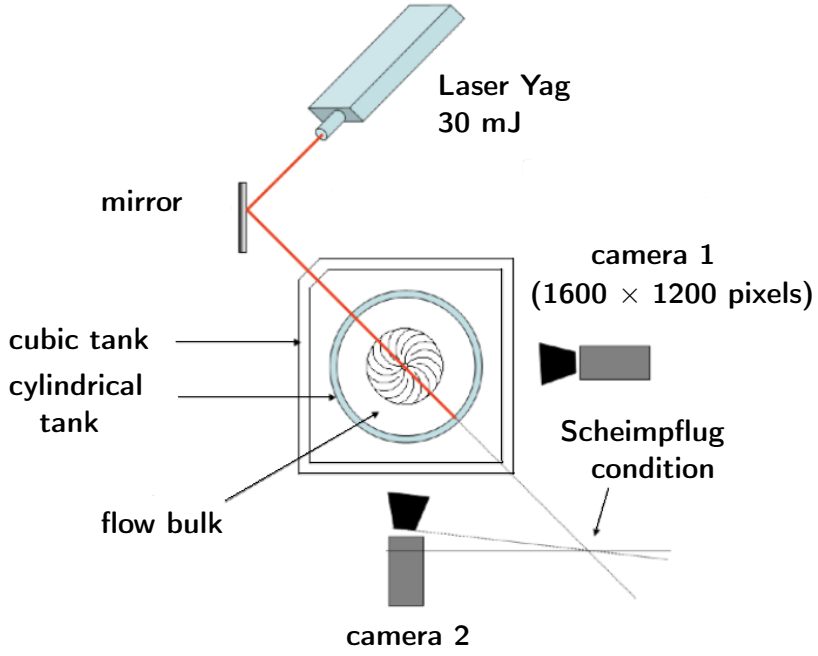

Figure 2.4: Stereoscopic particle image velocimetry set-up for the VK2 experiment.

et al., 2014]. Therefore, torque measurements also provide accurate estimates for the mean global dissipated power D expressed as

$$D = K_{p1}\left(1+\theta\right) + K_{p2}\left(1-\theta\right), \tag{2.3}$$

for $\theta \in [-1, 1]$. The mean dimensionless energy dissipation rate per unit mass then takes the form

$$\epsilon = D\frac{R^3}{\mathcal{V}}. \tag{2.4}$$

Velocimetry measurements

Local velocimetry measurements are performed in the stationary regime using a Stereoscopic Particle Image Velocimetry (SPIV) system provided by DANTEC Dynamics (see *e.g.* [Riethmuller, 1994; Brossard et al., 2009] for reviews on PIV). A sketch of the PIV set-up along with typical instantaneous and time-averaged frames of the velocity field are displayed on Fig. 2.4 and Fig. 2.5. The typical size of the trackers is a few tens of micrometers and their density is 1.4. The SPIV system is constituted of a laser which produces a 1.5 mm thick sheet, and two digital cameras which take successive pictures of the flow at a 15 Hz frequency. The resolution of our camera frame is 1600×1200 pixels, and the reconstruction of the velocity field is done using peak correlation performed over overlapping windows of size 32×32 pixels. The investigation plane covers a whole

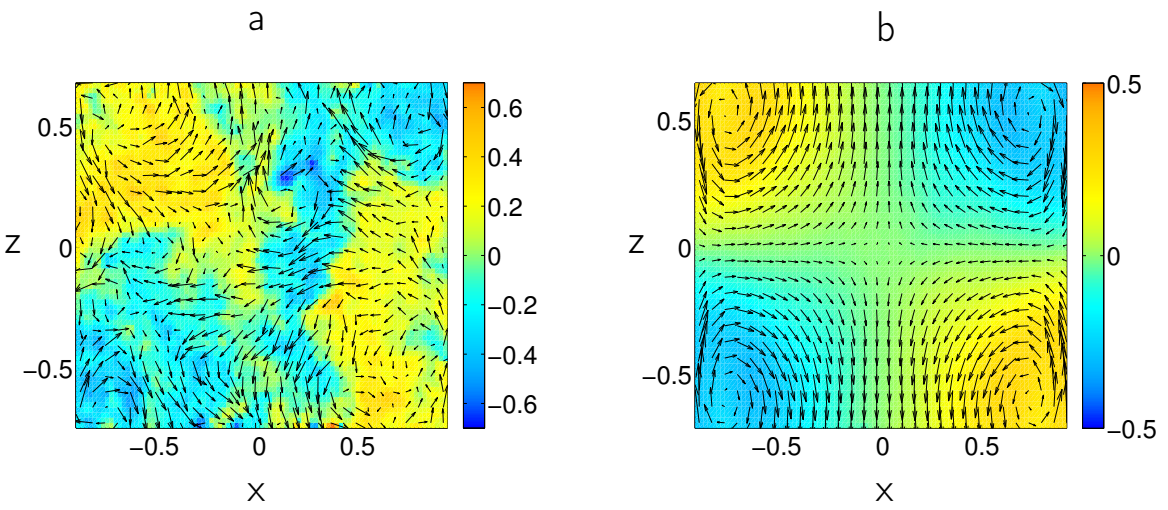

Figure 2.5: Typical instantaneous and mean velocity frames obtained from stereoscopic particle image velocimetry in the meridional plane of measurements at $Re \approx 3 \times 10^5$, and generated with TM87(+). The arrows represent the in-plane component of the velocity while the colors code the orthogonal component.

meridional plane contained inside the volume of interest between the two impellers. The covered area is approximately 20×14 cm^2 and, at the end, we get the three components of the velocity field on a grid of approximate size 59×64 points as time series of statistically independent samples. The maximum spatial resolution we reach is therefore of the order of 3 mm, which is about 10 to 100 times larger than the dissipative scale, depending on Re. The resulting velocity fields are therefore windowed so as to fit to the boundaries of the flow and remove spurious velocities measured in the impellers and at the boundaries. Two types of filtering are further applied to clean the data: first, a global filter to get rid of all velocities larger than $3 \times R\Omega$; then, a local filter (based on velocities of nearest neighbors) to remove isolated spurious vectors. Typically, 1% of the data are changed by this processing. For more details about the experimental setup or the measurement techniques, see *e.g.* [Saint-Michel, 2013].

Zoom procedure

Since the resolution of our measurements is too low to resolve the Kolmogorov scale, Ewe-Wei implemented a zoom procedure in order to get a better resolution. SPIV measurements are now performed by adapting lenses on the objectives of our two cameras. The lenses are *Tokina AT-X M100 F2.8 PRO D* and their manufacturer specifications are given in Tab. 2.2.

For the PIV algorithm to be able to reconstruct the velocity field, the number of tracers inside the flow had to be increased so as to keep their number per reconstruction cells approximately the same. Two main problems are encountered in the quest for very high resolution PIV data.

Focal length	100 mm
Aperture max.	F/2.8
Aperture min.	F/32
Optical system	9 lenses in 8 groups
Diaphragm	9 blades
Close Focus	300 mm
Filter thread	55 mm
Dimensions	73×95.1 mm^2
Weight	540 g
Auto-Focus	yes

Table 2.2: Manufacturer specifications of the lens.

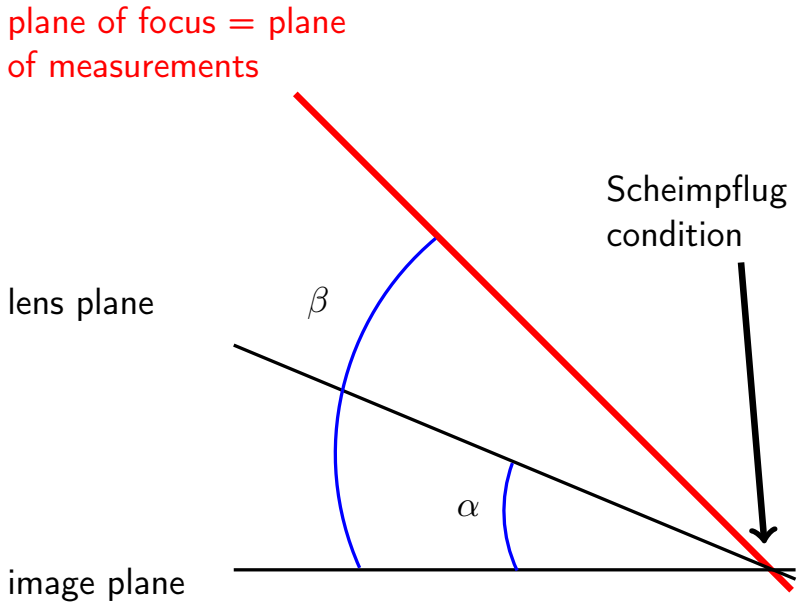

Figure 2.6: The Scheimpflug condition.

First, as is briefly mentioned on Fig. 2.4, the Scheimpflug condition must be satisfied by each cameras in order to make their planes of focus coincide with the Laser sheet. Let us call α the angle between the image and lens planes, and β the angle between the plane of focus and the image plane (see Fig. 2.6 for a sketch). It is known that

$$\tan\alpha = \frac{m}{m+1}\tan\beta, \tag{2.5}$$

where m is the magnification of the optical system. In our experimental set-up, both the plane of measurements and the image plane are fixed so that β should be kept constant for the plane of focus to coincide with the plane of measurements. What Eq. (2.5) tells us, is that keeping β constant, α increases with m. This obviously limits how much one can zoom in the flow with such a technique, and these considerations had to be taken into account by Ewe-Wei.

The second problem is that in order to accurately reconstruct the velocity field from snapshots of the flow, the PIV algorithm needs a minimum number of tracker particles per reconstruction cell. Therefore, as one magnifies the flow, more trackers must be added. Clearly, this also limits the maximum magnification of the flow since adding more particles makes the flow opaque, thus preventing the laser sheet to pass through. However, after some discussions with Ewe-Wei, the main limitation came from the Scheimpflug condition described above, and this second problem was not really one.

Once all of these considerations have been taken into account, Ewe-Wei was able to perform SPIV measurements on areas of approximate size 40×30 mm^2. Typical instantaneous and mean flow are provided on Fig. 2.7 at the center and close to the wall, in the middle shear layer (see Chap. 4 as to why these areas were chosen). Seeding the flow with enough tracers, the velocity field could be reconstructed, now using a post processing system provided by LaVision, with overlapping windows of size 32×32 or 16×16 pixels so as to get different resolutions. The minimum gridstep we can reach using 16×16 pixels windows is of the order of $\Delta_g = 0.25$ mm. As a consequence we gain an order of magnitude in the flow resolution. The total acquisition time was up to two hours, i.e. two order of magnitudes longer than the characteristic time scale of the slowest patterns of the turbulent flow. Fast scales are statistically sampled. In the end, around 30000 statistically independent frames of approximate size 80×80 or 160×160 (depending on the size of the reconstruction cells) are processed which, as we will see in Chap. 4, provide enough data for well converged third order statistics.

All the informations about the flows and corresponding high resolution data which we are going to study in further chapters are provided in Tab. 2.3 and Tab. 2.4.

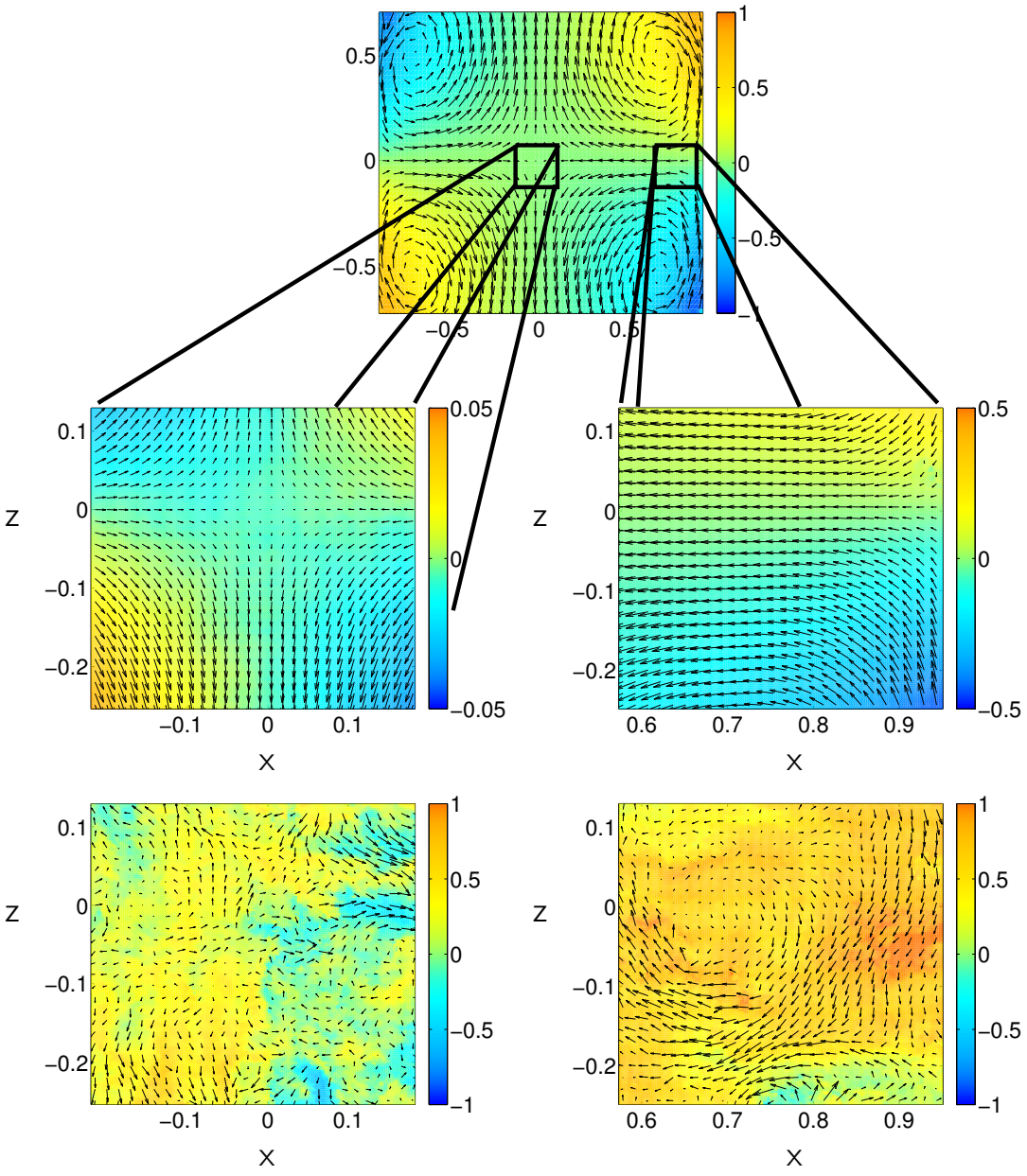

Figure 2.7: Typical instantaneous and mean high resolution velocity fields. These data have been obtained from stereoscopic particle image velocimetry at the center of the flow and near the wall, in the meridional plane of measurements at $Re \approx 3 \times 10^5$, and generated by TM87(-). The arrows represent the in-plane component of the velocity while the colors code the orthogonal component.

name	glycerol (%)	f (Hz)	forcing	Re	η	ϵ
TM60(+)2H_nozoom32_center_glyc100	100	2	(+)	1.5×10^2	4.3×10^{-2}	0.088
TM87(-)1H_zoom16_center_glyc59	59	1.2	(-)	5.9×10^3	3.2×10^{-3}	0.049
TM87(+)5H_zoom16_center_water	0	5	(+)	3.1×10^5	2.1×10^{-4}	0.016
TM87(-)5H_zoom16_center_water	0	5	(-)	3.1×10^5	1.6×10^{-4}	0.046
TM87(+)5H_zoom32_center_water	0	5	(+)	3.1×10^5	2.1×10^{-4}	0.016
TM87(-)5H_zoom32_center_water	0	5	(-)	3.1×10^5	1.6×10^{-4}	0.046
TM87(+)5H_nozoom32_center_water	0	5	(+)	3.1×10^5	2.1×10^{-4}	0.016
TM87(-)5H_nozoom32_center_water	0	5	(-)	3.1×10^5	1.6×10^{-4}	0.046

Table 2.3: Space of hydrodynamic parameters for the flows under investigation.

name	zoom	location	PIV cells size	grid size	Δ_g/η	number of frames
TM60(+)2H_nozoom32_center_glyc100	×	center	32×32	13×11	0.8	50
TM87(-)1H_zoom16_center_glyc59	✓	center	16×16	109×105	0.7	30188
TM87(+)5H_zoom16_center_water	✓	center	16×16	107×103	10	34676
TM87(-)5H_zoom16_center_water	✓	center	16×16	107×103	15	29997
TM87(+)5H_zoom32_center_water	✓	center	32×32	53×51	25	29997
TM87(-)5H_zoom32_center_water	✓	center	32×32	53×51	30	29228
TM87(+)5H_nozoom32_center_water	×	center	32×32	13×11	100	3000
TM87(-)5H_nozoom32_center_water	×	center	32×32	13×11	135	29999

Table 2.4: Settings of the SPIV system for the flows described in Tab. 2.3.

2.3 Symmetries of the set-up

The VK experimental set-up is axisymmetric, *i.e.* it is invariant under any rotation around the axis (Oz)[3]. This means that $SO(2,\mathbb{R})$ (special orthogonal group in dimension 2) is a symmetry group of the system. In the special case of the exact counter rotating regime, the system is, in addition, invariant under a rotation of π around any horizontal axis going through the center of the cylinder. This symmetry is called $\mathcal{R}_\pi$ and is illustrated on Fig. 2.2. As shown in [Nore et al., 2003], this additional invariance enlarges the group of symmetry of the VK set-up to $O(2,\mathbb{R})$ (orthogonal group in dimension 2). Indeed, let us call $\mathcal{R}_z(\psi)$ a rotation of ψ around (Oz) and $\mathcal{R}_\pi$ a rotation of π around any horizontal axis going through the center of the set-up like *e.g.* (Ox). For any vector field $u_i(r,\theta,z)$, $i = 1,2,3$, sharing the same symmetry properties as the VK set-up, we have

$$\mathcal{R}_z(\psi)\begin{pmatrix}u_1\\u_2\\u_3\end{pmatrix}(r,\theta,z) = \begin{pmatrix}u_1\\u_2\\u_3\end{pmatrix}(r,\theta+\psi,z)\,, \tag{2.6}$$

$$\mathcal{R}_\pi\begin{pmatrix}u_1\\u_2\\u_3\end{pmatrix}(r,\theta,z) = \begin{pmatrix}u_1\\-u_2\\-u_3\end{pmatrix}(r,-\theta,-z)\,. \tag{2.7}$$

The key remark is that $\mathcal{R}_z$ and $\mathcal{R}_\pi$ do not commute, thereby generating a group isomorphic $O(2,\mathbb{R})$.

For $|\theta| \ll 1$, the $O(2,\mathbb{R})$ symmetry is slightly broken. Since, in this case, hydrodynamic quantities vary linearly with θ, this parameter can then be taken as a measure of the distance to the exact $O(2,\mathbb{R})$ symmetry. Perturbative methods have been applied in [Chossat, 1993; Porter and Knobloch, 2005].

2.4 Flow topology, multistability and spontaneous symmetry breaking

Naively, it would be expected that VK flows share the same degree of symmetry as the set-up. SPIV measurements allow us to study the topology of VK flows at various Re, and to check whether this is true or not. Fig. 2.8(a) displays an instantaneous velocity frame obtained in the meridional plane of measurement at $Re = 150$ and $\theta = 0$ for TM60(+). At such value of Re, the flow is laminar, steady, and time fluctuations are almost inexistent. We see that the velocity field is indeed $\mathcal{R}_\pi$ symmetric, and is constituted of two recirculation cells separated by an azimuthal shear layer at $z = 0$. These cells are created through Ekman pumping in the neighbourhood of each impellers,

[3] Actually, for impellers mounted with blades, the set-up is only invariant under a discrete number of these rotations. In the discussion that follows, one must keep in mind that axisymmetry is actually slightly broken.

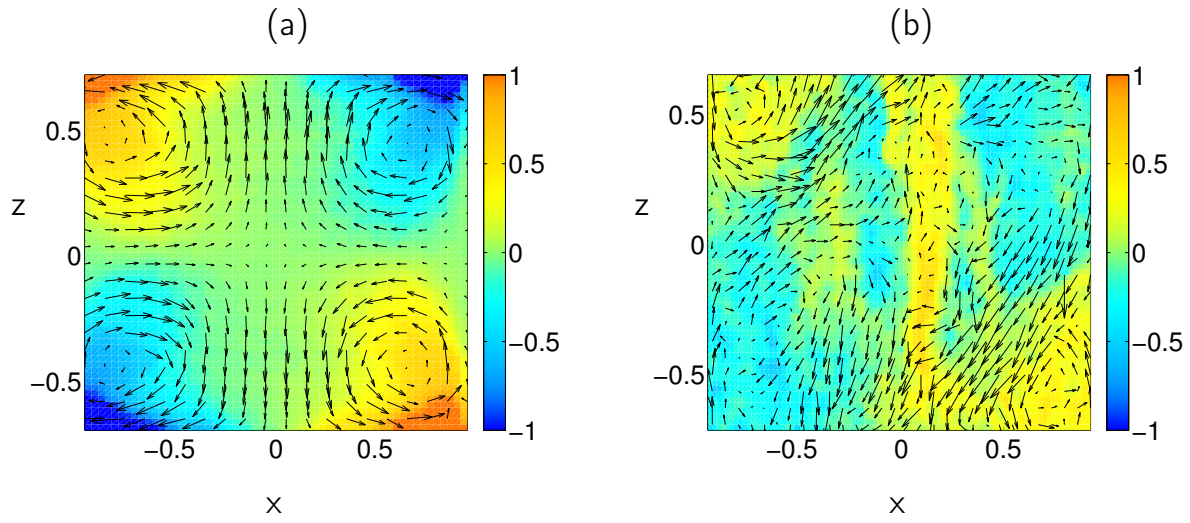

Figure 2.8: Instantaneous frames of the velocity field obtained from stereoscopic particle image velocimetry in the meridional plane of measurements for (a) a laminar flow at $Re \approx 150$ generated with TM60(+) and (b) a fully turbulent flow at $Re \approx 3\times10^5$ generated with TM87(+), both at $\theta = 0$. The arrows represent the in-plane component of the velocity while the colors code the orthogonal component. It can be seen that the laminar flow displays the same degree of symmetry as the VK set-up, while the turbulent flow does not exhibit any obvious symmetry.

and are superimposed to an azimuthal flow generated by the rotation of the nearest impeller. For $\theta \neq 0$, one impeller rotates faster than the other and is going to impose its regime in a wider volume. As a consequence, as $|\theta|$ approaches unity, the median shear layer is progressively sent towards the slower impeller, going from a two-cells to a one-cell topology.

We have seen in Chap. 1 that as Re is increased, the various symmetries of the flow spontaneously break down. This also applies to VK flows and Fig. 2.8(b) displays an instantaneous velocity frame of a fully turbulent VK flow at $Re = 3 \times 10^5$ and $\theta = 0$ for TM87(+). We see that turbulent fluctuations prevent the flow from conserving its axisymmetry as well as its $\mathcal{R}_\pi$ symmetry. This illustrates spontaneous symmetry breaking: even if the system (or equivalently the equations of motion) is $O(2,\mathbb{R})$ symmetric, the flow (or equivalently the solution to the equations of motion) has a lower degree of symmetry. However, as mentioned in Chap. 1, these broken symmetries are recovered in a statistical sense, meaning that even though instantaneous quantities do not share the symmetries of the system, statistical quantities such as the mean flow do, assuming ergodicity. This is illustrated on Fig. 2.9(a) which displays the mean flow for the same set of data as in Fig. 2.8(b), and which exhibits the same topology as the instantaneous laminar case showed on Fig. 2.8(a).

Multistability and spontaneous statistical symmetry breaking

In the case of TM60(-)/TM87(-), and for $Re \gtrsim 10^4$, the ground state of VK flows is degenerate. This degeneracy can be observed when considering time-averages, as illustrated on Fig. 2.9. The mean flows displayed on Fig. 2.9 have been obtained at $Re = 3 \times 10^5$ and $\theta = 0$. The one displayed on Fig. 2.9(b) is, from our discussion above, the expected canonical mean flow. It is $\mathcal{R}_\pi$ symmetric and will therefore be denoted (s). However, quite surprisingly, a bifurcation to one of the two equally stable states displayed on Fig. 2.9(c) and (d) can be observed. These flows are not $\mathcal{R}_\pi$ symmetric, but rather have the one-cell topology which would be expected when $\theta \approx \pm 1$. These bifurcated states are denoted (b_1) when the bottom impeller (labelled 1 on Fig. 2.2) imposes its regime and (b_2) when the top impeller (labelled 2 on Fig. 2.2) does. The existence of such multistability in VK flows was first reported in [Ravelet et al., 2004], and studied in more details in [Ravelet, 2005]. This study revealed that the symmetric state (s) is actually only metastable and that at any time t, the probability of remaining in this state until the bifurcation time $t_{bif} > t$ decreases exponentially: $P(t < t_{bif}) \propto \exp(-t/\tau)$. The parameter τ is a function of θ, and diverges to infinity as $\theta \to 0$. Of course, in real experiments, θ is never exactly vanishing, and there always remain some nonzero fluctuations which, in the long term, make the flow end up in one of the two bifurcated states. When this occurs, the flow spontaneously loses its statistical $\mathcal{R}_\pi$ symmetry which held for time-averaged quantities. This further break-down of the $\mathcal{R}_\pi$ symmetry is thus called *statistical symmetry breaking*. However, due to the random fluctuations of θ, the choice of final state appears to be equiprobable between (b_1) and (b_2), so that the $\mathcal{R}_\pi$ symmetry, broken for time-averaged quantities, still holds when considering ensemble averages. As a consequence, since tran-

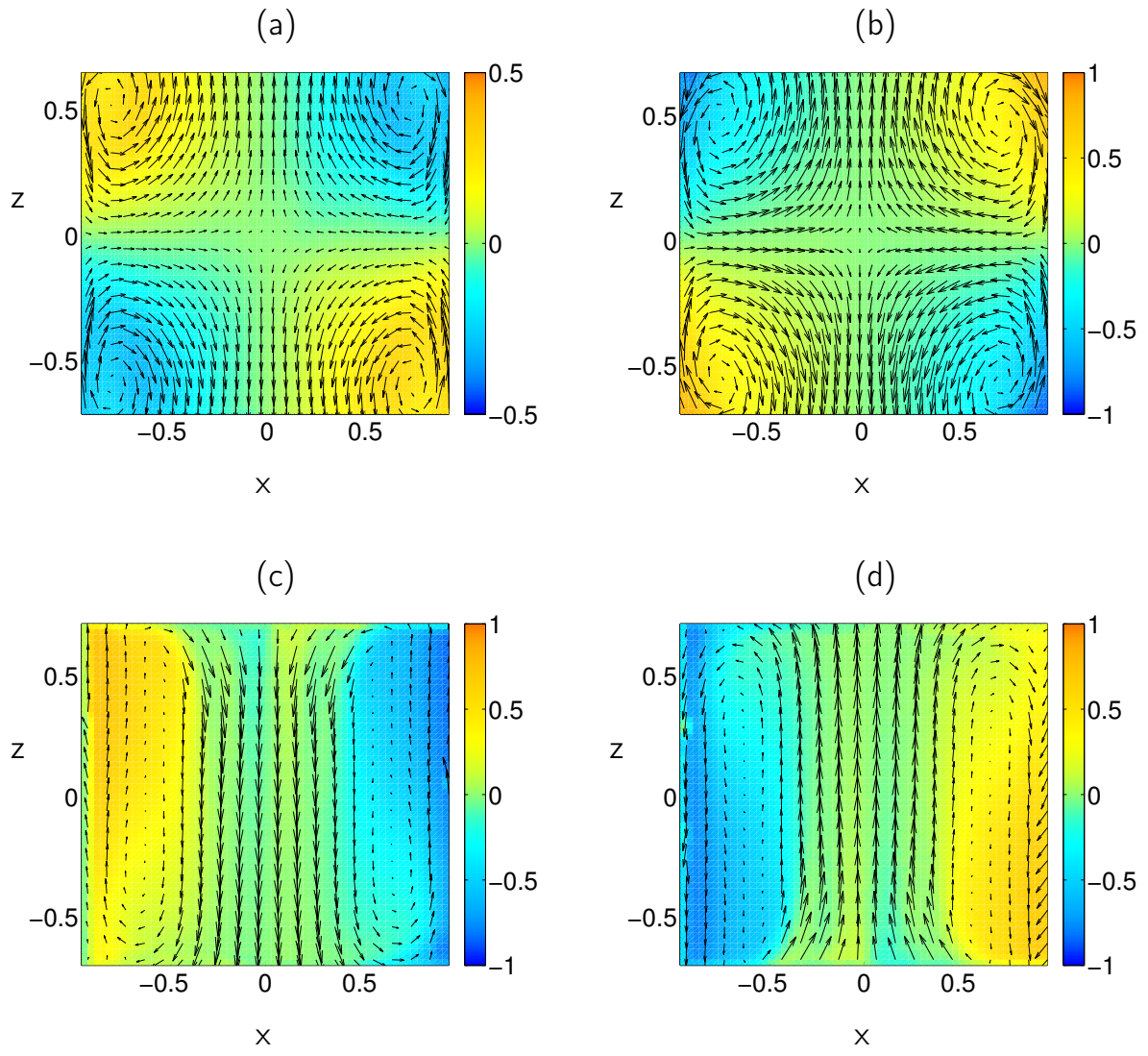

Figure 2.9: The four possible large-scale topologies for mean VK flows generated by (a) TM87(+), (b) TM87(-) symmetric state (s), (b) TM87(-) bifurcated state (b_1), (d) TM87(-) bifurcated state (b_2). These maps illustrate the statistical spontaneous symmetry breaking which occurs for $Re \gtrsim 10^4$ in VK flows.

sitions between the two bifurcated states, or from one bifurcated state to (s) do not occur, this statistical symmetry breaking makes the system lose its ergodicity.

Multistability and spontaneous dynamical symmetry breaking

Spontaneous statistical symmetry breaking does not occur for TM60(+)/TM87(+) because the forcing do not produce large enough fluctuations to induce a bifurcation. Nonetheless, in this case, VK flows still exhibit multistability. In [Cortet et al., 2010], the authors consider time series obtained from SPIV measurements of the dimensionless space-averaged vertical component of the angular momentum $L_z(t)$. It was noted that for $Re \approx 4\times10^4$ and $\theta = 0$, $L_z(t)$ does not fluctuate in a random fashion around 0, but instead exhibits a tendency to lock on plateaus for which $L_z = \pm L_z^*$. This is another example of multistability in VK flows: at a critical value of Re, there appear metastable, $\mathcal{R}_\pi$ asymmetric states which the system is now able to explore dynamically. This dynamics occurs over two well separated time scales. The smaller one corresponds to fluctuations due to the usual small-scale turbulence, while the larger one corresponds to periods during which the flow occupies one of the two metastable states. This spontaneous "momentization" dynamically breaks down the time-averaged $\mathcal{R}_\pi$ symmetry for short periods of time, and is therefore referred to as *dynamical symmetry breaking*. However, since the flow shares an equal amount of time between the two states, the $\mathcal{R}_\pi$ symmetry (and therefore ergodicity) still holds for very large times. For further discussions, see also [Cortet et al., 2011].

Analogy with ferromagnetism

In [Cortet et al., 2010; 2011], the authors introduced parameters typically used for the study of phase transitions in lattice models. They define the analogs of an order parameter $I = L_z$, a susceptibility $\chi = \partial\overline{I}/\partial\theta$, and a temperature $T \sim 1/\log Re$. They exhibited the singular behaviour of $\chi(\theta = 0)$ for $Re \approx 4\times10^4$, and even provided the value of the critical exponent $\gamma = 1$ in accordance with [Castaing, 1996]. These features therefore suggest that the mechanisms responsible for statistical and dynamical spontaneous symmetry breakings in VK flows are analogous to the mechanisms leading to phase transitions in appropriate corresponding lattice models. In order to understand these mechanisms, a toy model of an out-of-equilibrium system which can be mapped onto a real VK flow was first designed in [Saint-Michel et al., 2014a]. This model exhibits spontaneous symmetry breaking through a zero-mode mechanism, and manages to reproduce the experimental results reported by [Cortet et al., 2010; 2011] in a quantitative way, by specifying only three parameters. In a following work, strong evidences were provided that coherent structures in VK flows can be described as equilibrium states of an Ising model [Thalabard et al., 2015]. In this framework, one can define hydrodynamic analogs of the notions of spin, magnetization, temperature, external field and susceptibility. The bifurcation from the $\mathcal{R}_\pi$ symmetric state (s) to (b_1) or (b_2) then appears as a transition between the analogs of a paramagnetic and a ferromagnetic phase. The deep analogy which seems

to exist between the physics of VK flows at large scales and ferromagnetism is quite remarkable as it allows to understand some properties of an out-of-equilibrium system in the framework of equilibrium statistical physics. For more discussions see [Thalabard, 2013; Saint-Michel, 2013].

2.5 Axisymmetric turbulence: a journey in 2.5D

In Chap. 1, we insisted on the fact that there does not exist any complete statistical theory of turbulence. The most successful theory we have is due to Kolmogorov which, however, does not account for experimental results such as intermittency [Frisch, 1995]. The 3D case being too complicated, the intuitive approach would be to first build a statistical theory for 2D turbulence, and then investigate how such a theory can be generalized to the 3D case.

In 1949, Onsager built a hamiltonian equilibrium statistical mechanics of 2D inviscid turbulence [Onsager, 1949]. In this work, Onsager models the vorticity field by discrete point vortices, and notices that whenever there exist negative "temperatures", strong vortices will cluster and create large coherent structures, as is experimentally observed in 2D turbulence. However, Onsager was aware [Onsager, 1949] that the discrete nature of his description makes it incomplete and that a continuous description was needed. Building such a theory was achieved in [Miller, 1990; Robert, 1990; Sommeria and Robert, 1991] with a certain success [Sommeria et al., 1991; Chavanis and Sommeria, 1996; Chavanis et al., 1996; Chavanis and Sommeria, 1997; 1998a;b; Bouchet and Sommeria, 2002; Chavanis, 2004].

Therefore, the question is whether it is possible to extend these considerations to 3D turbulent flows, but the generalization is actually difficult for various reasons. First of all, the physics of 2D turbulent flows (see *e.g.* [Tabeling, 2002] for a review) is quite different from the 3D case because in 2D, the enstrophy, which is defined as $\Omega = \boldsymbol{\omega}^2/2$, is conserved. As a consequence, the vortex stretching mechanism which plays a central role in 3D turbulence (see Chap. 1) does not exist in 2D where vorticity is simply redistributed within the flow, and the zeroth law does not apply. In order to make progress, the key remark is that the work of Robert and Sommeria [Robert, 1990; Sommeria and Robert, 1991] is based upon the existence of a conserved scalar quantity which allows for the existence of a Liouville theorem. Therefore, their approach can be applied whenever the turbulent dynamics conserve such a quantity. Axisymmetric turbulence then appears as an interesting framework because it conserves angular momentum, so that Robert and Sommeria's ideas can be applied, whilst maintaining features of 3D turbulence like, for instance, the validity of the zeroth law. In this sense, axisymmetric flows are intermediates between 2D and 3D turbulence, sometimes called 2.5D flows. A statistical theory for axisymmetric flows was built by [Leprovost et al., 2006].

2.6 Energy cascade in VK flows

As we mentioned in Sec. 2.5, the mechanisms through which energy is dissipated in 2D and 3D turbulent flows are quite different. In 3D, the quadratic quantities conserved by Euler equations are the kinetic energy $E = \boldsymbol{u}^2/2$ and the helicity $H = \boldsymbol{\omega} \cdot \boldsymbol{u}/2$ (see Chap. 1). Energy cascades towards small scales with a spectrum $E^{(1D)}(k) \sim k^{-5/3}$ for homogeneous isotropic turbulence, while a cascade of helicity is also expected [Kraichnan, 1973; Borue and Orszag, 1997; Ditlevsen and Giuliani, 2001]. On the other hand, in 2D, the conserved quadratic quantities are the energy E and the enstrophy $\Omega = \boldsymbol{\omega}^2/2$. Therefore, vortex stretching is absent, so that Taylor's mechanism is irrelevant. Instead, Kraichnan scenario [Kraichnan, 1967] occurs where energy cascades towards large scales with $E^{(1D)}(k) \sim k^{-5/3}$, while enstrophy cascades towards small scales with $E^{(1D)}(k) \sim k^{-3}$. The difference between 2D and 3D can be explained by the nature of the conserved quadratic quantities: in 2D, both E and Ω are sign definite while, in 3D, only E is [Brissaud et al., 1973; Kraichnan, 1973].

As we saw in Sec. 2.4, fully developed turbulent VK flows are not axisymmetric but remain statistically axisymmetric. Since axisymmetric flows can be considered as intermediate between 2D and 3D turbulence, the obvious question is whether energy dissipation mechanisms in VK flows are closer to the 2D or 3D case. It was experimentally shown that stationary states in VK flows are close to Beltrami states as Re is increased [Monchaux et al., 2006; 2008]. Beltrami flows are defined by a vorticity everywhere proportional to the velocity $\boldsymbol{\omega} = \alpha \boldsymbol{u}$. This class of flows has been widely studied [Joseph, 1964; Truesdell, 1954; Constantin and Majda, 1988] as they appear in DNS of turbulent flows [Pelz et al., 1985; Yakhot et al., 1987], and constitute an analytical solution to the 3D Euler equations. The key remark is that for such flows, helicity becomes sign definite so that both quadratic invariants in 3D are now sign definite, as in the 2D case. Moreover, the energy and helicity spectra are related via $H^{(1D)}(k) = kE^{(1D)}(k)$ which is the analog of the relation $\Omega^{(1D)}(k) = k^2 E^{(1D)}(k)$ in 2D turbulence. Therefore, the cascading process is dominated by helicity transfers at small scales and by energy transfers at large scales. Now, all these remarks tend to suggest that the energy dissipation mechanism in VK flows is close to what occurs in 2D turbulence.

The question of the direction of the energy and helicity cascades, their localities, and the dependence of the corresponding spectra on the wavenumber k in a VK flow generated with TM87(+) was addressed in [Herbert et al., 2012]. The authors reported the first experimental observation of a dual cascade of energy and helicity, where it was shown that the energy spectra at large wavenumbers scales as k^{-2}, and changes to $k^{-7/3}$ as Re is increased. This is explained as the relative influence of local and non-local interactions in the scale dynamics. These results suggest that Kolmogorov's theory can be excluded for the description of turbulence in the inertial range of high Re stationary VK flows[4]. Interestingly enough, it was also noted that the value of Re for which the interactions switch from a non-local to a local dynamics is associated with the critical Re at which

[4]Which is not too surprising since turbulence in VK flows are neither homogeneous nor isotropic.

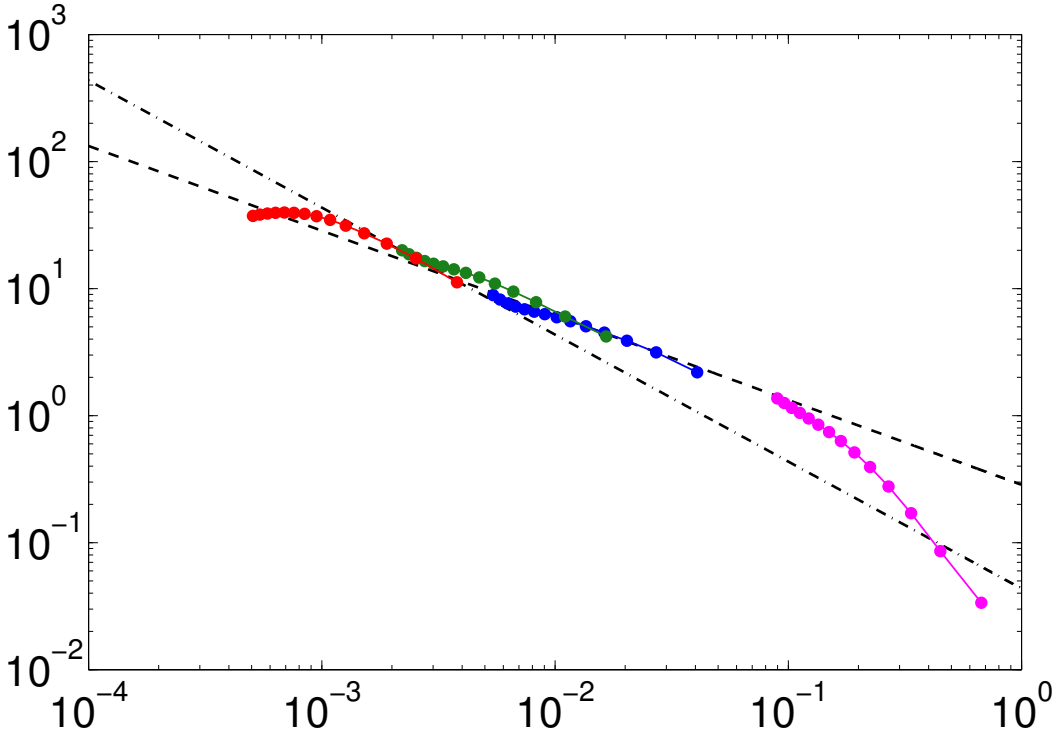

Figure 2.10: Energy spectrum computed from stereoscopic particle image velocimetry obtained in VK flows generated with TM87(-). (−●−) TM87(-)5H_nozoom32_center_water, (−●−) TM87(-)5H_zoom32_center_water, (−●−) TM87(-)5H_zoom16_center_water, (−●−) TM87(-)1H_zoom16_center_glyc59.

the dynamical spontaneous symmetry breaking observed in [Cortet et al., 2010] appears.

From the data presented in Tab. 2.3, it is possible to compute the energy spectrum of fully turbulent VK flows directly in the space domain, at smaller scales than what was done in [Herbert et al., 2012]. Moreover, according to K41, all the spectra in the inertial and intermediate dissipation ranges can be collapsed onto a single curve [Frisch, 1995; Gibson and Schwarz, 1963]. Fig. 2.10 displays the normalized energy spectrum, compensated by $k = 1/\ell$, obtained from SPIV measurements performed at the center of the tank for TM87(-). We are able to span three decades in $k\eta$ by changing the resolution of our cameras, the size of the interrogation cells in the PIV processing, and by decreasing the Reynolds number in order to increase the Kolmogorov scale. At the beginning of the inertial range, we find the same scaling for the energy spectrum as in [Herbert et al., 2012]. However, at larger wavenumbers, we observe that the scaling changes to $E^{(1D)} \sim k^{-5/3}$ showing that K41 applies at smaller scales, and indicating an energy dissipation mechanism like in 3D. This is a very nice result because it is the first time (to our knowledge) that such a spectrum is computed directly in the space domain over such a wide range of scales. Finally, it can be observed from Fig. 2.10 that at small scales, the energy spectrum departs from the universal, infinite Reynolds number curve.

This confirms the result obtained by [Gibson and Schwarz, 1963] that the dissipation range begins at scales of the order of 10η.

2.7 Zeroth law in VK flows

Experimental results

A central assumption in K41 is that the mean energy dissipation rate per unit mass ϵ in turbulent flows remains finite in the limit $Re \to \infty$. In VK flows, its value depends on the control parameters, the characteristics of the impellers, and the mean flow geometry [Ravelet et al., 2008]. The variations of ϵ as a function of Re at $\theta = 0$ are provided on Fig. 2.11 for TM87(±) and TM60(±). At low Reynolds numbers, the dissipation rate decays as Re^{-1} (dotted line), until $Re \approx 300$ where turbulence sets in. The dissipation rate then levels off (zeroth law) at a value which depends upon the large scale mean flow geometry. For TM87(+) (●), ϵ is the lowest and increases for state (s) (◆) due to the larger amount of turbulent fluctuations generated by TM87(-). For bifurcated states, the mixing layer is sent towards one of the impellers, the other one "trying" to impose its regime in the whole bulk. As a consequence, a greater amount of energy must be spent by the receiving impeller in order to maintain its rotation frequency. In this case, the dissipation rate is larger (▲). In conclusion, these measurements show that whatever the mean flow geometry, the zeroth law of turbulence holds for the four possible configurations at $\theta = 0$.

Direct numerical simulations

DNS of von Kármán flows are performed in the group of Caroline Nore at the Laboratoire d'Informatique pour la Mécanique et les Sciences de l'Ingénieur (LIMSI) in Orsay, and in collaboration with Jean-Luc Guermond at Texas A&M, in order to study the dynamo effect. During the second year of my Ph.D, a collaboration began between them and our group. The first step of this collaboration was to compare diagnostics obtained both numerically and experimentally in order to calibrate the hydrodynamic part of their numerical scheme. The first quantity we looked at was ϵ for flows generated by TM87(±). However, the only torque measurements performed with TM87 which were available at the time were made by Brice [Saint-Michel, 2013] at $Re \geqslant 10^5$ (● - ◆ - ▲), which is a range still out of reach for DNS. Therefore, new torque measurements have been performed by Cécile at lower Re which have then been post-processed by Bérengère and I. In the meantime, Loïc Cappanera and Caroline provided us with their numerical estimates of ϵ obtained with the SFEMaNS code [Cappanera, 2015]. The comparison between experiments and DNS is provided on Fig. 2.11. The values of ϵ obtained by DNS (★ - ★) are in very good agreement with experimental measurements (■ - ■), even though the numerical estimates seem to decrease slightly slower than our measurements in the Stokes regime.

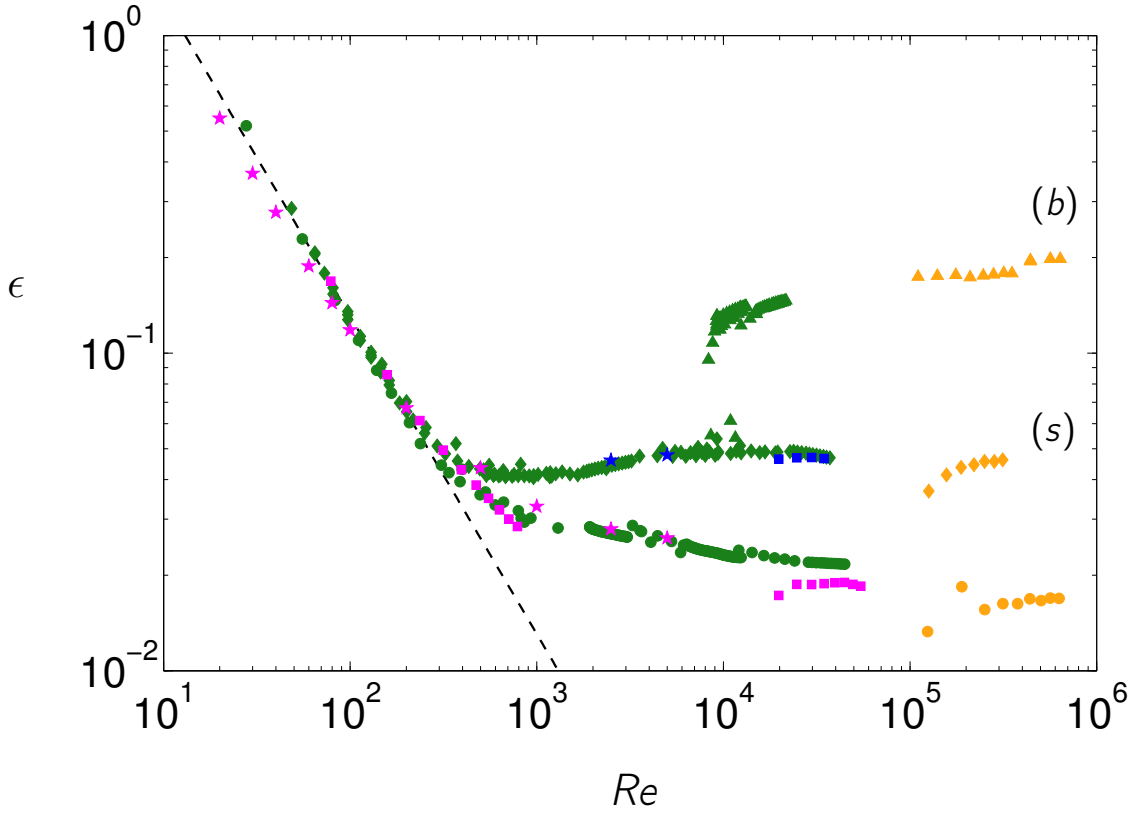

Figure 2.11: Estimates of the mean energy dissipation rate per unit mass ϵ as a function of the Reynolds number. These estimates have been obtained via torque measurements for symmetric forcing conditions. (● - ◆ - ▲) torque measurements performed using TM60 impellers [Ravelet, 2005], (● - ◆ - ▲) torque measurements performed using TM87 impellers [Saint-Michel, 2013]. (● - ●) (+) forcing condition, (◆ - ◆) $\mathcal{R}_\pi$ symmetric state (s), and (▲ - ▲) bifurcated states (b). No distinction is made between the two bifurcated states since they have the same mean energy dissipation rate. (■ - ■) torque measurements performed by Cécile for TM87(±). The results obtained from DNS of VK flows with TM87(±) by Loïc Cappanera are displayed as (★ - ★) following the same colour code. At low Re, both experimental measurements and DNS show a variation $\epsilon \sim Re^{-1}$. For $Re \geqslant 10^5$, ϵ stabilizes at a nonzero value for the four possible states.

In conclusion, we see that the zeroth law of turbulence holds in experimental VK flows for any symmetric large-scale configuration at $\theta = 0$, and that there are strong evidences that this is also the case in DNS. The time reversal symmetry, explicitly broken by viscous forces, is not recovered as $\nu \to 0$. As a consequence, the VK geometry offers an interesting framework in order to investigate the dissipation anomaly in fully developed turbulence.

Chapter 3

Onsager's Mechanism For Energy Dissipation

> The difficulty lies not so much in developing new ideas as in escaping from old ones.
>
> *John Maynard Keynes*

Contents

Figure 3.1: Lars Onsager.

In the 1930's, the French mathematician Jean Leray investigated the possibility for solutions to the INSE to lose their regularity in finite time. In 1949, Onsager realized that the development of such singularities may have physical consequences as they may lead to a break-down of energy conservation in the limit of infinite Reynolds number. Since then, the regularity of the INSE has been widely studied, and several results have been analytically derived. However, the regularity of the INSE is still unknown. In this chapter, we introduce Onsager's and Leray's ideas and connect them to the more classical picture of turbulence presented in Chap. 1. We present some mathematical results on the regularity of the INSE, and discuss the results obtained by [Duchon and Robert, 2000], which are central to the study performed in this thesis and presented in the following chapters.

3.1 Onsager's conjecture

For the INSE to be well defined, the velocity field need to only be twice continuously differentiable and the pressure field once, *i.e.* $\boldsymbol{u} \in C^2(\mathcal{V}, \mathbb{R}^+)$ and $p \in C^1(\mathcal{V}, \mathbb{R}^+)$. However, as remarked by [Leray, 1934b], it is not unreasonable to believe that starting from an incompressible velocity field $\boldsymbol{u}^0 \in C^2(\mathcal{V})$, the mechanism which tends to smooth out possible irregularities, *i.e.* the viscous forces, might not be efficient enough to ensure that $\boldsymbol{u}$ will remain in $C^2(\mathcal{V})$ for all later times. Actually, the question of knowing whether such singularities can develop starting from a given smooth initial condition is still an open, one million dollars problem [Fefferman, 2006]. This question also arises for Euler equations,

and the two problems, despite some differences, are deeply connected. However, these problems were largely ignored by physicists, until it was realized that they may have important practical consequences.

The chemist Lars Onsager was the first to make the connection between the regularity properties of the velocity field and anomalous dissipation [Onsager, 1949]. In order to explain this, let us consider a local space averaged (low-pass filtered) velocity field[1]. In the INSE, the unknown velocity and pressure fields contain informations about the flow at all possible scales. Let us define a coarse-grained velocity field by taking the convolution of $\boldsymbol{u}$ with some kernel G_ℓ

$$u_i^\ell(\boldsymbol{x},t) = \int d\boldsymbol{r}\; G_\ell(r)\, u_i(\boldsymbol{x}+\boldsymbol{r},t), \tag{3.1}$$

where G is a smooth filtering function, non-negative, spatially localized and such that $\int d\boldsymbol{r}\; G(r) = 1$. The function G_ℓ is rescaled with ℓ as $G_\ell(r) = \ell^{-3} G(r/\ell)$. This process of coarse-graining thus averages out fine details about the fields while keeping informations about large scales. One can think of this as taking a picture of the Empire State Building with a camera having a finite resolution. It can be seen on Fig. 3.2 that details about the building can be seen from the building size scale down to the windows scale. However, details finer than the size of the windows, like *e.g.* a fly which would have landed on the building at the moment of the picture cannot be recovered, even by zooming on the picture. In image processing, the scales we have access to from the picture are called resolved while those which have been averaged out are called unresolved. We shall keep this terminology in the following.

Let us now derive the equations satisfied by u_i^ℓ. Starting from the INSE and applying the coarse-graining procedure we get

$$\partial_t u_i^\ell + u_j^\ell \partial_j u_i^\ell = f_i^\ell - \partial_i p^\ell + \nu \partial_{jj} u_i^\ell, \tag{3.2}$$

$$\partial_j u_j^\ell = 0, \tag{3.3}$$

where $f_i^\ell = -\partial_j \tau_{ij}^\ell$ is called the turbulent force, and $\tau_{ij}^\ell = \left(u_i u_j\right)^\ell - u_i^\ell u_j^\ell$ is the subscale stress tensor. We thus obtain a sequence of equations describing the dynamics of large scales. From these equations, we can derive a local energy balance at scale ℓ

$$\partial_t E^\ell + \partial_j \mathscr{E}_\nu^{\ell,j} = -\Pi^\ell - \mathscr{D}_\nu^\ell, \tag{3.4}$$

where $E^\ell = u_i^\ell u_i^\ell/2$, $\mathscr{E}_\nu^{\ell,j} = u_j^\ell\left(E^\ell + p^\ell\right) + u_i^\ell \tau_{ij}^\ell - \nu\left(\partial_j E^\ell + \partial_i\left(u_i^\ell u_j^\ell\right)\right)$, $\Pi^\ell = -S_{ij}^\ell \tau_{ij}^\ell$, $\mathscr{D}_\nu^\ell = 2\nu S_{ij}^\ell S_{ij}^\ell$, and $S_{ij}^\ell = \left(S_{ij}\right)^\ell$. Π^ℓ appears as a source term (*a priori* positive or negative) which stems from interactions between scales larger and smaller than ℓ. Therefore, energy is not conserved at large scales, even for $\nu = 0$, because small modes excite higher modes, their interactions being described by Π^ℓ. However, if $\boldsymbol{u}$ satisfies the regularity condition

[1] Which is what we get as the output of a PIV system. For more discussions on the relation between PIV measurements and the filtering approach, see Sec. 6.1.

Figure 3.2: The large scales of the Empire State Building.

given in Eq. (1.5), it is easy to show that τ_{ij}^{ℓ} vanishes as $\ell \to 0$ so that Eq. (3.4) gives back Eq. (1.21), and energy conservation is recovered for $\nu = 0$ (1.15).

Onsager studied turbulence in the 1940's [Eyink and Sreenivasan, 2006] and, during this period of time, published only one paper in this field [Onsager, 1949]. At the end of this paper, he noted that $\nu \to 0$ does not actually ensure conservation of energy because in this limit it is possible that the velocity field does not remain smooth enough for allowing Π^{ℓ} to vanish as $\ell \to 0$. The key realization of Onsager was that τ_{ij}^{ℓ} and S_{ij}^{ℓ} can be rewritten in terms of velocity increments as

$$\tau_{ij}^{\ell} = \left(\delta u_i \delta u_j\right)^{\ell} - \delta u_i^{\ell} \delta u_j^{\ell}, \tag{3.5}$$

$$S_{ij}^{\ell} = -\frac{1}{2\ell} \int d\boldsymbol{r}\ \partial_i G_{\ell}(r)\, \delta u_j(\boldsymbol{x}+\boldsymbol{r}, t) + \partial_j G_{\ell}(r)\, \delta u_i(\boldsymbol{x}+\boldsymbol{r}, t). \tag{3.6}$$

Let us assume that the velocity field has some regularity at small scale which can be expressed as a Hölder continuity condition with exponent h

$$|\boldsymbol{u}(\boldsymbol{x}+\boldsymbol{r}) - \boldsymbol{u}(\boldsymbol{x})| < C r^h, \tag{3.7}$$

or equivalently

$$|\delta \boldsymbol{u}(\boldsymbol{r})| = \underset{r \to 0}{O}\left(r^h\right). \tag{3.8}$$

Let us now define $\delta u(\ell) \overset{def}{=} \sup_{r<\ell} \delta u(\boldsymbol{r})$. We directly get that

$$\Pi^\ell = \underset{\ell\to 0}{O}\left(\frac{\delta u(\ell)^3}{\ell}\right). \tag{3.9}$$

Therefore, if $\boldsymbol{u}$ is Hölder continuous in space with exponent h, *i.e.* $\delta u(\ell) \sim \ell^h$, then

$$\Pi^\ell = \underset{\ell\to 0}{O}\left(\ell^{3h-1}\right). \tag{3.10}$$

As a consequence, we see that if $h > 1/3$, Π^ℓ vanishes as $\ell \to 0$ and Euler equations are seen to conserve energy. On the other hand, it may well be that this condition does not hold, in which case turbulent flows might keep on dissipating energy, even if $\nu \to 0$. Onsager's arguments lead to the conclusion that a necessary condition for the mean energy dissipation rate ϵ not to vanish in inviscid turbulence is $h \leqslant 1/3$, $h = 1/3$ being the K41 case. In this case, the non-vanishing of ϵ would stem from a lack of smoothness in the velocity field, and could be an alternative to Taylor's mechanism for energy dissipation. As a matter of fact, there are evidences coming from DNS that a continuous set of scaling (or Hölder) exponents h are allowed, with the most probable exponent close to 1/3 [Muzy et al., 1991; Kestener and Arneodo, 2004]. Therefore, Onsager's hypothesis is an interesting candidate for explaining the zeroth law of turbulence, and would allow for a deeper understanding of $\boldsymbol{H_3}$.

Finally, in his paper, Onsager also remarked that if the velocity field does not remain differentiable, the expression of the equations of motion as differential equations should be replaced by a more general formulation. This is what we discuss now (see [Eyink, 2008a] for more details).

3.2 Weak formalism

Since solutions to the INSE may lose their regularity in finite time, a more general mathematical framework to study fluid dynamics is needed. Indeed, if $\boldsymbol{u}$ cannot satisfy any regularity condition stronger than a Hölder condition with some exponent $h < 1$, then it is not differentiable. In this case, $\boldsymbol{u}$ cannot be a solution to the INSE in the usual sense and we must work in a more general framework than the one introduced in Chap. 1. We already know how to relax regularity constraints and generalize the concept of functions, we get distributions [Schwartz, 1997]. The weak formalism applies the idea of distributions in order to make sense of solutions to partial differential equations (PDE) which are not necessarily differentiable.

Weak formulation of the INSE

Before writing this part of the manuscript, I had the intention of providing a rigorous mathematical definition of weak solutions to the INSE. However, such a definition introduces notions of functional analysis which might not be familiar to all physicists.

Moreover, there exists different (but not unrelated) definitions for these weak solutions [Leray, 1933; 1934b;a; Hopf, 1951; Lions, 1969; Masuda, 1984]. Since all these notions are not of direct interest in this manuscript, and being too rigorous would only overwhelm the reader with a flood of unnecessary mathematical concepts which would not serve the intended clarity of this manuscript, I will restrict the definition of weak solutions to the necessary minimum, and give some of their most important properties.

The key idea of the weak formalism is to move differential operators on test functions through integration by parts, so as to impose minimum regularity assumptions on solutions to PDE. Let us assume that (u_i, p) is a solution to the INSE in the classical sense. Then, for any test functions ψ, φ_i, $i = 1, 2, 3$, with the right properties, we have

$$\int_{\mathbb{R}^3}\int_{\mathbb{R}} u_i \partial_t \varphi_i + \int_{\mathbb{R}^3}\int_{\mathbb{R}} u_i u_j \partial_j \varphi_i = -\int_{\mathbb{R}^3}\int_{\mathbb{R}} p\partial_i \varphi_i - \nu \int_{\mathbb{R}^3}\int_{\mathbb{R}} u_i \partial_{jj}\varphi_i, \tag{3.11}$$

$$\int_{\mathbb{R}^3}\int_{\mathbb{R}} u_i \partial_i \psi = 0. \tag{3.12}$$

This system of equations is called the weak form of the INSE (WINSE), and should be supplemented with appropriate initial and boundary conditions. Solutions which satisfy the WINSE are called weak solutions, by opposition to strong (or classical) solutions which have higher regularity properties. It can be seen that for the WINSE to make sense, regularity requirements on $\boldsymbol{u}$ and p are relaxed compared to their strong counterpart. Indeed, now we only need $\boldsymbol{u} \in L^2(\mathcal{V}, \mathbb{R}^+)$ and $p \in L^1(\mathcal{V}, \mathbb{R}^+)$.

Some results about weak solutions of the INSE

Showing the existence of strong solutions to the INSE at all times, for arbitrary smooth initial conditions, remains one of the greatest mathematical challenges. The usual strategy to prove the existence and regularity of solutions to PDE is to build a weak solution, and then show that every weak solution is actually a strong solution. This has been tried for the INSE in the pioneering work of Leray [Leray, 1933; 1934a;b]. However, Leray was able to show the global (in time) existence of solutions in $\mathbb{R}^3$ for any initial conditions, only at the cost of giving up regularity. However, Leray's idea opened the door for more studies on the regularity of the INSE and many results about weak solutions have been uncovered. For instance, [Hopf, 1951] was able to extend Leray's result to problems with boundaries. However, the unicity and regularity of these solutions remain unknown, and only partial regularity theorems exist. As an example, there exists a local (in time) existence theorem which states that for any regular initial condition $\boldsymbol{u}^0$, a strong solution exists at least up to a time T_0 which depends on the regularity of $\boldsymbol{u}^0$. However, this result does not provide any information about the regularity of the solution at T_0, and it might be that nothing singular actually happens at that time. The work of Beale, Kato and Majda (BKM) exhibited a necessary criterion for a solution to lose its regularity [Beale et al., 1984]. They proved that if $\boldsymbol{u}$, along with its weak derivatives up to order at least

3, are initially square-integrable (*i.e.* are in L^2), then this remains the case until the blow-up time T_* for which

$$\int_0^{T_*} ||\boldsymbol{\omega}||_\infty dt = \infty, \tag{3.13}$$

so that

$$\lim_{t \to T_*} |\boldsymbol{\omega}| = \infty. \tag{3.14}$$

It immediately follows that if there exists a time T_0 such that the norm of the vorticity remains finite on any interval $[0, T]$ where $T < T_0$, then the solution is regular on $[0, T_0]$. This result is of great importance as it shows that the norm of the vorticity alone controls the regularity of solutions to the INSE.

Since singularities might occur, it seems natural to study the spacetime distribution of these possible events. Considering the whole space $\mathbb{R}^3$, [Leray, 1934b] derived his "structure theorem" which states that the *time* set for which global weak solutions lose their regularities has zero Lebesgue measure. Later, in a series of papers [Scheffer, 1976a;b; 1977; 1980], Scheffer was able improve this result. In [Scheffer, 1976b], it was shown that Leray's structure theorem yields that the set of singular *times* has zero half-dimensional Hausdorff measure. This result was shown to hold for a bounded domain in [Foias and Témam, 1979]. In [Scheffer, 1976a], Scheffer showed that if the velocity field loses its regularity at a certain time T_*, then the *space* set of singularities at T_* has a finite one-dimensional Hausdorff measure. In [Scheffer, 1977], the *spacetime* set of singularities was proved to have finite two-dimensional Hausdorff measure. This result was refined in [Scheffer, 1980] where it was shown that for a bounded domain, the *spacetime* set of singularities has finite one-dimensional Hausdorff measure. Finally, this study culminated with the famous Caffarelli-Kohn-Nirenberg (CKN) theorem [Caffarelli et al., 1982] which states that for "suitable" (in a sense that will be made precise in Sec. 3.3) weak solutions, the *spacetime* set of singularities has zero one-dimensional Hausdorff measure. This is an important theorem since it says that singularities cannot curve in spacetime. As a consequence, these events do not persist in time, singularities pop up at one point in space and immediately disappear.

What is the singular quantity?

We have been using the word "singularity" quite often since the beginning of this chapter without clearly defining it. Singularities are events which can be mathematically characterized by a diverging quantity. The question therefore is: what is the quantity which diverges when solutions to the INSE lose their regularity?

[Onsager, 1949] explicitly states that in the limit of vanishing viscosity the flow might lose its differentiability, and conjecture that the minimum regularity condition for energy conservation is a Hölder condition. Therefore, at first sight, it seems that the diverging quantity is the gradient of the velocity. However, it has been shown that contrary to Euler equations, regularity of the solutions to the INSE is ensured if the velocity field

remains bounded [Serrin, 1962; Escauriaza et al., 2003; Constantin, 2008]. Therefore, the problem of Navier-Stokes regularity is a velocity blow-up problem. An interesting remark is that if such blow-up occurs, this may experimentally result in a break-down of the incompressibility condition [Frisch, 1995; Constantin and Fefferman, 1994; Constantin, 1994].

3.3 Energetic aspects of weak solutions

Energy inequalities

For weak solutions, the different terms in Eq. (1.21) make sense as distributions. However, there is *a priori* not any reason why this balance should hold for the WINSE. Leray's structure theorem states that the global (in space) kinetic energy of a weak solution is a decreasing function of time in the absence of external forcing. Actually, it can be shown that Leray-Hopf weak solutions satisfy the global energy inequality

$$\frac{d}{dt}\int_{\mathcal{V}} d\boldsymbol{r}\ E(\boldsymbol{r},t) \leqslant -\int_{\mathcal{V}} d\boldsymbol{r}\ \mathscr{D}_\nu(\boldsymbol{r},t)\,, \tag{3.15}$$

keeping the same notations as in Sec. 1.2. This implies

$$\int_{\mathcal{V}} d\boldsymbol{r}\ E(\boldsymbol{r},t) \leqslant \int_{\mathcal{V}} d\boldsymbol{r}\ E(\boldsymbol{r},0) - \int_0^t dt \int_{\mathcal{V}} d\boldsymbol{r}\ \mathscr{D}_\nu(\boldsymbol{r},t)\,. \tag{3.16}$$

If, in addition, they also satisfy the local energy inequality

$$\partial_t E + \partial_j \mathscr{E}_\nu^j \leqslant -\mathscr{D}_\nu, \tag{3.17}$$

then they are called suitable in the sense of CKN. Eq. (3.15) - (3.17) state that a fluid in motion always loses energy quicker than the rate at which energy is dissipated by viscous forces. Therefore, if the velocity field happens to be irregular, the irregularities cannot be the source of a local or global (in spacetime) input of energy. This condition seems reasonable in order to accept a weak solution as physically realistic. However, these inequalities do not prevent for any additional energy dissipation. Such an additional dissipation would then stem from a lack of regularity in the velocity field, and thus break down the energy balance (1.21), even in the case where $\nu = 0$ (1.15). This dissipation is thus called the inertial energy dissipation. The question which was raised by Onsager can then be reformulated as follows: what is the minimum regularity requirement on solutions to the INSE for the inertial energy dissipation to vanish?

An expression for the inertial dissipation

The weak formalism constitutes a framework of choice for mathematicians wishing to prove Onsager's conjecture, and many results concerning the regularity of weak solutions have been derived. This study places weak solutions in interpolation spaces called Besov spaces, and is outside the scope of this thesis. The importance of the question of regularity

for turbulence phenomenology was emphasized in [Eyink, 1994], where a proof of the conservation of kinetic energy under a slightly stronger assumption than Hölder continuity was given. In the same year, it was demonstrated by [Constantin et al., 1994] that kinetic energy is still conserved under a weaker assumption than Hölder continuity, which requires $\boldsymbol{u}$ to belong to some particular Besov space. Following these lines of investigation, the two French mathematicians Jean Duchon and Raoul Robert, were able to derive an expression for the inertial dissipation [Duchon and Robert, 2000], and again weaken the conditions on $\boldsymbol{u}$ for kinetic energy to be conserved. The contribution of this thesis to the study of the zeroth law of turbulence is largely based upon their results. As a consequence, we are going to sum up the main steps of their approach, their paper being included in App. *A*.

The key idea of [Duchon and Robert, 2000] was to introduce a distribution $\mathscr{D}_I(\boldsymbol{u})$ such that

$$\mathscr{D}_I \overset{def}{=} -\partial_t E - \partial_j \mathscr{E}_\nu^j - \mathscr{D}_\nu. \tag{3.18}$$

Then, using the filtering approach described in Sec. 3.1, they proceed with the derivation of a balance equation for the point-split kinetic energy density at scale ℓ, defined as $e^\ell \overset{def}{=} u_i u_i^\ell/2$. They find

$$\partial_t e^\ell + \partial_j \left[u_j e^\ell + \frac{1}{2}\left(p^\ell u_j + p u_j^\ell\right) - \nu\left(\partial_j e^\ell + \frac{1}{2}\partial_i\left(u_i u_j^\ell + u_i^\ell u_j\right)\right)\right] = -\frac{1}{2}\Delta^\ell - 2\nu S_{ij} S_{ij}^\ell, \tag{3.19}$$

where $\Delta^\ell = u_i \partial_j \left(u_i u_j\right)^\ell - u_i u_j \partial_j u_i^\ell$. Note that Eq. (3.19) is different from what we derived in Sec. 3.1 since Eq. (3.4) gives the balance for $E^\ell = u_i^\ell u_i^\ell/2 \neq e^\ell$. They proceed by showing that Δ^ℓ converges in the sense of distributions towards $2\mathscr{D}_I$ when ℓ vanishes. Finally, they introduce the sequence of function

$$\Pi_{DR}^\ell(\boldsymbol{u}) = \frac{1}{4}\int_{\mathbb{T}^3} d\boldsymbol{r}\ \nabla G_\ell(\boldsymbol{r}) \cdot \delta\boldsymbol{u} |\delta\boldsymbol{u}|^2, \tag{3.20}$$

where G is a smooth test function with suitable properties (see Sec. 3.1). After another small computation, they show that Π_{DR}^ℓ and $\Delta^\ell/2$ have the same limit as $\ell \to 0$. In the end, the following energy balance is obtained

$$\partial_t E + \partial_j \mathscr{E}_\nu^j = -\mathscr{D}_I - \mathscr{D}_\nu, \tag{3.21}$$

where

$$\mathscr{D}_I = \lim_{\ell \to 0}\ \Pi_{DR}^\ell, \tag{3.22}$$

does not depend on the choice of G. Following the same line of reasoning which brought us to Eq. (3.10), we get from Eq. (3.20) that

$$\Pi_{DR}^\ell = \underset{\ell \to 0}{O}\left(\ell^{3h-1}\right). \tag{3.23}$$

As a consequence, Onsager's assertion about energy conservation for velocity fields with Hölder exponent $h > 1/3$ directly follows from Eq. (3.20) and Eq. (3.22). If the velocity field has $h > 1/3$ globally in spacetime, then there does not exist any inertial energy dissipation, and conservation of energy holds for Euler equations. However, if there exist local areas where $h \leqslant 1/3$, then inertial dissipation *might*[2] occur[3]. Actually, we mentioned in Sec. 3.1 that there are evidences that exponents $h \leqslant 1/3$ are allowed [Muzy et al., 1991; Kestener and Arneodo, 2004] so that areas where a nonzero inertial energy dissipation are likely to exist.

We have now presented the mathematical arguments explaining why the zeroth law of turbulence might stem from the existence of singularities in solutions to the INSE. They provide a deeper understanding of Kolmogorov's assumption $\boldsymbol{H_3}$. However, it is not clear whether such arguments are actually relevant to real turbulence. A question raised in [Duchon and Robert, 2000] is about the existence[4] of a weak solution for which $\mathscr{D}_I(\boldsymbol{u}) \neq 0$. Indeed, if it happens that all weak solutions to the INSE are regular enough so that $\mathscr{D}_I(\boldsymbol{u}) = 0$, then the result derived by Duchon and Robert will not have any practical interest for the physics of turbulence.

3.4 Further remarks on the DR results

Relation to the 4/5 law

In Sec. 1.7, we discussed third order structure functions in the classical theory of turbulence, and linked them to energy fluxes and second order correlation functions of the velocity field through the KHM relation. Assuming a smooth velocity field, we get that $\overline{|\delta\boldsymbol{u}|^2\delta\boldsymbol{u}(\boldsymbol{\ell})} \sim \ell^3$ since velocity increments vary linearly at small scales. As observed in [Frisch, 1995], if we keep $\nu > 0$ and let $\ell \to 0$, we obtain from the KHM relation that $\Pi(\boldsymbol{\ell})$ vanishes and we have

$$\partial_t \frac{\overline{u_i u_i}}{2} = \overline{f_i u_i} + \nu \overline{u_i \partial_{jj} u_i}. \tag{3.24}$$

This expression simply states that changes in the mean kinetic energy can only come from forcing and viscous frictions, $\nabla_{\boldsymbol{\ell}} \cdot \overline{|\delta\boldsymbol{u}|^2\delta\boldsymbol{u}(\boldsymbol{\ell})}$ simply representing the redistribution of energy within in the flow. However, regularity of $\boldsymbol{u}$ is not ensured as viscosity vanishes.

In the case where $Re \to \infty$ and assuming only homogeneity, the 4/5 law becomes Eq. (1.45). It is interesting to note that the expression for Π^{ℓ}_{DR} given in Eq. (3.20) for weak solutions of the INSE is obtained from Eq. (1.45) by simply moving the gradient operator on the test function. However, the expression for $\mathscr{D}_I$ was derived without any

[2] We insist on the word "might" because $h \leqslant 1/3$ is only a necessary condition for inertial dissipation to be nonzero.

[3] Actually, Duchon and Robert showed that their expression for $\mathscr{D}_I$ vanishes under regularity conditions weaker than Onsager's estimate.

[4] Another question raised by the authors is whether $\mathscr{D}_I(\boldsymbol{u}) \geqslant 0$ is a strong enough criterion to imply uniqueness of weak solutions to the INSE which, we recall, is still unknown.

assumption of homogeneity or isotropy, and therefore appears as a generalization of Eq. (1.45). In the last section of their paper, Duchon and Robert choose a radially symmetric test function, and make use of the fact that $\mathscr{D}_I$ does not depend on the choice of G in order to derive

$$\mathscr{D}_I = -\frac{3}{16\pi} \lim_{\ell \to 0} \frac{1}{\ell} \int d\Sigma(\boldsymbol{\ell}) \ \frac{\boldsymbol{\ell}}{\ell^3} \cdot \delta \boldsymbol{u}(\boldsymbol{\ell}) |\delta \boldsymbol{u}|^2, \tag{3.25}$$

where $d\Sigma(\boldsymbol{\ell})$ denotes the area measure on the sphere of radius ℓ. On the other hand, they note that integrating Eq. (1.45) over a ball of radius ℓ leads to

$$\epsilon = -\frac{3}{16\pi} \lim_{\ell \to 0} \frac{1}{\ell} \overline{\int d\Sigma(\boldsymbol{\ell}) \ \frac{\boldsymbol{\ell}}{\ell^3} \cdot \delta \boldsymbol{u}(\boldsymbol{\ell}) |\delta \boldsymbol{u}|^2}. \tag{3.26}$$

They therefore conclude that Eq. (3.25) provides a local non-random expression for the inertial dissipation. It follows from Eq. (3.25) and Eq. (3.26) that under the assumptions of homogeneity, isotropy and smoothness of the velocity field, Kolmogorov's 4/5 law is recovered. As a consequence, Onsager's theory satisfy the expected "boundary condition" discussed in Sec. 1.7.

Testability of Onsager's theory

A strong feature of the mathematical theory for inertial dissipation is that it only involves quantities which can be experimentally measured or obtained in DNS. Indeed, being able to compute Π^ℓ_{DR} only requires to know velocity increments, which are easily accessible from *e.g.* PIV measurments. The only challenge in computing $\mathscr{D}_I$ is to be able to obtain measurements with a high enough resolution since Eq. (3.22) explicitly requires to take the limit $\ell \to 0$. This problem will be discussed in Chap. 4, which is dedicated to the computation of Π^ℓ_{DR} from experimental PIV measurements in various situations, and for various scales ℓ. We are going to see that the structure of Π^ℓ_{DR} is not trivial, even at the Kolmogorov scale, and that this has important consequences on the choice of theoretical and phenomenological models suitable for describing small scale turbulence.

3.5 Cascade of circulation

In [Chen et al., 2006; Eyink and Aluie, 2006; Eyink, 2008a], Eyink proposed to study the conservation of circulation for high Re turbulence. In this work, an analog version of Onsager's arguments was derived, and a necessary condition for the break-down of Kelvin theorem in terms of Hölder exponents was given. This phenomenon was termed by the authors "cascade of circulations". This is an important statement because Kelvin theorem plays an important role in Taylor's mechanism for energy dissipation (see Sec. 1.6). In order to explain this cascade, let us define the large scale velocity circulation Γ^ℓ as

$$\Gamma^\ell = \oint_{\mathscr{C}^\ell} \boldsymbol{u}^\ell \cdot d\boldsymbol{s}, \tag{3.27}$$

where $\mathscr{C}^\ell$ is a closed loop advected by the large scale velocity field $\boldsymbol{u}^\ell$. We obtain from the coarse-grained Euler equations a balance for Γ^ℓ which takes the form

$$\partial_t \Gamma^\ell + \partial_j \left(u_j^\ell \Gamma^\ell \right) = -\Upsilon^\ell, \tag{3.28}$$

where $\Upsilon^\ell = -\oint_{\mathscr{C}^\ell} \boldsymbol{f}^\ell \cdot d\boldsymbol{s}$. Therefore, as for energy, circulation of velocity is not conserved at scale ℓ, and there exist transfers of circulation between scales. Using Eq. (3.5), we get that

$$\boldsymbol{f}^\ell \underset{\ell \to 0}{=} O\left(\frac{\delta u\,(\ell)^2}{\ell} \right). \tag{3.29}$$

As a consequence, if the velocity is Hölder continuous with $h > 1/2$, Υ^ℓ vanishes as $\ell \to 0$ and Kelvin theorem holds. On the other hand, if this condition is not satisfied, a break-down of Kelvin theorem may be observed. In the theory of Kolmogorov, $h = 1/3$ everywhere so that K41 allows for such a break-down. Actually, we have said in Sec. 3.1, there are evidences supporting the fact that a continuous set of exponents h are allowed, with the most probable exponent close to 1/3 [Muzy et al., 1991; Kestener and Arneodo, 2004]. The problem was numerically studied in a 1024^3 DNS of a forced 3D turbulent flow [Chen et al., 2006], where it was shown that a continuous range of values are allowed for Υ^ℓ, with a symmetric probability density function (PDF) peaking around 0. Therefore, it seems that Kelvin's theorem only holds on average. More interesting is the fact that the PDF and root-mean-square of Υ^ℓ appear as nearly independent of ℓ in the inertial range. This means that the cascade of circulation persists in scale. Further investigations were performed in [Eyink and Aluie, 2006] where a detailed physical theory for this cascade of circulation was developed. The cascade is found to be local in scale space, and the physical mechanism responsible for the break-down of Kelvin's theorem is shown to be the diffusion of lines of large scale vorticity out of the advected loop $\mathscr{C}^\ell$.

As we have said, the aim of this thesis is to investigate the inertial mechanism conjectured by Onsager for energy dissipation, which would explain the zeroth law of turbulence, and cast some light on Kolmogorov's hypothesis $\boldsymbol{H_3}$. The interest of the circulation cascade mechanism for this work lies in the following relation

$$f_i^\ell u_i^\ell = -\partial_j \left(\tau_{ij}^\ell u_i^\ell \right) - \Pi^\ell. \tag{3.30}$$

Therefore, in the small scale limit, the power of the turbulent force is related to the inertial energy dissipation and thus to Duchon and Robert's result (3.22).

3.6 A side remark on 2D turbulence

In Chap. 2, we have discussed the classical picture for energy dissipation in 2D turbulence. In Kraichnan picture, there exists a direct (*i.e.* from the forcing scale to smaller scales) cascade of enstrophy together with an inverse (*i.e.* from the forcing scale to larger scales) cascade of energy, so that small unstable eddies combine into larger ones [Kraichnan,

Figure 3.3: An example of large structures formed in 2D turbulence. Hurricane Isabel seen from the International Space Station (2003).

1967]. This phenomenon is at the origin of the formation of very large atmospheric structures such as the one displayed in Fig. 3.3. The dimensional arguments we used in Sec. 1.7 in order to derive the scaling of the energy density spectrum in 3D did not depend on the direction of the cascade, and we therefore still have the same scaling associated to the inverse cascade of energy in 2D for homogeneous isotropic turbulence

$$E^{(1D)}(k) \sim \epsilon^{2/3} k^{-5/3}. \tag{3.31}$$

Let us now introduce the enstrophy dissipation rate ϵ_ω. From the definition of the enstrophy, and using dimensional analysis, we get the Kraichnan spectrum associated to the direct cascade of enstrophy

$$E^{(1D)}(k) \sim \epsilon_\omega^{2/3} k^{-3}, \tag{3.32}$$

where the dimensionless constants in Eq. (3.31) and Eq. (3.32) are different *a priori*. The Kraichnan dual cascade picture has been confirmed in high resolution DNS in *e.g.* [Boffetta, 2007].

Based on the work of [Leray, 1933], the question of the regularity of the INSE in 2D has been answered [Lions and Prodi, 1959]. For any smooth initial condition $\boldsymbol{u}^0 \in L^2(\mathcal{V})$, Leray-Hopf solutions are unique and regular, and Eq. (3.16) becomes an equality

$$\int_{\mathcal{V}} d\boldsymbol{r}\ E(\boldsymbol{r},t) = \int_{\mathcal{V}} d\boldsymbol{r}\ E(\boldsymbol{r},0) - \int_0^t dt \int_{\mathcal{V}} d\boldsymbol{r}\ \mathscr{D}_\nu(\boldsymbol{r},t), \tag{3.33}$$

where $\mathcal{V}$ may be a bounded domain [Ladyzhenskaya, 1958; Lions and Prodi, 1959; He, 2012]. In [Duchon and Robert, 2000], Duchon and Robert showed that this unique solution also satisfies $\mathscr{D}_I = 0$, as expected from regular solutions. As a consequence,

Taylor's and Onsager's mechanism for energy dissipation do not exist in 2D turbulence. This is consistent with the well known fact that there is not any dissipation anomaly in this case [Tabeling, 2002]. For more discussions on the regularity of the INSE in 2D, and the differences from the 3D case, see *e.g.* [Giga, 1983; Constantin, 1995].

3.7 Regularity of the axisymmetric Navier-Stokes equations

Solutions to the 2D INSE exist, are unique and regular, while in 3D, only the existence of weak solutions is known. The main difference between the two cases comes from the fact that vortex stretching is absent in 2D, which leads to the conservation of an additional quadratic quantity: the enstrophy. In 3D on the other hand, the lack of information about how vortex are stretched is the main issue which prevents from making any final conclusion on the global regularity of weak solutions. In Chap. 2, we discussed axisymmetric flows as being an interesting framework to study turbulence, because it is intermediate between 2D and 3D. The question we ask now is: what can be said about the regularity of the axisymmetric INSE?

Let us work in a cylindrical coordinate system (r, θ, z) with vector basis $(\boldsymbol{e_r}, \boldsymbol{e_\theta}, \boldsymbol{e_z})$ in $\mathbb{R}^3$. We say that a solution to the INSE is axisymmetric if and only if the fields u_i, p are independent of θ, *i.e.*

$$\partial_\theta p = 0 \text{ and } \partial_\theta u_\alpha = 0, \ \alpha = r, \theta, z. \tag{3.34}$$

In the case of zero swirl, *i.e.* $u_\theta = 0$, further simplifications arise. The vorticity $\boldsymbol{\omega}$ takes the form $\boldsymbol{\omega} = (\partial_z u_r - \partial_r u_z)\, \boldsymbol{e_\theta}$ so that the vortex stretching term simply becomes $\omega_j \partial_j u_i = \omega_\theta u_r / r$. Using the stream-function vorticity formulation [Lopez, 1990], we can get rid of the pressure field p in the equations of motion, and the change of variables $(u_r, u_z) \to (\psi, \xi)$ can be made, where $\xi = \omega_\theta / r$ and ψ is the stream function such that

$$u_r = -\frac{1}{r}\partial_z \psi, \quad \text{and} \quad u_z = \frac{1}{r}\partial_r \psi. \tag{3.35}$$

Changing variables from (r, z) to (y, z) where $y = r^2/2$, and after some calculations, it can then be shown that the dynamics of the vorticity reduces to one partial differential equation, supplemented with one mathematical constraint, which takes the compact form [Leprovost et al., 2006]

$$\partial_t \xi + \{\psi, \xi\} = \nu \left(\Delta \xi + \frac{2}{r} \partial_r \xi \right), \tag{3.36}$$

$$\partial_{yy} \psi + \frac{1}{2y} \partial_{zz} \psi = -\xi. \tag{3.37}$$

For any two fields ψ, φ, $\{\psi, \varphi\} \overset{def}{=} \partial_y \psi \partial_z \varphi - \partial_z \psi \partial_y \varphi$. The interesting feature of Eq. (3.36) is that the vortex stretching term $u_r \xi$ has disappeared. This is a direct consequence

of introducing the field ξ which is conserved in axisymmetric inviscid turbulence. It can then be shown that for a suitable norm[5], $\xi(t)$ remains bounded by its initial value $\xi(t=0)$, everywhere in space. It then follows by the BKM criterion that axisymmetric solutions to the INSE with zero swirl remain regular at all times. These results were independently derived in [Ukhovskii and Yudovich, 1968] and [Ladyzhenskaya, 1968], who also proved the existence and uniqueness of axisymmetric solutions in the absence of swirl. Later, the assumptions on the initial conditions which ensure global regularity were weakened in [Leonardi et al., 1999; Abidi, 2008]. However, despite many attempts [Chae and Lee, 2002; Kim, 2003; Chen and Zhang, 2007; Agélas, 2013; Chen et al., 2015; He et al., 2016; Pan, 2016], the problem is still open for nonzero swirl.

In the case of viscous axisymmetric flows with non zero swirl, if singularities develop, we know from the CKN theorem that they can only lie on the axis of symmetry. However, this is not necessarily the case for inviscid flows, and strong evidences of the finite time blow-up of a solution to an axisymmetric Euler equations were provided in [Luo and Hou, 2014]. In this paper, the authors find a blow-up in the vorticity field at the solid boundary which takes the form of a ring due to axisymmetry. The blow-up of the vorticity is confirmed by the rapid growth of $\|\boldsymbol{\omega}\|_\infty$ which grows faster than double exponential. This blow-up is interpreted as resulting from a compression mechanism.

Mathematically, it is not known whether the VK geometry prevents from the development of finite-time singularities. Inertially forced VK flows are not axisymmetric, however they remain axisymmetric on time average. Areas in the flow which therefore appear to be of potential great interest to our study are the vicinity of the axis (Oz) and the vicinity of the wall. In addition, areas lying in the middle shear layer are expected to contain a greater amount of the total energy dissipation. This explains why we have chosen to zoom in the areas represented on Fig. 2.7 in order to obtain our high resolution data described in Tab. 2.3 and Tab. 2.4.

[5]Here, the norm on the Lebesgues spaces L^p, denoted $\|\cdot\|_p$, for any $p \geqslant 1$

Part II

What is new

Chapter 4

Testing Onsager's Theory in Turbulent von Kármán Flows: From Injection to Dissipative Scales

> "Come, Watson, come!" he cried. "The game is afoot. Not a word! Into your clothes and come!"
>
> *Sir Arthur Conan Doyle*

Contents

The discovery of the zeroth law of turbulence by [Taylor, 1935], and the assumed existence of an energy dissipation anomaly in K41, were both interpreted by Onsager as a possible loss of regularity in the velocity field. This idea naturally leads to a reformulation of the laws of motion in a more general framework provided by the weak formalism. Following these lines of reasoning, Duchon and Robert derived the corresponding energy balance given in Eq. (3.21), where an inertial dissipation term unrelated to viscosity appears. However, it is not known whether inertial dissipation is a relevant concept to real turbulence and, to our knowledge, the possibility that $\mathscr{D}_I$ might be nonzero in real flows has never been experimentally investigated. In this chapter, we provide the first study of Duchon and Robert's results from experimental data. These data have been obtained from the VK2 set-up described in Chap. 2. Our study follows the direction of the cascade: we first review the informations we have about energy injection at large scales, then we study energy transfers in the inertial range using the tools introduced in Chap. 3, and finally we use the zoomed data in order to continue our investigations in the dissipative range and close to Kolmogorov scale.

This chapter presents some results published in [Kuzzay et al., 2015] (see App. B) and some others published in [Saw et al., 2016] (see App. D).

4.1 At injection scales

In fully developed turbulence, the injection and dissipation scales are well separated. In between lies the inertial range (as illustrated on Fig. 4.1) where energy is neither directly injected nor dissipated, but instead cascades in an infinite number of local continuous steps due to nonlinear interactions. In the VK2 set-up, turbulence is maintained stationary by two counter-rotating impellers, the typical injection scale being the size of the impellers. As described in Chap. 2, global quantitative informations about the amount of energy injected into the flow are obtained via torque measurements, and the total dimensionless injected power is denoted $2K_p$ for symmetric forcing conditions, where we recall that K_p is the dimensionless energy injection rate of one impeller. Since, in the stationary regime, there is not any accumulation or loss of energy at any scale on time-average, the same measurements will also be used to infer the amount of energy scattered through any wavenumber k per unit time, along with the total amount of dissipated power. This is illustrated on Fig. 4.1 where the symbol "$\sim$" stands for "estimates". Of course, Fig. 4.1 is just an illustration, and does not accurately describe all the results we have discussed in Sec. 2.6.

4.2 In the inertial range

When the field of view of the cameras covers the whole volume located between the two impellers, the cut-off due to their finite resolution lies in the inertial range. As a consequence, it is possible to check the relative contributions of Π^ℓ_{DR} and $\mathscr{D}^\ell_\nu$ at this scale.

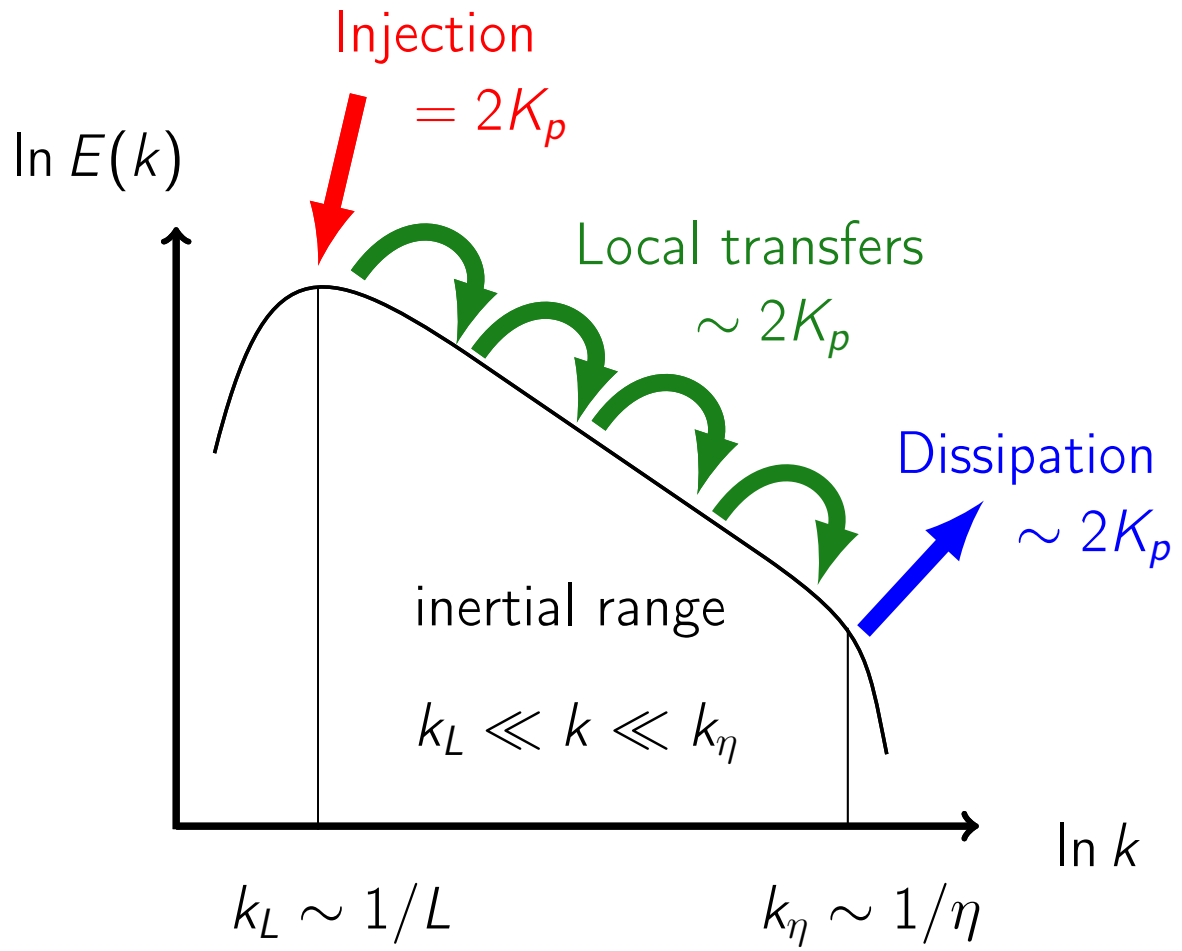

Figure 4.1: Illustration of the energy cascade in Fourier space with notations used in von Kármán flows.

Global energy balance

In Eq. (3.19), it can be shown that locally, $\Delta^\ell/2$ and Π^ℓ_{DR} only differ by the divergence of a current which vanishes as $\ell \to 0$ [Eyink, 2008b]. Therefore, Π^ℓ_{DR} appears as the local amount of point-split kinetic energy e^ℓ transferred through scale ℓ. The important remark is that e^ℓ is an alternative definition to E^ℓ (defined in Eq. (3.4)) for the kinetic energy at scale ℓ [Eyink, 2008b]. As a consequence, one would like to interpret Π^ℓ_{DR} as the local amount of kinetic energy scattered through scale ℓ due to nonlinear interactions. In the statistically stationary regime, energy cascades through the inertial range at the same rate as it is injected at large scales. Introducing the notations $\epsilon_{DR}(\ell) = \left\langle \overline{\Pi^\ell_{DR}} \right\rangle$ and $\epsilon_\nu(\ell) = \left\langle \overline{\mathscr{D}^\ell_\nu} \right\rangle$, we have

$$\underbrace{2K_p \frac{R^3}{\mathcal{V}}}_{\text{energy injection at large scales}} = \underbrace{\epsilon_{DR}(\ell) + \epsilon_\nu(\ell)}_{\text{energy scattered through scale } \ell} , \tag{4.1}$$

where $\epsilon_\nu(\ell)$ is negligible if ℓ lies in the inertial range, and all the terms have been made dimensionless as described in Chap. 2.

We would like to check whether Eq. (4.1) holds in our von Kármán set-up. In order to implement the computation of Π^ℓ_{DR}, the choice of G which has been made is

$$G(r) = \begin{cases} \frac{1}{N} \exp\left(-\frac{1}{1-r^2/4}\right) & \text{for } 0 \leqslant r \leqslant 2, \\ 0 & \text{otherwise,} \end{cases} \tag{4.2}$$

where N is a normalization constant such that $\int_{\mathcal{V}} d^3\boldsymbol{r}\ G(\boldsymbol{r}) = 1$. This test function has the properties required in Sec. 3.1, is C^∞, and has compact support [Duchon and Robert, 2000]. Clearly, the fact that our PIV system is stereoscopic and not tomographic implies that we cannot compute velocity increments in the three directions of space, as would be required. Therefore, there will be missing informations in our computations. Nevertheless, due to the statistical axisymmetry of our set-up, it can be hoped that only taking into account velocity increments on a meridional plane will be enough.

In addition to choosing ℓ in the inertial range in order to check Eq. (4.1), ℓ must also be such that it is sufficiently large with respect to the PIV smallest resolved scale, so as to guarantee statistical convergence through sufficient average in scale space (on the sphere of radius ℓ). To check these two points, Fig. 4.2 displays $\overline{\Pi^\ell_{DR}(\boldsymbol{u})}$ in two plots averaged in the radial (respectively, vertical) direction as a function of z (respectively, x) and ℓ for a flow generated by TM87(+) at $Re \approx 8 \times 10^5$ and θ =0. We see that the quantity $\overline{\Pi^\ell_{DR}}$ is close to zero at large scales ($\ell > 0.4$R), but that it increases in magnitude at small scales, and shows strong dissipation at the location of the median shear layer. For ℓ between 0.1R and 0.15R (i.e., approximately 4-5 times the smallest scale resolved by our PIV set-up), there is the start of a saturation indicating the beginning of the inertial range. While the extent of the inertial range increases with Re, its largest scale is likely to be independent of Re, as long as the flow is turbulent. Indeed, as discussed in [Thalabard et al., 2015], the geometry of the largest scales in VK flows appears fairly independent of

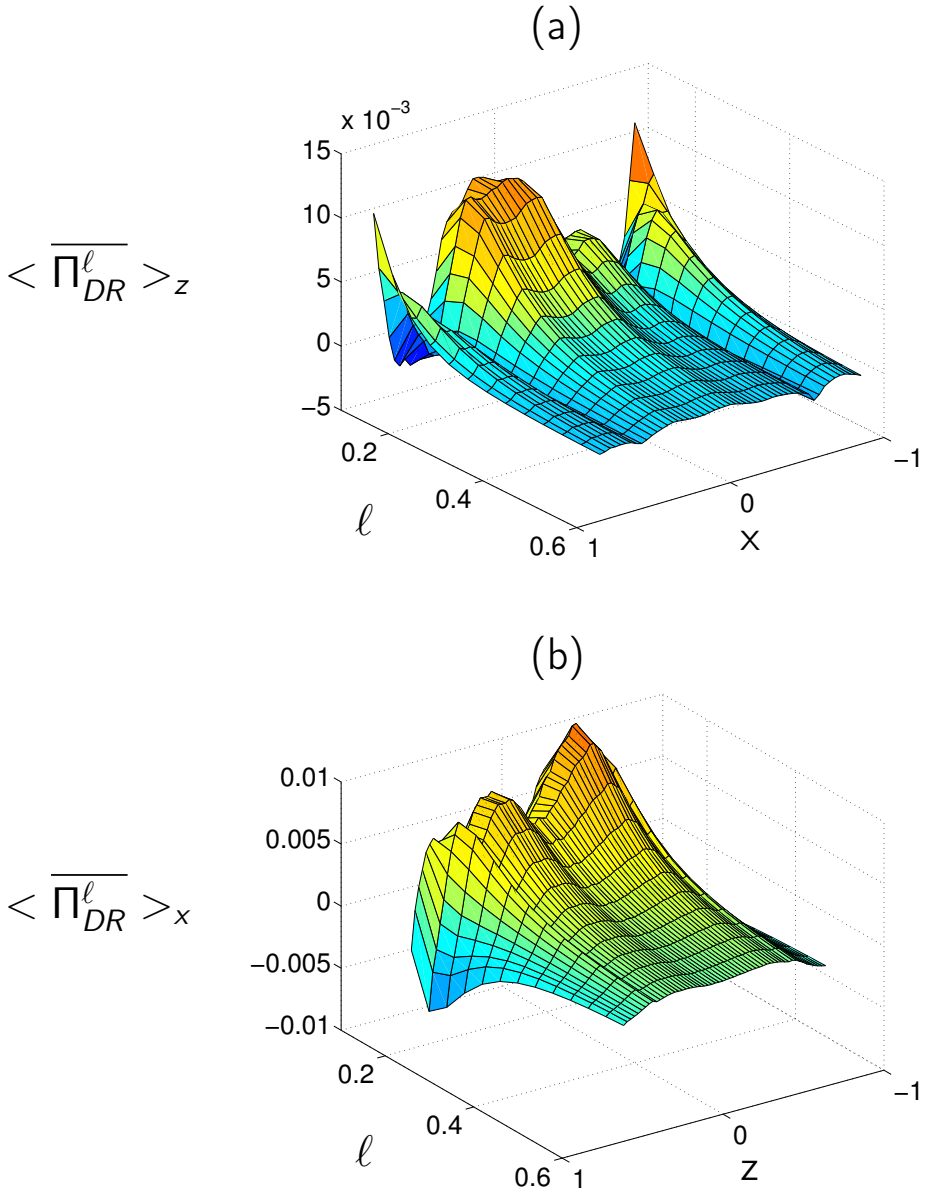

Figure 4.2: Variations of the time-averaged Duchon-Robert energy transfers $\overline{\Pi^{\ell}_{DR}}$, averaged over one coordinate of space, as a function of scale ℓ and coordinates (a) x and (b) z (in units of the radius R). The beginning of the plateau near $\ell \approx 0.1R$ indicates the beginning of the inertial range.

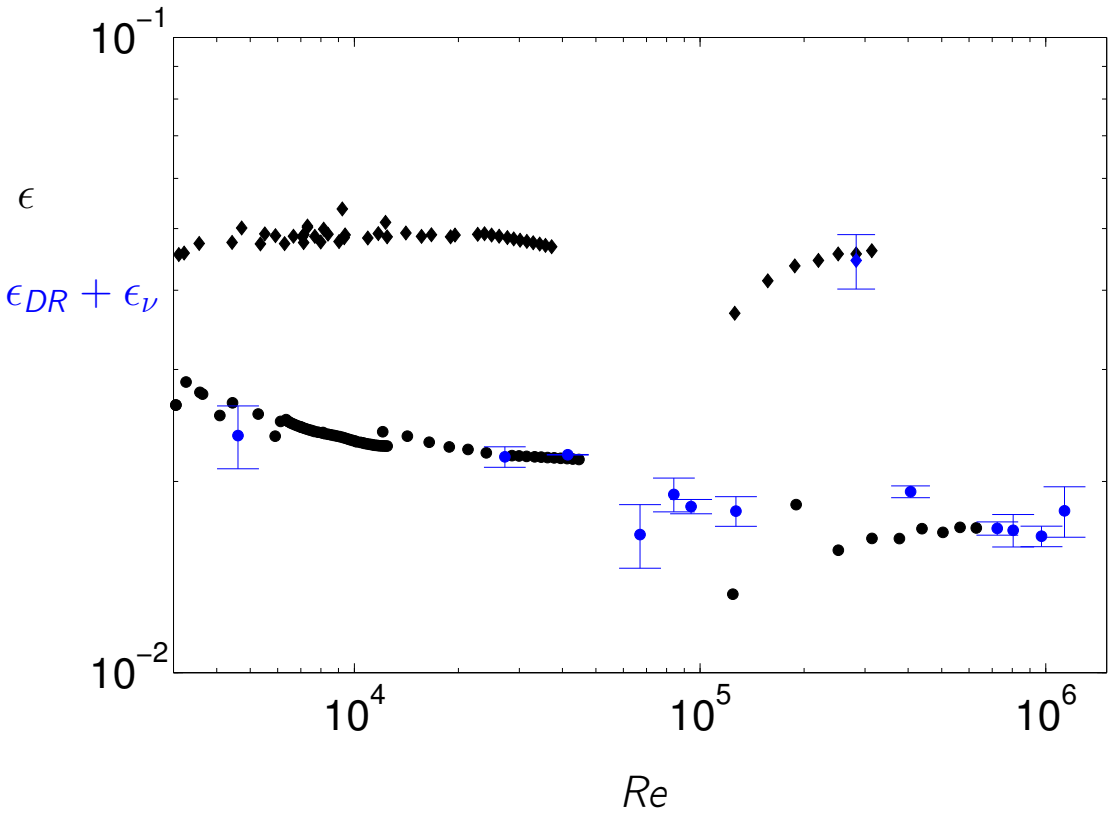

Figure 4.3: Comparison between torque estimates of the mean energy dissipation (● - ◆) and Duchon-Robert PIV estimates for TM87(+) (●) and TM87(-) (◆) at various Reynolds numbers, for $\mathcal{R}_\pi$ symmetric flows. The estimates are computed based on 2 to 15 realizations of the same flow where at least 600 instantaneous velocity snapshots have been taken for each of them. The symbols represent the mean of our computations over these realizations, while the error bars represent the standard deviation.

the Reynolds number, except around $Re = 10^5$ where it may experience abrupt changes due to the phase transition discussed in Chap. 2. Since, in the Kolmogorov picture, energy cascades from large to small scales, it is reasonable to assume that the beginning of the inertial range is solely determined by the large scale topology, thereby becoming independent of the Reynolds number.

As a consequence, we have computed the contribution of $\epsilon_{DR}(\ell)$ at scale $\ell = 0.1R$ from our PIV measurements. The results are displayed on Fig. 4.3 for $\mathcal{R}_\pi$ symmetric flows, where each point has been obtained by computing $\epsilon_{DR}(\ell)$ at the same scale, for several realizations (2 to 15) of the same experiment. For each of these realizations, time-averages have been performed using at least 600 instantaneous velocity snapshots. Points represent the average of $\epsilon_{DR}(\ell)$ over these realizations, while the error bars represent the

standard deviation. It can be seen that even though velocity increments could only be computed on a plane, the PIV estimates for TM87(+) (●) and TM87(-) (◆) are in very good agreement with direct torque measurements (● - ◆), with fairly small error bars. It can be checked that for $Re \approx 4 \times 10^3$, the viscous term accounts for a non-negligible part of the estimated mean dissipation rate (around 30%). For all the other points, viscous effects can be neglected. For the highest values of Re, ϵ_{DR} coincides with $2K_p$ within 2%. Therefore, as argued in [Duchon and Robert, 2000], we deduce that ϵ_{DR} indeed provides an exact form for the energy transfers towards subgrid scales, valid even for non-homogeneous, non-isotropic flows. We can then complete Fig. 4.1 as shown on Fig. 4.4.

The same study has been performed in the paper provided in App. B for $\mathcal{R}_\pi$ asymmetric flows by considering bifurcated states and by varying $\theta \in [-.5, .5]$ at $Re \approx 10^5$. It was found that for these configurations, the discrepancies between PIV estimates and direct torque measurements grow larger as θ is shifted away from zero. This is explained by the fact that the mixing layer, where most of the dissipation occurs, gradually leaves the field of view of our PIV system. As a consequence, Fig. 4.3 only displays the computation of ϵ_{DR} for non bifurcated flows, and statistically $\mathcal{R}_\pi$ asymmetric flows will not be further considered in this thesis.

Local energy transfers

A strong feature of the point-split kinetic energy balance is that it provides the dynamics of the kinetic energy at scale ℓ locally in space and time, whereas the KHM equation (see Chap. 1) is global in space and time since it relates time-averaged quantities and assumes homogeneity. As a consequence, we can look at local maps of Π^ℓ_{DR} in order to visualize areas in the flow where energy transfers occur.

Fig. 4.5(a) and (b) respectively show time-averaged and instantaneous maps of Π^ℓ_{DR} for TM87(+), while Fig. 4.5(c) and (d) show the same maps for TM87(-). Both of these flows were generated at $Re = 3 \times 10^5$. Clear localized structures symmetrically distributed with respect to the midplane can be observed on Fig. 4.5(a). These structures are reminiscent of the mean poloidal recirculation cells observed on the mean flow in Fig. 2.9(a), and are statistically significant since they are not observed on instantaneous frames. They may, therefore, trace the intense vortices of the shear layer. In addition, one observes a clear localization of energy injection (blue areas) close to the tip of the impellers, with energy transfers mostly occurring close to the rotation axis and near the recirculation cells. Regarding Fig. 4.5(b), it is interesting to note that energy transfers are characterized by intense, localized events that can reach up to twenty times the maximum average local dissipation.

For Fig. 4.5(c) and (d), the remarks are essentially the same: energy transfers towards subgrid scales are mostly located close to the rotation axis in the median shear layer. However, a noticeable difference is that the color scale is wider for this configuration. We thus recover the fact that the flow dissipates more energy for TM87(-) than for TM87(+), so that the motors have to apply a greater torque to maintain the turbulence stationary.

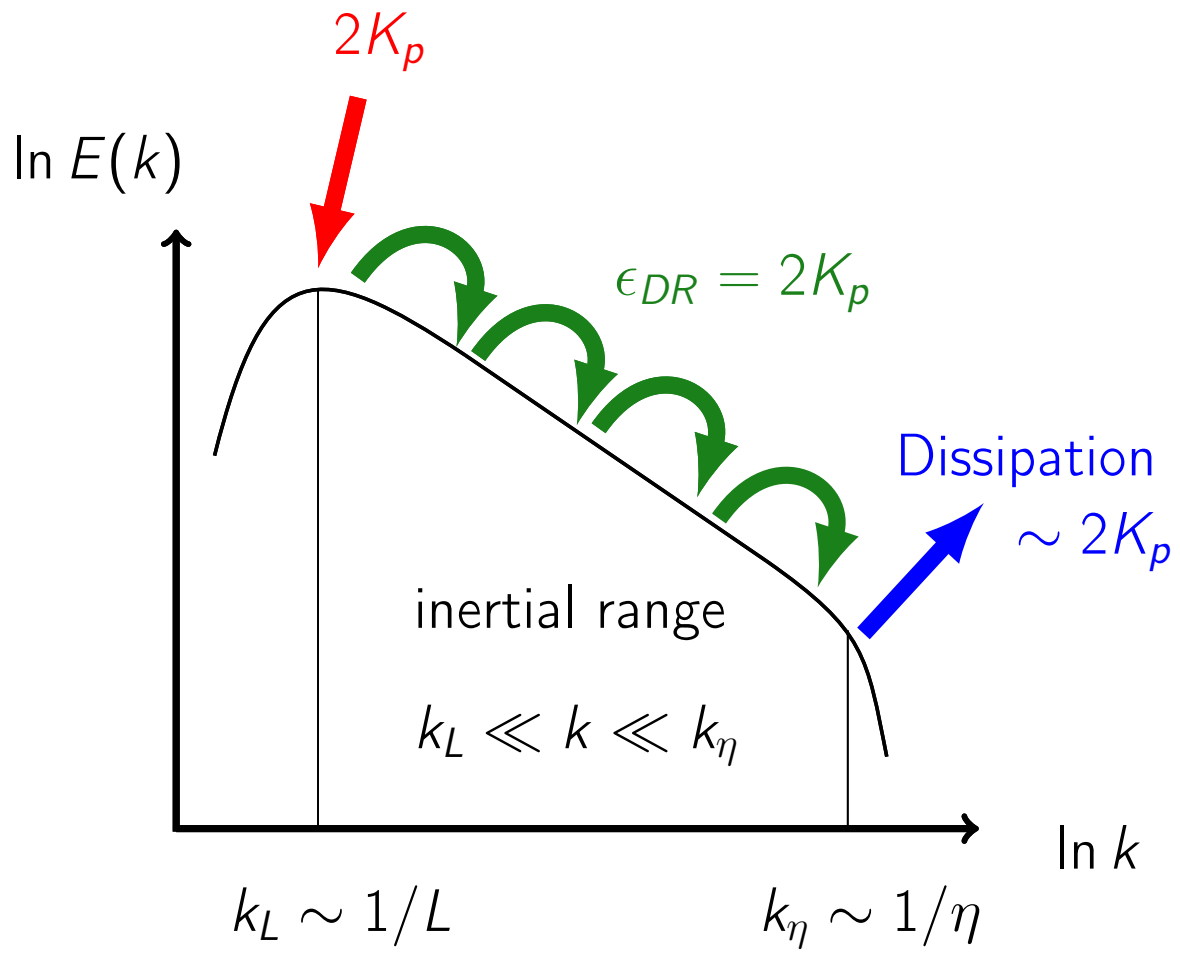

Figure 4.4: Illustration of the energy cascade for turbulent von Kármán flows. The results of this section show that ϵ_{DR} captures the energy cascade with very good accuracy when ℓ lies in the inertial range, and opens the question as to what happens in the dissipative range.

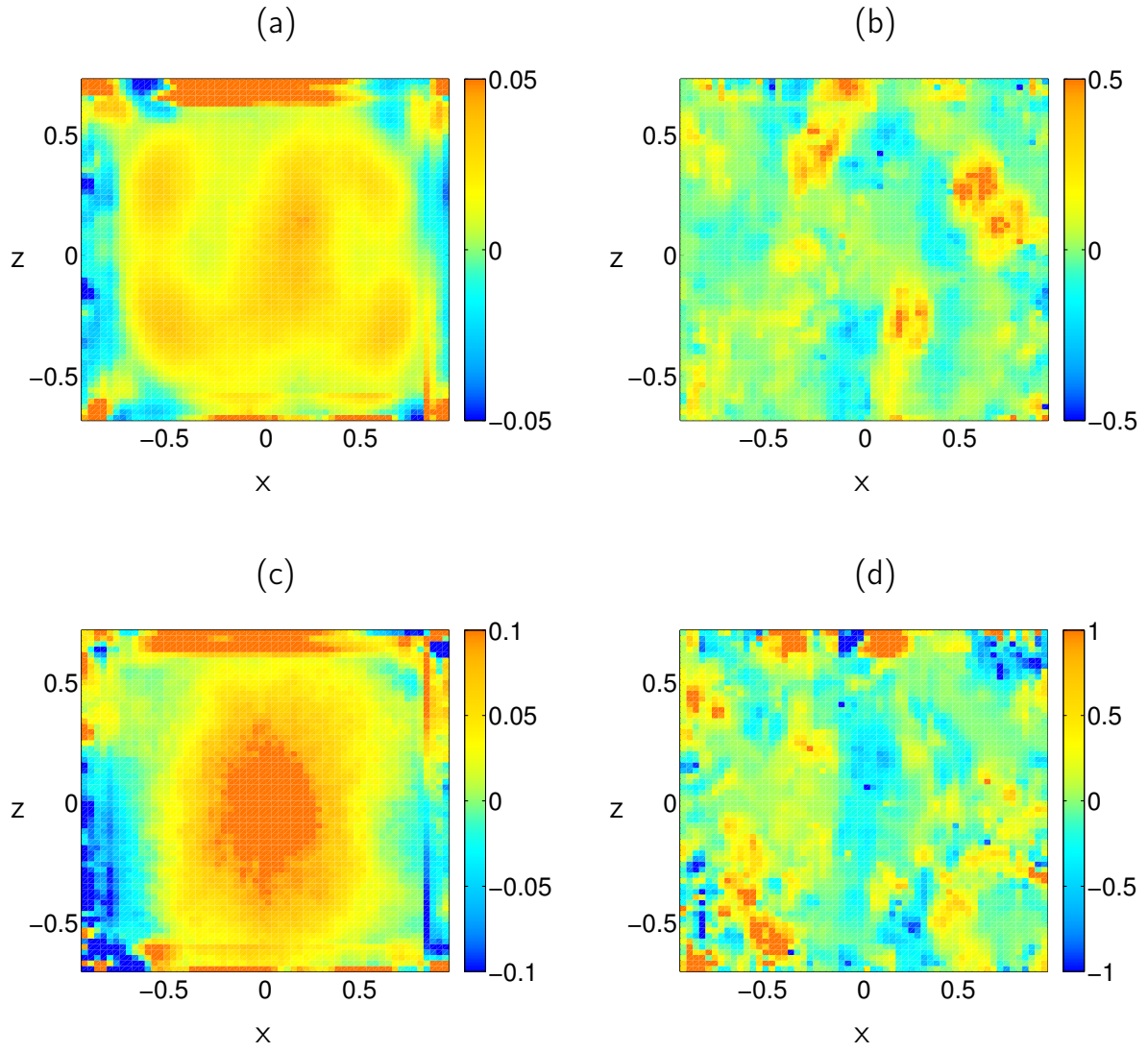

Figure 4.5: Typical maps of (a) and (c): $\overline{\Pi^{\ell}_{DR}}$, and (b) and (d): Π^{ℓ}_{DR}, for flows generated with (a) and (b): TP87(+), and (c) and (d): TP87(-), at $Re \approx 3 \times 10^5$.

4.3 From inertial to dissipative scales

Our investigations of the energy cascade have shown that $\Pi^\ell_{DR} \neq 0$ for ℓ lying in the inertial range. Even more, the global contribution of Π^ℓ_{DR} over the whole flow bulk accurately captures the energy transfers through scale ℓ. These results are promising, and encourage us to push our investigations further down the cascade.

The possible inertial energy dissipation introduced by Onsager has been expressed by Duchon and Robert as the zero scale limit of Π^ℓ_{DR}. Of course this "zero scale limit" has to be understood in the mathematical sense since, when ℓ becomes of the order of the atomic scales, the continuous approximation of matter and all our considerations up to now break down. Translated into physical terms, $\ell \to 0$ means $\lambda \ll \ell \ll \eta_I$, where η_I is the typical scale over which the inertial mechanisms leading to inertial dissipation occur, and λ is the mean free path of the molecules constituting the fluid, and at which scale the INSE should be replaced by Boltzmann's equation. The problem which arises is that η_I is not known, so that we do not know what resolution we should aim for to study Onsager's conjecture. In the classical picture of turbulence, dissipation occurs close to the Kolmogorov scale η where gradients of velocity are strong enough so that all of the dissipation is taken up by viscous frictions. At this scale, inertial effects are assumed to be negligible. An interesting question therefore appears to be: is Π^η_{DR} nonzero? And, if this is the case, what are the properties of Π^η_{DR}? In the remaining of this chapter, we use the zoomed data described in Chap. 2, and provide the detailed analysis of Π^ℓ_{DR} for ℓ in the dissipative range.

4.4 Data processing and related problems

A problem that we encountered, and for which we still have not found any satisfactory solution, is how computations of Π^ℓ_{DR} near the boundaries of the grid should be dealt with. The problem comes from the fact that Π^ℓ_{DR} is computed from velocity increments over a sphere of approximate size ℓ. As illustrated on Fig. 4.6, we take into account every increments between e.g. points in the green area around P_1 and P_1. Therefore, for points located farther away from the boundaries than length ℓ, every increments can be computed. However, for points like P_2, some increments cannot be computed as they fall out of the grid (red area). The first idea that we had was therefore to compute $\Pi^\ell_{DR}(P_2)$, taking only into account increments between points included into the green area and P_2. However, this leads to spurious structures which can be observed on the time-averaged field near the boundaries. All the results which we showed in Sec. 4.2 have been obtained in this way, spurious values of $\overline{\Pi^\ell_{DR}}$ at the boundaries being discarded.

In order to get rid of these finite size effects, another idea is to use the method of images. We try to discard boundaries by creating a larger imaginary velocity field which replicates our boundary conditions. To do this, we create in our code an intermediate larger grid $\mathscr{G}_{code}$, superimposed to the PIV grid $\mathscr{G}_{PIV}$. This is illustrated on Fig. 4.7 where $\mathscr{G}_{code}$ is represented with dashed lines. Therefore, if we denote $N_{\ell max}$ the size of

the largest velocity increment we want to compute, if $\mathscr{G}_{PIV}$ is *e.g.* 80^2, then $\mathscr{G}_{code}$ is $(80+2N_{\ell max})^2$. Let us denote $\boldsymbol{u}^{PIV}$ the velocity field measured by the SPIV set-up at each point of $\mathscr{G}_{PIV}$. We define the imaginary velocity field $\boldsymbol{u}^{image}$ as:

- $\boldsymbol{u}^{image}(P) \overset{def}{=} \boldsymbol{u}^{PIV}(P),\ \forall P \subset \mathscr{G}_{code} \bigcap \mathscr{G}_{PIV}$.
- For every other points, if the boundary of $\mathscr{G}_{PIV}$ is not associated to any physical solid boundary (typically for measurements at the center of the flow), then $\boldsymbol{u}^{image} = \boldsymbol{u}^{PIV}$ as illustrated in Fig. 4.8.
- If the end of $\mathscr{G}_{PIV}$ is associated to a physical solid boundary, then the parallel and orthogonal components with respect to the boundary of both fields are related via $\boldsymbol{u}_{\parallel}^{image} = \boldsymbol{u}_{\parallel}^{PIV}$ and $\boldsymbol{u}_{\perp}^{image} = -\boldsymbol{u}_{\perp}^{PIV}$ as illustrated in Fig. 4.8.

However, this did not remove finite size effects as can be seen on Fig. 4.9. Fig. 4.9(a) displays the local quantity Π_{DR}^{ℓ} computed for TM87(+)5H_zoom32_center_water from one instantaneous velocity frame, and Fig. 4.9(b) shows the time average over 3×10^4 samples. We can observe on the former that nothing strange happens at the boundaries while there appears spurious bands of thickness $N_{\ell max}$ on the latter. As a consequence, in the remaining of this thesis, we will cut off boundaries and focus our data analyses on the domain

$$\mathcal{D}_{center} = \{(x,z) \in [-0.16, 0.1] \times [-0.18, 0.07]\}, \tag{4.3}$$

which does not include any spurious bands for all the flows listed in Tab. 2.3. Therefore, the analysis we are going to present from Sec. 4.5 to the end of Chap. 5 focuses on what happens at the center of the flow. We have started to perform the same analysis at the wall, however, we still have not obtained enough results to include them in this thesis.

4.5 Data analysis at the center

Variations of energy transfers as a function of scale: a global study

In the classical picture of turbulence, the velocity field remains smooth at all scales, and the only mechanism dissipating energy stems from viscous frictions. We saw in Sec. 4.2 that ϵ_{DR} is the dominant source term in the global balance (4.1) when ℓ lies in the inertial range. As a consequence, as dissipative scales are approached, it would be expected that Π_{DR}^{ℓ} vanishes so that $\mathscr{D}_{\nu}^{\ell}$ takes up all of the dissipation. Fig. 4.10 displays the variations of both ϵ_{DR}/ϵ and ϵ_{ν}/ϵ computed at the center of the flow at various scales. All the computations obtained from the data described in Tab. 2.3 and Tab. 2.4 are displayed.

Using water, we are able to reach fairly high values of Re, so that the corresponding data have been obtained in the inertial range (● - ◆ - −●− - −◆−). At these scales,

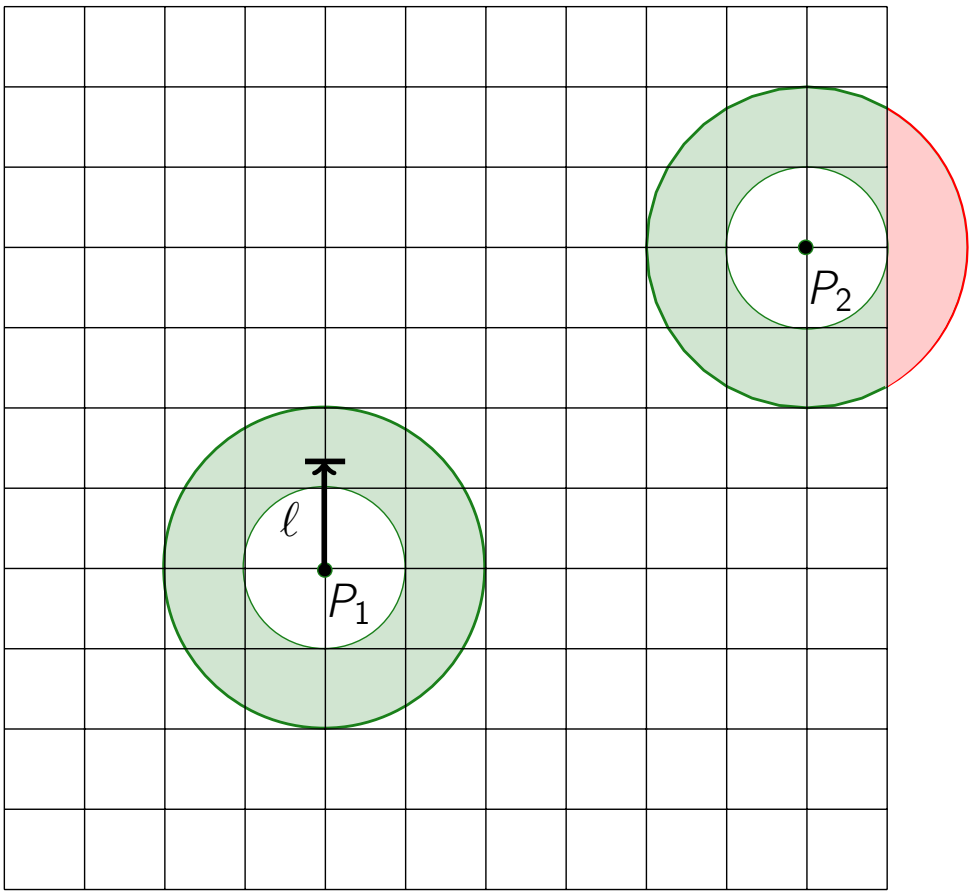

Figure 4.6: Illustration of how Π^{ℓ}_{DR} is computed in our code, and the issue encountered at the boundaries of the gird. The increments falling in the green areas can be computed, but those in the red area cannot.

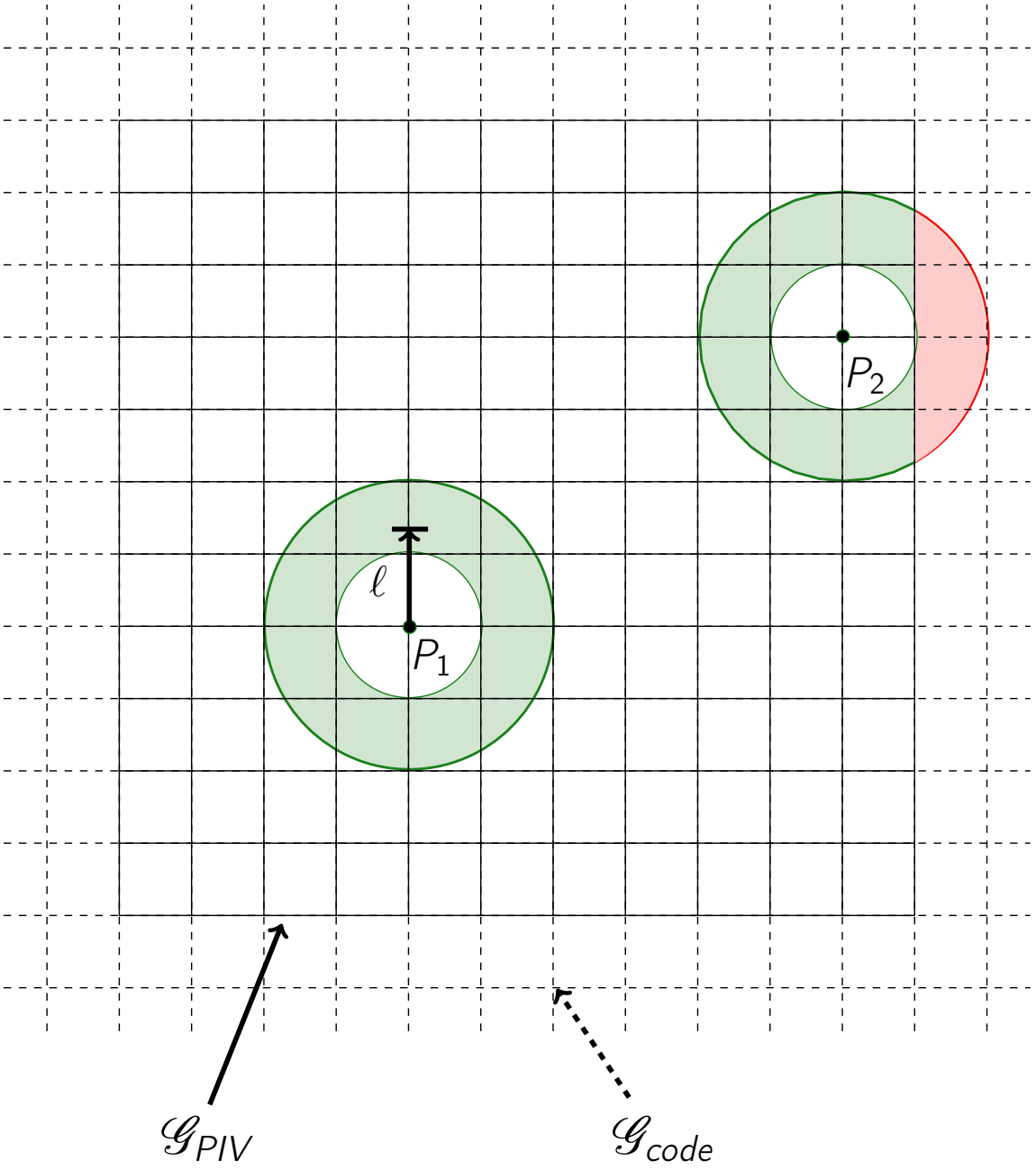

Figure 4.7: Illustration of how the problem at the boundary of the grid is dealt with. We create a larger grid...

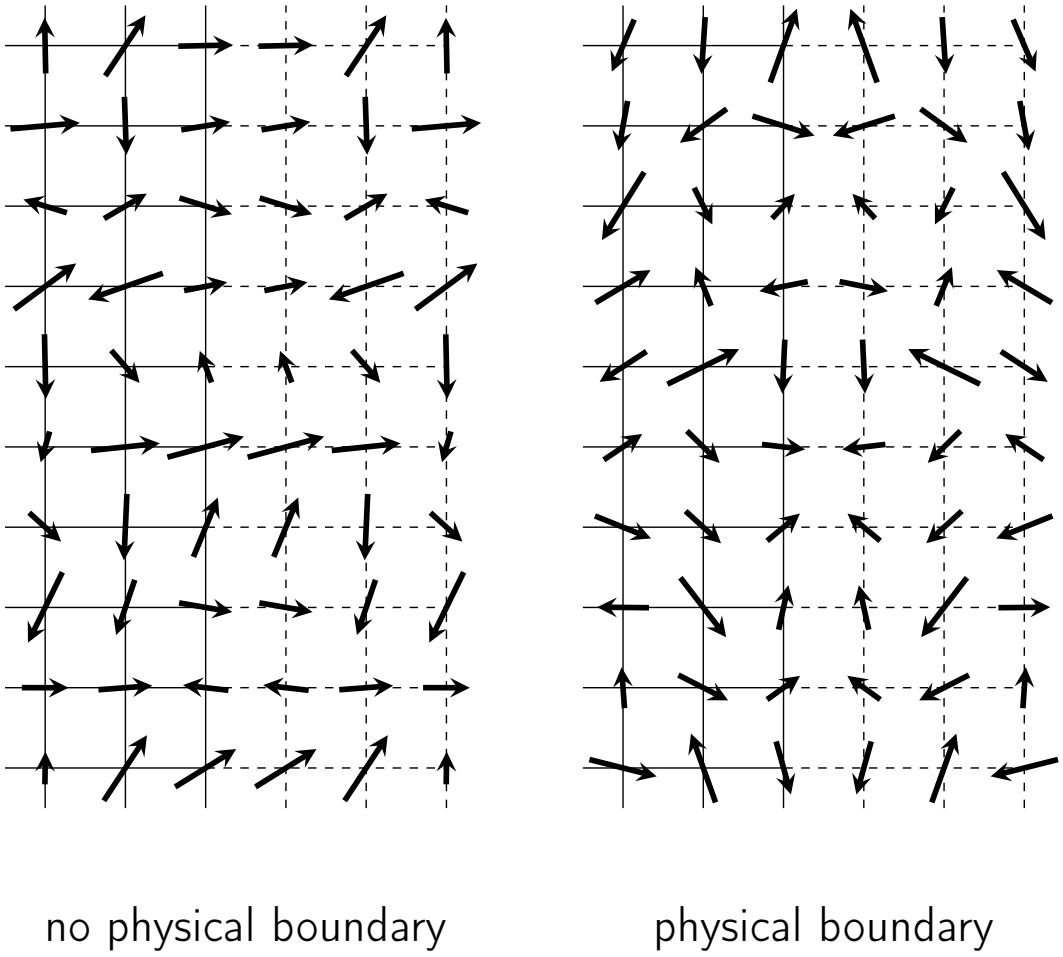

Figure 4.8: ...on which we create an imaginary field whose orthogonal component with respect to the boundary is: symmetric if the end of the grid does not correspond to any physical solid boundary, and antisymmetric if it does.

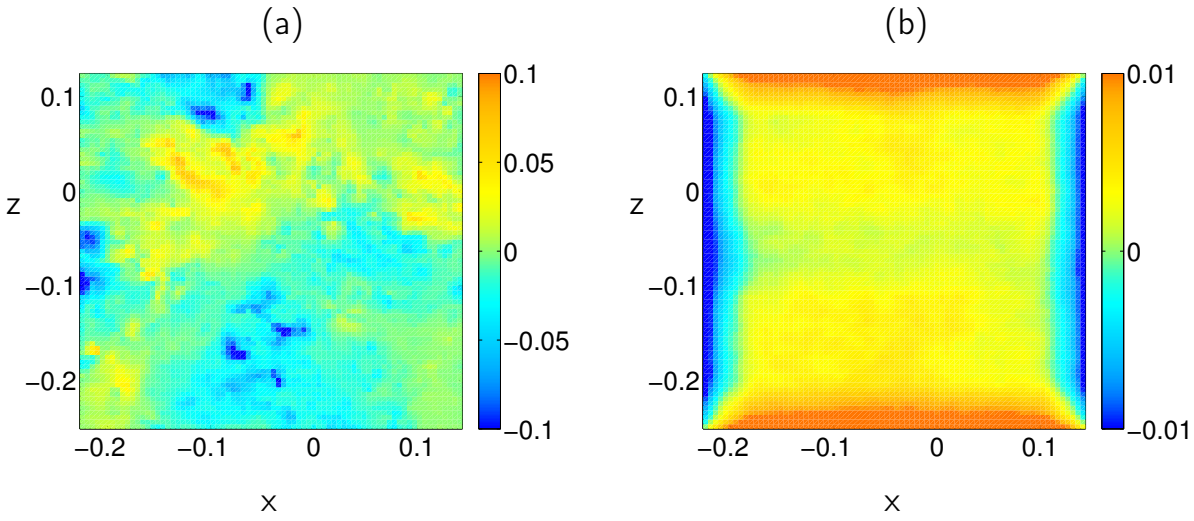

Figure 4.9: Maps of (a) Π^{ℓ}_{DR} and (b) $\overline{\Pi^{\ell}_{DR}}$ for TM87(+)5H_zoom32_center_water. We see that even though nothing strange is observed at the edges of the grid on the instantaneous field, spurious bands which have the same size as the largest velocity increments we compute appear on the time-averaged field.

we see that ϵ_{DR} is indeed much greater than ϵ_ν by more than one order of magnitude, in agreement with the results in Sec. 4.2. In addition, as ℓ/η decreases keeping Re constant, both ϵ_{DR} and ϵ_ν take up an increasing fraction of the cascade (reaching up to 50% of ϵ) at the center of the flow, this fraction being larger for TM87(-) than TM87(+). The striking feature of the variations of $\epsilon_\nu(\ell)$ with ℓ/η is that they follow a power law. This can be understood from the two-thirds law of turbulence stating that $\overline{\delta u\,(\ell)^2} \sim (\epsilon\ell)^{2/3}$ so that

$$\frac{\mathscr{D}^{\ell}_{\nu}}{\epsilon} \sim \frac{\nu}{\epsilon}\left(\frac{\Delta u}{\Delta_g}\right)^2 \sim \frac{\nu}{\epsilon}\,(\epsilon\ell)^{2/3}\,\ell^{-2} \sim \left(\frac{\ell}{\eta}\right)^{-4/3}, \tag{4.4}$$

independently of all other parameters. The dotted line in Fig. 4.10 represents $\epsilon_\nu/\epsilon \sim (\ell/\eta)^{-4/3}$.

In order to get a better resolution and resolve the flow down to the Kolmogorov scale, we decreased Re so as to increase η. (● - −●−) and (◆ - −◆−) have been respectively obtained from TM60(+)2H_nozoom32_center_glyc100 and TM87(-)1H_zoom16_ center_glyc59. At these scales, the fraction of ϵ contained into ϵ_{DR} is smaller, which is probably due to the combined effect of a decreasing ℓ/η and a decreasing Re. Nonetheless, the important result is that close to the Kolmogorov scale, ϵ_{DR} does not vanish and still accounts for around 10% of ϵ. In addition, we observe that at fixed resolution and close to η, the magnitude of ϵ_{DR} is very small for laminar flows and increases with Re. This is consistent with the possibility that inertial dissipation occurs in turbulent

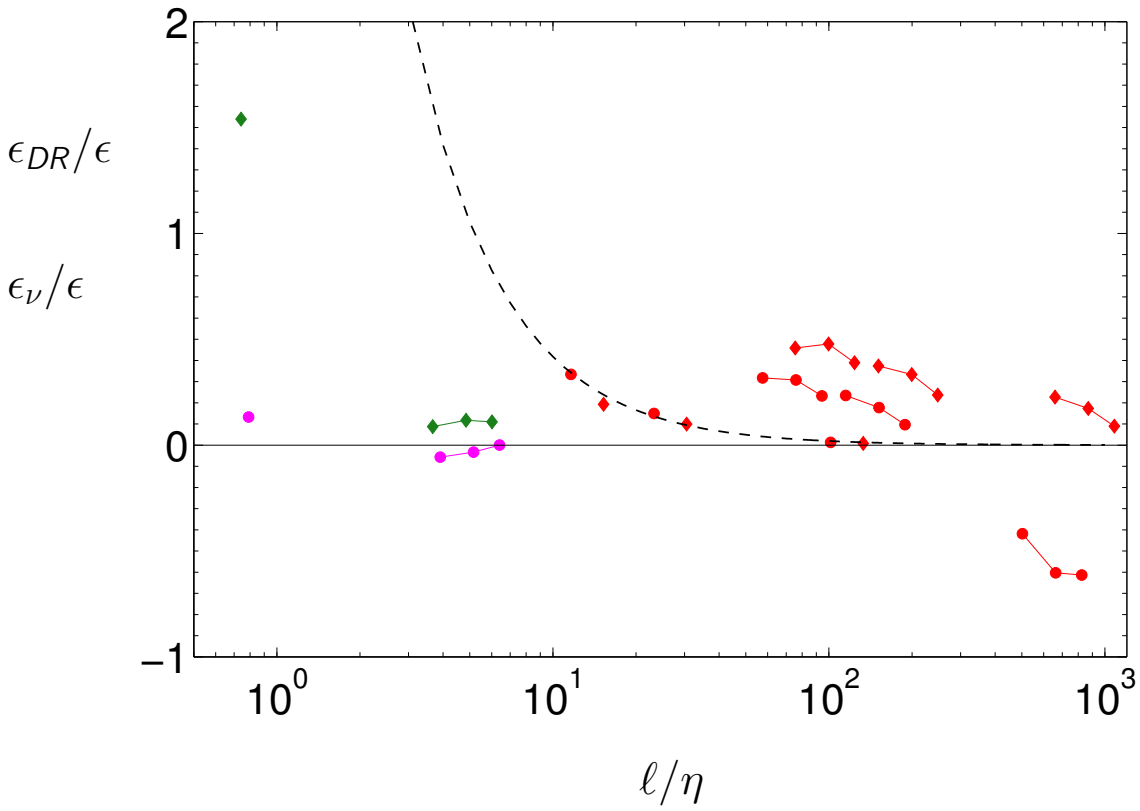

Figure 4.10: Variations of the fraction of energy dissipation ϵ taken up by ϵ_{DR} and ϵ_ν as a function of the resolution of our PIV set-up ℓ/η. These results have been obtained from data at the center of the flow, at various Reynolds numbers: $Re = 150$, $Re = 5900$, and $Re = 3 \times 10^5$. (● - ● - ●) flows generated by TM87(+), (◆ - ◆ - ◆) flows generated by TM87(-). Isolated symbols: ϵ_ν/ϵ, linked symbols: ϵ_{DR}/ϵ. The dotted line represents the fit $\epsilon_\nu = 9\,(\ell/\eta)^{-4/3}$.

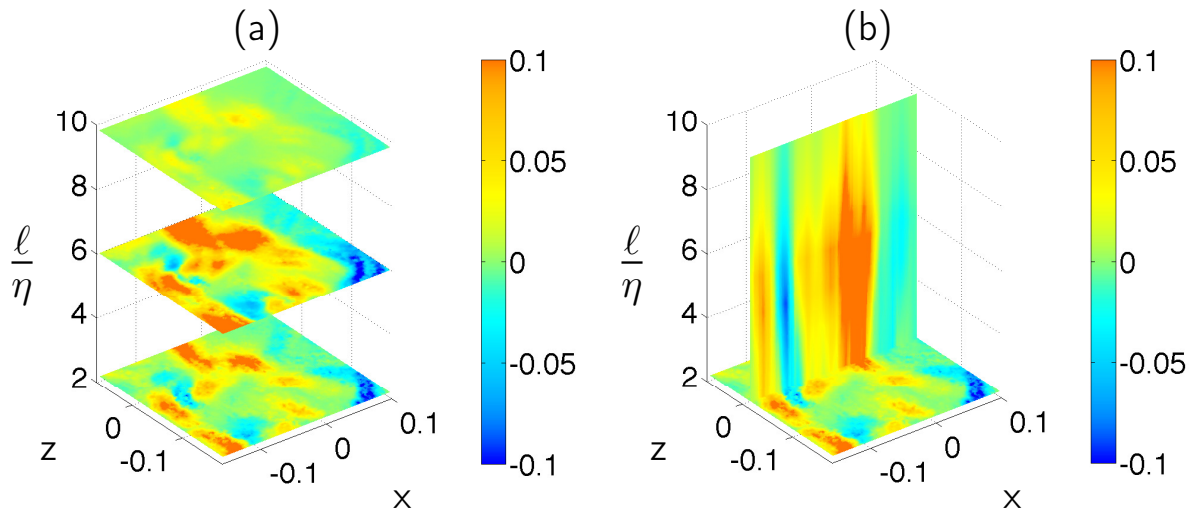

Figure 4.11: Local variations of Π^{ℓ}_{DR} as a function of scale at the center of the tank. (a) at three different scales, and (b) along a plane in scale space going through several intense structures.

flows and not in the laminar regime. However, one should be careful when making interpretations based on the data for which $\epsilon_{DR} < 0$ in Fig. 4.10. Indeed, this change of sign occurs for the cases with the smallest number of frames, so that the statistics might not be converged. A discussion about statistical convergence is provided at the end of this chapter. Finally, it is quite striking that the ratio ϵ_ν/ϵ is larger than unity for TM87(-)1H_zoom16_center_glyc59 (◆). This would mean that $\epsilon_{DR} < 0$ over the whole flow. This is very unlikely, and might be explained by our lack of informations concerning the variations of the velocity field along the orthogonal direction to our plane of measurements.

A local study

We have seen in Sec. 2.6 that the beginning of the dissipative range, characterized by the departure of the variations of the energy spectrum from the $-5/3$ slope, occurs at $\ell \approx 10\eta$ in agreement with [Gibson and Schwarz, 1963]. Fig. 4.11 shows the local variations of Π^{ℓ}_{DR} as a function of ℓ in the dissipative range for TM87(-)1H_zoom16_center_glyc59. We see that Π^{ℓ}_{DR} does not vanish as η is approached, but instead points towards localized intense structures. In addition, we observe that the topology of Π^{ℓ}_{DR} does not vary much, and that only the magnitude of the structures appear to change.

In order to study the influence of the Reynolds number and understand how the dissipated power is split between viscous and inertial effects, we show on Fig. 4.12 instantaneous maps of these two quantities at the highest resolution accessible for three different cases:

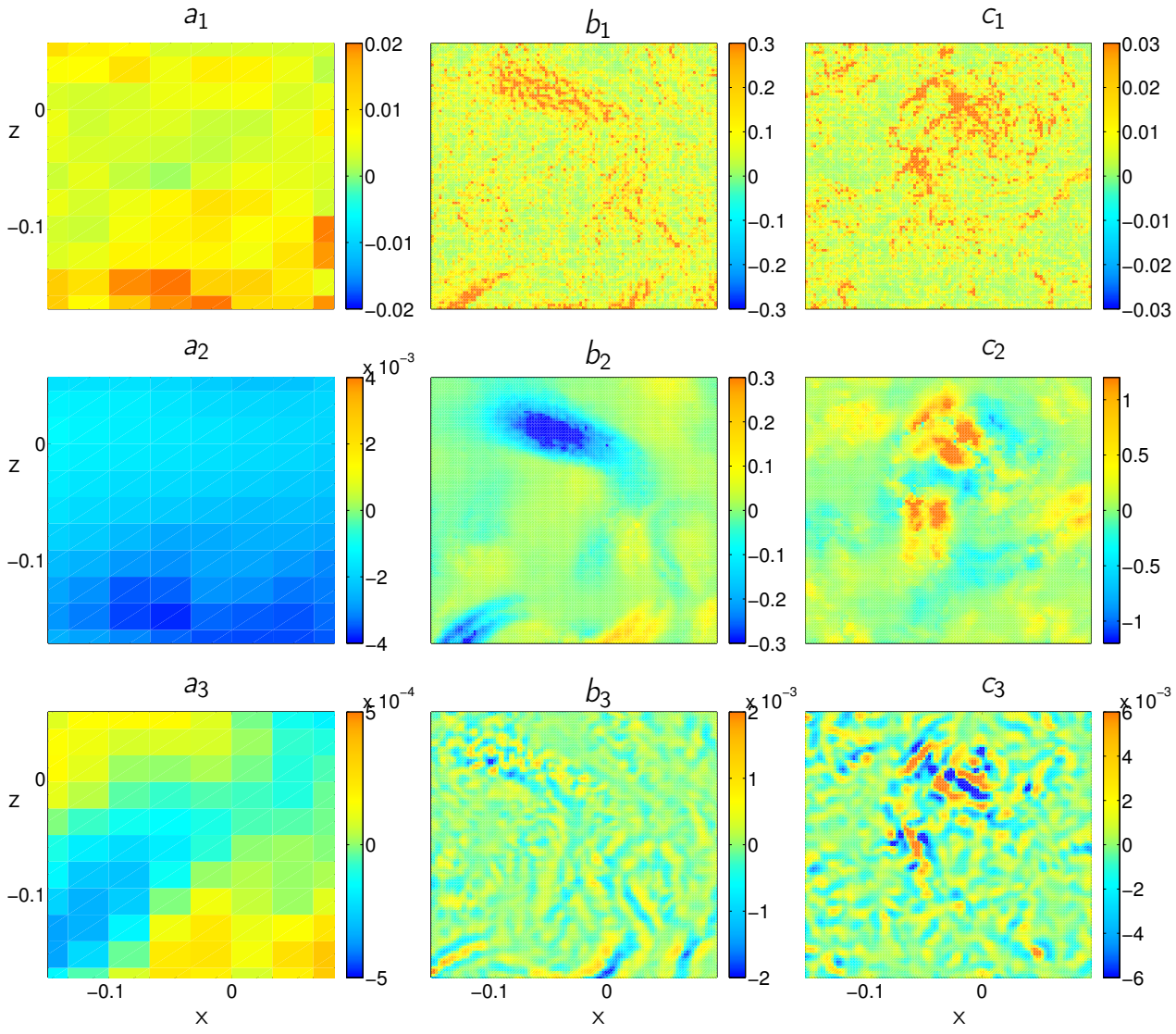

Figure 4.12: Maps of (1) $\mathscr{D}_\nu^\ell$, (2) Π_{DR}^ℓ, and (3) $d\Gamma^\ell/dt$ for cases A, B and C. We observe that the inertial dissipation remains strong in case B and C. Panels (a_3), (b_3) and (c_3) show that a non-zero circulation rate persists down to the dissipative scale, and areas of high viscous dissipation seem correlated with the location of extreme events of inertial dissipation.

- case A = TM60(+)2H_nozoom32_center_glyc100,
- case B = TM87(-)1H_zoom16_center_glyc59,
- case C = TM87(-)5H_zoom16_center_water.

Case A is a laminar flow while case B and C are fully turbulent. Only for case C is the Kolmogorov scale not resolved (see Tab. 2.3 and Tab. 2.4). In addition, we also provide maps of the local rate of circulation decay predicted by Eyink $d\Gamma^\ell/dt$. We note, in all three cases, the smaller noise in the estimates of Π^ℓ_{DR} and $d\Gamma^\ell/dt$ compared to $\mathscr{D}^\ell_\nu$. This is due to the inherent smoothing procedure in the expression of these two quantities, where the gradient operator acts on the test function rather than directly on the velocity increments. As we can see from Fig. 4.12(b_2) and (c_2), Π^ℓ_{DR} detects clear structures, which can be both positive and negative. However, as reported in Fig. 4.10, their time average remains positive. This peculiar feature is parallel to the behavior of entropy in non-equilibrium systems, where the entropy production can be positive or negative, but remains positive on time-average, in agreement with generalized fluctuation-dissipation theorems [Gallavotti and Cohen, 1995; Jarzynski, 1997; Ciliberto et al., 2010]. Π^ℓ_{DR} can also be locally very strong, sometimes over three orders of magnitude larger than the standard deviation σ_{DR}. The probability density functions (PDF) for case B for both Π^ℓ_{DR} and $\mathscr{D}^\ell_\nu$ are displayed in Fig. 4.14. Furthermore, a comparison of maps of Π^ℓ_{DR} with $d\Gamma^\ell/dt$ reveals that areas where Π^ℓ_{DR} is large are also areas of nonzero local rate of velocity circulation decay, which could be the footprints of singularities providing local source of circulation/vorticity, as conjectured by Eyink [Chen et al., 2006; Eyink and Aluie, 2006; Eyink, 2008a].

If we now turn to the laminar case (case A), the resolution of our measurements over the whole flow is smaller than Kolmogorov scale, so that all scales are resolved. There are no clear dissipation structures in the map of Π^ℓ_{DR} given in Fig. 4.12(a_2), which is negative over the whole observation window, and on average, much smaller than the viscous dissipation. The latter is also very small in this area, over one order of magnitude smaller than the total energy injection (see Fig. 4.10). In a similar way, we observe that the magnitude of $d\Gamma^\ell/dt$ is also very small at the center compared to viscous dissipation, and compared to its value for the two other (fully turbulent) flows. This is in agreement with the idea that the contribution of singularities is more important at high Reynolds numbers while viscous effects decrease. For case A, it can be checked that if the energy balance is performed over the whole experiment, ϵ_ν accounts for all of the injected power and supersedes by two order of magnitudes ϵ_{DR}.

Finally, we also see by comparing Fig. 4.12(b_1) with (b_2) and (c_1) with (c_2) that areas of high viscous dissipation tend to be correlated with areas where strong inertial transfers are localized. This is not too surprising since Π^ℓ_{DR} is nonzero at the locations where the velocity field loses its regularity. Therefore, in these areas we expect to find strong gradients and strong viscous dissipation. This argument can be made a little more quantitative by stating that if $\delta u \sim \ell^h$, then $\Pi^\ell_{DR} \sim \ell^{3h-1}$ and $\mathscr{D}^\ell_\nu \sim \ell^{2(h-1)}$. However, for $0 \leq h \leq 1/3$, $2(h-1) < 3h-1 \leq 0$, so that in the limit $\ell \to 0$, $\mathscr{D}^\ell_\nu$ grows faster than

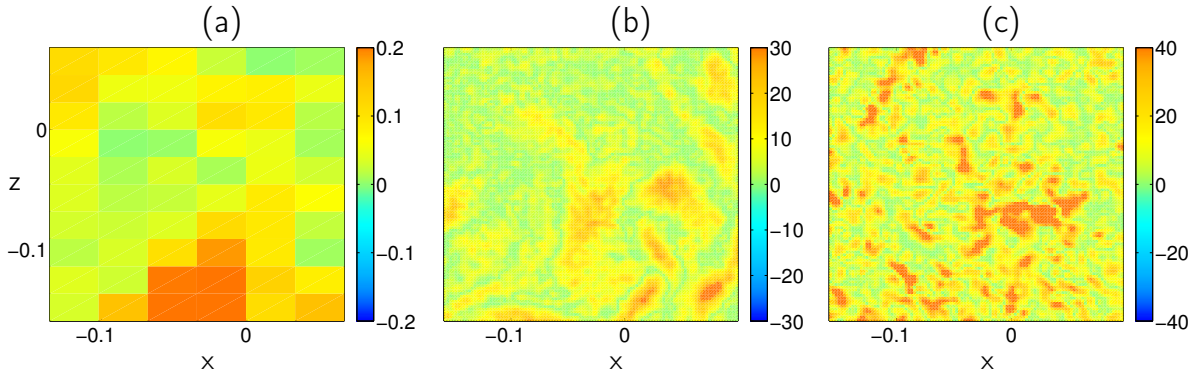

Figure 4.13: Local maps of the norm of the y-component of the vorticity ω_y for cases A, B and C.

Π^ℓ_{DR}. This is what we have shown on Fig. 4.10, and is also confirmed by the fact that the correlation between Π^ℓ_{DR} and $\mathscr{D}^\ell_\nu$ appears qualitatively stronger in case B where η is resolved, than in case C where it is not. As a consequence, in the light of the discussion in Sec. 3.3 about suitable weak solutions and the fact that we observe structures where $\Pi^\ell_{DR} < 0$ on Fig. 4.12(b_2), we may ask the question as to whether we actually observe inertial dissipation, or we still only capture transfers (as described in Sec. 4.2) to scales smaller than η, where all of the energy dissipation comes from viscous effects. If this is the case, this would mean that η is not the smallest relevant scale for viscous dissipation as *e.g.* in the multiractal model (more discussions are provided in Chap. 5).

In order to see whether the structures on Fig. 4.12(a_2), (b_2) and (c_2) are located in areas of high vorticity (BKM criterion), we may compare them with maps of the magnitude of the vorticity. In our case, we only have access to $|\omega_y|$ at the resolution scale, which is displayed on Fig. 4.13 for case A, B and C. Comparing Fig. 4.13(b) with Fig. 4.12(b_2) we find that there is some agreement between maps of $|\omega_y|$ and maps of Π^ℓ_{DR}. However, we see that some structures in Π^ℓ_{DR} are not mirrored in the vorticity field, and that the agreement is worse for case A and C, showing that the link between vorticity and inertial dissipation might be restricted to turbulent flows, when dissipative scale is resolved.

Fig. 4.14(a) shows the PDF of Π^ℓ_{DR} which appears to be highly non-Gaussian with very large tails. Fig. 4.14(b) shows the PDF of the logarithm of the viscous dissipation along with a normal distribution of same mean and standard deviation. It can be seen that the log-normal model holds well [Kolmogorov, 1962] for values of $\log(\mathscr{D}^\ell_\nu)$ close to their mean, while a clear discrepancy is observed in the tails of the distribution. However, zooming in the center of the distribution, a slight discrepancy from the log-normal law is observed (see inset on Fig. 4.14(b)). This slight discrepancy might be due to the fact that since we perform SPIV measurements, we estimated the viscous dissipation without taking into account the variations of the velocity along the orthogonal direction to the plane of measurements. However, this might not be enough to explain the stronger discrepancy in the tails.

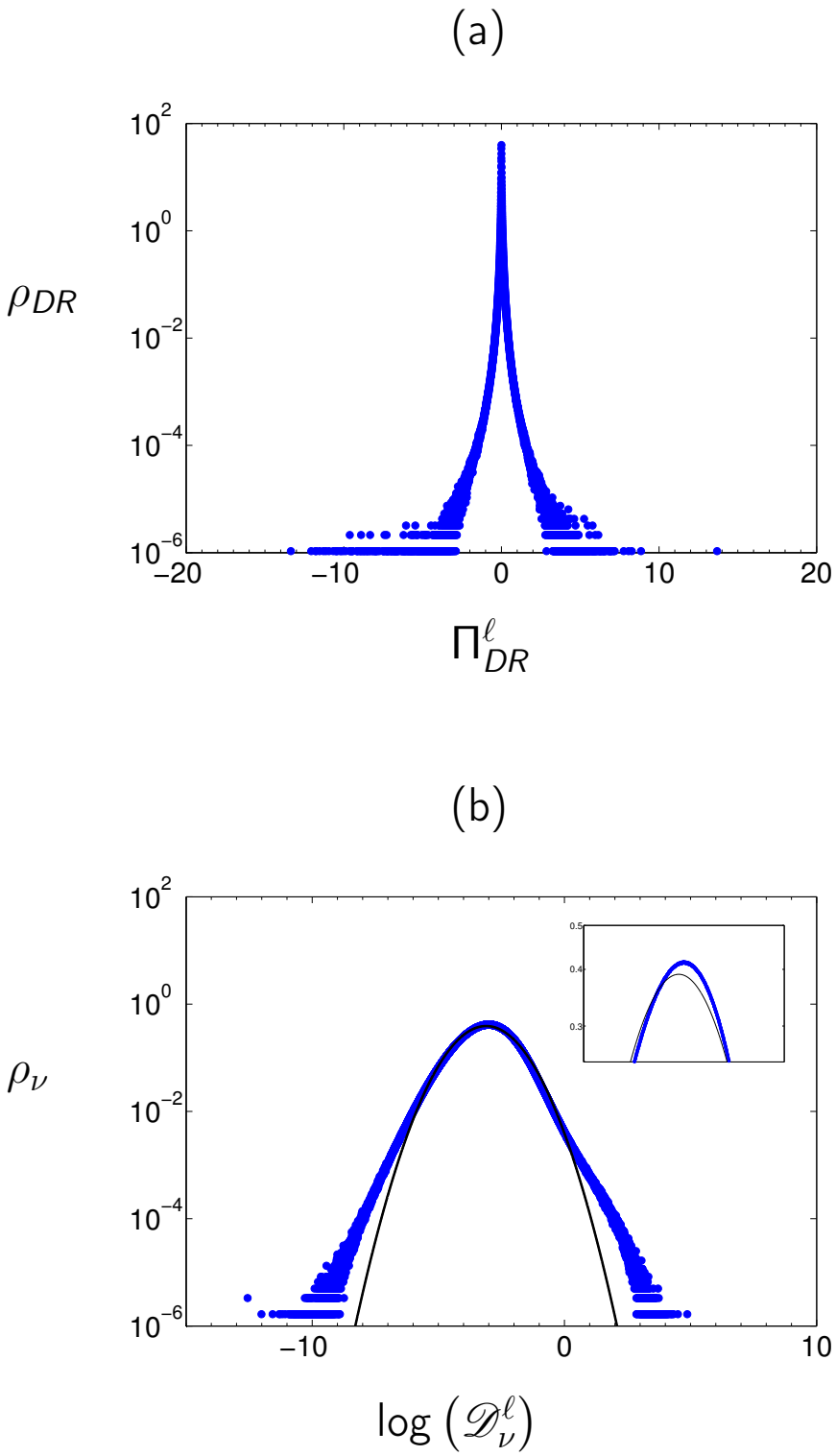

Figure 4.14: Probability density function for (a) Π^{ℓ}_{DR} and (b) $\log\left(\mathscr{D}^{\ell}_{\nu}\right)$. The solid line on panel (b) represents a Gaussian distribution of same mean and standard deviation as $\log\left(\mathscr{D}^{\ell}_{\nu}\right)$. The inset on panel (b) is a zoom on the peak of the distribution to show the slight discrepancy from the log-normal law.

A brief remark on statistical convergence

It might be wondered whether in our study we have collected enough data to have well converged statistics. Moreover, the PDF of Π^{ℓ}_{DR} being strongly non-Gaussian, it is not obvious that all the quantities we have used up to now such as averages or standard deviation are well defined. Indeed, Π^{ℓ}_{DR} being characterized by extreme events, it might be that each time such an event occurs, this completely changes the value of the statistical quantities. To check whether or not this is the case, Fig. 4.15 displays the evolution of both the spacetime average ϵ_{DR} and the standard deviation σ_{DR} of Π^{ℓ}_{DR} as a function of the number of frames for case B. It can be observed that both of these quantities are not converged when few number of frames are used to perform the statistics. However, for a number of frames around 20000, both of them saturate. Since we have collected around 30000 instantaneous frames for our high resolution data, this indicates that we have enough data to perform our study, and that it makes sense to define statistical quantities.

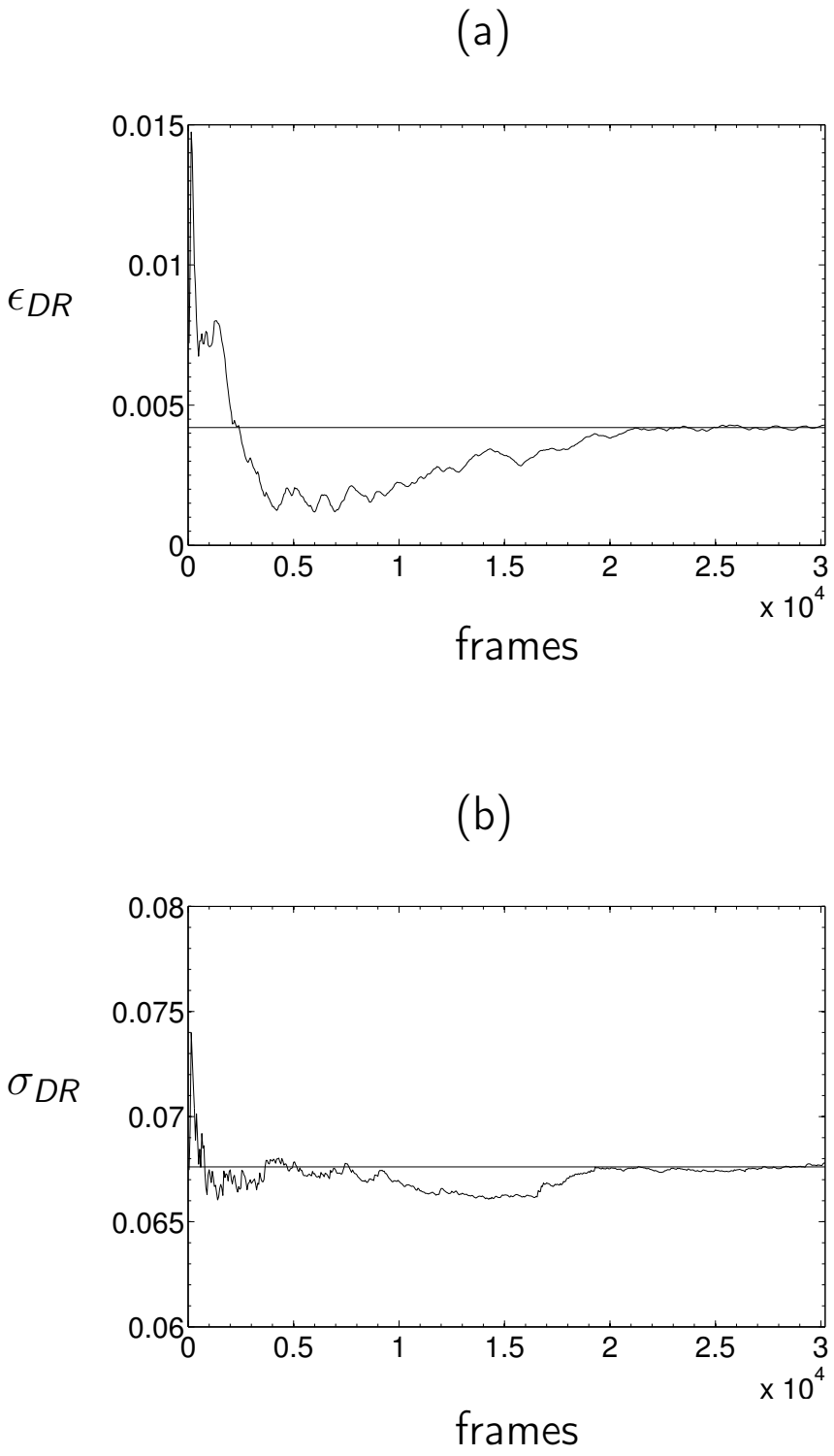

Figure 4.15: Variations of ϵ_{DR} and σ_{DR} as a function of the number of frames used to compute these quantities. We see that these two quantities converge for high enough statistics and are thus well-defined.

Chapter 5

Detection and Characterization of Quasi-Singular Structures in a von Kármán Flow

> Our eyes only see the big dimensions, but beyond those there are others that escape detection because they are so small.
>
> *Brian Greene*

Contents

Chap. 4 was concerned with the analysis from experimental data of the quantities introduced in Chap. 3. Our study provided encouraging new results, and we now want to push our investigations further. We have seen from Fig. 4.11 that as the scale ℓ is decreased, Π^{ℓ}_{DR} organizes into localized structures in the physical space. Moreover, we know that in the limit of infinitely small scale, Π^{ℓ}_{DR} converges towards its limit $\mathscr{D}_I$, which is an energy dissipation term stemming from singularities in the velocity field (*i.e.* independent of viscosity). These observations therefore lead to the idea of using Π^{ℓ}_{DR} as a detection criterion for potential singularities in turbulent flows. We are going to track local structures where $\Pi^{\ell}_{DR} \neq 0$ and, if these structures do not disappear as ℓ becomes small, then we have found good candidates for dissipative singularities, and we can then study the topology of the flow at the location of these structures.

In this chapter, we first present the main idea of our detection method, and compare the results obtained from SPIV measurements with those obtained from TPIV in the turbulent boundary layer of a wind tunnel. Then, we apply our detection criteria to the high resolution data obtained in our VK flow and, finally, we exhibit quasi-singular topologies in the velocity field and provide arguments for the existence of different types of singularities.

5.1 Singularity detection method

In this section, we review the main idea and results of the singularity detection method introduced in [Kuzzay et al., 2016] (paper provided in App. C).

The main idea

We saw in Chap. 3 that if the velocity is locally characterized by a scaling exponent $h > 1/3$, then $\mathscr{D}_I = 0$. In this section, we will make use of the converse statement of this result, *i.e.* if locally $\mathscr{D}_I \neq 0$, then the flow in the region where this is observed is no more regular than Hölder continuous with some $h \leqslant 1/3$. If this is the case, then the velocity field is not differentiable, which necessarily comes from a blow-up of the velocity field itself (see Chap. 3). However, from our discussions in Chap. 2 and Chap. 3, there are several reasons why such singularities cannot be directly detected from our experimental PIV measurements. First of all, measurement systems inevitably have a coarse spacetime resolution while blow-ups occur on infinitely small spacetime scales [Caffarelli et al., 1982]. Furthermore, post-processing techniques, which provide the output velocity field, smooth the data by performing local averages and by considering very large velocities as spurious vectors which, in the end, are discarded (see Chap. 2). The key idea is therefore to track singularities through the behaviour of Π^{ℓ}_{DR} as one comes across the dissipative scale η. If Π^{ℓ}_{DR} vanishes as one approaches or goes to smaller scales than η, then we have only seen local energy transfers through scales (see Chap. 4), which are ultimately converted into heat by viscous frictions as in the traditional Taylor view of turbulence. If, on the other hand, we see that Π^{ℓ}_{DR} keeps a nonzero value larger than some threshold $\mathcal{Q}$ (in absolute

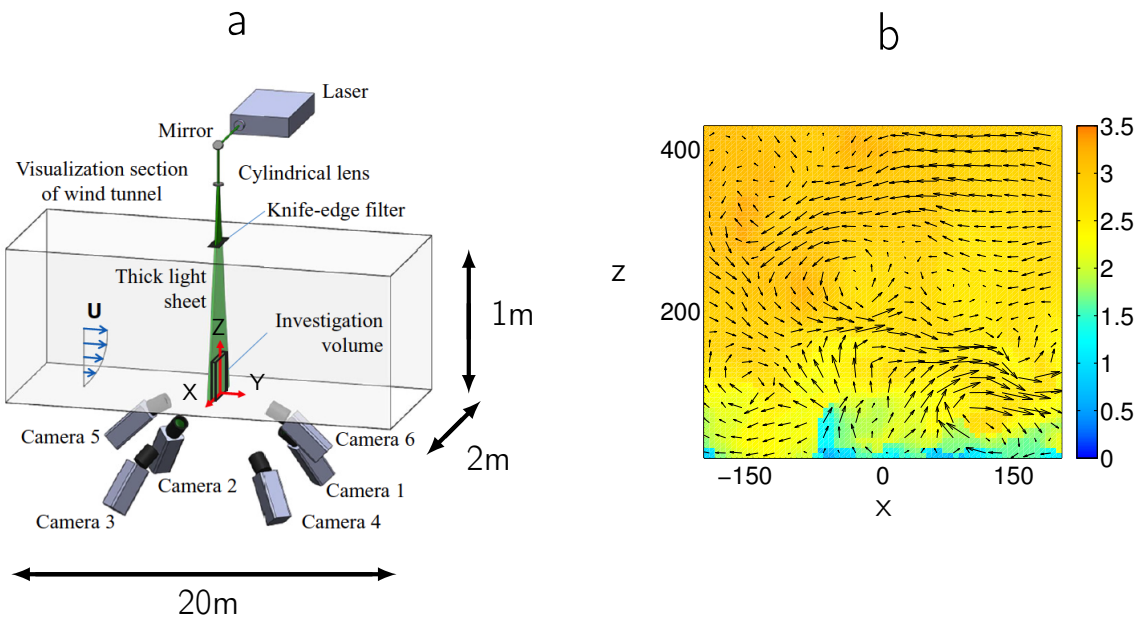

Figure 5.1: (a) sketch of the experimental set-up and (b) typical instantaneous velocity field, obtained from TPIV measurements in a plane orthogonal to the mean flow. The arrows represent the in-plane component of the velocity field while the colors code the normal component.

value), then we have detected a structure connected to a singularity with $h \leqslant 1/3$. This structure becomes fully singular in the exact limit $\ell \to 0$. Therefore, Eq. (3.22) will be used as a criterion (hereafter referred to as DR criterion) to detect singularity candidates through scales (which we call quasi-singularities). The only adjustable parameter in our detection method is the threshold $\mathcal{Q}$, and we argue in App. C that a natural choice is to take

$$\mathcal{Q}(\ell) = Q\sigma_{DR}(\ell), \tag{5.1}$$

where Q is an arbitrary dimensionless parameter, and σ_{DR} is the standard deviation of the spacetime distribution of Π^{ℓ}_{DR}.

Implementation from TPIV data and first tests

We apply the DR criterion to TPIV data obtained inside a fully turbulent flow generated in the boundary layer of a wind tunnel located at the Laboratoire de Mécanique de Lille, France. A sketch of the experimental set-up is displayed in Fig. 5.1 along with a typical instantaneous frame in a plane orthogonal to the mean flow (details of the set-up can be found in App. C or, more extensively, in [Martins et al., 2015]). In this experiment, the grid step is $\Delta_g \approx 0.7$ mm while the Kolmogorov scale is $\eta \approx 0.35$mm. As a consequence, our study is performed in the dissipative range close to the Kolmogorov scale. As already

discussed in Chap. 4 for VK flows, we observe that at these scales, Π^ℓ_{DR} does not vanish, and in this case remains larger than $Q = 10$ at localized areas which we identify as possible singularities with $h \leqslant 1/3$. In addition, the validity of our method is confirmed by comparison with the BKM criterion (the quantitative comparison is provided in App. C).

Stereoscopic vs tomographic detection

In the beginning, the main purpose of the study performed in App. C was to check whether areas of strong Π^ℓ_{DR} detected from SPIV measurements also correspond to areas of strong Π^ℓ_{DR} computed from TPIV measurements. In other words, can the DR criterion be applied to SPIV measurements ? This is an important question for us because our PIV set-up in the VK experiment is stereoscopic, and the possibility of detecting spurious structures would challenge our conclusions from Chap. 4. As a consequence, the paper provided in App. C was first intended as a preliminary study for the one performed in App. D. In order to answer the question, we provide mathematical arguments to show that spurious structures are not detected from SPIV measurements.

Let us define a new quantity based on (3.22), which is built from the three components of the velocity increments on a two-dimensional plane

$$\mathscr{D}_I^{2D}(\boldsymbol{u}) \overset{def}{=} \lim_{\ell\to 0} \Pi_{DR}^{2D,\ell}(\boldsymbol{u}) = \lim_{\ell\to 0} \frac{1}{4}\int_{\mathcal{S}} d\boldsymbol{r}\ \nabla G_\ell(\boldsymbol{r}) \cdot \delta^{2D}\boldsymbol{u}(\boldsymbol{r})\ |\delta^{2D}\boldsymbol{u}(\boldsymbol{r})|^2, \tag{5.2}$$

where $\delta^{2D}\boldsymbol{u}(\boldsymbol{r}) = \boldsymbol{u}(\boldsymbol{x}^{2D} + \boldsymbol{r}^{2D}) - \boldsymbol{u}(\boldsymbol{x}^{2D})$, $\boldsymbol{x}^{2D}$ and $\boldsymbol{r}^{2D}$ being the projection onto the plane of measurements of the 3D coordinates. We now argue that areas where $\mathscr{D}_I^{2D}$ is nonzero are also areas where the full field $\mathscr{D}_I$ is nonzero, thus proving that it is sufficient to look for singularities in SPIV data.

To prove this, we first consider a situation where the velocity field is regular in the direction perpendicular to the plane of measurement, that we call y. In such a case, as $\ell \to 0$ we may expand the velocity increments in Taylor series in the y-direction. Using the notations introduced in Eq. (5.2), we get

$$\delta\boldsymbol{u}(\boldsymbol{r}) = \delta^{2D}\boldsymbol{u}(\boldsymbol{r}) + r_y\partial_y\boldsymbol{u} + \underset{r_y\to 0}{O}(r_y^2). \tag{5.3}$$

where r_y is the y-component of $\boldsymbol{r}$ and $\delta^{2D}\boldsymbol{u}(\boldsymbol{r})$ the velocity increments on the (XZ) plane. We then take the cube of this expression which leads to

$$[\delta^{2D}\boldsymbol{u}(\boldsymbol{r})]^3 = [\delta\boldsymbol{u}(\boldsymbol{r})]^3 + \underset{r_y\to 0}{O}([\delta\boldsymbol{u}(\boldsymbol{r})]^2 r_y). \tag{5.4}$$

As we know from Chap. 3, $\Pi^\ell_{DR}(\boldsymbol{u}) = O(\delta u(\ell)^3/\ell)$. So that if $\delta u(\ell) \sim \ell^h$, then

$$\Pi_{DR}^{2D,\ell}(\boldsymbol{u}) = \Pi^\ell_{DR}(\boldsymbol{u}) + \underset{\ell\to 0}{O}\left(\ell^{2h}\right), \tag{5.5}$$

where the first term is $O(\ell^{3h-1})$. So if the velocity field is regular with $h = 1$, then

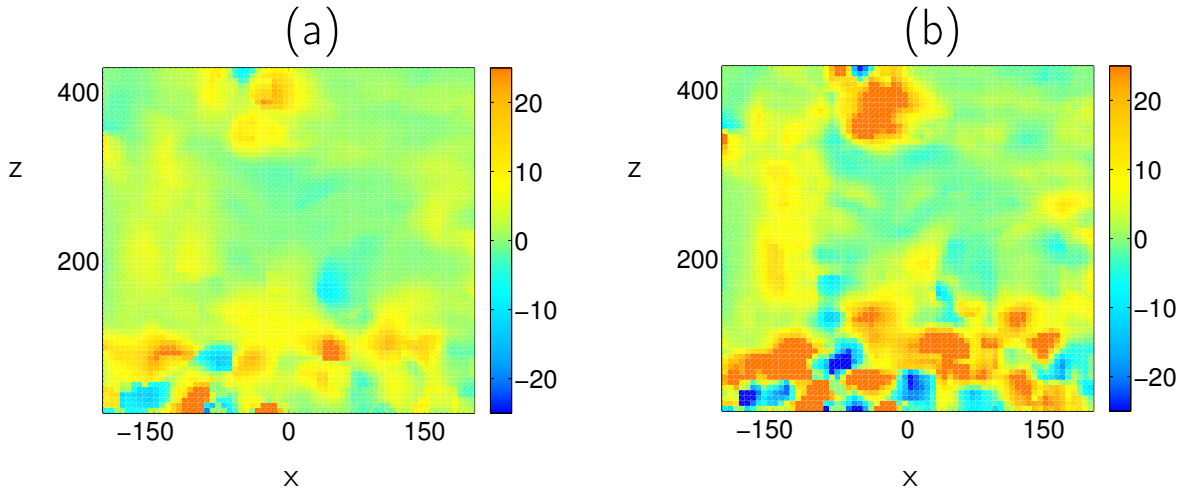

Figure 5.2: Comparison between two instantaneous maps of the Duchon-Robert (DR) criterion computed from both SPIV and TPIV data. (a) map of the DR energy transfers $\Pi_{DR}^{2D,\ell}$ and (b) map of the DR energy transfers Π_{DR}^{ℓ} (normalized by their space-time averages) at the smallest resolved scale. The results are displayed in the plane $y = 0$ orthogonal to the streamwise direction.

$$\lim_{\ell\to 0} \Pi_{DR}^{2D,\ell}(\boldsymbol{u}) = \lim_{\ell\to 0} \Pi_{DR}^{\ell}(\boldsymbol{u}) = 0. \tag{5.6}$$

If, on the other hand, the velocity field is singular with $h < 1$, the limit of $\Pi_{DR}^{2D,\ell}(\boldsymbol{u})$ is controlled by the first term on the right-hand side of Eq. (5.5) and we have

$$\lim_{\ell\to 0} \Pi_{DR}^{2D,\ell}(\boldsymbol{u}) = \lim_{\ell\to 0} \Pi_{DR}^{\ell}(\boldsymbol{u}). \tag{5.7}$$

This means that if the flow is regular in the y direction, all areas where the flow is smooth in TPIV data are also smooth in SPIV data. Therefore, all singularities detected using SPIV measurements will correspond to singularities detected using TPIV. That is to say, computing the inertial energy dissipation from SPIV measurements does not introduce any spurious structures which would disappear when performing the full 3D computation. However, we cannot detect singularities lying only on the orthogonal direction to the plane of measurements. As a consequence, $\mathscr{D}_I^{2D} \neq 0$ is a sufficient but not necessary condition to detect singularities.

An illustration of this result is also provided in Fig. 5.2 where a comparison between $\Pi_{DR}^{2D,\ell}$ and Π_{DR}^{ℓ} shows a very high correlation between intense structures in both cases (the quantitative comparison is provided in App. C). Moreover, another comparison with the norm the vorticity shows that the agreement between the DR and BKM criteria is still strong for SPIV data.

5.2 Application to von Kármán flows

We are now going to apply our detection method to TM87(-)1H_zoom16_center_glyc59 (case B in Chap. 4) in order to track extreme events of Π^{ℓ}_{DR} and study the flow topology at the location of these events. The threshold $\mathcal{Q}$ we introduced in Sec. 5.1 was expressed in units of the spacetime average ϵ_{DR}. However, a more usual choice is to use the average deviation from ϵ_{DR}: the standard deviation σ_{DR}. This makes sense because we have shown in Chap. 4 that this quantity converges towards a definite value when computed from a large enough amount of data. As a consequence, in this section, we take

$$\mathcal{Q}_{\pm}(\ell) = \epsilon_{DR}(\ell) \pm Q\sigma_{DR}(\ell). \tag{5.8}$$

For TM87(-)1H_zoom16_center_glyc59, we have $\epsilon_{DR} = 0.0043$ and $\sigma_{DR} = 0.0679$. As might be expected, the number of events which correspond to $\Pi^{\ell}_{DR} > \mathcal{Q}_{+}(\ell)$ or $\Pi^{\ell}_{DR} < \mathcal{Q}_{-}(\ell)$ strongly depends on the choice of Q. For instance, if we choose $Q = 50$, we detect that these events are distributed on approximately 100 instantaneous frames. However, for $Q = 100$, only 6 frames contain such events. This therefore raises the question of the appropriate choice of Q. In extreme value theory, there is no general rule as to what quantile should be used in order to consider an event as extreme. The most common choice when the events are normally distributed is to take $Q = 3 - 5$. In this section, we are going to set $Q = 75$. This choice is motivated by the fact that the events which are above this threshold correspond to $|\Pi^{\ell}_{DR}| > 100\epsilon$ (see Tab. 2.3), and in this respect can truly be qualified as extreme. The probability of finding such extreme events can be computed from the PDF of Π^{ℓ}_{DR} displayed in Fig. 4.14a) and is less than 10^{-6}. When looking at the corresponding flow topologies, we observe many different patterns, some examples being displayed on Fig. 5.3. In App. D, we proposed a first classification of these patterns which we categorize in fronts, spirals, jets and vorticity cusps. Of course, we must be careful in trying to interpret such classification since it does not rely on any systematic and detailed analysis, but rather on "how the flow looks like". Moreover some of the detected topologies do not appear to enter any of the categories we just mentioned in any obvious way. For instance, Fig. 5.3(e) and (f) show a flow which seems to originate from a source point, where $\Pi^{\ell}_{DR} < 0$ as would be expected in such a case. However, we observe that most of the patterns we detect resemble those which occur in the neighbourhood of critical points in inviscid, constant vorticity flows with slip at the boundary [Perry and Fairlie, 1974]. For example, Fig. 5.3(a) and (b) seem to correspond to a saddle, Fig. 5.3(c) and (d) to a focus and Fig. 5.3(g) and (h) to a node. This is quite surprising for at least two reasons. First, we saw in Chap. 3 that areas where the velocity field loses its regularity are areas where $\boldsymbol{u}$ blows up whereas $\boldsymbol{u} = 0$ at critical points. Second, the analysis performed in [Perry and Fairlie, 1974] is based on the assumption that $\boldsymbol{u}$ can be expanded in Taylor series which is not the case at the location of singularities. Clearly, more investigations are needed in order to improve the understanding of our results. In any case, a general observation is that whatever the in-plane flow, very intense structures of Π^{ℓ}_{DR} lie along a frontier across which u_y changes abruptly.

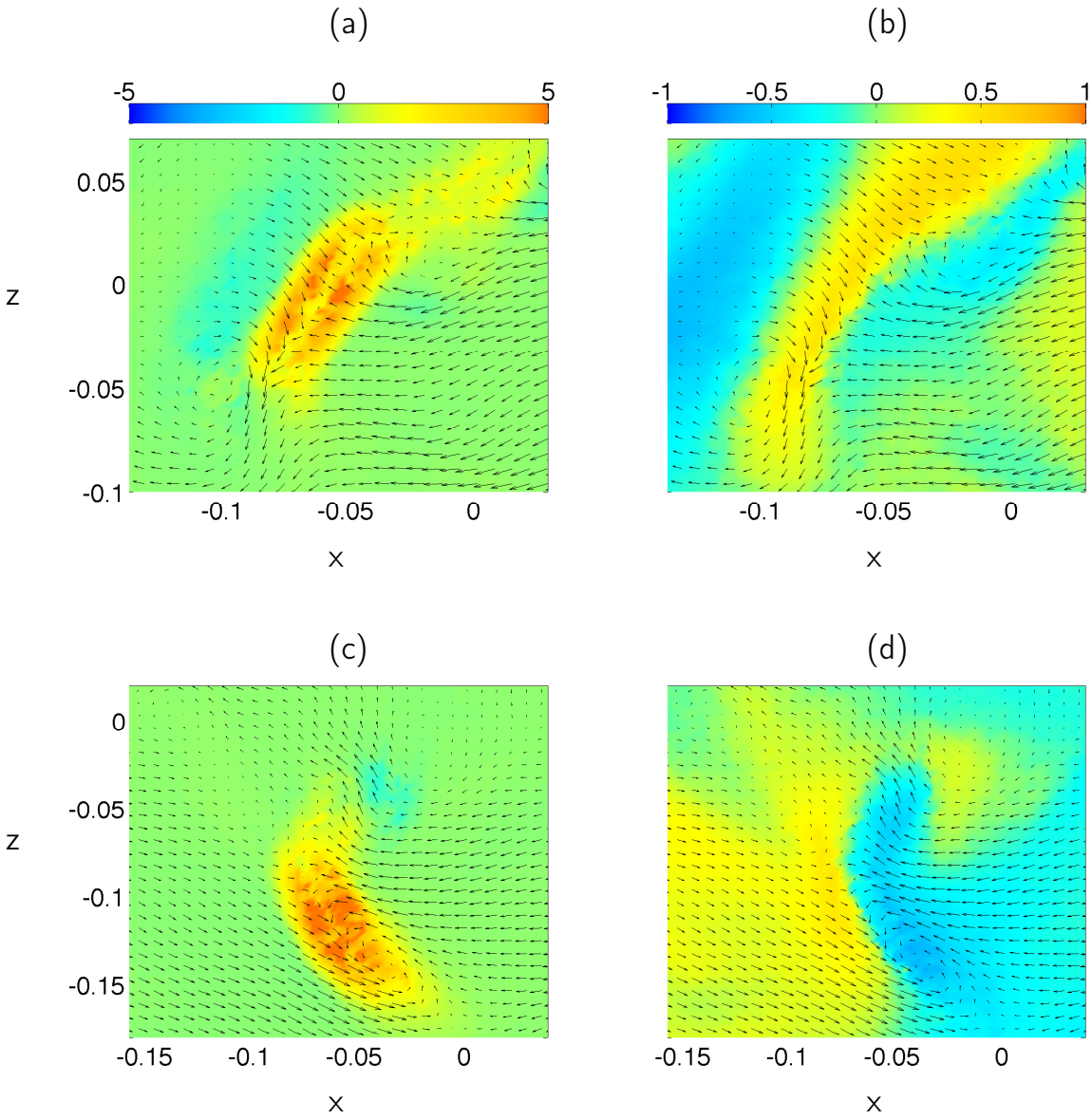
(a)
(b)
(c)
(d)
-5
0
5
-1
-0.5
0
0.5
1
0.05
0
-0.05
-0.1
-0.15
z
x
-0.1
-0.05
0

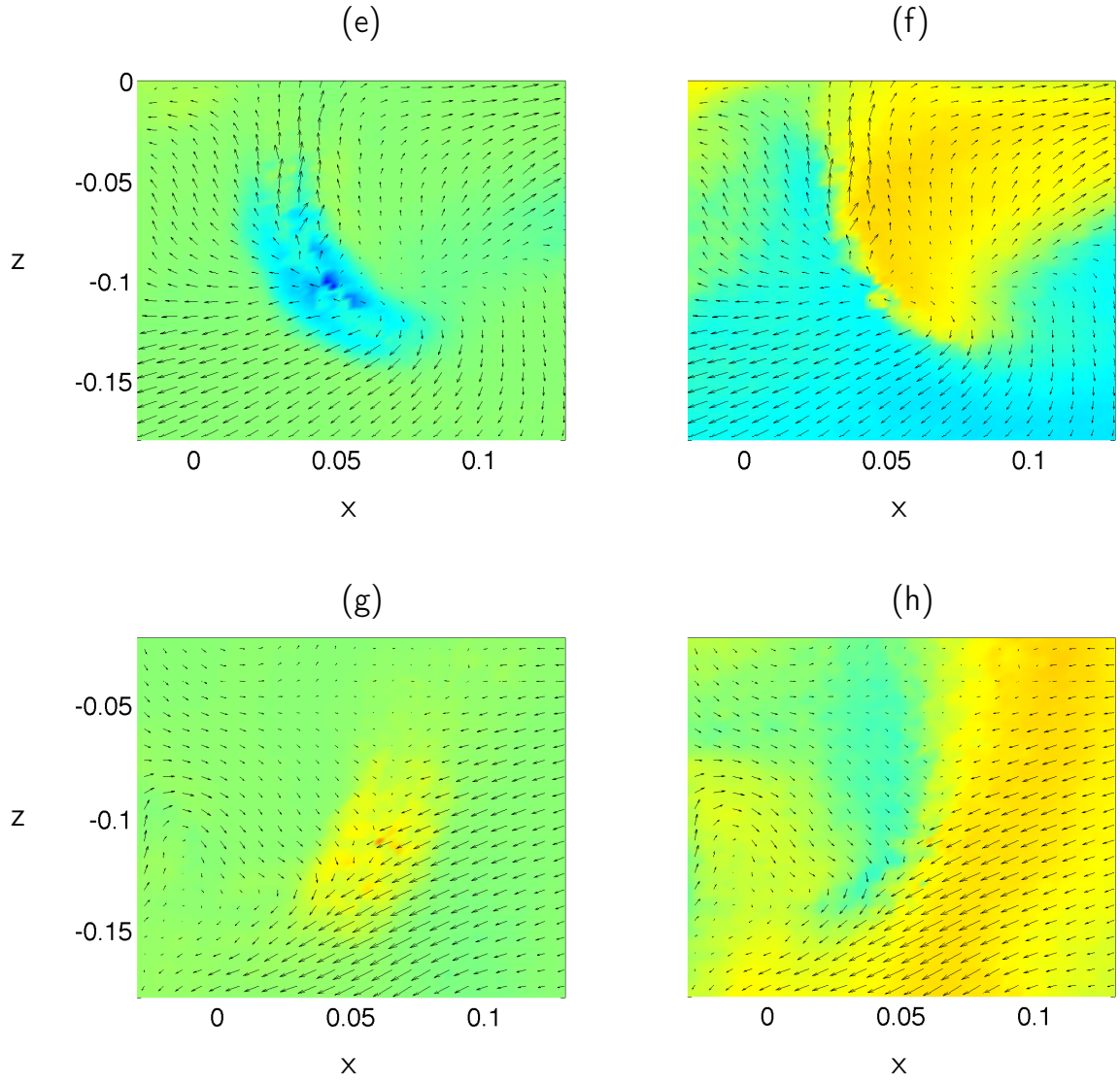

Figure 5.3: Examples of flow topologies observed at the location of extreme events of Π^{ℓ}_{DR} for TM87(-)1H_zoom16_center_glyc59. Left panels show maps of Π^{ℓ}_{DR} (colours) along with the in-plane component of the velocity field (arrows). Right panels show the three components of the velocity field. The colour codes for all the right and left panels are the same.

5.3 Discussion

In this chapter, we have presented a new method for detecting potential singularities in real turbulent flows from PIV measurements, and applied it in the case of a VK flow where the Kolmogorov scale is resolved. Our results provide a further indication of the non-trivial structures of turbulent flows at small scales, complementary to previous scaling based studies of dissipative intermittency (see e.g [Sreenivasan and Antonia, 1997]). We have shown that extreme events in Π^{ℓ}_{DR} are associated with the existence of nearly singular structures in the topology of the velocity field, a classification being proposed in App. D. These kinds of topologies are typically associated with special configurations of eigenvalues of the velocity strain tensors around critical points of flow patterns. At such points, it is often the case that Lagrangian trajectories cross [Perry and Fairlie, 1974], which would make these extreme events possible locations of shock-like singularities. In any case, the flow topology around an extreme event is different from the usual flow topology associated with viscous dissipation. For instance, [Moisy and Jiménez, 2004] used box counting to study the fractal structure of regions of intense vorticity and energy dissipation in a direct numerical simulation of isotropic turbulence. Their work suggests that the geometry of the regions of intense dissipation resemble sheets or ribbons. This further suggests the existence of an inertial mechanism contributing to energy dissipation.

Another interesting observation is that extreme events of Π^{ℓ}_{DR} provide significant local contributions to energy balance at dissipative scales, regardless of whether the energy lost pertaining to these events is eventually dissipated by genuine singularities or by viscosity at yet smaller scales. This suggests that Kolmogorov scale might not be the only characteristic scale for energy dissipation. This seemingly surprising conjecture is in fact compatible with the multi-fractal picture of turbulence, which predicts that for a given flow singularity of exponent h there is a specific dissipation scale η_h scaling like $Re^{-1/(1+h)}$ [Paladin and Vulpiani, 1987b]. For $h = 1/3$, we recover the classical Kolmogorov scale η. For the case where $h < 1/3$, we have $\eta_h < \eta$ so that energy dissipation can occur at much smaller scales than the expected one in K41. Our findings are therefore compatible with the multi-fractal picture of turbulence, if the extreme events of inertial dissipation are the footprints of singularities of exponent $h < 1/3$, as suggested in App. C. Whether this interpretation is valid or not is still debatable, as we have no means to follow the inertial dissipation down to $\ell = 0$, as required in Eq. (3.22). In order to unambiguously distinguish between inertial and viscous dissipation, and to answer the question as to whether these extreme events are simply energy transfers to yet smaller scales or not, one may need to resolve the flow down to the kinetic limit and track the evolution of these extreme events in time until they fully dissolve, which represents an experimental challenge for future works.

Perhaps a more immediate practical question one could ask is: knowing the significance of such extreme events even at the dissipative scales, how should one truncate models and simulations at tractable hydrodynamic scales with the correct physics reflecting their properties ? In compressible fluid dynamics, these kinds of questions are usually addressed in relation with the building of a singularity through shock formation. In these

cases, it has been common practice starting with [Von Neumann and Richtmyer, 1950] to select physically admissible solutions, and ensure the stability of numerical schemes via the introduction of an appropriate numerical viscosity [Guermond et al., 2011]. Our results suggest that the same kind of procedure should also be introduced in incompressible numerical simulations, in order to account for extreme events of inertial dissipation that are not captured at the model resolution scale.

Chapter 6

First Discussions on Numerical Simulations

> Real programmers don't comment their codes. They were hard to write, they should be hard to read.
>
> *Unknown*

Contents

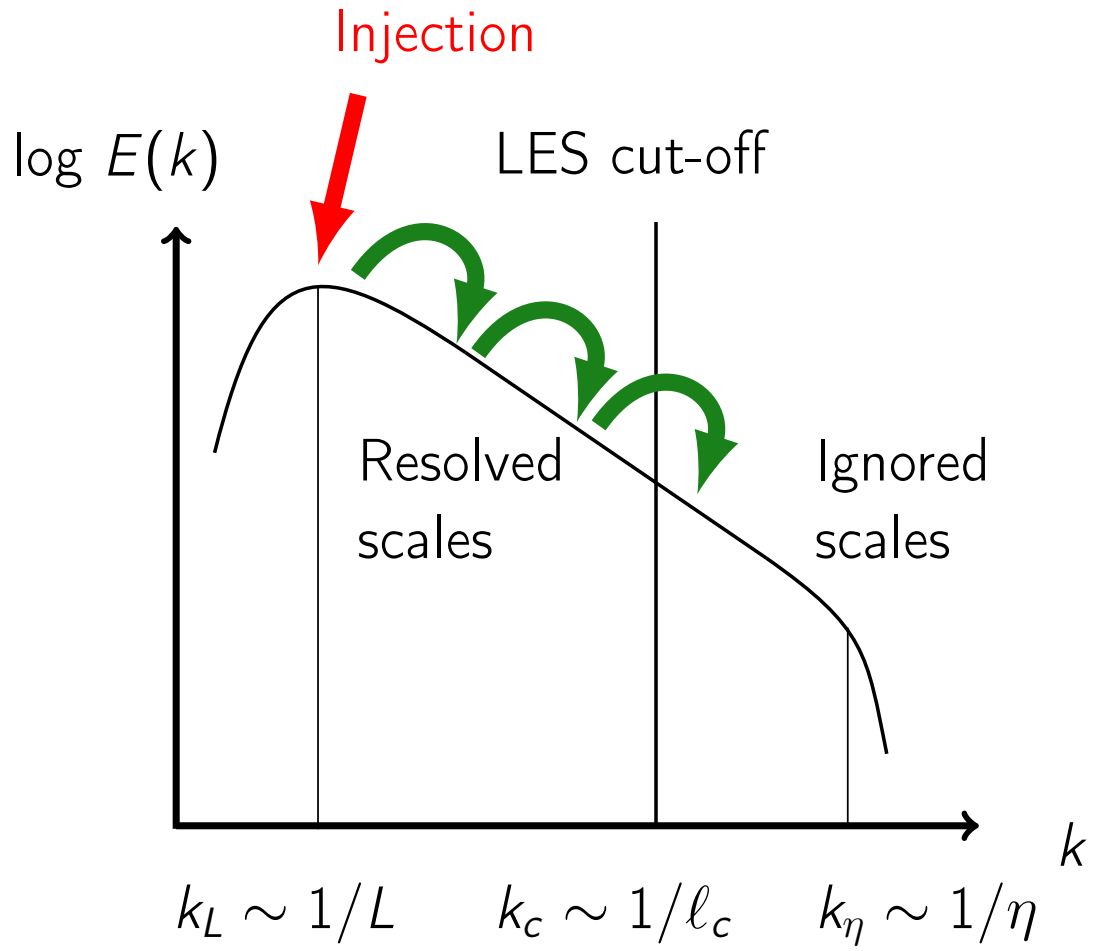

Figure 6.1: Illustration of the idea of large eddy simulations. The INSE are directly solved for the wavenumbers smaller than some cut-off, while higher modes are averaged out and modeled.

6.1 Large eddy simulations

This section presents the main results published in [Kuzzay et al., 2015] (see App. B).

Principle

Performing DNS of turbulent flows requires to solve the INSE and keep track of all the scales from the energy injection scale down to dissipative scales. As we discussed at the end of Chap. 1, the number N of grid points needed to fully resolve the flow down to Kolmogorov scale grows like $N \sim Re^{9/4}$, which rapidly becomes expensive in terms of data storage and computational power as Re increases. Therefore, DNS are limited to fairly low values of Re. For instance, the DNS of VK flows performed by Caroline Nore and

Jean-Luc Guermond do not go beyond $Re \approx 2500$ (see Chap. 2), and if one wants to simulate flows at higher Re, other solutions must be come up with.

The idea of large eddy simulations (LES) was first proposed by [Smagorinsky, 1963] in order to simulate atmosphere's general circulation. As illustrated on Fig. 6.1, the idea of LES is to reduce computational cost by ignoring the scales smaller than some cut-off ℓ_c, usually lying in the inertial range, and numerically solve the INSE for large scales only. The interaction between large and small scales must then be modeled in terms of the resolved velocity field in order to have a closed problem. Physically, this approach is justified by the fact that large-scale structures in turbulent flows are the ones which absorb energy from the mean flow and pass it on to smaller scales. As a consequence, they are very anisotropic and depend on various large-scale parameters such as forcing conditions, flow geometry, etc... Small scales on the other hand are the ones which dissipate energy. They are assumed to be isotropic and universal, *i.e.* they do not depend on the details of the flow (see Kolmogorov's universality assumptions discussed in Chap. 1).

In LES, small scales are averaged out via some low-pass filter applied to the INSE: this is exactly the approach we have introduced at the beginning of Chap. 3. We have seen that the dynamics of the coarse-grained velocity field defined in Eq. (3.1) by

$$u_i^{\ell_c}(\boldsymbol{x},t) = \int d\boldsymbol{r}\; G_{\ell_c}(\boldsymbol{r})\, u_i(\boldsymbol{x}+\boldsymbol{r},t)\,, \tag{3.1}$$

obeys Eq. (3.2) and (3.3)

$$\partial_t u_i^{\ell_c} + u_j^{\ell_c}\partial_j u_i^{\ell_c} = f_i^{\ell_c} - \partial_i p^{\ell_c} + \nu\partial_{jj} u_i^{\ell_c}, \tag{3.2}$$

$$\partial_j u_j^{\ell_c} = 0, \tag{3.3}$$

which have the same form as the INSE with the added turbulent force $f_i^{\ell_c} = -\partial_j \tau_{ij}^{\ell_c}$. $\tau_{ij}^{\ell_c}$ is the subscale stress tensor defined as $\tau_{ij}^{\ell_c} = (u_i u_j)^{\ell_c} - u_i^{\ell_c} u_j^{\ell_c}$. However, if scales smaller than ℓ_c are ignored, $(u_i u_j)^{\ell_c}$ cannot be computed, and a closure relation must be found in order to solve Eq. (3.2) and (3.3) numerically. Historically, the first one was introduced in [Smagorinsky, 1963], who proposed to write $\tau_{ij}^{\ell_c} = -2\nu_e S_{ij}^{\ell_c}$, where ν_e is the eddy viscosity and must be tuned depending on the type of flow under investigation. It follows that the scale-to-scale energy transfers represented by $\Pi_{LES}^{\ell_c} = -\tau_{ij}^{\ell_c} S_{ij}^{\ell_c}$ are modeled by a viscous dissipation, which therefore does not allow for backscatter of energy, known to occur in real turbulence.

Large eddy approach to PIV measurements

Designing new LES models is an active area of research. However, a question which can be raised is whether these models accurately describe the physics of turbulent flows at small scales.

PIV measurements are obtained by computing correlations between two successive snapshots of the flow. As a consequence, the output velocity field is obtained through local

averages over interrogation cells, and its properties are similar to the low-pass filtered field studied in LES. In this case, the cut-off ℓ_c is imposed by the resolution of the PIV system. In order to estimate the energy dissipated in turbulent flows where PIV measurements can be performed and where $\eta \ll \ell_c$, it has therefore recently been suggested in [Sheng et al., 2000] to use LES models for the estimation of energy transfers towards subgrid scales (SGS). This approach has been successfully applied for various flow geometries in [Saarenrinne and Piirto, 2000; Baldi and Yianneskis, 2003; Tanaka and Eaton, 2007; Delafosse et al., 2011; Tokgoz et al., 2012; Kuzzay et al., 2015].

The VK2 set-up offers a framework of choice in order to test the accuracy of LES models from experimental data. As discussed in Chap. 2, torque measurements provide precise estimations of the global power dissipated within the flow, and SPIV measurements allow to implement techniques borrowed from LES. In addition, we also know from Chap. 4 that ϵ_{DR} computed over the whole volume between the impellers agrees with torque measurements within 2%. The idea is therefore to test our results obtained in Chap. 4 in the inertial range against results obtained using LES models for the estimation of the subgrid energy transfers.

In order to perform this study, we use the gradient model first introduced in [Clark et al., 1979]. In this model, the subscale stress tensor is expressed as an inner product of the resolved velocity gradients

$$\tau_{ij}^{\ell_c} = C\Delta_r^2 \partial_k u_i^{\ell_c} \partial_k u_j^{\ell_c}, \tag{6.1}$$

where C is a constant to be calibrated and Δ_r is the width of the filtering. This model is known to ensure forward and backscatter of energy between resolved scales and SGS.

Application to von Kármán flows

In order to apply the LES approach to the PIV data obtained from our VK set-up, the first step is therefore to find the value of the constant C in order to be able to compute $\Pi_{LES}^{\ell_c}$. The procedure we followed is based on the angular momentum balance given in Eq. (1.22), and is described in App. B. We choose C so as to recover the results of [Marié and Daviaud, 2004], who showed that the vertical flux of angular momentum in VK flows is a constant equal to the torque injected by the impellers. It is shown in App. B that the optimum value of the constant is $C \approx 4$, which is around 50 times larger than the conventional choice made in [Leonard, 1974; Eyink, 2006] for a Gaussian filter. Possible explanations for this large value of C are: our data are not filtered in a Gaussian way ; since we ignored azimuthal derivatives in our computations from SPIV measurements, the constant must be higher to compensate ; the turbulence is neither isotropic nor homogeneous.

Comparison between PIV estimates of $\epsilon_{LES} = \left\langle \overline{\Pi_{LES}^{\ell_c}} \right\rangle$ (● - ◆), ϵ_{DR} (● - ◆) and torque measurements (● - ◆) is provided on Fig. 6.2. We observe that, overall, the LES approach is in good agreement with direct torque measurements. At $Re \approx 4 \times 10^3$, the dissipative scale is of the order of 1mm, close to the PIV resolution. As a consequence,

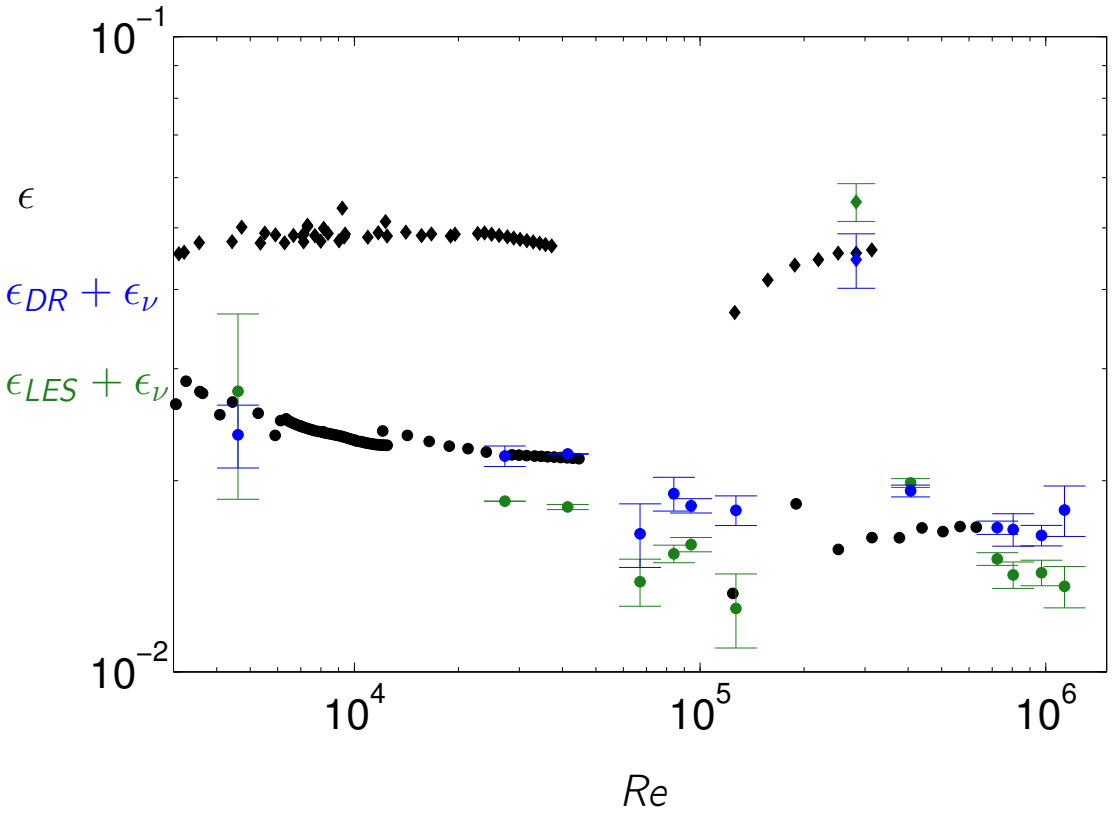

Figure 6.2: Comparison between estimates of ϵ obtained from torque measurements (● - ◆), from SPIV measurements by computing Π^ℓ_{LES} (● - ◆), and from SPIV measurements by computing Π^ℓ_{DR} (● - ◆). The estimates are computed based on 2-15 realizations of the same flows where at least 600 instantaneous velocity snapshots have been taken for each of them. The symbols represent the mean of our computations, while the error bars represent the standard deviation. ϵ_ν has been taken into account only for $Re \approx 4 \times 10^3$ and is negligible compared to ϵ_{DR} for all the other points.

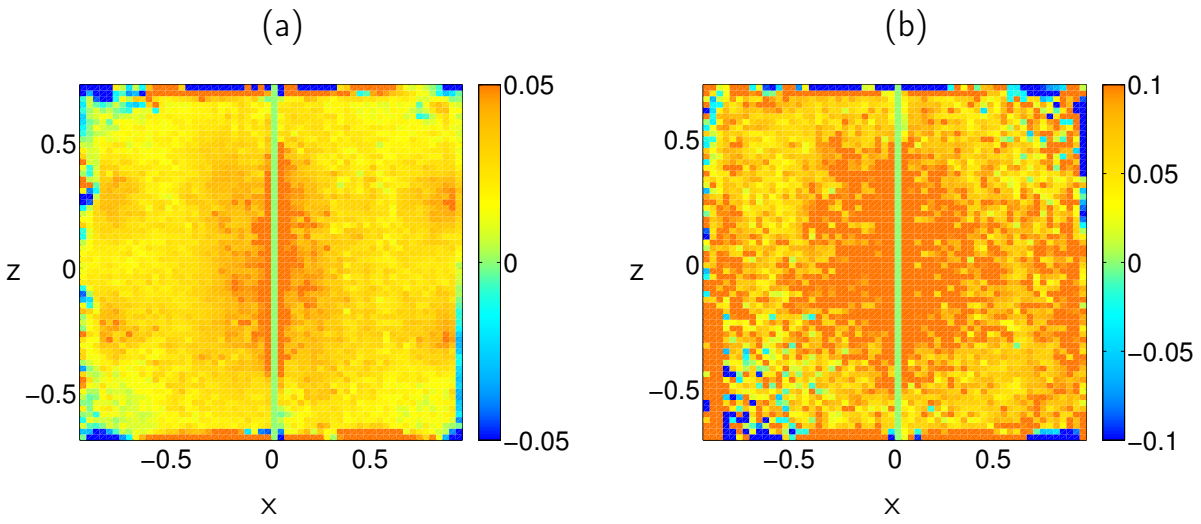

Figure 6.3: Maps of $\overline{\Pi^{\ell_c}_{LES}}$ at $Re = 3 \times 10^5$ for (a) TM87(+) and (b) TM87(-).

a non-negligible part of energy transfers (around 30%) is contained in the viscous term, and we find a very good estimation of the mean energy dissipation rate by taking into account both scale-to-scale transfers and viscous dissipation. This result is therefore in agreement with the observation of [Tokgoz et al., 2012] made for a Taylor-Couette flow. However, for all the other points, the contribution of viscous effects can be neglected compared to ϵ_{LES} and ϵ_{DR}. For $Re > 7 \times 10^5$, the LES approach allows to capture up to 90% of the actual energy dissipation. In any case, it appears that ϵ_{DR} is in better agreement with torque measurements than ϵ_{LES}. Indeed, as we discussed in Chap. 4, DR-PIV estimates allow to capture up to 98% of the actual dissipation with smaller error bars. As a consequence, since the expression of Π^{ℓ}_{DR} is an exact result derived from the INSE, and since it provides better estimates of ϵ without introducing any free parameter to be calibrated, the conclusion from this study is that Π^{ℓ}_{DR} offers a very promising alternative to LES methods for the computation of scale-to-scale energy transfers from PIV measurements in real turbulent flows.

Finally, if we compare the maps of $\overline{\Pi^{\ell_c}_{LES}}$ displayed on Fig. 6.3 with the ones of $\overline{\Pi^{\ell_c}_{DR}}$ from Fig. 4.5(a) and (c) obtained from the same data, we observe that they contain the same qualitative informations so that our discussion from Chap. 4 holds for the results displayed on Fig. 6.3. However, a noticeable difference is that the maps of $\Pi^{\ell_c}_{DR}$ are less noisy than those of $\Pi^{\ell_c}_{LES}$. As discussed in Chap. 4, this is due to the fact that in $\Pi^{\ell_c}_{DR}$ the gradient operator acts on a smooth test function rather than directly on the velocity field.

6.2 Energy balance in the DNS of a dynamical mixer

Some details about the geometry

DNS of turbulent incompressible flows generated inside a dynamical mixer are studied by Salur Basbug in the group of Dr. Georgios Papadakis and Prof. Christos Vassilicos at Imperial College, London. The geometry in which these simulations are performed is described on Fig. 6.4. The tank is cylindrical of axis (Oz), radius R, height $H = 2R$, for an aspect ratio of $H/R = 2$. An impeller, constituted of four straight blades of length $R_{\rm imp} = R/2$, is located at the center of the tank and rotates with angular velocity Ω. The Reynolds number based on the length of the blades is

$$Re = \frac{R_{\rm imp}^2 \Omega}{\nu} \approx 500. \tag{6.2}$$

The structure of the grid which has been used for the DNS, along with the ratio of the cell size over the Kolmogorov length scale are displayed on Fig. 6.5 and Fig. 6.6. We see that everywhere the cell size is smaller than (or very close to) η, which indicates that the flow is spatially well resolved. In this section, we perform our study in a specific volume $\mathcal{V}$ represented on Fig. 6.4, fixed in the reference frame of the rotating impeller. Typical maps of the instantaneous and mean flows in $\mathcal{V}$ are provided in Fig. 6.7.

Energy balance

A strong feature of numerical simulations compared to the VK set-up discussed in previous chapters, is that one has access to the pressure field at every point where velocity is probed. Therefore, it can be checked whether viscous dissipation and advection balance the variations of kinetic energy globally in space and time. When this balance is performed from the numerical data at the resolution of the grid, it is found to hold well and the relative discrepancy between the two sides of Eq. (1.21) is close to 2%.

The question we ask is whether this discrepancy (which we shall call ϵ_0 from now on) can be accounted for by taking into account the contribution of Π_{DR}^{ℓ}. In order to check that, Salur provided us with six sets of data. Each set contains the three components of the velocity field on a 3D cartesian grid in $\mathcal{V}$. The difference between these sets lies in the number of points at which Salur probed the velocity field, which are: 8^3, 15^3, 22^3, 29^3, 36^3, and 43^3. These resolutions correspond to a ratio of the gridstep over the Kolmogorov scale of: 6.8, 3.4, 2.3, 1.7, 1.4, and 1.1. Fig. 6.8 displays the results of our computations of ϵ_{DR} (—●— - —●— - —●— - —●— - —●— - —●—) from these data along with $\langle -3S_3/4 \rangle$ (—■— - —■— - —■— - —■— - —■— - —■—), and we see that the variations of these two quantities are quite similar. Moreover, we see that we are not able to compute ϵ_{DR} down to the Kolmogorov scale because we need to compute velocity increments over a few grid steps for ϵ_{DR} to be well converged. However, we can fit the variations of $\langle -3S_3/4 \rangle$ by a quadratic function in order to extrapolate its behaviour at smaller scales, and we see that the fit reaches ϵ_0 at $\ell/\eta = 1.8$.

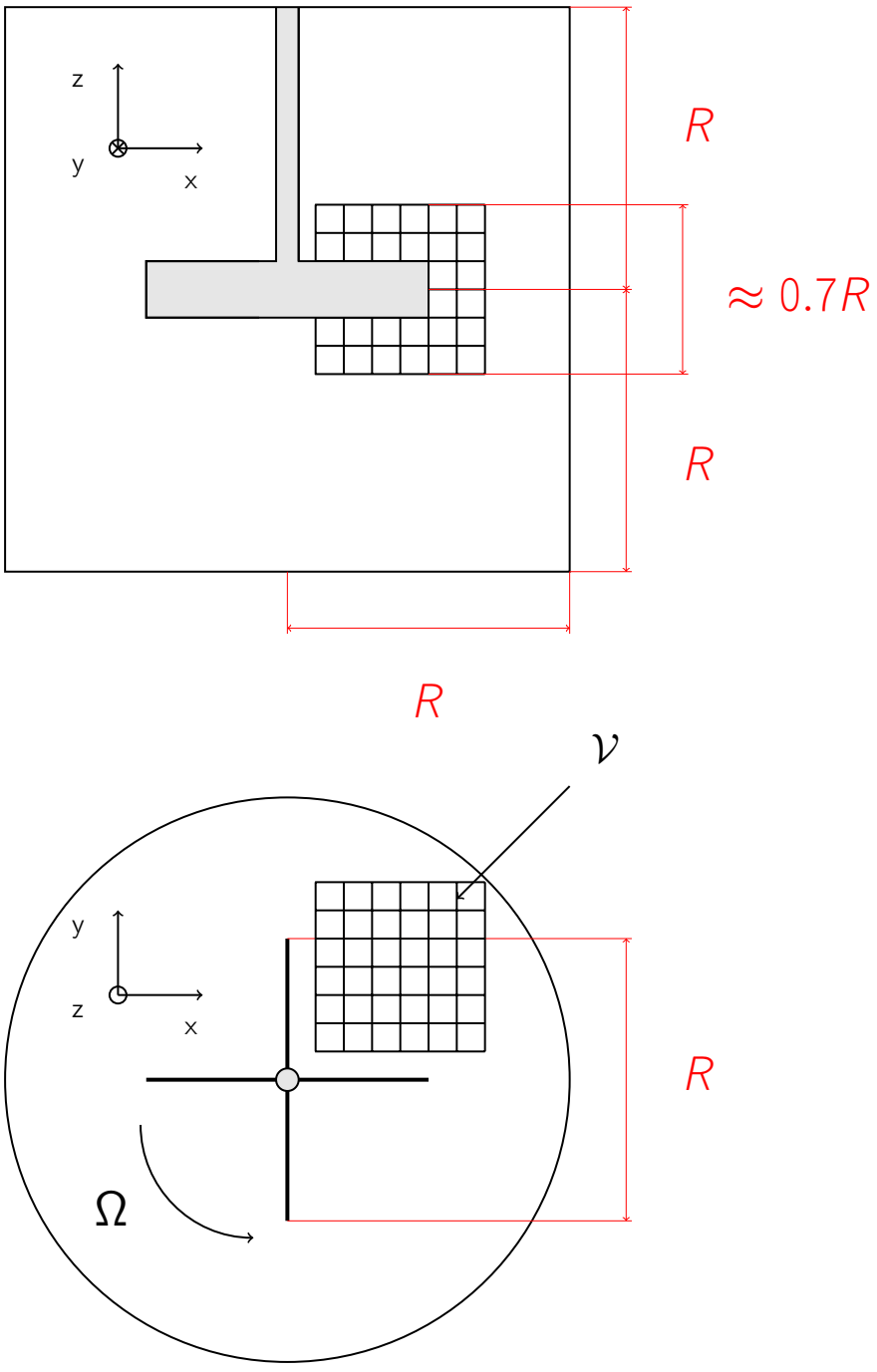

Figure 6.4: Geometry of the dynamical mixer.

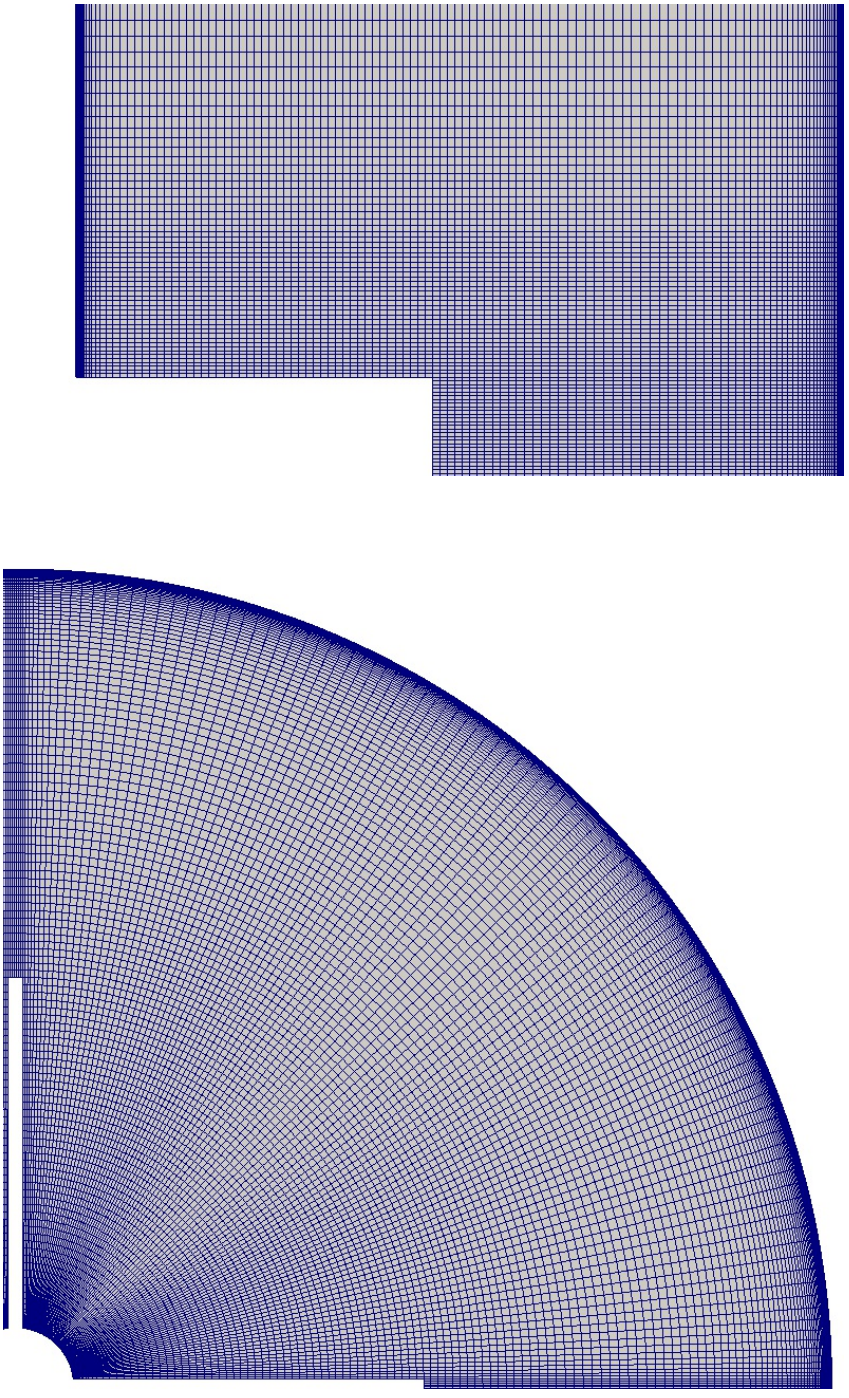

Figure 6.5: Structure of the grid in the meridional plane and at mid-height. Courtesy of Salur Basbug

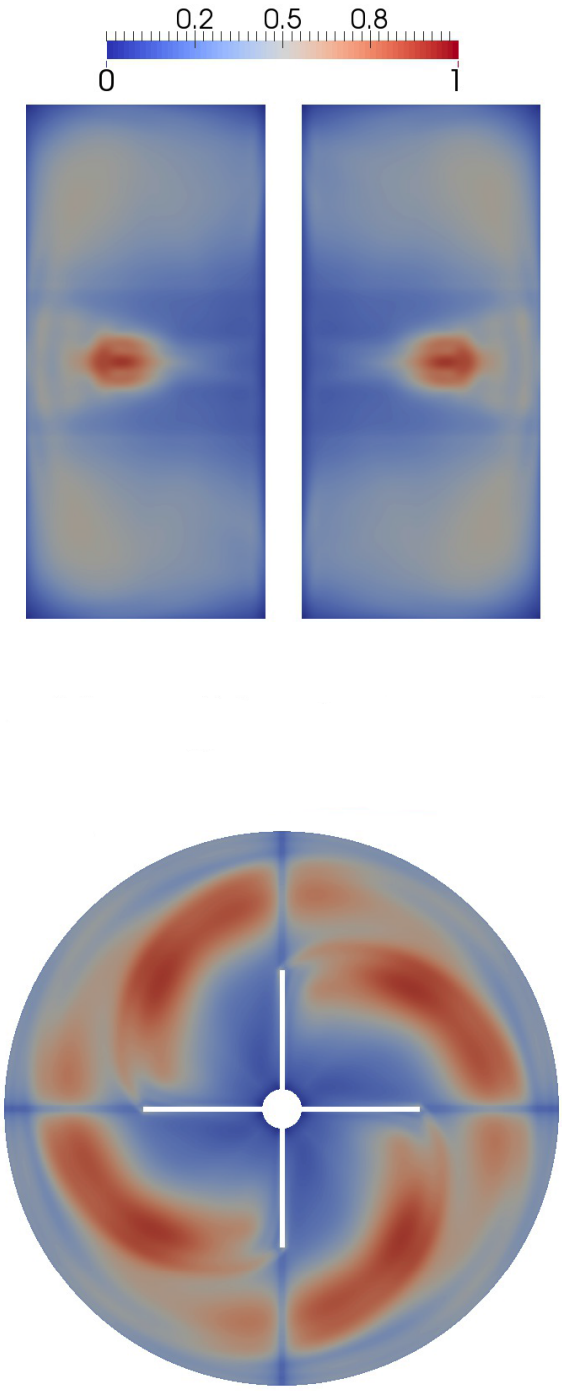

Figure 6.6: Ratio of the size of the mesh over Kolmogorov length scale. Courtesy of Salur Basbug

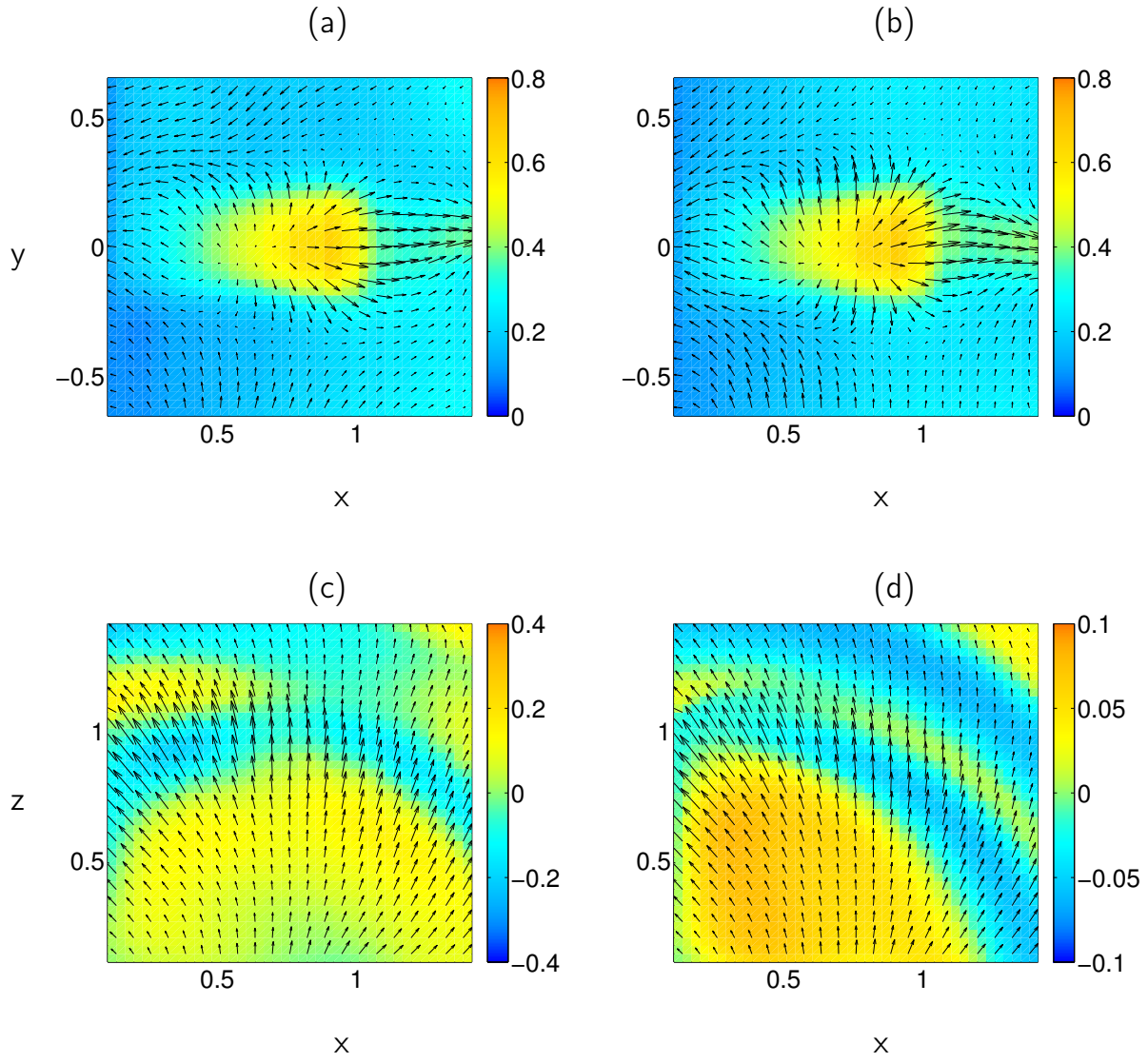

Figure 6.7: Typical instantaneous and mean velocity field in $\mathcal{V}$. (a) instantaneous frame in the meridional plane and (b) the corresponding time-average. (c) instantaneous frame in the mid-height plane and (d) the corresponding time-average

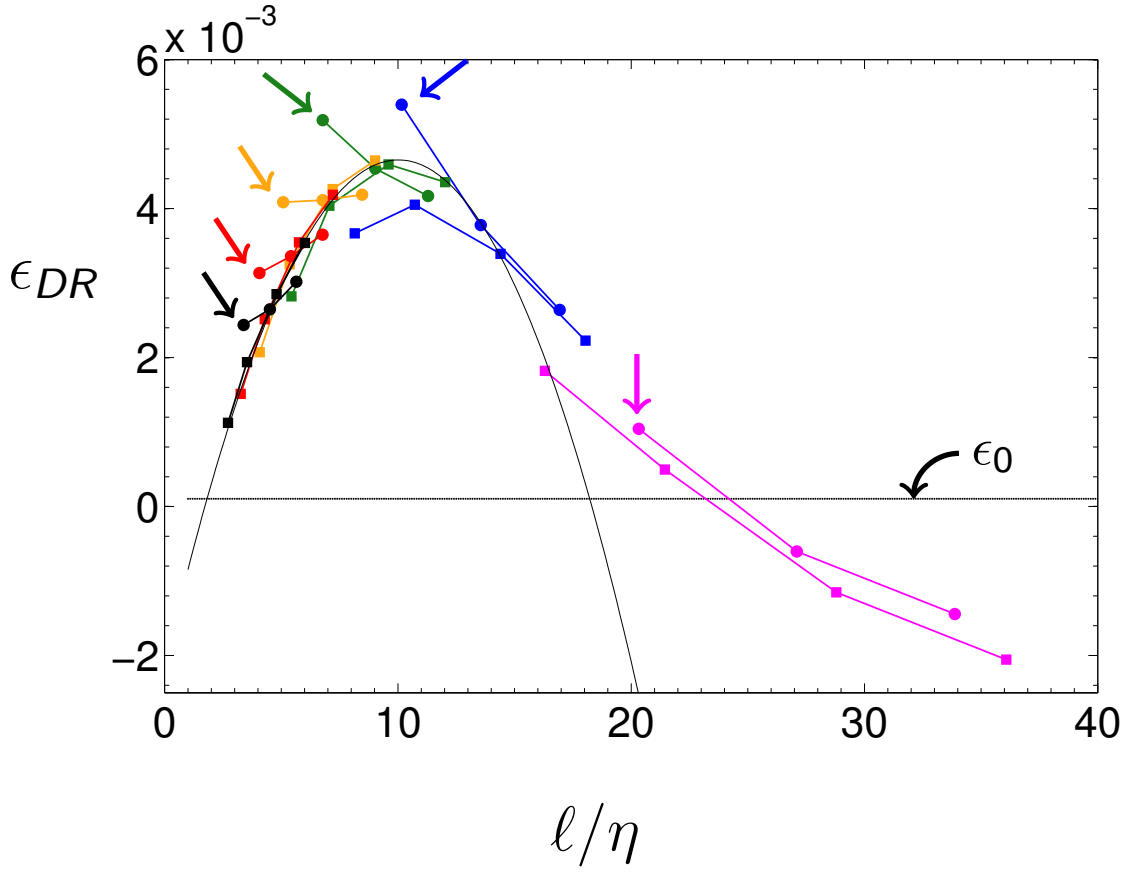

Figure 6.8: Variations of ϵ_{DR} (—●— - —●— - —●— - —●— - —●— - —●—) and $\langle -3S_3/4 \rangle$ (—■— - —■— - —■— - —■— - —■— - —■—) as a function of ℓ/η in $\mathcal{V}$, computed from data on grids of size 8^3, 15^3, 22^3, 29^3, 36^3, and 43^3. When the energy balance is computed, there exists a discrepancy from the exact balance obtained from Eq. (1.21). This discrepancy is denoted ϵ_0. The arrows indicate the points corresponding to the time-average of the dashed curves displayed in Fig. 6.10 (same colour code).

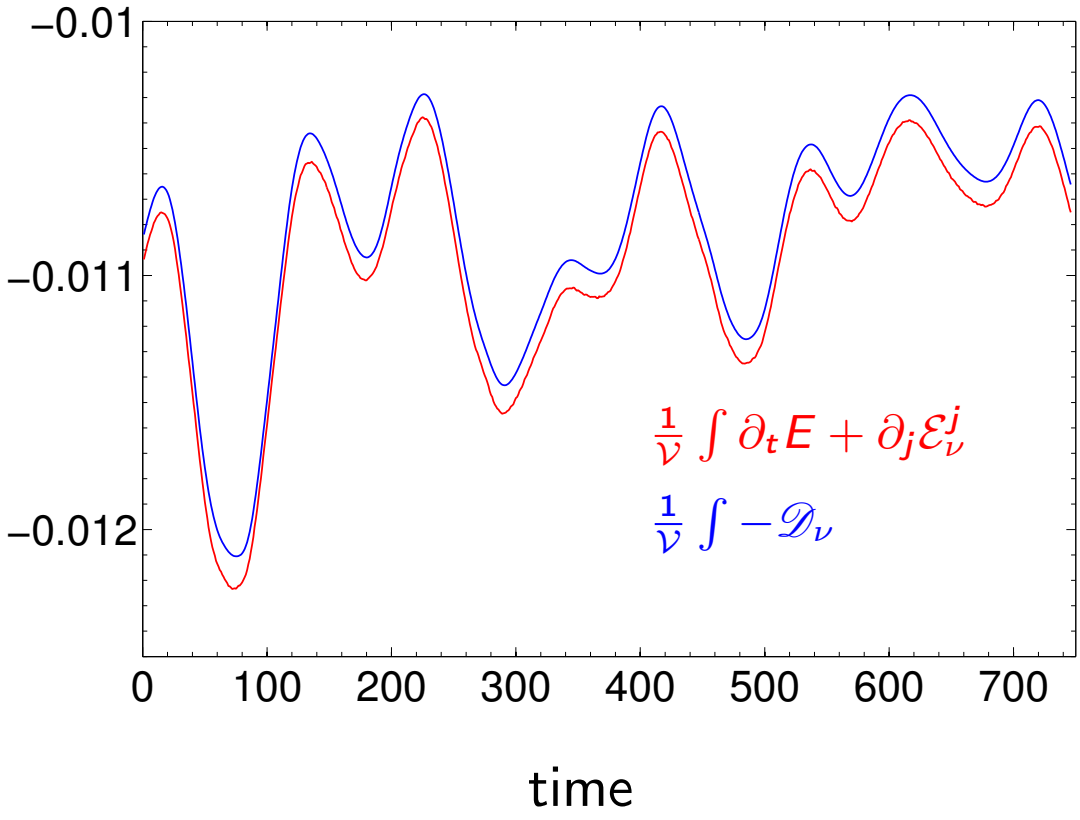

Figure 6.9: Global (in space) energy balance in $\mathcal{V}$ as a function of time obtained from numerical data. The relative discrepancy between the two curves is close to 2% at all times.

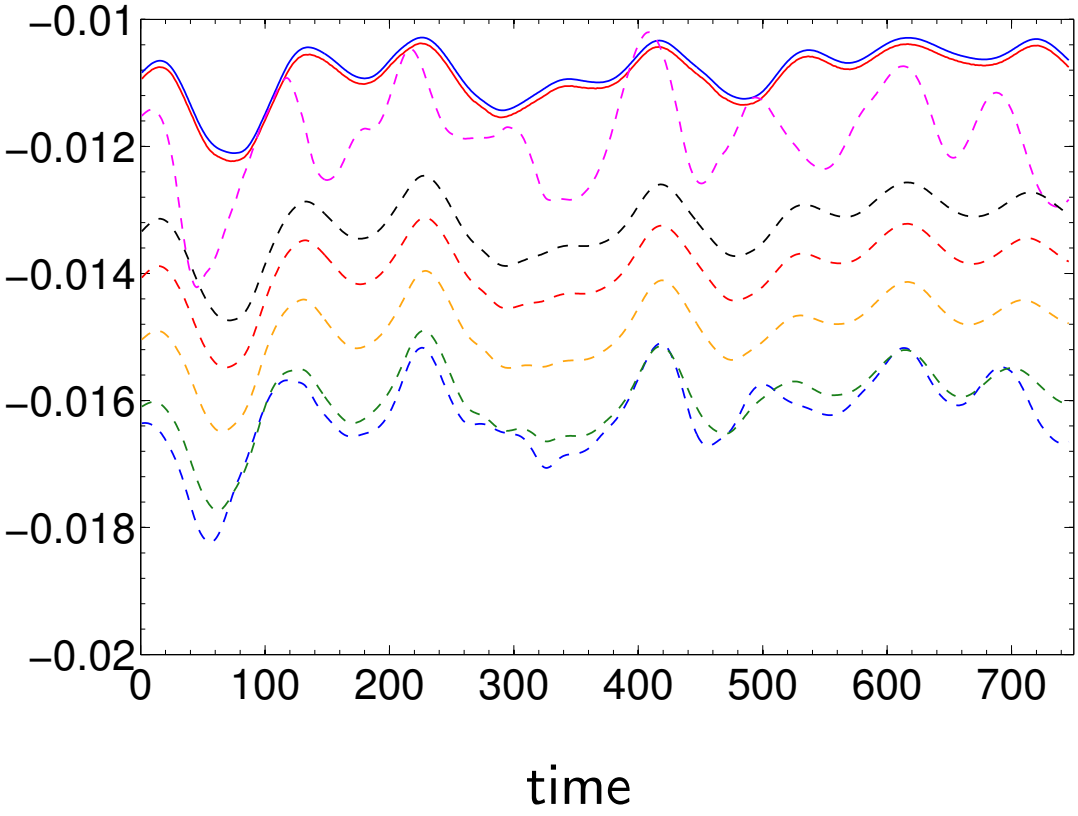

Figure 6.10: Global (in space) energy balance in $\mathcal{V}$ as a function of time, taking into account the contribution of Π^{ℓ}_{DR} at various grid size. (−−) 8^3, (−−) 15^3, (−−) 22^3, (−−) 29^3, (−−) 36^3, (−−) 43^3.

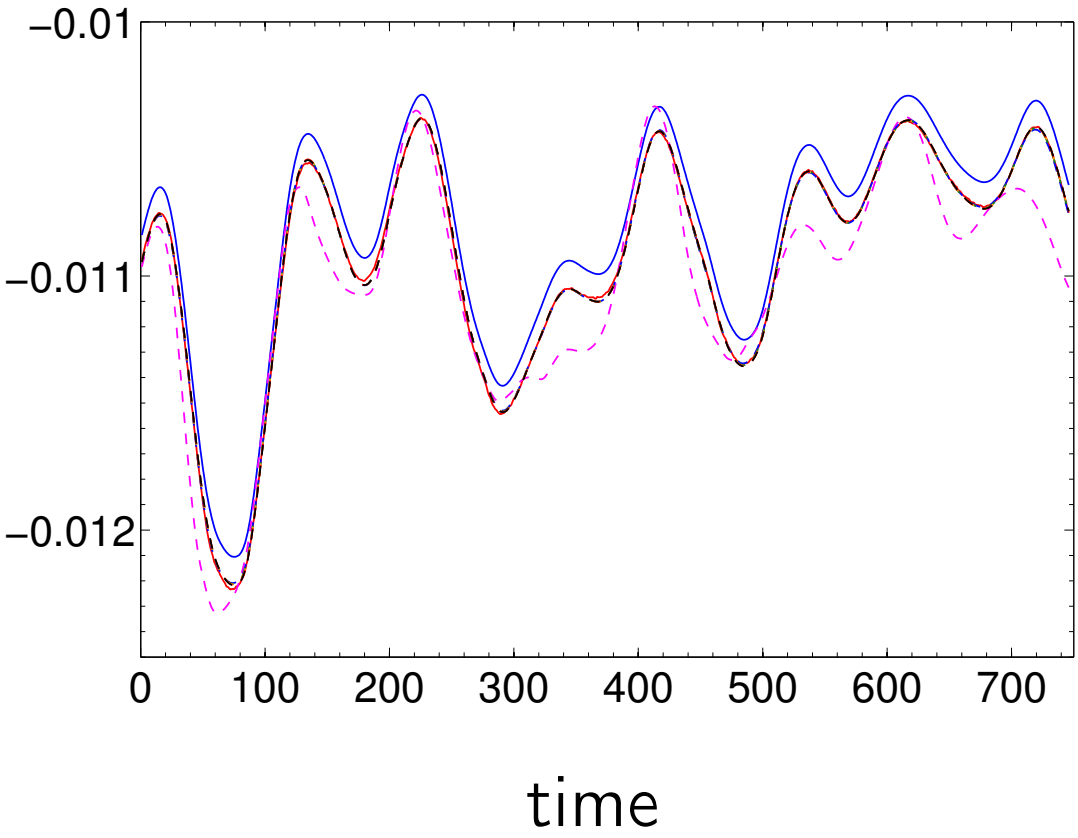

Figure 6.11: Collapse of the dashed curves in Fig. 6.10 onto the solid red one.

Fig. 6.9 displays the energy balance obtained by Salur as a function of time. The relative discrepancy between the two curves remains close to 2% at all times. When we add the contribution of Π^ℓ_{DR}, we obtain the dashed curves displayed in Fig. 6.10. Each of these curves corresponds to the points indicated by the arrows of the same colour in Fig. 6.8. We see that adding the contribution of $\langle\Pi^\ell_{DR}\rangle$ does not improve the balance, and actually makes it even worse. However, this is not surprising since we know from our discussion of Fig. 6.8 that Π^ℓ_{DR} has not been computed at a small enough scale for ϵ_{DR} to be equal to ϵ_0. However, we notice that as our computation is performed onto finer grids, the discrepancy between the dashed curves and the solid red curve decreases. Actually, we observe that the dashed curves can be collapsed onto the solid red one by multiplying Π^ℓ_{DR} by $\epsilon_0/\epsilon_{DR}(\ell)$, where we recall that $\epsilon_{DR}(\ell) = \left\langle\overline{\Pi^\ell_{DR}}\right\rangle$. This is illustrated on Fig. 6.11, which shows the balance

$$\frac{1}{\mathcal{V}}\int_{\mathcal{V}}\left(\partial_t E + \partial_j J^j\right) = -\frac{1}{\mathcal{V}}\int_{\mathcal{V}}\left(\frac{\epsilon_0}{\epsilon_{DR}(\ell)}\Pi^\ell_{DR} + \mathscr{D}_\nu\right). \tag{6.3}$$

At the highest resolution, the maximum relative discrepancy in the energy balance is 3‰. This suggests that taking ϵ_{DR} into account at smaller scales actually improves the balance and that Π^ℓ_{DR} should be computed in DNS.

Chapter 7

Conclusion

"[...] and, as you can see, we observe singularities."
"Well, you observe... something."

A discussion between Bérengère and François.

Contents

7.1 Contributions

In this thesis, we provide the first investigations on the possible existence of an inertial mechanism for energy dissipation in real turbulent flows. This mechanism for the breaking of the time-reversal symmetry of Euler equations was conjectured by [Onsager, 1949] as stemming from a possible lack of smoothness in the velocity field, and has since remained at the heart of the mathematical analysis of the INSE. However, these ideas have been largely ignored by the physics community in which the consensus is that the velocity and pressure fields in experimental incompressible flows remain regular at all times. Here, we provide a physicist's approach to the study of Navier-Stokes regularity from experimental data. This approach is made possible by mainly two things: first, the derivation of the analytical expression of the inertial dissipation by [Duchon and Robert, 2000] in terms of velocity increments, and second, the development of particle image velocimetry (PIV) systems which provide measurements for the three components of the velocity field, at several points in the flow bulk at the same time. Using these tools, we are able to investigate the energy cascade in a turbulent von Kármán (VK) flow. This type of flows provide a framework of choice for studying Onsager's conjecture because the energy input is well controlled, they have a finite mean energy dissipation rate ϵ at large Reynolds numbers, and their regularity is not known.

We were able to show in Chap. 4 that in the inertial range, Duchon and Robert's results capture the energy cascade with very good accuracy, and provide better estimations of the mean dissipation rate than large-eddy-simulation (LES) techniques. In addition, we observe by looking at the local variations of Π^ℓ_{DR} that when ℓ is decreased, areas where Π^ℓ_{DR} is nonzero do not vanish but instead become more localized in the physical space. This naturally leads to the idea presented in Chap. 5 of introducing Π^ℓ_{DR} as a criterion to detect candidates for singularities in our PIV data through scales. When computed in the dissipative range close to the Kolmogorov scale at the center of the flow, we show that $\Pi^{\gtrsim\eta}_{DR}$ does not vanish as might be expected, but instead has a non trivial structure with extreme events where at one grid point $\Pi^{\gtrsim\eta}_{DR} > 100\epsilon$. By looking at the flow topology at the location of these extreme events, we are able exhibit quasi-singular structures, different from those expected at the location of extreme viscous dissipation. First studies suggest that it is possible to classify the types of structures we observe, and we make an attempt in this direction. Finally, we provide discussions of our results in the framework of computational fluid dynamics.

7.2 Perspectives

Whether we observe the signature of actual irregularities or structures which are smoothed out at smaller scales, the work presented in this thesis opens many perspectives for future work. For instance, the irregular topologies which we detect at Kolmogorov scale resemble the topologies observed at critical points described in [Perry and Fairlie, 1974]. However, velocity at critical points is zero while the regularity of the INSE is a blow-up

problem. Therefore, more systematic investigations are needed in order to be able to really characterize the structures we observe, and understand what happens at the level of the flow topology at the location of extreme events of Π^{η}_{DR}.

Another interesting question, which we are not able to answer until further improvements of our PIV set-up, is whether these quasi-singular structures persist at smaller scales or whether viscosity smoothes them out and takes up all of the energy dissipation. Whatever the answer to this question may be, our results strongly suggest that Kolmogorov scale is not the smallest relevant scale for energy dissipation. As discussed in Chap. 5, this naturally leads to the idea of connecting our results to intermittency and the multifractal picture.

In this thesis, we only have performed our study at the center of the flow. However, as explained in Chap. 3, another area of interest is located in the middle shear layer, close to the solid wall. The question is whether the properties of Π^{ℓ}_{DR} are the same close to the axis of rotation and close to the wall, or whether we observe differences in *e.g.* the probability density functions or in the kind of irregular topologies which we detect. Actually, preliminary investigations show that what happens in these two parts of the flow is different.

Moreover, the results we have presented were obtained for TM87(-) only. The same study could be performed for TM87(+), at the center and at the wall, in order to investigate whether different forcing conditions lead to different statistical properties of Π^{ℓ}_{DR}, or different flow topologies at the location of extreme events.

Our work focused on the experimental study of Π^{ℓ}_{DR}, and to a lesser extent on the velocity circulation decay $d\Gamma^{\ell}/dt$. As discussed in Chap. 3, the these two quantities are related via the turbulence force $\boldsymbol{f}^{\ell}$, the properties of which have not been directly investigated in this thesis. For instance, the properties of Υ^{ℓ} (see Chap. 3) could be studied down to Kolmogorov scale from our SPIV data. In theory, based on the results obtained by [Chen et al., 2006; Eyink and Aluie, 2006], it would be possible to detect quasi-singular structures where $d\Gamma^{\ell}/dt \neq 0$ and $\Pi^{\ell}_{DR} = 0$. These would be characterized by a scaling exponent $1/3 < h \leqslant 1/2$. The same analyses as those performed in this thesis could then be repeated based on the properties of Υ^{ℓ}, and the flow topology at the location of extreme events of velocity circulation decay could then be studied. The parallel study of the properties of Π^{ℓ}_{DR} and $\boldsymbol{f}^{\ell} \cdot \boldsymbol{u}^{\ell}$ should also yield interesting results as briefly mentioned in Chap. 3.

Considering numerical simulations, our results may have an impact on computational fluid dynamics, as we discussed in Chap. 6. The fact that Π^{ℓ}_{DR} provides better estimates for ϵ than LES models in our experimental set-up confirms that Π^{ℓ}_{DR} may be viewed as a local non-random form for the energy transfers towards small scale. Of course, we are aware that this study has only been performed globally, in a specific geometry, and tested against only one LES model. Therefore, we cannot claim that LES models should be dropped yet. However, the results presented in Chap. 4 are pointing in this direction.

In addition, the results we presented in Chap. 5 highlight the important contribution to the local energy balance of Π^{ℓ}_{DR} close to the Kolmogorov scale. These quasi-singular structures are not known to occur in direct numerical simulations (DNS) of incompressible

flows, which might be due to mainly two reasons: either they exist in DNS but have never been detected, or numerical schemes intrinsically prevent such structures from developing. In the last case, this would mean changing the numerical scheme, and implementing procedures similar to what is done in DNS of compressible fluids where singularities are known to occur during *e.g.* shock formations. In any case, more investigations are needed, which will provide deeper insights on the results obtained in this thesis.

Finally, it might be wondered what happens at the transition to turbulence. In this thesis, we have shown that Π^{ℓ}_{DR} is very small for laminar VK flows, and studied its statistical properties in fully turbulent flows. However, an interesting question is what happens at intermediate Reynolds numbers when the flow becomes chaotic but is not fully turbulent yet. Of course, all these considerations can be applied to other geometries where PIV measurements can be implemented.

Appendix A

Duchon and Robert's paper: Inertial energy dissipation for weak solutions of incompressible Euler and Navier-Stokes equations

Inertial energy dissipation for weak solutions of incompressible Euler and Navier-Stokes equations

Nonlinearity **13** (2000) 249–255. Printed in the UK PII: S0951-7715(00)04594-1

Inertial energy dissipation for weak solutions of incompressible Euler and Navier–Stokes equations

Jean Duchon† and Raoul Robert‡

† Université Lyon 1, Laboratoire d'Analyse Numérique, CNRS UMR 5585, Bât. 101, 43 bd du 11 novembre 1918, 69622 Villeurbanne Cedex, France
‡ Institut Fourier CNRS UMR 5582, 100 rue des Mathématiques, BP 74, 38402 Saint Martin d'Hères Cedex, France

E-mail: Raoul.Robert@ujf-grenoble.fr

Received 25 May 1999
Recommended by P Constantin

Abstract. We study the local equation of energy for weak solutions of three-dimensional incompressible Navier–Stokes and Euler equations. We define a dissipation term $D(\boldsymbol{u})$ which stems from an eventual lack of smoothness in the solution $\boldsymbol{u}$. We give in passing a simple proof of Onsager's conjecture on energy conservation for the three-dimensional Euler equation, slightly weakening the assumption of Constantin *et al*. We suggest calling weak solutions with non-negative $D(\boldsymbol{u})$ 'dissipative'.

AMS classification scheme numbers: 35Q30, 76D05

1. Introduction

Here we consider the three-dimensional (for the most part) incompressible Navier–Stokes and Euler equations. For simplicity we limit ourselves to flows on the torus $\mathcal{T} = (\mathbb{R}/\mathbb{Z})^3$, i.e. with periodic boundary conditions.

Let us take the Navier–Stokes equation first. For an initial velocity field $\boldsymbol{u}_0$ with finite energy, as is well known (Leray [4,5]), there exists at least one weak solution (i.e. in the sense of distributions) to the Cauchy problem. *A priori* such a solution belongs to $L^\infty(0,T;L^2) \cap L^2(0,T;H^1)$ and there is not enough smoothness to ensure the classical energy equality; all we know is that one can define some weak solution satisfying, in addition,

$$\frac{\mathrm{d}}{\mathrm{d}t}\int \tfrac{1}{2}\boldsymbol{u}^2\,\mathrm{d}\boldsymbol{x} + \nu\int(\nabla\boldsymbol{u})^2\,\mathrm{d}\boldsymbol{x} \leqslant 0.$$

As a first step we show that for any weak solution $\boldsymbol{u}$ of the Navier–Stokes equation, the local equation of energy

$$\partial_t(\tfrac{1}{2}\boldsymbol{u}^2) + \operatorname{div}(\boldsymbol{u}(\tfrac{1}{2}\boldsymbol{u}^2 + p)) - \nu\Delta\tfrac{1}{2}\boldsymbol{u}^2 + \nu(\nabla\boldsymbol{u})^2 + D(\boldsymbol{u}) = \boldsymbol{0}$$

is satisfied, with $D(\boldsymbol{u})$ defined in terms of the local smoothness of $\boldsymbol{u}$. Thus the non-conservation of energy originates from two sources: viscous dissipation and a possible lack of smoothness in the solution.

0951-7715/00/010249+07$30.00

For the Euler equation, we consider weak solutions in $L^3(0, T; L^3)$. Although there is no general result at present for the global-in-time existence of such solutions, some examples are known (consider any two-dimensional weak solution given by Yudovich's [10] theorem).

According to an approach in the study of turbulence that goes back to Onsager [7], it might be true that such weak solutions of the three-dimensional Euler equation describe the turbulent flow correctly (in the limit of infinite Reynolds number of course). Smooth solutions conserve energy as is shown by a simple integration by parts, but this calculation does not extend to weak solutions. Some weak solutions have been constructed without energy conservation (Scheffer [9], Shnirelman [8]). Onsager had conjectured that weak solutions of the Euler equation satisfying a Hölder continuity condition of order $>\frac{1}{3}$ should conserve energy. The great interest of this question was duly emphasized by Eyink [2], who also gave a proof of energy conservation under a stronger assumption. Then Constantin *et al* [1] gave a simple and elegant proof of energy conservation under the weaker and more natural assumption that $\boldsymbol{u}$ belongs to the Besov space $B_3^{\alpha,\infty}$ with $\alpha > \frac{1}{3}$.

Our considerations above on dissipation in the Navier–Stokes equation apply to weak solutions of Euler as well: one has a local equation of energy

$$\partial_t(\tfrac{1}{2}\boldsymbol{u}^2) + \operatorname{div}(\boldsymbol{u}(\tfrac{1}{2}\boldsymbol{u}^2 + p)) + D(\boldsymbol{u}) = \boldsymbol{0}$$

and the explicit form of $D(\boldsymbol{u})$ makes it possible to prove energy conservation under a slightly weaker assumption.

We then come to the problem of distinguishing, among weak solutions of Euler or Navier–Stokes equations, which ones may be considered physically acceptable. We first see that the weak solutions of Navier–Stokes constructed by Leray [4,5] do satisfy $D(\boldsymbol{u}) \geqslant 0$. We also show that any weak solution of the Euler equation which is a strong limit of smooth solutions of the Navier–Stokes equation satisfies this same condition. Finally, we are led to a definition of dissipative weak solutions: those satisfying $D(\boldsymbol{u}) \geqslant 0$.

2. The local equation of energy for weak solutions of Navier–Stokes and Euler equations

Our main point is expressed in the following two results:

Proposition 1. *Let $\boldsymbol{u} \in L^2(0, T; H^1) \cap L^\infty(0, T; L^2)$, a weak solution of the Navier–Stokes equation on the three-dimensional torus $\mathcal{T}$:*

$$\begin{aligned} &\partial_t \boldsymbol{u} + \partial_i(u_i \boldsymbol{u}) - \nu\Delta\boldsymbol{u} + \nabla p = 0 \\ &\operatorname{div} \boldsymbol{u} = 0. \end{aligned} \tag{1}$$

Let φ be any infinitely differentiable function with compact support on $\mathbb{R}^3$, even, non-negative with integral 1 and $\varphi^\varepsilon(\xi) = (1/\varepsilon^3)\varphi(\xi/\varepsilon)$.

Put $D_\varepsilon(\boldsymbol{u})(x) = \frac{1}{4}\int \nabla\varphi^\varepsilon(\xi) \cdot \delta\boldsymbol{u}(\delta\boldsymbol{u})^2 \,\mathrm{d}\xi$, where $\delta\boldsymbol{u} = \boldsymbol{u}(x+\xi) - \boldsymbol{u}(x)$.

Then, as ε goes to 0, the functions $D_\varepsilon(\boldsymbol{u})$ (which are in $L^1(]0, T[\times\mathcal{T})$) converge, in the sense of distributions on $]0, T[\times\mathcal{T}$, towards a distribution $D(\boldsymbol{u})$, not depending on φ, and the following local equation of energy is satisfied:

$$\partial_t(\tfrac{1}{2}\boldsymbol{u}^2) + \operatorname{div}(\boldsymbol{u}(\tfrac{1}{2}\boldsymbol{u}^2 + p)) - \nu\Delta\tfrac{1}{2}\boldsymbol{u}^2 + \nu(\nabla\boldsymbol{u})^2 + D(\boldsymbol{u}) = 0.$$

Proof. Using Sobolev inclusion of H^1 in L^6, one easily sees that $\boldsymbol{u}$ is in $L^3(0, T; L^3)$ and therefore $u_i u_k$ is in $L^{3/2}(0, T; L^{3/2})$; and the same for p since, taking the divergence of (1), one obtains

$$-\Delta p = \partial_k\partial_i(u_i u_k)$$

and if p is the only solution with mean zero, the linear operator $u_i u_k \to p$ is strongly continuous on L^q for $1 < q < \infty$, and so $p \in L^{3/2}(0, T; L^{3/2})$.

Now let us regularize equation (1): denoting $\boldsymbol{u}^\varepsilon = \varphi^\varepsilon * \boldsymbol{u}$, $p^\varepsilon = \varphi^\varepsilon * p$, $(u_i \boldsymbol{u})^\varepsilon = \varphi^\varepsilon * (u_i \boldsymbol{u})$, etc one has

$$\partial_t \boldsymbol{u}^\varepsilon + \partial_i (u_i \boldsymbol{u})^\varepsilon - \nu \Delta \boldsymbol{u}^\varepsilon + \nabla p^\varepsilon = 0.$$

This equation multiplied scalarly by $\boldsymbol{u}$, plus equation (1) multiplied by $\boldsymbol{u}^\varepsilon$, gives

$$\partial_t (\boldsymbol{u} \cdot \boldsymbol{u}^\varepsilon) + \operatorname{div}((\boldsymbol{u} \cdot \boldsymbol{u}^\varepsilon)\boldsymbol{u} + p^\varepsilon \boldsymbol{u} + p\boldsymbol{u}^\varepsilon) + E_\varepsilon - \nu \Delta (\boldsymbol{u} \cdot \boldsymbol{u}^\varepsilon) + 2\nu \nabla \boldsymbol{u} \cdot \nabla \boldsymbol{u}^\varepsilon = 0$$

where

$$E_\varepsilon(t, x) = \partial_i (u_i u_j)^\varepsilon u_j - u_i u_j \partial_i u_j^\varepsilon.$$

Since $\boldsymbol{u} \in L^3(0, T; L^3)$, $\boldsymbol{u} \cdot \boldsymbol{u}^\varepsilon$ converges to $\boldsymbol{u}^2$ and $(\boldsymbol{u} \cdot \boldsymbol{u}^\varepsilon)\boldsymbol{u} + p^\varepsilon \boldsymbol{u} + p\boldsymbol{u}^\varepsilon$ converges to $(\boldsymbol{u}^2 + 2p)\boldsymbol{u}$ in the sense of distributions on $]0, T[\times \mathcal{T}$. Moreover, $\nabla \boldsymbol{u}^\varepsilon$ tends to $\nabla \boldsymbol{u}$ strongly in $L^2(]0, T[\times \mathcal{T})$, thus $E_\varepsilon(t, x)$ converges in the sense of distributions towards

$$-\partial_t (\boldsymbol{u}^2) - \operatorname{div}(\boldsymbol{u}(\boldsymbol{u}^2 + 2p)) + \nu \Delta \boldsymbol{u}^2 - 2\nu (\nabla \boldsymbol{u})^2.$$

Another calculation gives

$$\int \nabla \varphi^\varepsilon(\xi) \cdot \delta \boldsymbol{u} (\delta \boldsymbol{u})^2 \, \mathrm{d}\xi = -\partial_i (u_i u_j u_j)^\varepsilon + 2\partial_i (u_i u_j)^\varepsilon u_j + \partial_i (u_j u_j)^\varepsilon u_i - 2 u_i u_j \partial_i u_j^\varepsilon.$$

However, $\partial_i (u_j u_j)^\varepsilon u_i = \partial_i (u_i (u_j u_j)^\varepsilon)$, due to the incompressibility of $\boldsymbol{u}$.

Moreover, $\partial_i (u_i (u_j u_j)^\varepsilon - (u_i u_j u_j)^\varepsilon)$ tends to 0 in the sense of distributions on $]0, T[\times \mathcal{T}$ and thus $\int \nabla \varphi^\varepsilon(\xi) \cdot \delta \boldsymbol{u} (\delta \boldsymbol{u})^2 \, \mathrm{d}\xi$ has the same limit as $2E_\varepsilon$. □

The same reasoning applies entirely for a weak solution of the Euler equation ($\nu = 0$) and gives

Proposition 2. *Let $\boldsymbol{u} \in L^3(0, T; L^3)$ be a weak solution of the Euler equation. Then the functions $D_\varepsilon(\boldsymbol{u})$ converge, in the sense of distributions, to a distribution $D(\boldsymbol{u})$, not depending on φ, and the following local equation of energy holds:*

$$\partial_t (\tfrac{1}{2} \boldsymbol{u}^2) + \operatorname{div}(\boldsymbol{u}(\tfrac{1}{2} \boldsymbol{u}^2 + p)) + D(\boldsymbol{u}) = 0.$$

Remark. In the two previous propositions $D(\boldsymbol{u})$ measures a possible dissipation (or production) of energy caused by a lack of smoothness in the velocity field $\boldsymbol{u}$, this term is by no means related to the presence or absence of viscosity.

Now let us state a simple smoothness condition which implies $D(\boldsymbol{u}) = 0$.

Proposition 3. *Let $\boldsymbol{u}$ satisfy $\int |\boldsymbol{u}(t, x + \xi) - \boldsymbol{u}(t, x)|^3 \, \mathrm{d}x \leqslant C(t) |\xi| \sigma(|\xi|)$, where $\sigma(a)$ tends to 0 with a, and $\int_0^T C(t) \, \mathrm{d}t < +\infty$. Then $D(\boldsymbol{u}) = 0$.*

Proof. One has

$$\left| \int \nabla \varphi^\varepsilon(\xi) \cdot \delta \boldsymbol{u} (\delta \boldsymbol{u})^2 \, \mathrm{d}\xi \right| \leqslant \int \left| \nabla \varphi^\varepsilon(\xi) \right| |\delta \boldsymbol{u}|^3 \, \mathrm{d}\xi$$

integrating over $]0, T[\times\mathcal{T}$ yields

$$\int \mathrm{d}t \int \left|D_\varepsilon(\boldsymbol{u})\right| \mathrm{d}x \leqslant \int \mathrm{d}t \int \left|\nabla\varphi^\varepsilon(\xi)\right| \mathrm{d}\xi \int \left|\delta\boldsymbol{u}\right|^3 \mathrm{d}x$$
$$\leqslant \int_0^T C(t)\,\mathrm{d}t \int \frac{1}{\varepsilon^4}\left|\nabla\varphi\left(\frac{\xi}{\varepsilon}\right)\right| |\xi|\sigma(|\xi|)\,\mathrm{d}\xi$$

and putting $\xi = \varepsilon\eta$, one can see that this tends to 0 with ε. □

Remark. If $\boldsymbol{u}$ is a weak solution of the Euler equation and satisfies the smoothness condition in proposition 2 above, then the kinetic energy of $\boldsymbol{u}$ is conserved (just integrate the local equation of energy over x). This provides a proof of Onsager's conjecture [1,2,7] under an assumption slightly weaker than $\boldsymbol{u} \in L^3(0, T; B_3^{\alpha,\infty})$ with $\alpha > \frac{1}{3}$.

3. Relevance to real turbulence?

There is still some doubt as to whether weak solutions of the Navier–Stokes equation, the uniqueness of which is unknown, or hypothetical weak solutions of the Euler equation, are relevant to the description of turbulent flows at high Reynolds number. It seems reasonable to require some extra conditions: one of them might be that the lack of smoothness could not lead to local energy creation. In other words, one should have $D(\boldsymbol{u}) \geqslant 0$ on $]0, T[\times\mathcal{T}$.

It is quite remarkable that this condition is satisfied by every weak solution of the Navier–Stokes equation obtained as a limit of (a subsequence of) solutions $\boldsymbol{u}_\varepsilon$ of the regularized equation introduced by Leray [4,5]:

$$\partial_t \boldsymbol{u}_\varepsilon + \partial_i((\varphi^\varepsilon * \boldsymbol{u}_{\varepsilon i})\boldsymbol{u}_\varepsilon) - \nu\Delta\boldsymbol{u}_\varepsilon + \nabla p_\varepsilon = 0$$
$$\operatorname{div}(\boldsymbol{u}_\varepsilon) = 0 \qquad \boldsymbol{u}_\varepsilon(0) = \varphi^\varepsilon * \boldsymbol{u}_0.$$

For $\boldsymbol{u}_0$ given in L^2 and $\varepsilon > 0$, this equation has a unique C^∞ solution $\boldsymbol{u}_\varepsilon$.

The sequence $(\boldsymbol{u}_\varepsilon)$ is bounded in $L^2(0, T; H^1) \cap L^\infty(0, T; L^2)$ and a subsequence converges to $\boldsymbol{u}$, a weak solution of Navier–Stokes, weakly in $L^2(0, T; H^1)$ and strongly in $L^3(0, T; L^3)$. However, for the regularized equation, one has the local energy balance

$$\partial_t\left(\tfrac{1}{2}\boldsymbol{u}_\varepsilon^2\right) + \operatorname{div}\left(\left(\varphi^\varepsilon * \boldsymbol{u}_\varepsilon\right)\tfrac{1}{2}\boldsymbol{u}_\varepsilon^2 + p_\varepsilon\boldsymbol{u}_\varepsilon\right) - \nu\Delta\tfrac{1}{2}\boldsymbol{u}_\varepsilon^2 + \nu\left(\nabla\boldsymbol{u}_\varepsilon\right)^2 = 0$$

hence $\nu(\nabla\boldsymbol{u}_\varepsilon)^2$ converges in the sense of distributions towards

$$-\partial_t(\tfrac{1}{2}\boldsymbol{u}^2) - \operatorname{div}(\boldsymbol{u}(\tfrac{1}{2}\boldsymbol{u}^2 + p)) + \nu\Delta\tfrac{1}{2}\boldsymbol{u}^2.$$

For every function $\psi(t, x)$ infinitely differentiable and non-negative, the functional $\boldsymbol{u} \to \iint (\nabla\boldsymbol{u})^2\,\psi(t, x)\,\mathrm{d}x\,\mathrm{d}t$ is convex and lower semicontinuous on the weak space $L^2(0, T; H^1)$, and thus

$$\lim_{\varepsilon\to 0} \iint (\nabla\boldsymbol{u}_\varepsilon)^2\,\psi(t, x)\,\mathrm{d}x\,\mathrm{d}t \geqslant \iint (\nabla\boldsymbol{u})^2\,\psi(t, x)\,\mathrm{d}x\,\mathrm{d}t$$

which implies $\lim_{\varepsilon\to 0} \nu(\nabla\boldsymbol{u}_\varepsilon)^2 - \nu(\nabla\boldsymbol{u})^2 = D(\boldsymbol{u}) \geqslant 0$. This fact is well known; see, for example, [6].

Remark. Two natural questions arise at this point:

(a) Does there exist a weak solution of Navier–Stokes in $L^2(0, T; H^1) \cap L^\infty(0, T; L^2)$ with $D(\boldsymbol{u}) \neq 0$?

(b) Does the condition $D(\boldsymbol{u}) \geqslant 0$ imply uniqueness for weak solutions of Navier–Stokes?

Let us call 'dissipative' such weak solutions with $D(\boldsymbol{u}) \geqslant 0$.

In the case of the inviscid Burgers equation in one space dimension, $D(\boldsymbol{u}) \geqslant 0$ coincides with the usual entropy condition of negative jumps, which does imply uniqueness.

The following proposition shows that the condition $D(\boldsymbol{u}) \geqslant 0$ appears naturally for weak solutions of the Euler equation.

Proposition 4. *Let $\boldsymbol{u} \in L^3(0, T; L^3)$ be a weak solution of the Euler equation, which is the strong limit of a sequence of dissipative weak solutions of Navier–Stokes as viscosity goes to zero. Then $D(\boldsymbol{u}) \geqslant 0$.*

Proof. The weak solution of Navier–Stokes $\boldsymbol{u}^\nu$ satisfies

$$\partial_t(\tfrac{1}{2}\boldsymbol{u}^{\nu 2}) + \operatorname{div}((\tfrac{1}{2}\boldsymbol{u}^{\nu 2} + p^\nu)\boldsymbol{u}^\nu) - \nu\Delta\tfrac{1}{2}\boldsymbol{u}^{\nu 2} + \nu(\nabla \boldsymbol{u}^\nu)^2 + D(\boldsymbol{u}^\nu) = 0.$$

Since $\boldsymbol{u}^\nu$ tends to $\boldsymbol{u}$ in $L^3(0, T; L^3)$ strong, one has

$$\lim_{\nu\to 0}(\nu(\nabla \boldsymbol{u}^\nu)^2 + D(\boldsymbol{u}^\nu)) = -\partial_t(\tfrac{1}{2}\boldsymbol{u}^2) - \operatorname{div}((\tfrac{1}{2}\boldsymbol{u}^2 + p)\boldsymbol{u}) = D(\boldsymbol{u})$$

in the sense of distributions, and thus $D(\boldsymbol{u}) \geqslant 0$. □

Remark. Let $\boldsymbol{u} \in L^3(0, T; L^3)$ be a weak solution of the Euler equation, dissipative in the sense that $D(\boldsymbol{u}) \geqslant 0$. Then it is a dissipative solution of the Euler equation in the sense of Lions [6]. Indeed, every weak solution with $(\mathrm{d}/\mathrm{d}t)\int \frac{1}{2}\boldsymbol{u}^2\,\mathrm{d}x \leqslant 0$ is a dissipative solution in Lions' sense. Notice that this last condition does not prevent *a priori* local creation of energy in some regions of the flow.

4. The two-dimensional case

In two space dimensions the situation is clearer for the Navier–Stokes equation. For every initial velocity field $\boldsymbol{u}_0$ in L^2 one has a unique weak solution in $L^2(0, T; H^1) \cap L^\infty(0, T; L^2)$ and this solution satisfies the global energy balance

$$\tfrac{1}{2}\int \boldsymbol{u}^2(T, x)\,\mathrm{d}x + \nu\int_0^T \mathrm{d}t \int (\nabla \boldsymbol{u})^2\,\mathrm{d}x = \tfrac{1}{2}\int \boldsymbol{u}_0^2(x)\,\mathrm{d}x.$$

In fact, one has a slightly stronger result:

Proposition 5. *Let $\boldsymbol{u}$ be the unique weak solution of the two-dimensional Navier–Stokes equation above. Then $D(\boldsymbol{u}) = 0$.*

Proof. We use the interpolation inequality $\|\boldsymbol{v}\|_{L^3} \leqslant C\|\boldsymbol{v}\|_{L^2}^{2/3}\|\boldsymbol{v}\|_{H^1}^{1/3}$ together with $\|\delta\boldsymbol{u}\|_{L^2} \leqslant |\xi|\|\boldsymbol{u}\|_{H^1}$ and $\|\delta\boldsymbol{u}\| \leqslant 2\|\boldsymbol{u}\|$ (for any norm).

From the expression for $D_\varepsilon(\boldsymbol{u})$ one has

$$\|D_\varepsilon(\boldsymbol{u})\|_{L^1(\mathrm{d}x)} \leqslant \frac{1}{4\varepsilon}\iint |\nabla\varphi(\xi)||\boldsymbol{u}(t, x + \varepsilon\xi) - \boldsymbol{u}(t, x)|^3\,\mathrm{d}x\,\mathrm{d}\xi$$

and since $\boldsymbol{u} \in L^\infty(0, T; L^2)$, this is bounded from above, for almost every $t \in [0, T]$, by a fixed integrable function $C\|\boldsymbol{u}(t)\|_{H^1}^2$.

On the other hand, for almost every $t \in [0, T]$, $\boldsymbol{u}(t)$ is in H^1 and

$$\big\|\boldsymbol{u}(t, x + \varepsilon\xi) - \boldsymbol{u}(t, x)\big\|_{L^3(\mathrm{d}x)}^3 \leqslant C\varepsilon^2|\xi|^2\|u\|_{H^1}^3$$

so that $\|D_\varepsilon(\boldsymbol{u})\|_{L^1(\mathrm{d}x)} \to 0$ as ε goes to 0.

Applying Lebesgue's dominated convergence theorem, one obtains $D(\boldsymbol{u}) = 0$. □

The case of the 2D Euler equation

For $\boldsymbol{u}_0$ in L^2 such that $\omega_0 = \operatorname{curl} \boldsymbol{u}_0 \in L^r$, $1 < r < \infty$, there exists at least one weak solution of the Euler equation in the space $C([0, \infty[; W^{1,r})$ [6]. From Sobolev inclusion, for $r \geqslant \frac{6}{5}$ one has $W^{1,r} \subset L^3$, then $D(\boldsymbol{u})$ is defined and the local energy balance holds with $D(\boldsymbol{u})$.

Moreover, we have

Proposition 6. *Let $\boldsymbol{u}$ be a weak solution of the 2D Euler equation as above with $r > \frac{3}{2}$, then $D(\boldsymbol{u}) = 0$.*

Proof. Apply the Hölder inequality

$$\|\delta \boldsymbol{u}\|_{L^3} \leqslant \|\delta \boldsymbol{u}\|_{L^r}^{\alpha} \|\delta \boldsymbol{u}\|_{L^q}^{1-\alpha} \qquad \frac{1}{3} = \frac{\alpha}{r} + \frac{1-\alpha}{q}.$$

Taking $q = 2r/(2-r)$, so that $\| \ \|_{L^q} \leqslant c \| \ \|_{W^{1,r}}$, and using $\|\delta \boldsymbol{u}\|_{L^r} \leqslant |\xi| \|\boldsymbol{u}\|_{W^{1,r}}$, one obtains

$$\|\delta \boldsymbol{u}\|_{L^3} \leqslant c|\xi|^{\alpha} \|\boldsymbol{u}\|_{W^{1,r}} \qquad \text{with} \quad \alpha = \frac{5}{3} - \frac{2}{r}.$$

If $r > \frac{3}{2}$, then $\alpha > \frac{1}{3}$ and proposition 3 applies. □

5. Inertial dissipation and the four-fifth law

We have already seen that $D(\boldsymbol{u})$ does not depend on φ. Assuming some space continuity of $\boldsymbol{u}$, we are able to express it more explicitly using a radially symmetric function $\varphi(|\xi|)$.

Let us put

$$S(\boldsymbol{u})(x, r) = \int_{|\xi|=1} (\boldsymbol{u}(x + r\xi) - \boldsymbol{u}(x))^2 (\boldsymbol{u}(x + r\xi) - \boldsymbol{u}(x)) \cdot \xi \, \mathrm{d}\Sigma(\xi)$$

where $\mathrm{d}\Sigma$ denotes the area measure on the sphere.

An easy computation gives

$$D_{\varepsilon}(\boldsymbol{u}) = \tfrac{1}{4} \int_0^{\infty} \varphi'(r) \, r^3 \frac{S(\boldsymbol{u})(x, \varepsilon r)}{\varepsilon r} \, \mathrm{d}r.$$

Now let us assume that, as $\varepsilon \to 0$, $S(\boldsymbol{u})(x, \varepsilon)/\varepsilon$ tends to a limit $s(\boldsymbol{u})(x)$. Then

$$D_{\varepsilon}(\boldsymbol{u}) \to \tfrac{1}{4} s(\boldsymbol{u}) \int_0^{\infty} \varphi'(r) \, r^3 \, \mathrm{d}r = -\frac{3}{16\pi} s(\boldsymbol{u}).$$

The four-fifth law (von Karman and Howarth, Kolmogorov) says that for a stationary, homogeneous and isotropic random turbulent velocity field $\boldsymbol{u}$ one should have

$$\left\langle \left(\delta \boldsymbol{u} \cdot \frac{\xi}{|\xi|} \right)^3 \right\rangle = -\tfrac{4}{5} D|\xi|$$

where D is the mean rate of (inertial) energy dissipation per unit mass and $\langle \, \rangle$ denotes the statistical mean.

Without isotropy, one proves (Monin, cf Frisch [3])

$$D = -\tfrac{1}{4} \operatorname{div}_{\xi} \langle (\delta \boldsymbol{u})^2 \delta \boldsymbol{u} \rangle \big|_{\xi=0}$$

integrating in ξ over the ball $|\xi| \leqslant \varepsilon$ one obtains

$$D = -\frac{3}{16\pi} \lim_{\varepsilon \to 0} \frac{1}{\varepsilon} \left\langle \int_{|\xi|=1} (\boldsymbol{u}(x + \varepsilon\xi) - \boldsymbol{u}(x))^2 (\boldsymbol{u}(x + \varepsilon\xi) - \boldsymbol{u}(x)) \cdot \xi \, \mathrm{d}\Sigma(\xi) \right\rangle.$$

Our expression of

$$s(u) = \lim_{\varepsilon \to 0} \frac{1}{\varepsilon} \int_{|\xi|=1} (\boldsymbol{u}(x + \varepsilon\xi) - \boldsymbol{u}(x))^2 (\boldsymbol{u}(x + \varepsilon\xi) - \boldsymbol{u}(x)) \cdot \xi \, \mathrm{d}\Sigma(\xi)$$

thus simply gives a local non-random form of the above expression of the inertial dissipation.

References

[1] Constantin P, E W, Titi E S 1994 Onsager's conjecture on the energy conservation for solutions of Euler's equation *Commun. Math. Phys.* **165** 207–9

[2] Eyink G 1994 Energy dissipation without viscosity in ideal hydrodynamics I. Fourier analysis and local energy transfer *Physica* D **78** 222–40

[3] Frisch U 1995 *Turbulence* (Cambridge: Cambridge University Press)

[4] Leray J 1933 Etude de diverses équations intégrales nonlinéaires et de quelques problèmes que pose l'hydrodynamique *J. Math. Pures Appl.* **12** 1–82

[5] Leray J 1934 Essai sur le mouvement d'un liquide visqueux emplissant l'espace *Acta Math.* **63** 193–248

[6] Lions P L 1996 *Mathematical Topics in Fluid Mechanics* vol 1 *Incompressible Models* (Oxford: Clarendon)

[7] Onsager L 1949 Statistical hydrodynamics *Nuovo Cimento Suppl.* **6** 279

[8] Shnirelman A I 1996–7 Weak solutions of incompressible Euler equations with decreasing energy *Séminaire EDP, Ecole Polytechnique, exposé no 16*

[9] Scheffer V 1993 An inviscid flow with compact support in space-time *J. Geom. Anal.* **3** 343–401

[10] Yudovich V I 1963 Non-stationary flow of an ideal incompressible liquid *Zh. Vychisl. Mat. Mat. Fiz.* **3** 1032–66

Appendix B

Global vs local energy dissipation: The energy cycle of the turbulent von Kármán flow

Global vs local energy dissipation: The energy cycle of the turbulent von Kármán flow

Denis Kuzzay, Davide Faranda, and Bérengère Dubrulle

Citation: Physics of Fluids **27**, 075105 (2015); doi: 10.1063/1.4923750
View online: http://dx.doi.org/10.1063/1.4923750
View Table of Contents: http://scitation.aip.org/content/aip/journal/pof2/27/7?ver=pdfcov
Published by the AIP Publishing

PHYSICS OF FLUIDS **27**, 075105 (2015)

Global vs local energy dissipation: The energy cycle of the turbulent von Kármán flow

Denis Kuzzay,[1,a)] Davide Faranda,[2] and Bérengère Dubrulle[1]
[1]*Laboratoire SPHYNX, Service de Physique de l'Etat Condensé, DSM, CEA Saclay, CNRS UMR 3680, 91191 Gif-sur-Yvette, France*
[2]*LSCE CEA Saclay, CNRS UMR 8212, 91191 Gif-sur-Yvette, France*

(Received 20 January 2015; accepted 23 June 2015; published online 9 July 2015)

In this paper, we investigate the relations between global and local energy transfers in a turbulent von Kármán flow. The goal is to understand how and where energy is dissipated in such a flow and to reconstruct the energy cycle in an experimental device where local as well as global quantities can be measured. In order to do so, we use particle image velocimetry (PIV) measurements and we model the Reynolds stress tensor to take subgrid scales into account. This procedure involves a free parameter that is calibrated using angular momentum balance. We then estimate the local and global mean injected and dissipated powers for several types of impellers, for various Reynolds numbers, and for various flow topologies. These PIV estimates are then compared with direct injected power estimates provided by torque measurements at the impellers. The agreement between PIV estimates and direct measurements depends on the flow topology. In symmetric situations, we are able to capture up to 90% of the actual global energy dissipation rate. However, our results become increasingly inaccurate as the shear layer responsible for most of the dissipation approaches one of the impellers and cannot be resolved by our PIV setup. Finally, we show that a very good agreement between PIV estimates and direct measurements is obtained using a new method based on the work of Duchon and Robert ["Inertial energy dissipation for weak solutions of incompressible Euler and Navier-Stokes equations," Nonlinearity **13**, 249–225 (2000)] which generalizes the Kármán-Howarth equation to nonisotropic, nonhomogeneous flows. This method provides parameter-free estimates of the energy dissipation rate as long as the smallest resolved scale lies in the inertial range. These results are used to evidence a well-defined stationary energy cycle within the flow in which most of the energy is injected at the top and bottom impellers and dissipated within the shear layer. The influence of the mean flow geometry and the Reynolds number on this energy cycle is studied for a wide range of parameters. © *2015 AIP Publishing LLC.* [http://dx.doi.org/10.1063/1.4923750]

I. INTRODUCTION

Understanding how and where energy is dissipated in turbulent flows has been a great challenge for many years and would have important implications in many areas such as fundamental research, aeronautics, or industry. In the classical three-dimensional turbulence phenomenology, energy is injected at large scales by the forcing mechanism, transferred downscale at a constant rate ϵ following a self-similar cascade, and then dissipated into heat at the Kolmogorov length scale, where viscous effects become dominant. In ideal stationary, homogeneous, and isotropic turbulence, the measurement of energy dissipation can therefore be achieved via 3 independent and equivalent means: (i) by monitoring the injected energy, (ii) by monitoring the dissipated heat, and (iii) by monitoring the cascade energy rate via multiscale single points measurements of the velocity (via, e.g., anemometers or array of hot wires). The first two measurements are global and the last is one local, but

a)Electronic address: denis.kuzzay@cea.fr

given the homogeneity in space and time, they all provide the same information. In most realistic situations, however, the turbulence is anisotropic and/or inhomogeneous and/or non-stationary. In such cases, there is not any necessary equivalence between global energy injection, global energy dissipation, and local energy dissipation. The study of these three quantities requires detailed knowledge of the forcing, the heat distribution, and velocity over the whole domain.

In that respect, it is interesting to focus on intermediate situations, where the turbulence is generated by a well controlled mechanism, in a simplified geometry, as achieved, for example, in classical laboratory experiments such as Taylor-Couette or von Kármán setups. In such cases, it is easy to monitor the forcing and implement a cooling mechanism so as to achieve stationarity, where global energy injection and dissipation equilibrate on average. The local energy dissipation can then be computed from stationary energy budgets derived from Navier-Stokes equation, using local measurements of velocity obtained, for example, using the now classical Particle Image Velocimetry (PIV). This technique provides measurements of the instantaneous velocity field u_i at several points of a plane (or of a volume) at the same time. From this, one may compute the Reynolds stress tensor $S_{ij} = \frac{1}{2}(\partial_i u_j + \partial_j u_i)$ and study the local dissipated power $\epsilon_v = 2\nu S_{ij} S_{ij}$. A detailed comparison between this local estimate and the global energy dissipation rate in a Taylor-Couette flow at various Reynolds numbers has recently been made by Tokgoz *et al.*[1] using tomographic PIV measurements. They observe that the local and global estimates coincide within 10% as long as the laminar flow and Taylor vortex flow regimes are fully resolved. However, as the Reynolds number increases, the dissipative scale decreases and becomes smaller than the finite resolution of the PIV (set by the camera resolution and the velocity reconstruction algorithm). In that case, the estimate of local energy dissipation based on the velocity gradients and on the viscosity ϵ_v becomes increasingly inaccurate and underestimates the global energy dissipation. In order to remedy this problem, it has been suggested to use techniques borrowed from Large Eddy Simulation (LES).[2] This allows us to model the subgrid scales (SGS) in terms of the large scale velocity field resolved by the PIV and allows computation of all terms in the energy budget[3–6] including the terms responsible for the scale-to-scale energy transfer. By the Richardson-Kolmogorov cascade picture, this allows an estimate of the local energy dissipation as long as the scale used in the computation lies in the inertial range.

In this paper, we test these methods in a turbulent flow generated by two contra-rotating impellers (von Kármán flow) for Reynolds numbers ranging from 10^3 up to more than 10^6. At such Reynolds numbers, the dissipative scale ranges from a few millimeters to a few tens of micrometer. With fixed velocity of the impellers and cooling, the resulting flow is stationary, highly anisotropic, and inhomogeneous,[7] thereby providing a unique laboratory flow to test local energy dissipation procedure. This closed flow geometry permits direct estimates of the global energy injection by torque monitoring at the two impellers. Using a large scale Helium facility with calorimetric measurements,[8] we were able to show that in a stationary state, the global injected power and the global dissipated heat coincide within a few percent at large Reynolds number and for a wide range of operating conditions (including differential rotation of the impellers). Moreover, the simple cylindrical geometry allows for stereoscopic PIV measurements of the velocity field over a vertical plane spanning the whole experiment, at a resolution of a few millimeters. Since measurements have only been made in a meridional plane, we do not have access to orthoradial derivatives. Hence, it is challenging to have an accurate estimate of the local energy dissipation rate despite this lack of information. To do this, we first use a LES method using statistical axisymmetry and angular momentum budget to calibrate the model. Then, we test a generalization of the Kármán-Howarth formula derived by Duchon and Robert[9] that provides a parameter-free estimate of the local energy dissipation for any nonhomogeneous, nonisotropic flow. Both estimates are then averaged over the whole volume for comparison with the global estimate of the energy dissipation based on torque monitoring. This is done for a wide range of control parameters, varying the Reynolds number, the mean flow geometry, and the flow asymmetry. We then use these measurements to evidence a stationary energy cycle within the flow where energy is injected at the top and the bottom impellers and dissipated within the shear layer.

This paper is organized as follows: in Section II, we summarize the theoretical tools needed for the implementation of the LES technique and the Duchon-Robert (DR) formula in our analysis of

the energy dissipation rate. In Section III, we review the von Kármán geometry and specialize these formulae to the case of cylindrical geometry. The flow diagnostics based on PIV measurements are derived and summarized. In Section IV, we apply these results to a set of measurements drawn from our database of von Kármán flow. We first tune our LES model using angular momentum balance. Then, we compare PIV estimates of the global dissipated power with direct torque measurements using both the LES technique and the DR formula. Finally, in Section V, we evidence the energy cycle of the von Kármán flow and we discuss its evolution, as well the evolution of our diagnostics, as a function of the flow topology.

II. THEORETICAL BACKGROUND AND METHODOLOGY

In this section, we use a filtering approach to derive energy and angular momentum balance at a given scale ℓ from Navier-Stokes equations and we give the expression of the different terms that we will use in our analysis of the injected and dissipated powers. We consider Navier-Stokes equations

$$\begin{cases} \partial_t u_i + u_j \partial_j u_i = -\partial_i P + \nu \partial_j \partial_j u_i, & (1) \\ \partial_j u_j = 0, & (2) \end{cases}$$

where we use Einstein summation convention over repeated indices.

A. The filtering approach

Following the procedure in Ref. 10, we define a coarse-grained velocity field at scale ℓ as

$$u_i^\ell(\vec{x}) = \int d\vec{r}\, G_\ell(\vec{r}) u_i(\vec{x} + \vec{r}), \tag{3}$$

where G is a smooth filtering function, non-negative, spatially localized, and such that $\int d\vec{r}\, G(\vec{r}) = 1$. The function G_ℓ is rescaled with ℓ as $G_\ell(\vec{r}) = \ell^{-3} G(\vec{r}/\ell)$. Coarse-graining the Navier-Stokes equations gives

$$\begin{cases} \partial_t u_i^\ell + u_j^\ell \partial_j u_i^\ell = -\partial_j \tau^{ij} - \partial_i P^\ell + \nu \partial_j \partial_j u_i^\ell, & (4) \\ \partial_j u_j^\ell = 0. & (5) \end{cases}$$

In Equation (4), we introduced $\tau^{ij} = (u_i u_j)^\ell - u_i^\ell u_j^\ell$ which is the stress tensor from the SGS.

In what follows, in order to simplify the formulae and for readability considerations, we will drop the index ℓ. Unless specified otherwise, *u_i now denotes the ith component of the coarse-grained velocity field* (same thing for P).

B. The energy balance equation

We now take the scalar product of Equation (4) with u_i, and after a few lines of algebra, we get the local energy balance equation

$$\partial_t \overline{E} + \partial_j(\overline{u_j E}) = -\partial_j(\overline{u_i \tau^{ij}}) + \overline{S_{ij}\tau^{ij}} - \partial_i(\overline{u_i P}) + \nu(\partial_j \partial_j \overline{E} + \partial_i \partial_j(\overline{u_i u_j})) - 2\nu \overline{S_{ij} S^{ij}}, \tag{6}$$

where $E = \frac{u_i u_i}{2}$ is the large scale kinetic energy per unit mass and $S_{ij} = \frac{1}{2}(\partial_i u_j + \partial_j u_i)$ is the large scale strain rate tensor. The overline denotes the statistical average of a quantity. Let us now define a vector $J^j = u_j(E + P) + u_i \tau^{ij} - \nu(\partial_j E + \partial_i(u_i u_j))$. We can then rewrite (6) as

$$\partial_t \overline{E} + \partial_j \overline{J^j} = \overline{S_{ij}\tau^{ij}} - 2\nu \overline{S_{ij} S^{ij}}. \tag{7}$$

This local equation is valid in any geometry, for any type of flow and for any filtering with the properties given above. In Sec. III D, we apply this formula to the specific axisymmetric von Kármán geometry to derive the local energy production and dissipation rate per unit mass.

C. The angular momentum balance equation

In a very similar fashion, it is also possible to derive an angular momentum balance equation at scale ℓ. We take the cross product of r_j and Equation (4), and after a few lines of algebra, we get

$$\partial_t \overline{L_i} + \partial_j(\overline{u_j L_i}) = -\epsilon_{ijk}\partial_k(\overline{r_j P}) - \epsilon_{ijk}\partial_m(\overline{r_j \tau^{km}}) + \nu(\partial_j\partial_j \overline{L_i} + \epsilon_{ijk}\partial_m\partial_k(\overline{r_j u_m})) - \nu\epsilon_{ijk}\partial_j\overline{u_k}, \tag{8}$$

where ϵ_{ijk} is the three dimensional, total antisymmetric Levi-Civita symbol so that $L_i = \epsilon_{ijk} r_j u_k$ is the ith component of the angular momentum per unit mass. Of course, it can be checked that it is also possible to derive (8) from (6) using (4) and the identity $E = \frac{1}{2\vec{r}^2}(\vec{L}^2 + (\vec{r}.\vec{u})^2)$. As before, we can write (8) as an equation of conservation for each component of $\vec{L}$,

$$\partial_t \overline{L_i} + \partial_j \overline{T^{ij}} = 0, \tag{9}$$

where $T^{ij} = u_j L_i - \epsilon_{ijk} r_k P + \epsilon_{imk} r_m \tau^{jk} - \nu(\partial_j L_i - \epsilon_{ijk}\partial_m(r_k u_m) + \epsilon_{ijk} u_k)$.

In Sec. IV A, we use this angular momentum balance as a constraint to calibrate the LES model that we will now describe.

D. LES method for balance equations

The computation of the different terms in (7) and (9) requires the knowledge of both the velocity field at scale ℓ and the Reynolds stress τ^{ij}. In most practical situations, e.g., when the flow is turbulent and the velocity is measured through a PIV system, only the former is available, since we cannot resolve the dissipative scale. A traditional way to overcome this problem is to use a LES-PIV approach[1,2] to model τ^{ij} in terms of the large scale velocity field.[11,12] Several models exist. In the present paper, we choose the gradient model[13] where

$$\tau^{ij} = C\Delta_r^2 \partial_k u_i \partial_k u_j, \tag{10}$$

where C is a constant to be calibrated and Δ_r is the width of the filtering. This model ensures forward scatter and backscatter of energy between resolved scales and SGS.

E. Duchon-Robert energy balance equation

An alternative local energy balance equation has been derived by Duchon and Robert[9] using Leray's weak solution formalism and Onsager's ideas.[14] The latter amounts to consider a sequence of coarse-grained solutions of Navier-Stokes equations (4) in the limit $\ell \to 0$ and to derive the corresponding energy balance that reads

$$\partial_t E + \partial_j \; u^j(E+P) - \nu\partial_j E \; = -\nu\partial_j u_i \partial^j u^i - \mathcal{D}(u^i), \tag{11}$$

where $\mathcal{D}(u^i)$ is expressed in terms of velocity increments $\delta\vec{u}(\vec{r}) = \vec{u}(\vec{x}+\vec{r}) - \vec{u}(\vec{x})$ as

$$\mathcal{D}(\vec{u}) \equiv \lim_{\ell\to 0}\mathcal{D}_\ell(\vec{u}) = \lim_{\ell\to 0}\frac{1}{4\ell}\int_{\mathcal{V}} d\vec{r}\,(\vec{\nabla}G_\ell)(\vec{r})\cdot\delta\vec{u}(\vec{r})\,|\delta\vec{u}(\vec{r})|^2, \tag{12}$$

where the dependence of $\delta\vec{u}$ and $\mathcal{D}$ in $\vec{x}$ is implied. As the Reynolds number tends to infinity, the scale ℓ can be chosen as small as one wants, and the quantity $\mathcal{D}(u^i)$ can be seen as the contribution to dissipation coming from a generalized cascade process (possibly linked with the formation of small-scale singularities). Since the result cannot depend on the filtering function G_ℓ, Duchon and Robert specialized the expression to a radially symmetric filter to get the alternative expression devoid of any free parameter

$$\mathcal{D}(\vec{u}) = -\frac{3}{16\pi}\lim_{\epsilon\to 0}\frac{1}{\epsilon}\int_{|\vec{\chi}|=1} d\Sigma(\vec{\chi})\,|\delta\vec{u}(\epsilon\vec{\chi})|^2\,\delta\vec{u}(\epsilon\vec{\chi})\cdot\vec{\chi}, \tag{13}$$

where $d\Sigma$ denotes the area measure on the sphere. As noticed by Duchon and Robert, this expression coincides with the statistical mean rate of inertial energy dissipated per unit mass derived from the anisotropic version of the Kármán-Howarth equation. They therefore argue that the previous formula provides a local non-random form of the Kármán-Howarth equation, valid even for

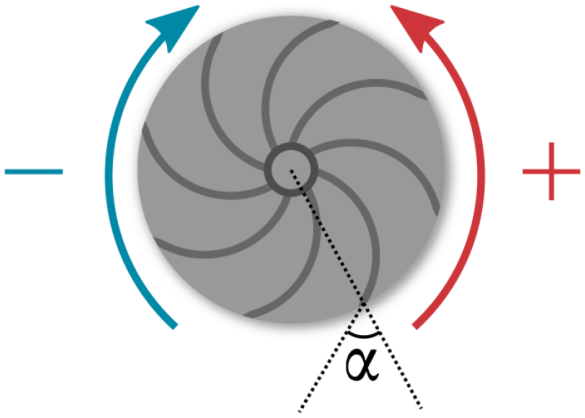

FIG. 1. Illustration of a TP87 type impeller, with 8 blades. The convention used to name the two different forcing conditions is represented: (+) when the convex face of the blade goes forward and (−) for the other. The angle α characterizes the curvature of the blades and is equal to $\alpha = 72°$ in the case of TP87 impellers. TM60 impellers look essentially the same, with 16 blades instead of 8.

anisotropic, inhomogeneous flows. In the sequel, we apply this formula to our PIV measurements to test whether it can provide a parameter-free estimate of the global dissipation, as well as local instantaneous maps of the local energy dissipation.

III. APPLICATION TO A VON KÁRMÁN GEOMETRY

The goal of the present paper is to compare global estimates of dissipated power with torque measurements, check their coincidence, and study maps of local energy dissipation rate to get some insight into the detailed processes governing energy transfers in a von Kármán flow.

A. Experimental setup

The von Kármán experiment has been extensively studied over the past years.[7,15–22] We give here a brief review of the main features of the setup.

Our von Kármán flow is generated in a vertical cylinder by two coaxial, contra-rotating impellers providing energy and momentum flux at the upper and the lower ends of the cylinder. The inner radius of the cylinder is $R = 100$ mm and the distance between the inner face of the impellers is $H = 180$ mm, which gives an aspect ratio of $H/R = 1.8$. The turbulence properties (anisotropy, fluctuations, and dissipation) are influenced by the geometry of the impellers, i.e., their nondimensional radius R_t, the oriented angle α between the blades (see Fig. 1), the number n of blades, and their heights h_b.[16] In the present paper, we consider only impellers with $h_b/R = 0.2$ and $\alpha = \pm 72°$. Those impellers are the so-called "TM60" (with 16 blades) and "TP87" impellers (with 8 blades), the characteristics of which are summarized in Table I. They are essentially similar, except for their number of blades and the material they are made of. A single impeller can be used to propel the fluid in two opposite directions, respectively, associated to the concave or convex face of the blades

TABLE I. Parameter space explored in this paper.

Impellers	Material	Number of blades	α (in deg)	Re	θ
TM60(+)	Stainless steel	16	72	$[10^3, 10^6]$	0
TP87(+)	Polycarbonate	8	72	10^5	$[-0.5, 0.5]$
TP87(−)	Polycarbonate	8	−72	10^5	$[-0.5, 0.5]$

going forward. This can be taken into account by a change of sign of the parameter α. In the sequel, we denote (−) (respectively, (+)) an impeller used with the concave (respectively, convex) face of its blades going forward. The impellers are driven by two independent motors which can rotate at frequencies up to 10 Hz. The motor frequencies can be either set equal to get exact counter-rotating regime or set to different values $f_1 \neq f_2$. To change the viscosity, we have used either water or glycerol at different dilution rates.

B. Control parameters

In the sequel, we choose R and $\Omega^{-1} = (\pi(f_1 + f_2))^{-1}$ as units of length and time. The von Kármán experiment is then characterized by two control parameters:

- the Reynolds number

$$Re = \pi(f_1 + f_2)R^2\nu^{-1},$$

  where ν is the fluid kinematic viscosity, ranges from 10^2 to more than 10^6 so that we can span a full range of regimes, from the purely laminar to the fully turbulent one;
- the rotation number

$$\theta = \frac{f_1 - f_2}{f_1 + f_2}$$

  measures the relative influence of global rotation over a typical turbulent shear frequency. Indeed, the exact counter-rotating regime corresponds to $\theta = 0$. For a nonzero rotation number, our experimental system is similar, within lateral boundaries, to an exact counter-rotating experiment at frequency $f = (f_1 + f_2)/2$, with an overall global rotation at frequency $(f_1 - f_2)/2$.[15,22] In our experiments, we vary θ from −1 to +1, exploring a regime of relatively weak rotation to shear ratio.

Table I summarizes the parameter space explored in this paper. The Reynolds variation is done at $\theta = 0$, while the rotation variation has been explored at $Re \approx 10^5$.

C. Measurements

The setup allows for both global and local flow diagnostics. Torque (global) measurements at each impeller are performed with SCAIME technology and provide values over the kHz range of C_1 and C_2, being, respectively, the torque applied to the bottom and the top shafts. Following the procedure described in Ref. 15, they are calibrated using measurements at different mean frequencies, so as to remove spurious contributions from genuine offsets or mechanical frictions. From this, we compute the nondimensional values K_{p1} and K_{p2} of the torque as $K_{pi} = C_i/(\rho R^5\Omega^2)$, where ρ is the density of the working fluid.

Local measurements of the velocity field of the flow have been made by PIV techniques in the stationary regime. The typical size of the particles used is a few tens of micrometers and their density is 1.4. Two cameras take between 600 and a few thousand successive pictures of the flow at a 15 Hz frequency. The resolution of our camera frame is 1600×1200 pixels, and the reconstruction is done using peak correlation performed over overlapping windows of size 16–32 pixels. As a result, we get measurements of velocity field on a grid of approximate size 60^2 in a vertical plane containing the axis of symmetry (Oz) in a cylindrical system of coordinate. The maximum spatial resolution we can reach for the velocity field with this setup is therefore of the order of $200/60 \approx 3$ mm, about 10–100 times larger than the dissipative scale. For more details about the experimental setup or the measurement techniques, see for instance Ref. 18. We can therefore estimate the derivatives of the velocity field only along the r and the z directions, but we do not have access to derivatives along θ. As a consequence, we will either set these derivatives to zero in the sequel or take them into account using hypothesis of statistical axisymmetry. We have checked that the two procedures give essentially the same result. In any case, we use incompressibility to estimate $\partial_\theta u_\theta$.

D. Diagnostics

1. Flow geometry

We are going to study different types of von Kármán flows (see Fig. 2). These types of flows happen depending on the forcing condition (+) or (−) and whether the system undergoes a spontaneous phase transition (bifurcation) or not.[19] There are, then, four types of flows: one corresponding to the (+) forcing condition where a phase transition cannot be observed (Fig. 2(a)), one corresponding to the (−) forcing condition where a phase transition is not observed (Fig. 2(b)), and two more corresponding to the two states of the flow that can be observed once the flow has undergone its phase transition (Figs. 2(c) and 2(d)). The difference between these flows can be characterized through our PIV measurements by their mean velocity profile in the vertical plane of measurements (see Fig. 2). In the first two types, the mean flow is symmetric with respect to the equatorial plane $z = 0$ and there is a strong shear layer in the middle. In the bifurcated states, the flow is no longer symmetric with respect to the equatorial plane. It consists in a one-cell flow in the vertical direction,

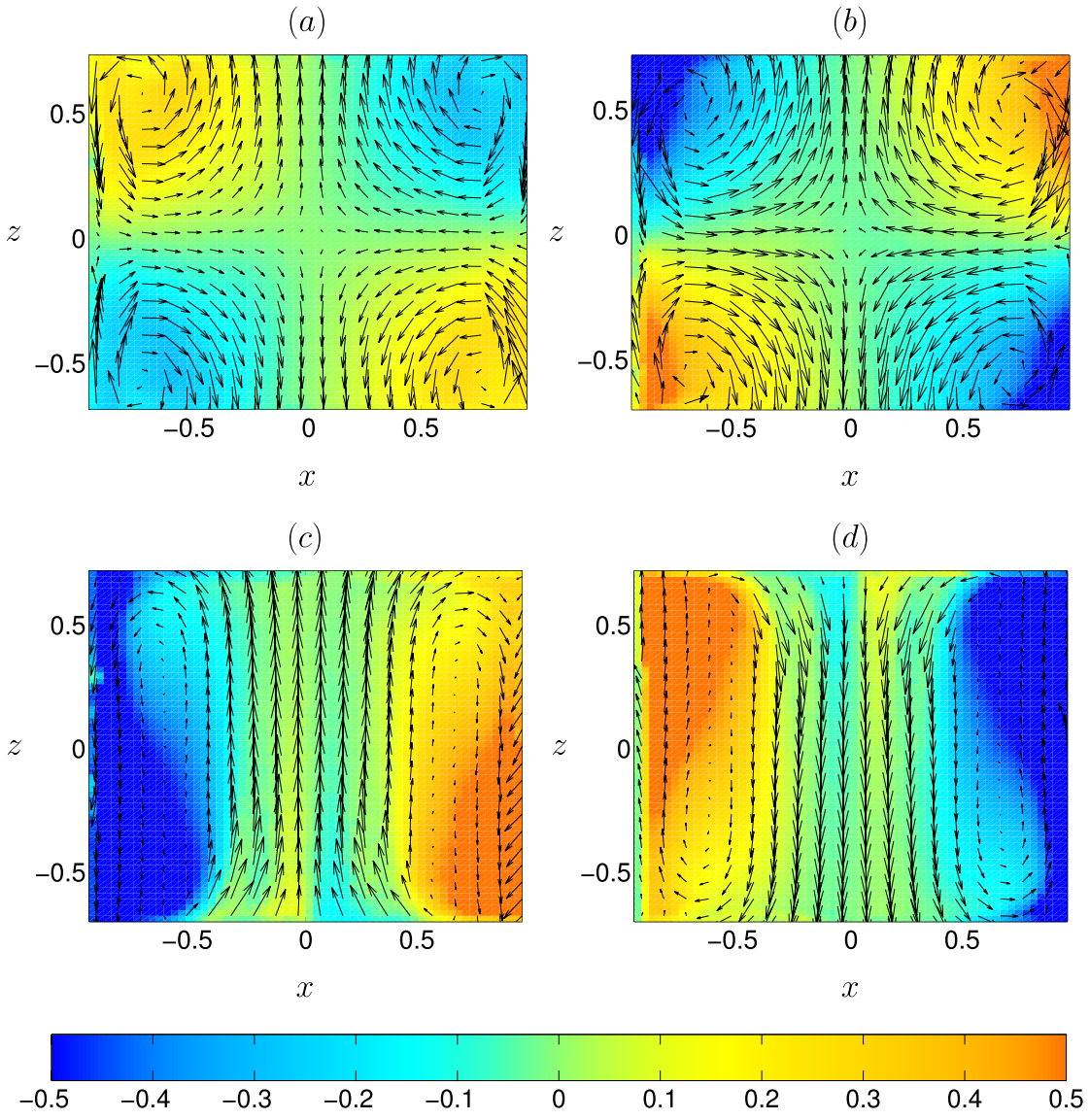

FIG. 2. The four types of flow characterized by their mean velocity profiles. Arrows represent the velocity field in the radial plane, while colours represent the orthogonal component to that plane. (a) The flow is forced under the (+) condition, no phase transition can be observed. (b)–(d) show the three different states of a flow forced under the (−) condition. (b) No phase transition has occurred, (c) (respectively, (d)) the shear layer has been sent downwards (respectively, upwards). In each of these flows, $Re \approx 3 \times 10^5$ and the two TP87 impellers rotate in opposite directions at $\theta = 0$.

with a strong shear layer at the impeller that rotates in the direction opposite to the orthoradial mean flow. The two bifurcated states are symmetric to each other. The interest of considering these different mean flow geometries is that they are characterized by well resolved (respectively, badly resolved) shear layer for the symmetric state (respectively, bifurcated state). Since we expect an important fraction of energy dissipation to be localized where there is a strong velocity gradient, this difference may be a large source of error in local estimates based on PIV measurements, as we will demonstrate later.

2. Global dissipation

Using torque measurements, we can get an accurate estimate of the global power injected into the flow. Indeed, since we study a stationary situation, this input must balance the rate of energy dissipation within the flow. This has been checked in a scale 4:1 version of our experiment (see Ref. 8). From these measurements, we get the global mean dissipation rate as $D = 2\pi(C_1 f_1 + C_2 f_2)$. From this, we compute the following diagnostics:

- the dimensionless mean dissipation rate

$$\mathcal{D} = \frac{D}{\rho R^5 \Omega^3} = K_{p1}(1+\theta) + K_{p2}(1-\theta), \tag{14}$$

- the dimensionless mean dissipated power per unit mass

$$\epsilon = \mathcal{D}\frac{R^3}{\mathcal{V}} = \frac{\mathcal{D}R}{\pi H}, \tag{15}$$

  which should not be confused with the Levi-Civita symbol. $\mathcal{V} = \pi R^2 H$ is the volume of the experiment.

These quantities depend on the Reynolds number, the rotation number, the characteristics of the impellers, and the mean flow geometry.[23] Examples of variation of ϵ as a function of Re are provided in Fig. 3(a) at $\theta = 0$, with TP87 and TM60 impellers, for the different flow geometries illustrated in Fig. 2. At low Reynolds numbers, the dissipation rate decays as Re^{-1}, until $Re \approx 300$ where the turbulence sets in. The dissipation rate then levels off at a value which depends upon the flow geometry: it is the lowest for the symmetric (+) flow, then increases for the (−) symmetric flow, and is the largest for the two bifurcated (−) flows. In Fig. 3(b), the mean dissipation rate is shown as a function of θ for TP87 (±) impellers at $Re = 3 \times 10^5$. In the (+) case (pink disks), it may be seen that the minimum of ϵ is obtained at $\theta = 0$. When θ is varied from, say, 0 to 0.5, ϵ increases and reaches a value twice as large as its minimum. In the (−) case, there is a discontinuity of the energy

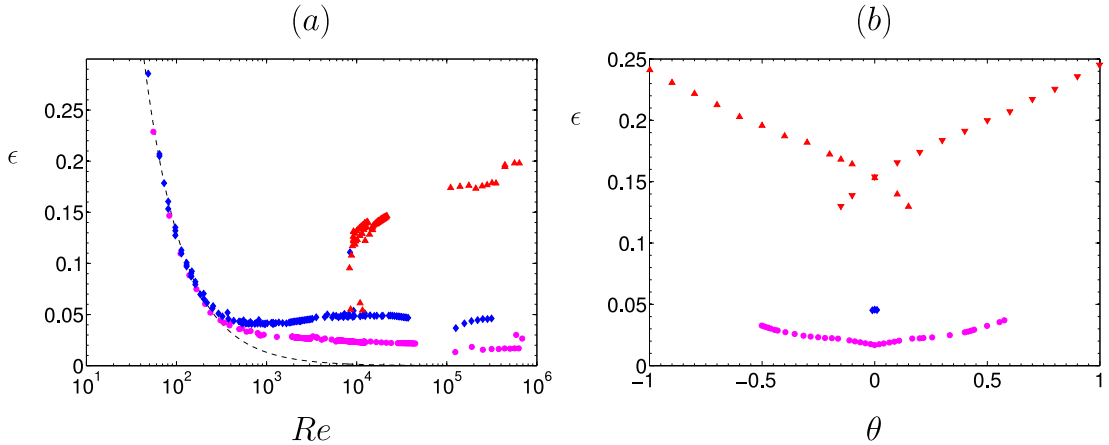

FIG. 3. Plots of the dimensionless dissipated power per unit mass. (a) As a function of Re for TP87 and TM60 impellers for the four geometries depicted in Fig. 2 at $\theta = 0$. Dotted line: Fit $\epsilon \approx 37 Re^{-1}$. Pink disks: Symmetric state (+). Blue rhombi: Symmetric state (−). Red triangles: Bifurcated states (−). (b) As a function of θ for TP87 impellers, $Re = 3 \times 10^5$. Pink disks: Symmetric state (+). Blue rhombi: Symmetric state (−). Red triangles: Bifurcated states (−).

dissipation at $\theta = 0$ due to the global symmetry breaking. We see that the symmetric state (blue rhombi) dissipates less energy than the two bifurcated states (red triangles). Another striking feature of Fig. 3(b) is the coexistence of two branches of dissipation, corresponding to the two bifurcated states, for a certain range of values of θ. This coexistence vanishes around $\theta = \pm 0.2$ (this value depends on the Reynolds number, see Ref. 21).

3. Local production and dissipation rates

Since the von Kármán flow is neither isotropic nor homogeneous, it is interesting to study more locally the production and dissipation of energy. Our setup being statistically axisymmetric, it is sufficient to perform the study in the vertical plane including the rotation axis, where we perform our velocity measurements. We thus consider the main stationary terms of local energy balance Eq. (7) and divide them by the experimental volume $\mathcal{V} = \pi R^2 H$ to get three local quantities:

- the local production rate per unit mass

$$\Gamma = -\frac{1}{\mathcal{V}} \partial_j \overline{J^j}. \tag{16}$$

  Integrating over the whole volume, one may then get from this the corresponding total production rate per unit mass Γ_T,

$$\Gamma_T = -\frac{1}{\mathcal{V}} \int_{\mathcal{V}} \partial_i \overline{J^i} d\mathcal{V} = -\frac{1}{\mathcal{V}} \oint_{\mathcal{S}} \overline{J^i} d\mathcal{S}_i, \tag{17}$$

  where the last equality comes from Green-Ostrogradsky formula;
- the positive local dissipation (transfer) rate per unit mass

$$\Pi = \frac{1}{\mathcal{V}} \left(-\overline{S_{ij} \tau^{ij}} + 2\nu \overline{S_{ij} S^{ij}} \right). \tag{18}$$

  The first term represents the energy dissipation due to energy transfers towards SGS, while the second one is the laminar energy dissipation;
- the positive local singularity dissipation (transfer) rate per unit mass

$$\Pi_{DR} = \frac{1}{\mathcal{V}} \overline{\mathcal{D}(\vec{u})}. \tag{19}$$

  As before, we denote by Π_T and Π_{DRT} the total dissipation rate per unit mass, obtained by volume integration of Π and Π_{DR}.

With our stereoscopic PIV measurements, we have access to all terms to compute these quantities, except for the pressure P in J^i, and the terms involving derivatives with respect to the azimuthal angle. In the sequel, we will present maps of the local quantities without the terms we do not have access to. In other words, we neglect all terms involving pressure and azimuthal derivatives. Moreover, the computation of the transfer terms requires the calibration of the constant C involved in the gradient model (see Eq. (10)). In Sec. IV A, we describe a calibration procedure using the angular momentum balance equation.

IV. DATA PROCESSING

A. Calibration of the gradient model using angular momentum balance

The first step is then to find the value of the C constant in order to be able to estimate the contribution of the terms containing τ^{ij} in (16) and (18). For this, we follow the work of the authors in Ref. 24 who have shown, by using high-resolution Laser Doppler Velocimetry (LDV) measurements, that in a symmetric situation ($\theta = 0$), the vertical flux of angular momentum is a constant equal to the torque injected by the impellers. This result stems from the z-component of angular momentum balance Eq. (9) integrated over a volume $V(z)$ that describes a cylinder extending from the bottom impeller to an altitude $h(z) = H/2 + z$ (see Fig. 4). In this case, the global z-component

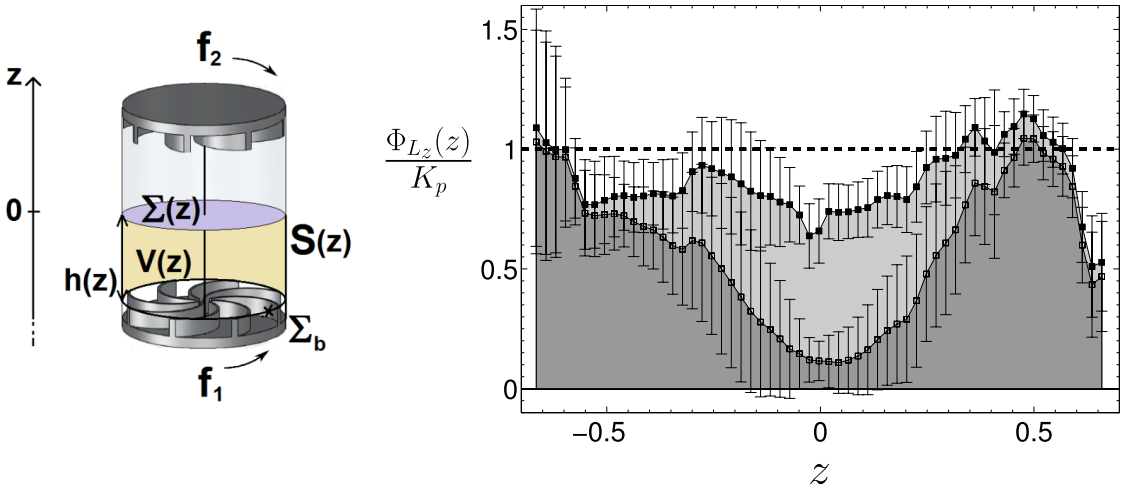

FIG. 4. Left: Control volume for the angular momentum budget. Right: Plot of the normalized vertical flux of vertical angular momentum as a function of z. The dark grey area represents convective transport due to the mean flow, while the light grey area represents convective transport due to fluctuations. Filled squares represent the sum of the two contributions so that the total convective transport is almost constant with z and equals to Kp. Each point has been obtained by taking the mean of several computations obtained from several flows at different Re. The error bars represent the standard deviation.

of angular momentum balance equation (8) reads

$$K_{p1} = -Re^{-1}\left(\int_{\mathcal{S}(z)} (\overline{u_\theta} + \overline{r\partial_r u_\theta})d\mathcal{S} - \int_{\Sigma(z)} \overline{r\partial_z u_\theta} d\Sigma\right) + \int_{\mathcal{S}(z)} \overline{r(u_r u_\theta + \tau^{r\theta})}d\mathcal{S} + \int_{\Sigma(z)} \overline{r(u_\theta u_z + \tau^{\theta z})}d\Sigma$$
$$\equiv -K_v(z) + \int_{\Sigma(z)} \overline{r(u_\theta u_z + \tau^{\theta z})}d\Sigma, \tag{20}$$

where $\Sigma(z)$ is a surface at altitude $h(z)$ from the bottom impeller and $S(z)$ is the lateral boundary (see Fig. 4). As discussed in Ref. 24, this equation states that the angular momentum transmitted by the motor to the fluid (measured by the dimensionless torque at the bottom K_{p1}) is either evacuated through the lateral boundary or transported to the upper layers of the fluid to be received by the upper motor as a drag. It was further shown in Ref. 24 that in a symmetric situation ($\theta = 0$), where the torques at the bottom and at the top are equal, the $K_v(z)$ term is negligible, so that there is a constant flux of angular momentum from the bottom to the top. For each $\theta = 0$ case, we thus compute the quantity

$$\Phi_{L_z}(z) = \int_{\Sigma_z} \overline{r(u_\theta u_z + \tau^{\theta z})}d\mathcal{S}, \tag{21}$$

and adjust the constant C, so that $\Phi_{L_z}(z) = K_{p1} = K_{p2} \equiv K_p$ for any z. In Fig. 4, we present the results of our computations for TM60(+) impellers. The adjustment of the constant C is done statistically by assuming that it does not depend on the Reynolds number (as it is supposed to depend only on the velocity reconstruction algorithm). We then fix $\Delta_r^2 = \Delta_x\Delta_z$, where $\Delta_x = 2R/58$ and $\Delta_z = (H - 2h_b)/63$ being the spatial resolutions of our PIV and we adjust C using 38 symmetrical flows at different Reynolds numbers so that their statistical mean provides a constant value of $\Phi(z)/K_p = 1$ within the (statistical) standard deviation.

The optimal value of C has to be taken equal to $C \approx 4$. This is around 50 times more than the conventional choice made in Refs. 12 and 25 for a Gaussian filter. We have identified several factors that may explain this difference: our data are not filtered in a Gaussian way; since we ignored azimuthal derivatives, the constant must be higher to compensate; the turbulence is neither isotropic nor homogeneous.

Dividing the flux into the contribution due to the time-average flow and the contribution due to the fluctuations, we also recover that near the impellers, the flux is only due to the mean flow, while at the center, it is almost only due to fluctuations.[24] We also checked that the diffusive terms in (20), going as Re^{-1}, are negligible at high Reynolds number. Likewise, the flux through $S(z)$ is also small, meaning that almost all of the flux goes in the vertical direction.

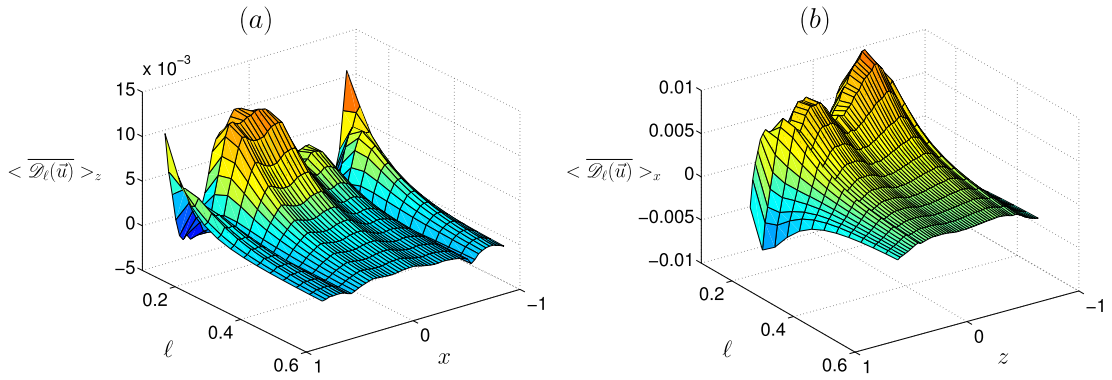

FIG. 5. Vertical (a) and radial (b) average of the local dissipation $\overline{\mathcal{D}_\ell(\vec{u})}$ for TM60(+) at $Re = 8\times10^5$ as a function of x, z, and ℓ.

B. Implementation of the Duchon-Robert formula

As we have seen in Section II E, $\mathcal{D}_\ell(\vec{u})$ provides the local dissipation for a given velocity field $\vec{u}$, at a given length scale ℓ. Since this formula is a generalization of the Kármán-Howarth equation to any kind of flow, it provides an estimate of the subgrid energy transfer as long as the considered scale ℓ is in the inertial range. Moreover, the considered scale must be sufficiently large with respect to the PIV smallest resolved scale, so as to guarantee statistical convergence through sufficient average in the scale space (on the sphere of radius ℓ). To check these two points, we present in Fig. 5 $\mathcal{D}_\ell(\vec{u})$ in two plots averaged in the radial (respectively, vertical) direction as a function of z (respectively, x) and ℓ for an experiment using TM60(+) impellers at very large Reynolds number ($Re \approx 8\times10^5$). We see that this quantity is close to zero at large scales ($\ell > 0.4$), but that it increases at small scales in the domain $|x| < 0.4, |z| < 0.7$, i.e., at the location of the median shear layer. For ℓ between 0.1 and 0.15 (i.e., approximately 4–5 times the smallest scale resolved by our PIV setup), there is the start of a saturation, indicating the beginning of the inertial range. While the extent of the inertial range is likely to vary (increase) with the Reynolds number, its largest scale is likely to be independent of the Reynolds number, as long as the flow is turbulent. Indeed, as discussed in Ref. 26, the geometry of the largest scales of the von Kármán flow appears fairly independent of the Reynolds number, except around $Re = 10^5$ where they may experiment abrupt changes due to the equivalent of a phase transition.[19] Since in the Kolomogorov picture energy cascades from large to small scales, it is reasonable to assume that the beginning of the inertial range is solely determined by the large scale topology, thereby becoming independent of the Reynolds number (except maybe around $Re = 10^5$). To check this, we report in Fig. 6(a) the comparison between the total dissipated power Π_{DRT} at $\ell = 0.1$ (blue symbols) and direct measurements of the injected power (black symbols). We observe that our estimates are in good agreement with direct measurements, especially for symmetric flows. In Fig. 6(b), the results of our computations to estimate the global dissipated power using the LES method are displayed. These results will be discussed in more detail later, but we can already observe that we obtain a good agreement with direct measurements. We can conclude from all our computations that the method using the DR formula may be seen as an interesting alternative to the widespread LES-PIV method, since it relies on very few arbitrary hypotheses. We explore its performances with other flow geometries in the sequel.

V. RESULTS

A. Symmetric case $\theta = 0$

1. Energy production and transport

To understand the flux of energy in the von Kármán flow, it is interesting to focus first on the symmetric case ($\theta = 0$), specifically on the case when both impellers rotate in the (+) sense with

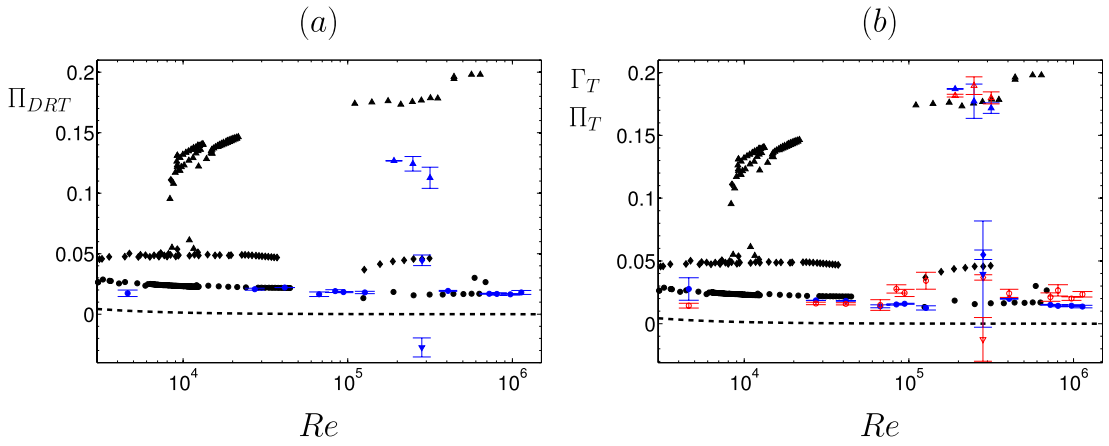

FIG. 6. Comparison between direct measurements of energy injection obtained using torque measurements (black symbols) and PIV estimates at various Reynolds numbers, for TM60 and TP87 impellers for the four different mean state geometries displayed in Fig. 2. Disks: (+) symmetric. Rhombi: (−) symmetric. Up triangles: (−) shear layer sent downwards. Down triangle: (−) shear layer sent upwards. (a) Energy dissipation Π_{DRT} using the DR method (blue symbol). (b) Energy injection Γ_T (red symbols) and dissipation Π_T (blue symbols) using the LES-PIV method. The dotted line represents the "laminar fit" $\epsilon = 37\,Re^{-1}$. The estimates are computed based on 2–15 realizations of the experiment where at least 600 instantaneous velocity snapshots have been taken for each of them. The symbols represent the mean of our computations, while the error bars represent the standard deviation.

the same frequency in a stationary regime. In such regime, the dissipated power equals the injected power. Through Green-Ostrogradski theorem, the total energy production Γ_T is equal to the entering flux of J^i at the boundaries. In this symmetric case, most of the flux is provided by the component J^z and appears to provide a fairly good estimate of the injected power at large enough Reynolds numbers ($Re \geq 10^5$). Indeed, we show in Fig. 6(b) the results of our computations for Γ_T (empty red symbols). We see that for $Re \geq 10^5$, these estimates coincide within 20%. However, at lower Reynolds numbers ($Re \approx 4 \times 10^3$), the PIV estimates only capture 55% of the actual injected power. This may be due to the fact that as the Reynolds number is decreased, an increasing part of the injected power is either through pressure effects, azimuthal variations, or viscous boundary layers that are not resolved by our measurements.

Given that the J^z contribution dominates the total energy production, it is interesting to focus on the spatial variation of this quantity. Fig. 7(a) shows such a local map of $\overline{J^z}$ for a symmetric flow at $Re \approx 3 \times 10^4$.

As can be seen, at the center of the cylinder, i.e., $x/R \in [-0.8\ 0.8]$, big structures reflect the advection of energy towards the impellers through the mean Ekman pumping by the impellers. In contrast, at the walls, smaller structures of opposite sign are observed, reflecting the injection of energy within the flow. These two kinds of structures are mirrored by the recirculation cells that we

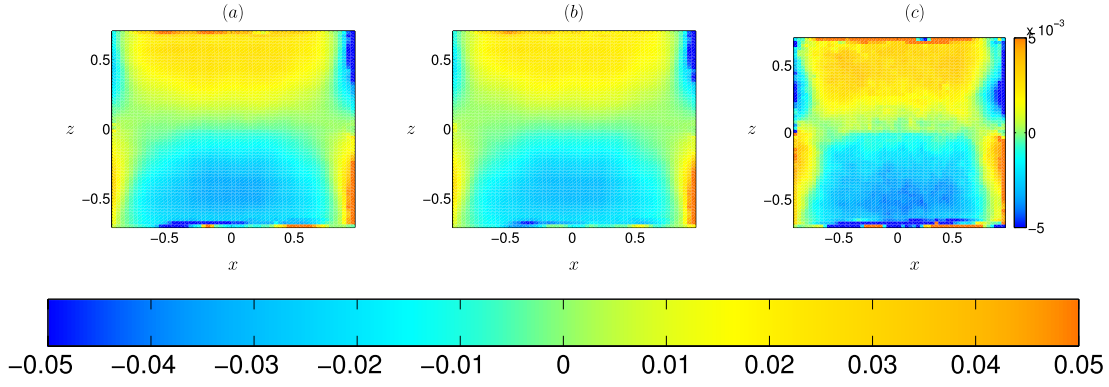

FIG. 7. Typical maps of $\overline{J^z}$: (a) mean energy transfer through the system, (b) contribution of the mean flow, and (c) contribution of the fluctuations.

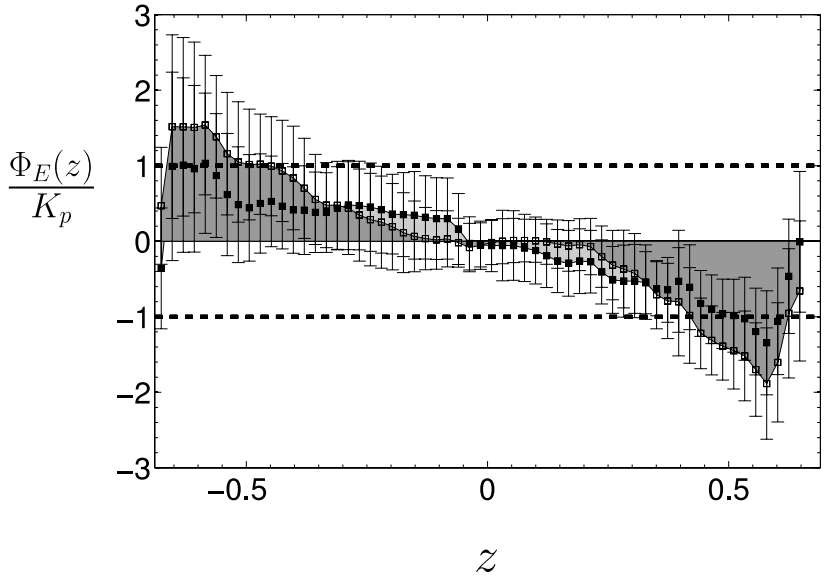

FIG. 8. Plot of the normalized vertical flux of energy as a function of z. The dark grey area represents convective transport due to the mean flow, while the light grey area represents convective transport due to fluctuations. Filled squares represent the sum of the two contributions so that the total convective transport is a decreasing function of z. Each point has been obtained by taking the mean of several computations obtained from several flows and the error bars represent the statistical standard deviation.

observed in Fig. 2. The local structure of $\overline{J^z}$ can be further used to get information about energy transport in the flow. Indeed, performing an integration of Equation (7) over the height-varying volume $V(z)$ (see Fig. 4) and setting $\partial_t \overline{E} = 0$, we can get an equation for the energy transport in the flow as

$$\oint_{\mathcal{S}} \overline{J^i} d\mathcal{S}_i = -K_{p1}(\theta + 1) - K_v'(z) + \int_{\mathcal{S}_z} \overline{J^z} d\mathcal{S}, \tag{22}$$

where K_v' is the contribution due to the lateral boundaries at height z. Ignoring this contribution, we can write

$$\oint_{\mathcal{S}} \overline{J^i} d\mathcal{S}_i = -K_{p1} + \Phi_E(z), \tag{23}$$

where $\Phi_E(z) = \int_{\mathcal{S}_z} \overline{J^z} d\mathcal{S}$. This quantity is displayed in Fig. 8.

We observe that near the impellers, the total flux of energy (filled black squares) equals the energy injected by the impellers. The change of sign comes from the fact that the impeller at the bottom injects energy in the $+z$ direction, whereas the upper impeller injects energy in the $-z$ direction. At the center of the experiment, the flux is zero, meaning that on average, there is not any energy going from one half of the cylinder to the other through the shear layer. Finally, it is interesting to see that, as before, the mean flow plays an important role in the transport of energy near the impellers, whereas near the shear layer, energy is carried by fluctuations. A slight difference is that near the impellers, as the mean flow sends energy towards the center of the cylinder, fluctuations create a flux which goes in the opposite direction and tries to send energy back to the impellers.

Altogether, the local map of injected power is shown in Fig. 9(a). We see that near the impellers, the divergence term brings energy into the system as is expected. We also see that energy leaves the center of the recirculation cells and tends to be advected towards the center of the impeller through Ekman pumping.

2. Energy dissipation

We now turn to the total energy dissipation estimated through the LES method Π_T.

Its values at various Reynolds numbers in the symmetric case are reported in Fig. 6(b). We observe that it is in very good agreement with direct measurements at $Re \approx 4 \times 10^3$. At such

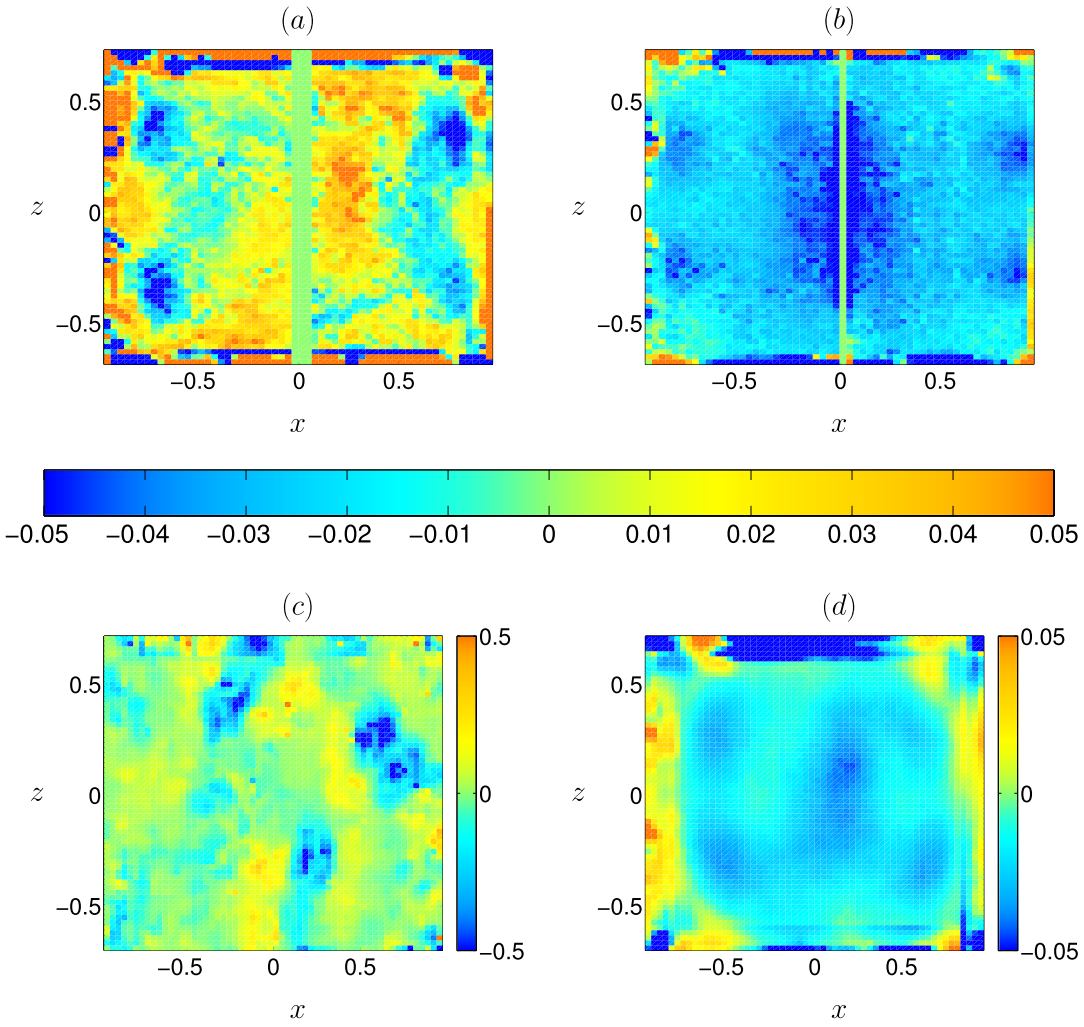

FIG. 9. Top: Maps of the energy production rate (a) and energy transfer rate (b) for the same flow as in Fig. 2(a), using LES-PIV estimates. Bottom: Instantaneous (c) and time averaged (d) maps of the local dissipation $\mathcal{D}_\ell(\vec{u})$ at $\ell = 0.1$ for the same flow. Areas where energy accumulates are represented in red, while those where energy leaves are represented in blue.

Reynolds number, the dissipative scale is of the order of 1 mm, close to the PIV resolution. This result is therefore in agreement with the observation of Tokgoz *et al.*[1] obtained for a Taylor-Couette flow. At larger Reynolds numbers, the estimates using the LES method are in good agreement with respect to direct measurements since we are able to capture up to 90% of the actual energy dissipation. The map of the local dissipation with this method is provided in Fig. 9(b) and appears fairly uniform across the vessel, with larger intensity along the vertical axis around $r = 0$ and near the lateral boundaries around $z = \pm 0.3$.

This map can be compared with the one obtained using the DR formula $\overline{\mathcal{D}_\ell(\vec{u})}$ at $\ell = 0.1$ in Fig. 9(d). One observes the same localized structures of energy dissipation near the walls at $x = \pm 0.6$, which are symmetrically distributed with respect to the midplane. These structures are statistically significant, since they are not observed on plots of the instantaneous local dissipation $\mathcal{D}_\ell(\vec{u})$ (see Fig. 9(c)). They may, therefore, trace the intense vortices of the shear layer. In addition, one observes a clear localization of energy injection (red areas) at the tip of the impellers, with an energy dissipation in the middle part of the cells. Regarding instantaneous maps, it is interesting to note that it is characterized by intense, localized events that can reach 10–20 times the maximum average local dissipation. Whether these intense events are connected to localized quasi singular structures is an interesting open question that we leave for future work.

Overall, these dissipation maps provide clear evidence that the maximum energy dissipation lies within the shear layer and that the DR formula provides a better estimate of the energy dissipation than the LES method in the symmetric case.

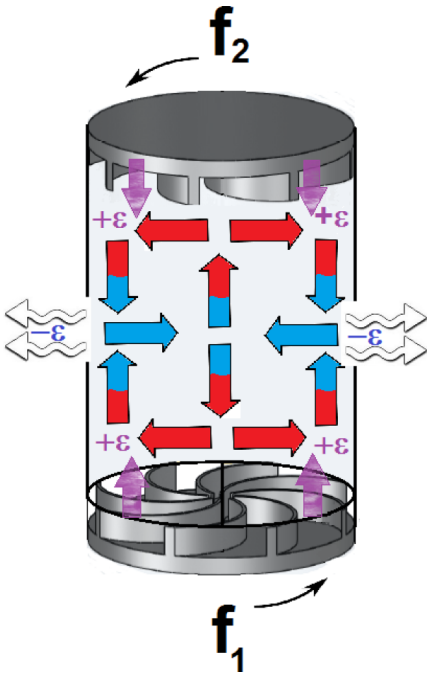

FIG. 10. Energy cycle in the von Kármán experiment: the energy is advected to the impellers via the Ekman pumping, the flow is then accelerated inside the impellers and expelled at the walls, providing an energy injection ϵ towards the mixing layer. In that mixing layer, turbulent fluctuations dissipate an energy equal to ϵ. The fluid is then pumped again into the impellers for further reinjection, closing the energy cycle and providing a stationary situation with energy dissipation ϵ.

3. Description of the energy cycle

Altogether, our results regarding energy production, transport, and dissipation can be summarized into a simple picture of the "energy cycle" for the von Kármán flow, which is sketched in Fig. 10: the energy is advected to the impellers via the Ekman pumping, the flow is then accelerated inside the impellers and expelled at the walls, providing an energy injection towards the mixing layer. In that mixing layer, turbulent fluctuations dissipate an energy equal to ϵ. The fluid is then pumped again into the impellers for further reinjection, closing the energy cycle and providing a stationary situation with energy injection and dissipation equal to ϵ.

In the sequel, we study the influence the flow topology and the forcing conditions onto this energy cycle. Since in this picture most of the energy is dissipated within the middle shear layer, there is good hope that we can capture its main contribution by the PIV measurements, *provided that the shear layer is not too close to the impeller* since in that case, the PIV measurements cannot resolve the flow. We check in Secs. V B and V C that this is indeed the case and provide detailed informations about the localization of energy dissipation to complete the picture of the energy cycle.

B. Influence of the flow topology

Let us now consider the case when both impellers rotate in the (−) sense at $\theta = 0$. For this type of forcing, at sufficiently high Reynolds numbers, there is coexistence of three different flow geometries for TP87 type impellers.

Considering the case where the flow has not undergone any phase transition, Fig. 6 shows that for this type of forcing, we measure a dissipation almost three times bigger than what was observed with the previous forcing condition. In this symmetric case, our estimates of the injected and dissipated powers are within 20% of the measured value using the LES-PIV method, whereas we reach 98% of the actual dissipation rate of energy with the DR formula (see Fig. 6(a)). Local maps of injected and dissipated power are plotted in Fig. 11. They correspond to the flows (b) displayed in Fig. 2 where the forcing is in the (−) sense. Here, Figs. 11(a) and 11(b) represent LES-PIV estimates, while Figs. 11(c) and 11(d) represent instantaneous and time averaged maps using the DR

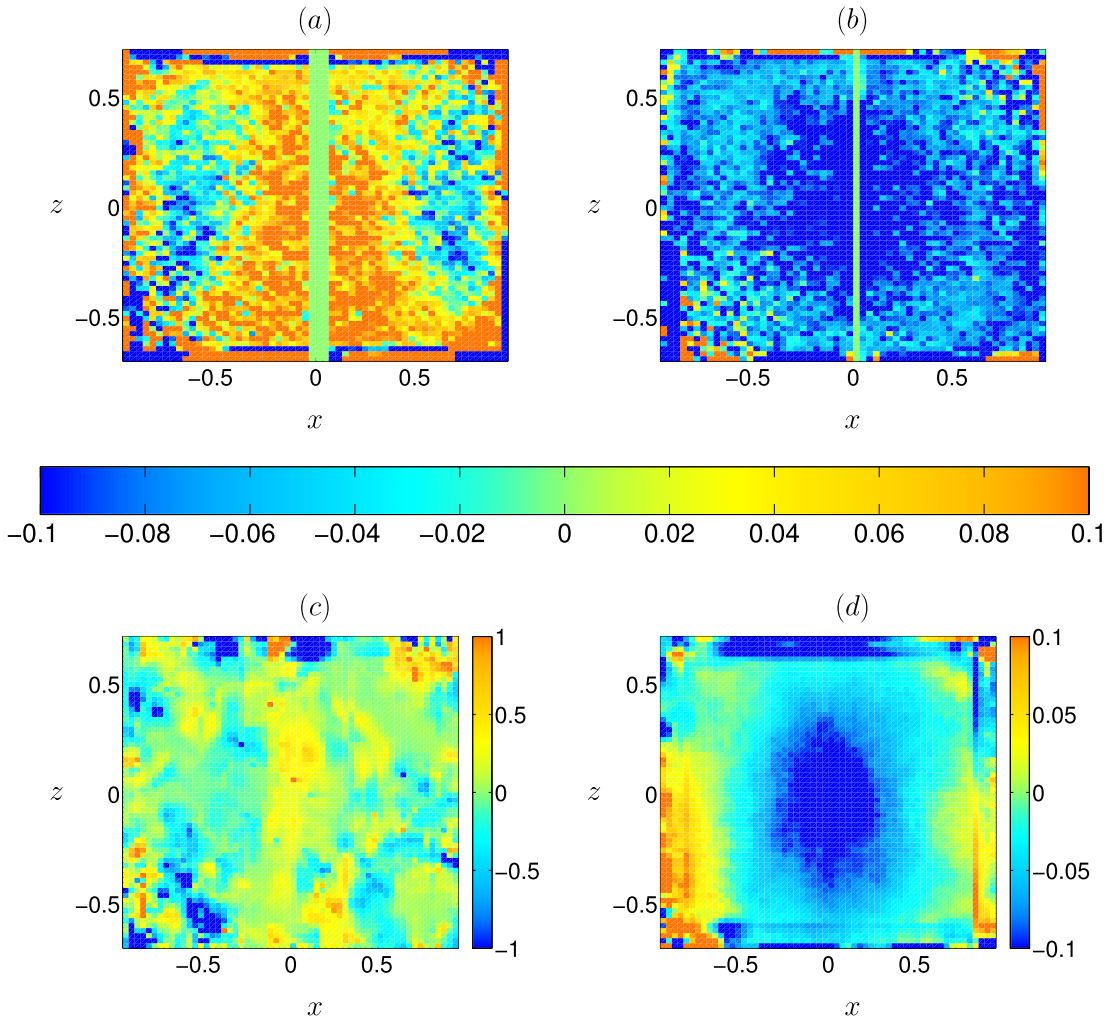

FIG. 11. Top: Maps of the energy production rate (a) and energy transfer rate (b) for symmetric (−) geometry corresponding to the flow in Fig. 2(b), using LES-PIV estimates. Bottom: Instantaneous (c) and time averaged (d) maps of the local dissipation $\mathcal{D}_\ell(\vec{u})$ at $\ell = 0.1$ for the same flow. Areas where energy accumulates are represented in red, while those where energy leaves are represented in blue.

method. Here, the remarks are essentially the same as in Fig. 9: near the impellers, the divergence term brings energy into the system, while energy leaves the center of the recirculation cells to accumulate at the center of the cylinder. The dissipation term does not change much either and is approximately constant throughout the plane of measurements. A noticeable difference however is that the color scale is bigger for this configuration. We thus recover the fact that the flow dissipates more energy than for a forcing in the (+) sense and, as a consequence, the torque of the impellers has to be higher.

The situation changes for the bifurcated (−) states. The shear layer is now very close to the upper or lower impeller, depending on the state "chosen" by the system. The mean velocity field for these two states is essentially the same, differing only by the transformation $z \to -z$. The measured injected power is also the same in these two states. However, in terms of PIV-estimated injected or dissipated power, a clear asymmetry occurs. Indeed, when the shear layer is sent downwards (up-pointing triangles), the LES-PIV method provides good estimates of both the injected and the dissipated powers (see Fig. 6(b)), while the DR method provides about 65% of the dissipated power. In the case where the shear layer is sent upwards (down pointing triangles), however, both the LES-PIV method and the DR method totally fail to reproduce the measured dissipated energy (giving the wrong sign). Since there is not any asymmetry observed in the mean flow, this difference must be attributed only to fluctuations and tiny asymmetries of the experimental setup (laser sheet location, focalization of cameras, etc.). This points out the importance of resolving the shear layer

in the PIV estimates of the injection or dissipation energy rate. We thus conclude that neither the LES-PIV nor the DR method is appropriate in cases when the shear layer is at the location of the impellers, where it cannot be resolved by our PIV setup.

Local maps of injected and dissipated powers in the bifurcated states are plotted in Fig. 12. They correspond to the flows (c) and (d) displayed in Fig. 2 where the forcing is in the (−) sense.

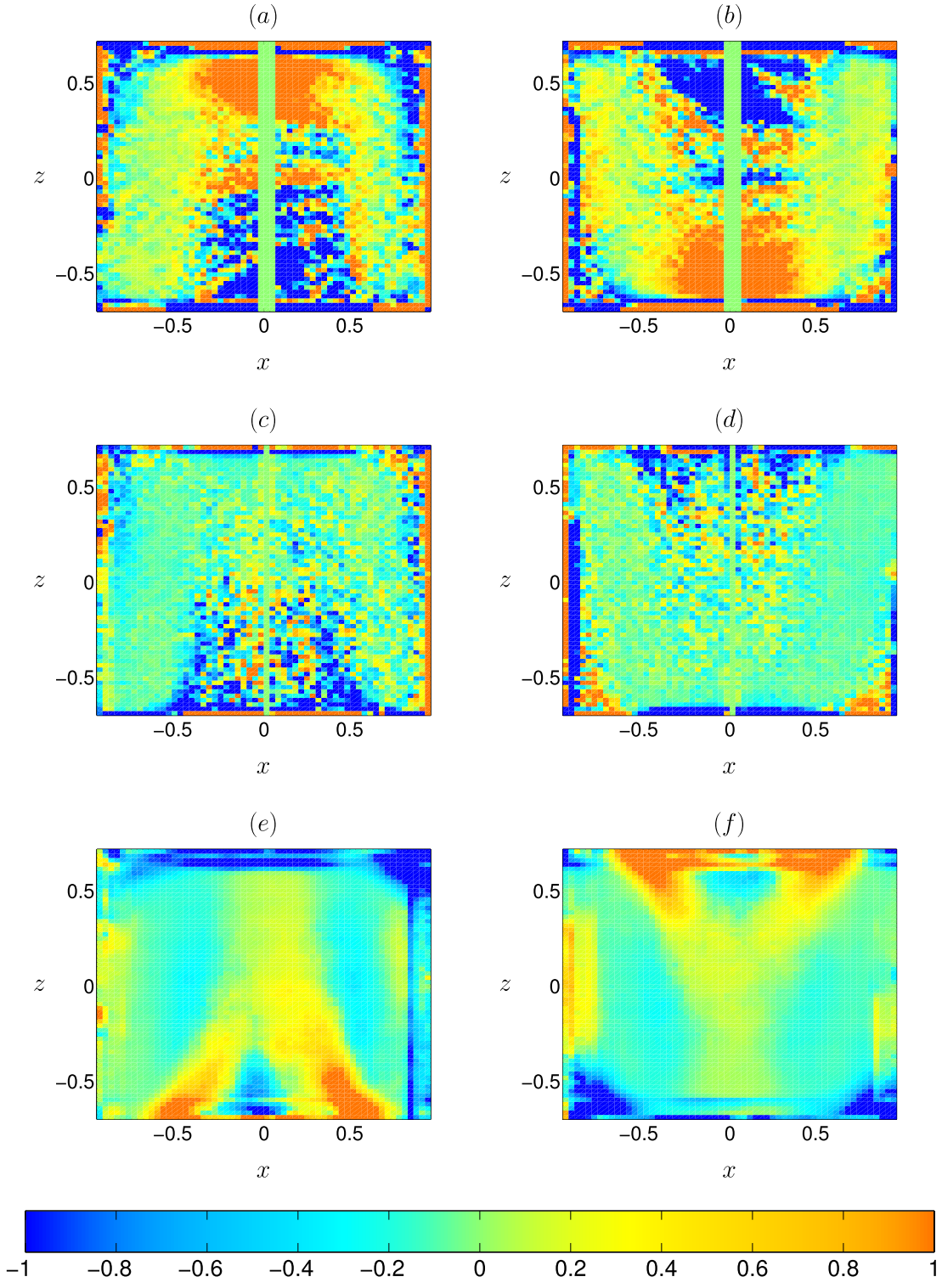

FIG. 12. Maps of the energy production rate and energy transfer rate for the two bifurcated geometries (−). Left: For the flow represented in Fig. 2(c). Right: For the flow represented in Fig. 2(d). Top line represents the estimated injected energy, using LES-PIV method. Middle line represents the estimated dissipated energy using the LES-PIV method. Bottom line represents the estimated dissipated energy using the DR method. Areas where energy accumulates are represented in red, and those where energy leaves are represented in blue.

Maps (a), (c), and (e) correspond to a flow where the shear layer has been sent near the lower impeller. As a consequence, we observe that energy enters from the top and is advected downwards to the shear layer. The map of the dissipation term for this flow looks quite like the production term. We see that most of the dissipation we are able to capture happens at the center of the cylinder but, as we said before, we miss all the dissipation that happens near the lower impeller where there is the shear layer. At first sight, maps (b), (d), and (f) are just symmetric of maps (a), (c), and (e) with respect to $z \to -z$. However, by looking closely, tiny differences are observed, especially near the walls and impellers. These differences explain the asymmetry between the two bifurcated states shown in Fig. 6.

C. Influence of the forcing asymmetry θ

We now investigate the case where the impellers are not exactly counter-rotating, so that the parameter θ varies from -0.5 to 0.5. In the $(-)$ case, the geometry observed at $|\theta| > 0$ is always bifurcated (see Fig. 3(b)), with the shear layer located at the top or bottom impeller. In the $(+)$ case, the transition is more gradual: the shear layer is increasingly shifted upwards (respectively, downwards) as θ goes from 0 to 1 (respectively, -1), allowing for finer tests of the accuracy of our PIV estimates as a function of the flow geometry.

In Fig. 13 are plotted our estimates for the total injected (red symbols) and dissipated powers (blue symbols) using both the LES-PIV method (Fig. 13(b)) and the DR formula (Fig. 13(a)). For each θ, our computations are based on sets of at least 600 instantaneous velocity snapshots. Because of the symmetry $z \to -z$, we expect all estimates to be symmetric with respect to $\theta \to -\theta$, provided the statistics are well converged and that the shear layer is sufficiently resolved. We see that this is indeed the case for $(+)$ forcing condition, where the shear layer always lies in between the two impellers. However, we observe that both methods become inaccurate when $|\theta|$ is too high, i.e., $|\theta| > 0.3$. For the $(-)$ forcing condition, the estimates give very good agreement for the symmetric state. However, when the phase transition occurs, one observes the same asymmetry as in the $\theta = 0$ case between the two possible states: when the shear layer is sent downwards, we get a good agreement between measurements and PIV estimates with the LES method. However, the DR method systematically underestimates the dissipation. In the case where with the shear layer is sent upwards, the estimates are really bad with both methods.

Corresponding maps of the injected and dissipated powers are provided in Fig. 14 at $\theta = -0.1$ in the $(+)$ and $(-)$ senses. They obey qualitatively the same behavior as in the symmetric case, so

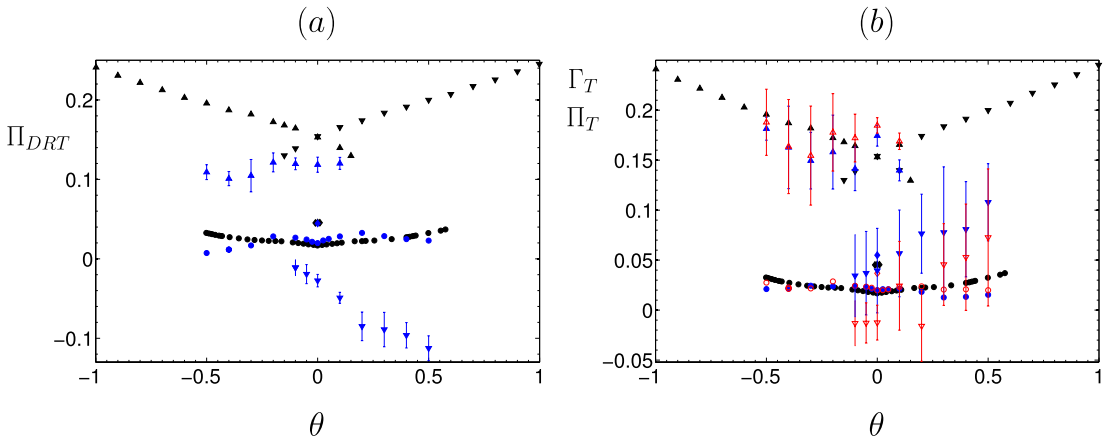

FIG. 13. Comparison between direct measurements of energy injection obtained through torque measurements (black symbols) and PIV based estimates at various θ, for TP87 impellers for the four different mean state geometries of Fig. 2. Disks (+). Rhombi: (−) symmetric. Up triangles: (−) shear layer sent downwards. Down triangle: (−) shear layer sent upwards. (a) Energy dissipation using DR method (blue symbols). (b) Energy injection Γ_T (red symbols) and dissipation Π_T (blue symbols) using the LES-PIV method. The estimates are computed based on 1–2 realizations of the same experiment where at least 600 instantaneous velocity snapshots have been taken for each of them. The symbols represent the mean of our computations, while the error bars represent the standard deviation.

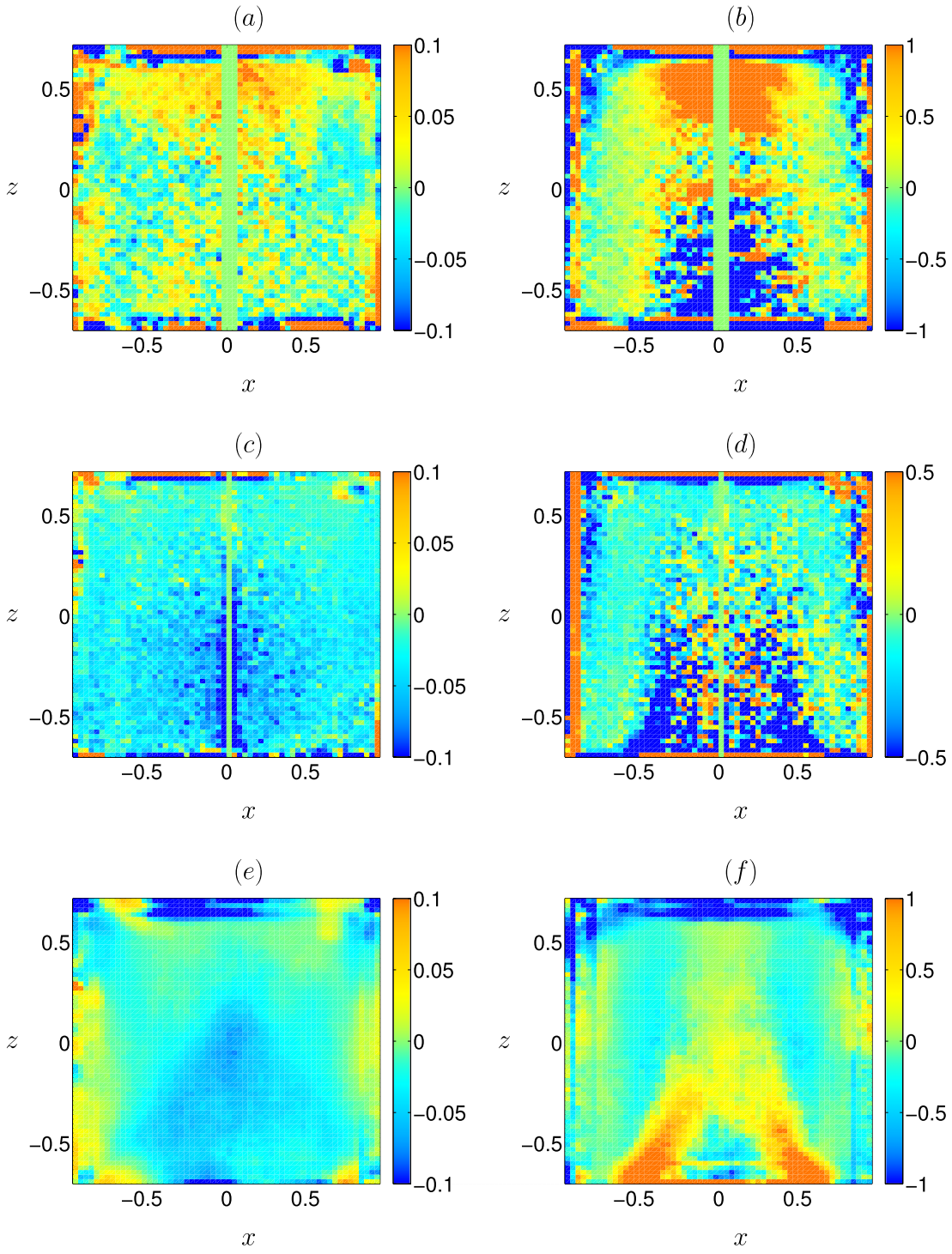

FIG. 14. Maps of the energy production rate and energy transfer rate at $\theta = -0.1$ for the two rotation directions. Left: (+). Right: (−). Top line represents the estimated injected energy, using LES-PIV method. Middle line represents the estimated dissipated energy using the LES-PIV method. Bottom line represents the estimated dissipated energy using the DR method. Areas where energy accumulates are represented in red, and those where energy leaves are represented in blue.

that the energy cycle description is qualitatively the same, with the shear layer location being moved as θ varies.

VI. CONCLUSION

In this paper, we investigate the energy cycle of a turbulent von Kármán flow. In this kind of setup, it is possible to control the mean energy flux inside the flow in order to get a statistically

stationary regime. It is also possible to monitor the torque and frequency of the impellers. In our case, we use PIV measurements to study local and global energy transfers inside the flow. This kind of measurements gives us access to the effective velocity field on a grid that does not resolve the dissipative scale. Therefore, we use a LES approximation to model the influence of unresolved scales. This procedure involves a free parameter which has to be calibrated for our setup. This is achieved by imposing angular momentum balance at the smallest resolved scale.[24] After deriving an energy balance equation at a fixed scale ℓ, we proceed to estimate four quantities from our PIV measurements: the local and global mean powers injected by the impellers and the local and global mean dissipated powers. This computation is performed for various Reynolds numbers and for various flow topologies. These PIV estimates are then compared with direct injected power estimates provided by torque measurements at the impellers. The agreement between PIV estimates and direct measurements depends on the flow topology. In symmetric situations, we capture up to 90% of the actual energy dissipation. However, our results become increasingly inaccurate as the shear layer responsible for most of the dissipation approaches one of the impellers and cannot be resolved by our PIV setup. At the same time, we explore a new method for PIV estimates of the energy dissipation based on the work of Duchon and Robert[9] that generalizes the Kármán-Howarth equation to nonisotropic, nonhomogeneous flows. This method provides parameter-free estimates of the energy dissipation as long as the smallest resolved scale lies in the inertial range and the shear layer is resolved by the PIV setup. With this method, we obtain a very good agreement between PIV estimates and direct measurements, and we are able to capture up to 98% of the actual dissipated power in symmetric situations. However, this method also gives increasingly inaccurate results as the mixing layer approaches one of the impellers. These results are used to evidence a well-defined stationary energy cycle within the flow in which the energy is injected by the top and the bottom impellers towards the shear layer. There, turbulent fluctuations dissipate energy and the flow is then pumped towards the impellers, closing the energy cycle.

[1] S. Tokgoz, G. E. Elsinga, R. Delfos, and J. Westerweel, "Spatial resolution and dissipation rate estimation in Taylor–Couette flow for tomographic PIV," Exp. Fluids **53**, 561–583 (2012).
[2] J. Sheng, H. Meng, and R. O. Fox, "A large eddy piv method for turbulence dissipation rate estimation," Chem. Eng. Sci. **55**, 4423–4434 (2000).
[3] P. Saarenrinne and M. Piirto, "Turbulent kinetic energy dissipation rate estimation from PIV velocity vector fields," Exp. Fluids **29**, 300–307 (2000).
[4] T. Tanaka and J. K. Eaton, "A correction method for measuring turbulence kinetic energy dissipation rate by PIV," Exp. Fluids **42**, 893–902 (2007).
[5] A. Delafosse, M. L. Collignon, M. Crine, and D. Toye, "Estimation of the turbulent kinetic energy dissipation rate from 2d-piv measurements in a vessel stirred by an axial mixel ttp impeller," Chem. Eng. Sci. **66**, 1728–1737 (2011).
[6] S. Baldi and M Yianneskis, "On the direct measurement of turbulence energy dissipation in stirred vessels with PIV," Ind. Eng. Chem. Res. **42**(26), 7006–7016 (2003).
[7] P.-P. Cortet, P. Diribarne, R. Monchaux, A. Chiffaudel, F. Daviaud, and B. Dubrulle, "Normalized kinetic energy as a hydrodynamical global quantity for inhomogeneous anisotropic turbulence," Phys. Fluids **21**(2), 025104 (2009).
[8] B. Rousset, P. Bonnay, P. Diribarne, A. Girard, J. M. Poncet, E. Herbert, J. Salort, C. Baudet, B. Castaing, L. Chevillard, F. Daviaud, B. Dubrulle, Y. Gagne, M. Gibert, B. Hébral, T. Lehner, P.-E. Roche, B. Saint-Michel, and M. Bon Mardion, "Superfluid high Reynolds von Kármán experiment," Rev. Sci. Instrum. **85**(10), 103908 (2014).
[9] J. Duchon and R. Robert, "Inertial energy dissipation for weak solutions of incompressible Euler and Navier-Stokes equations," Nonlinearity **13**, 249–255 (2000).
[10] M. Germano, "Turbulence - The filtering approach," J. Fluid Mech. **238**, 325–336 (1992).
[11] M. Lesieur, *Turbulence in Fluids* (Kluwer Academic Publishers, 1990).
[12] G. L. Eyink, "Multi-scale gradient expansion of the turbulent stress tensor," J. Fluid Mech. **549**, 159–190 (2006).
[13] R. A. Clark, J. H. Ferziger, and W. C. Reynolds, "Evaluation of subgrid-scale models using an accurately simulated turbulent flow," J. Fluid Mech. **91**, 1–16 (1979).
[14] L. Onsager, "Statistical hydrodynamics," Nuovo Cimento (Suppl.) **6**, 279–287 (1949).
[15] L. Marié, "Transport de moment cinétique et de champ magnétique par un écoulement tourbillonnaire turbulent: Influence de la rotation," Ph.D. thesis, Université Paris 7, 2003.
[16] F. Ravelet, "Bifurcations globales hydrodynamiques et magnétohydrodynamiques dans un écoulement de von Kármán turbulent," Ph.D. thesis, Ecole doctorale de l'Ecole Polytechnique, 2005.
[17] R. Monchaux, "Mécanique statistique et effet dynamo dans un écoulement de von Kármán turbulent," Ph.D. thesis, Université Paris 7, 2007.
[18] B. Saint-Michel, "L'écoulement de von Kármán comme paradigme de la physique statistique hors équilibre," Ph.D. thesis, Université Paris 6, 2013.
[19] P.-P. Cortet, A. Chiffaudel, F. Daviaud, and B. Dubrulle, "Experimental evidence of a phase transition in a closed turbulent flow," Phys. Rev. Lett. **105**(21), 214501 (2010).

[20] B. Saint-Michel, F. Daviaud, and B. Dubrulle, "A zero-mode mechanism for spontaneous symmetry breaking in a turbulent von Kármán flow," New J. Phys. **16**(1), 013055 (2014).
[21] B. Saint-Michel, E. Herbert, J. Salort, C. Baudet, M. Bon Mardion, P. Bonnay, M. Bourgoin, B. Castaing, L. Chevillard, F. Daviaud, P. Diribarne, B. Dubrulle, Y. Gagne, M. Gibert, A. Girard, B. Hébral, T. Lehner, and B. Rousset, "Probing quantum and classical turbulence analogy through global bifurcations in a von Kármán liquid Helium experiment," Phys. Fluids **26**, 125109 (2014); e-print arXiv1401.7117v2.
[22] F. Ravelet, A. Chiffaudel, F. Daviaud, and J. Léorat, "Toward an experimental von Kármán dynamo: Numerical studies for an optimized design," Phys. Fluids **17**(11), 117104 (2005).
[23] F. Ravelet, A. Chiffaudel, and F. Daviaud, "Supercritical transition to turbulence in an inertially driven von Kármán closed flow," J. Fluid Mech. **601**, 339–364 (2008).
[24] L. Marié and F. Daviaud, "Experimental measurement of the scale-by-scale momentum transport budget in a turbulent shear flow," Phys. Fluids **16**, 457–461 (2004).
[25] A. Leonard, "Energy cascade in large-eddy simulations of turbulent fluid flows," in *Turbulent Diffusion in Environmental Pollution*, edited by F. N. Frenkiel and R. E. Munn (Academic Press, 1974), pp. 237–248.
[26] S. Thalabard, B. Saint-Michel, É. Herbert, F. Daviaud, and B. Dubrulle, "A statistical mechanics framework for the large-scale structure of turbulent von Kármán flows," e-print arXiv1501.01182v2 (2015).

Appendix C

New method for detecting singularities in experimental incompressible flows

New method for detecting singularities in experimental incompressible flows

Denis Kuzzay,[1,*] Ewe-Wei Saw,[1,†] Fabio J. W. A. Martins,[2] Davide Faranda,[3] Jean-Marc Foucaut,[2] F. Daviaud,[1] and Bérengère Dubrulle[1]

[1] *SPEC, CEA, CNRS, Université Paris-Saclay, CEA Saclay, 91191 Gif-sur-Yvette, France*
[2] *Laboratoire de Mécanique de Lille, France*
[3] *Laboratoire des Sciences du Climat et de l'Environnement, LSCE/IPSL, CEA-CNRS-UVSQ, Université Paris-Saclay, F-91191 Gif-sur-Yvette, France*

We introduce two new singularity detection criteria based on the work of Duchon and Robert [J. Duchon and R. Robert, Nonlinearity, 13, 249 (2000)], and Eyink [G.L. Eyink, Phys. Rev. E, 74 (2006)] which allow for the local detection of Navier-Stokes singularities in experimental flows, using classical PIV measurements. These criteria allow to detect areas in a flow where the velocity field in no more regular than Hölder continuous with some Hölder exponent $h \leqslant 1/2$. We begin by discussing the link with the Beale-Kato-Majda [J.T. Beale, T. Kato, A. Majda, Commun. Math. Phys., 94, 61 (1984)] criterion based on the blow-up of vorticity. Then, we show that in order to detect such singularities, one does not need to have access to the whole velocity field inside a volume but can instead look for them from stereoscopic particle image velocimetry (SPIV) data on a plane. We illustrate our discussion using tomographic PIV data obtained inside a high Reynolds number flow generated inside the boundary layer of a wind tunnel. In such a case, BKM and DR criteria are well correlated with each other.

I. INTRODUCTION

Viscous incompressible fluids are described by the incompressible Navier-Stokes equations (INSE)

$$\partial_t u_i + u_j \partial_j u_i = -\frac{1}{\rho}\partial_i p + \nu \partial_j \partial_j u_i + f_i \tag{1}$$

$$\partial_j u_j = 0, \tag{2}$$

where u_i is the velocity field, p the pressure field, ρ the mass density, f_i some forcing and ν the molecular viscosity. A natural control parameter for the INSE is the Reynolds number $Re = LU/\nu$, which measures the relative importance of nonlinear effects compared to the viscous ones, and is built using a characteristic length L and velocity U. The INSE are the corner stone of many physical or engineering sciences, such as astrophysics, geophysics, aeronautics and are routinely used in numerical simulations.

However, from a mathematical point of view, it is not known whether the mechanism which tends to smooth out possible irregularities in the velocity field, i.e. viscous forces, is efficient enough to constrain u_i to remain smooth at all times. In two dimensions, the existence, unicity and smoothness theorems have been known for a long time [1–4]. In three dimensions however, it is still unclear whether the INSE are a well-posed problem, i.e. whether their solutions remain regular or develop finite time, small scale singularities. This motivated their inclusion in the AMS Millennium Clay Prize list [5]. Historically, the search for singularities in the INSE was initiated by Leray [6–8] who introduced the notion of weak solutions (i.e. in the sense of distribution). This notion has since remained a framework of choice for those wishing to study their regularity. However, only partial regularity theorems have been obtained up to now. For instance, we know that contrary to Euler equations, regularity of the solutions to the INSE is ensured if the velocity field remains bounded [9–11]. Therefore, the problem of Navier-Stokes regularity is a velocity blow-up problem, and may experimentally result in a break-down of the incompressibility condition (2) [12–14]. Another well-known result about these potential singularities, is that they are very rare events: according to the Caffarelli-Kohn-Nirenberg theorem [15] the singular set has zero one-dimensional Hausdorff measure in spacetime. This means that if they exist, singularities manifest themselves by a velocity which becomes arbitrarily large at one fixed point in space, reaches infinity and immediately after becomes finite again.

In 1949, Onsager published his only paper [16, 17] in the field of turbulence. In this work, he realized that far from simply being a mathematical curiosity, the possible loss of smoothness in the velocity field could have important

*Electronic address: denis.kuzzay@cea.fr
†Electronic address: ewe-wei.saw@cea.fr

practical consequences. More precisely, he argued that if, at point $\boldsymbol{x}$, the velocity field cannot satisfy any regularity condition stronger than a Hölder condition

$$|\boldsymbol{u}(\boldsymbol{x}+\boldsymbol{r})-\boldsymbol{u}(\boldsymbol{x})| < Cr^h, \tag{3}$$

with $h \leqslant 1/3$, then energy conservation is not ensured in the limit $\nu \to 0$ because there might exist an additional energy dissipation due to this lack of smoothness, and which has nothing to do with viscosity. Let us note that Hölder continuity (3) is a weaker regularity condition than differentiability. Therefore, at first sight, it seems that Onsager's assertion concerns the blow-up of the gradient of $\boldsymbol{u}$. However, since Navier-Stokes singularities are velocity blow-ups so that Onsager's statement truly is about the blow-up of $\boldsymbol{u}$ itself.

Onsager's arguments are important for turbulence because they provide an alternative mechanism to Taylor's [18, 19] in order to explain the fact that turbulent flows dissipate energy at a rate which is independent of Re, for sufficiently large Re. In the following years, Onsager's conjecture attracted a lot of attention from mathematicians, who tried to prove that $h > 1/3$ indeed imply that energy dissipation is zero when viscosity vanishes. In 2000, Duchon and Robert derived the corresponding local energy balance in Leray's weak formalism, and were in addition able to express Onsager's dissipation in terms of velocity increments [20]. Later, Eyink used the same formalism to prove that singularities may also produce a non-zero rate of velocity circulation decay, providing another interesting signature of singularities in terms of a cascade of circulation [21–23].

These physical consequences illustrate the interest of detecting potential singularities of the INSE in order to advance our understanding of turbulence. This task is however complicated by the scarcity of the putative singularities. For example, numerical detection of singularities requires solving of the full INSE at large Reynolds numbers, for a time long enough so that singularities might develop. These two constraints actually severely limit the quest for singularities and explain why there still is no final answer about numerical detection of singularities in INSE. Part of the numerical limitations are relaxed when performing experiments with turbulent flows. Indeed, in a well-designed experiment, one can reach fairly easily large Reynolds numbers and monitor the results for a time long enough (minutes to hours) to accumulate enough statistics for reliable data analysis. In the past, experimental detection of singularities of INSE has been limited by the instrumentation, since only global (torque), or localised in space (Pitot, hot wire) or in time (slow imaging) velocity measurements were available. With the advent of modern Particle Image Velocimetry (PIV), measurements of the velocity field at several points at the same time over the decimetric to sub-millimetric size range is now available, at frequencies from 1Hz to 1kHz, reviving the interest in experimental detection of singularities of INSE. The main challenge remains to find an appropriate detection method.

Clearly, the naive method consisting in tracking the velocity field and locate areas where the velocity becomes very large is unlikely to prove successful: it would require time and space resolved measurements, localized at the place where the singularity appears. With the present technology, this means zooming over a small area of the flow (typically a few mm^2) and wait until a singularity appears. Since singularities are very scarce, there is little chance that one will be able to detect one. Moreover, if the velocity is indeed very high at this location, any neutral particle in the area will move very fast and leave the observation window in an arbitrarily small time. This is a problem for PIV or Particle Tracking Velocimetry (PTV) measurements, which are based on particle tracking. An interesting alternative is provided by multifractal analysis, which is a classical but powerful method to detect singularities based on statistical multiscale analysis. Classical reviews on the method are provided in [24, 25]. With velocity field as the input, the so-called multifractal spectrum can be obtained, quantifying the probability of observation of a singularity of scaling exponent h through the fractal dimension of its supporting set $D(h)$. This method has been applied to experimental measurements of one velocity component at a single point at high Reynolds numbers in [24], who showed that the data are compatible with the multifractal picture, with a most probable h close to $1/3$. Later Kestener et al. [25] extended the method to 3D signals (3 components of the velocity field), and showed on a numerical simulation that the picture provided by the 1D measurements was still valid, with the most probable h shifting closer to $1/3$. To our knowledge, this method has never been applied to 3D experimental data. Moreover, due to the statistical nature of the analysis, it appears difficult to obtain information regarding the possible instantaneous spatial distribution of singularities.

In the present paper, we suggest a new method to detect singularities inside experimental turbulent incompressible flows. This method is inspired from Onsager's conjecture (summarized in Sec. II A) and based directly on the energy balance derived by Duchon-Robert (DR) [20] (see Sec. II B). The idea is to track singularities through scales by detecting the energy transfers that they produce. We will use Duchon and Robert's results [20] as a criterion (hereafter referred to as DR criterion) which will tell us where to look (Sec. III). This criterion is easily implementable from now classical velocity measurements such as tomographic PIV (TPIV) or stereoscopic PIV (SPIV). Furthermore, we show that our approach provides a natural connection with the traditional cascade picture of turbulence, facilitating the interpretation of the detected singularities. We further discuss how the DR criterion compares with another well known criterion called the Beale-Kato-Majda (BKM) criterion in Sec III C. Finally, a result obtained by Eyink

[21–23], and which resembles Duchon and Robert's, will be investigated. This result concerns Kelvin's theorem (Sec. IV), and will give us indications on singularities with $h \leqslant 1/2$. Our discussion is illustrated using tomographic PIV (TPIV) data obtained inside the boundary layer of flow generated in a wind tunnel [26].

II. MATHEMATICAL TOOLS

A. Background on Onsager's conjecture

Lars Onsager was the first to make the connection between the regularity properties of the velocity field and kinetic energy conservation [17, 23]. In order to explain this, let us consider a local space averaged (low-pass filtered) velocity field. In the INSE, the unknown velocity and pressure fields contain informations about the flow at all possible scales. Let us define a coarse-grained velocity field by taking the convolution of $\boldsymbol{u}$ with some kernel G_ℓ

$$u_i^\ell(\boldsymbol{x},t) = \int d\boldsymbol{r}\; G_\ell(\boldsymbol{r})\, u_i(\boldsymbol{x}+\boldsymbol{r},t), \tag{4}$$

where G is a smooth filtering function, non-negative, spatially localized and such that $\int d\boldsymbol{r}\; G(\boldsymbol{r}) = 1$. The function G_ℓ is rescaled with ℓ as $G_\ell(\boldsymbol{r}) = \ell^{-3} G(\boldsymbol{r}/\ell)$. This process of coarse-graining thus averages out fine details about the fields while keeping informations about large scales. Let us now derive the equations satisfied by u_i^ℓ. Starting from the INSE and applying the coarse-graining procedure we get

$$\partial_t u_i^\ell + u_j^\ell \partial_j u_i^\ell = f_i^\ell - \partial_i p^\ell + \nu \partial_{jj} u_i^\ell, \tag{5}$$

$$\partial_j u_j^\ell = 0, \tag{6}$$

where $f_i^\ell = -\partial_j \tau_{ij}^\ell$ is called the turbulent force, and $\tau_{ij}^\ell = (u_i u_j)^\ell - u_i^\ell u_j^\ell$ is the subscale stress tensor. We thus obtain a sequence of equations describing the dynamics of large scales. From these equations, we can derive a local energy balance at scale ℓ

$$\partial_t E^\ell + \partial_j \mathscr{E}_\nu^{\ell,j} = -\Pi^\ell - \mathscr{D}_\nu^\ell, \tag{7}$$

where $\mathscr{E}_\nu^{\ell,j} = u_j^\ell \left(E^\ell + p^\ell\right) + u_i^\ell \tau_{ij}^\ell - \nu\left(\partial_j E^\ell + \partial_i\left(u_i^\ell u_j^\ell\right)\right)$, $E^\ell = u_i^\ell u_i^\ell/2$, $\Pi^\ell = -S_{ij}^\ell \tau_{ij}^\ell$, $\mathscr{D}_\nu^\ell = 2\nu S_{ij}^\ell S_{ij}^\ell$, and $S_{ij}^\ell = \left(\partial_i u_j^\ell + \partial_j u_i^\ell\right)/2$. Π^ℓ appears as a source term (a priori positive or negative) which stems from interactions between scales larger and smaller than ℓ. It represents the energy transfers through scale ℓ. Therefore, energy is not conserved at large scales, even for $\nu = 0$, because of the well-known energy cascade. However, if $\boldsymbol{u}$ is a smooth function, it is easy to show that τ_{ij}^ℓ vanishes as $\ell \to 0$ so that Eq. (7) gives the usual energy balance, and energy conservation is recovered for $\nu = 0$.

Onsager studied turbulence in the 1940's [16] and, during this period of time, published only one paper in this field [17]. At the end of this paper, he noted that $\nu \to 0$ does not actually ensure conservation of energy because in this limit it is possible that the velocity field does not remain smooth enough for allowing Π^ℓ to vanish as $\ell \to 0$. As explained in [23], the key realization of Onsager was that τ_{ij}^ℓ and S_{ij}^ℓ can be rewritten in terms of velocity increments as

$$\tau_{ij}^\ell = (\delta u_i \delta u_j)^\ell - \delta u_i^\ell \delta u_j^\ell, \tag{8}$$

$$S_{ij}^\ell = -\frac{1}{2\ell}\int d\boldsymbol{r}\; \partial_i G_\ell(\boldsymbol{r})\, \delta u_j(\boldsymbol{x}+\boldsymbol{r},t) + \partial_j G_\ell(\boldsymbol{r})\, \delta u_i(\boldsymbol{x}+\boldsymbol{r},t). \tag{9}$$

Hölder continuity is expressed as

$$|\boldsymbol{u}(\boldsymbol{x}+\boldsymbol{r}) - \boldsymbol{u}(\boldsymbol{x})| < C r^h, \tag{10}$$

at small scales, or equivalently

$$|\delta\boldsymbol{u}(\boldsymbol{r})| = \underset{r\to 0}{O}\left(r^h\right). \tag{11}$$

Let us now define $\delta u(\ell) \overset{def}{=} \underset{r<\ell}{sup} |\delta \boldsymbol{u}(\boldsymbol{r})|$. We directly get that

$$\Pi^\ell = \underset{\ell \to 0}{O} \left(\frac{\delta u(\ell)^3}{\ell} \right). \tag{12}$$

Therefore, if $\boldsymbol{u}$ is Hölder continuous in space with exponent h, i.e. $\delta u(\ell) \sim \ell^h$, then

$$\Pi^\ell = \underset{\ell \to 0}{O} \left(\ell^{3h-1} \right). \tag{13}$$

As a consequence, we see that if $h > 1/3$, Π^ℓ vanishes as $\ell \to 0$ and Euler equations are seen to conserve energy. On the other hand, it may well be that this condition does not hold, in which case turbulent flows might keep on dissipating energy even if $\nu = 0$. The non vanishing of the mean energy dissipation rate ϵ in the limit of arbitrarily large Re is a central assumption in the 1941 Kolmogorov's theory of turbulence (K41) [27–30]. Onsager's arguments lead to the conclusion that a necessary condition for $\epsilon \neq 0$ in inviscid turbulence is $h \leqslant 1/3$, $h = 1/3$ being the K41 case. In this case, the non-vanishing of ϵ would stem from a lack of smoothness in the velocity field, and could replace Taylor's mechanism [18, 19] for energy dissipation. As a matter of fact, there are evidences coming from DNS that a continuous set of scaling (or Hölder) exponents h are allowed, with the most probable exponent close to 1/3 [24, 25]. Therefore, such are likely to occur in real flows. Onsager's hypothesis then constitutes an interesting candidate for explaining why turbulent flows dissipate energy at a rate independent of Re at very large Re, and would allow for a deeper understanding of turbulent energy dissipation (see [23] for a more detailed discussion).

B. Inertial energy dissipation

Onsager's conjecture has been investigated by many mathematicians wishing to study the regularity of the INSE. Actually, it is possible to obtain an exact expression for Π^ℓ as $\ell \to 0$. This result was derived by Duchon and Robert [20] using Leray's weak solution formalism [7] and Onsager's ideas [17]. For this, they introduce a distribution

$$\mathscr{D}_I \overset{def}{=} -\partial_t E - \partial_j \mathscr{E}_\nu^j - \mathscr{D}_\nu, \tag{14}$$

where $\mathscr{E}_\nu^j = \mathscr{E}^j - \nu \left(\partial^j E + \partial^{ij} \left(u^i u^j \right) \right)$, $\mathscr{D}_\nu = 2\nu S_{ij} S_{ij}$, and $S_{ij} = \left(\partial_i u_j + \partial_j u_i \right)/2$ (all these terms should be understood as distributions). Then, using the filtering approach described in Sec. II A, they proceed with the derivation of an exact expression for $\mathscr{D}_I$. In the end, the following energy balance is obtained

$$\partial_t E + \partial_j \mathscr{E}_\nu^j = -\mathscr{D}_I - \mathscr{D}_\nu, \tag{15}$$

where

$$\mathscr{D}_I = \lim_{\ell \to 0} \mathscr{D}_\ell(\boldsymbol{u}) = \lim_{\ell \to 0} \frac{1}{4} \int d\boldsymbol{r}\ \boldsymbol{\nabla} G_\ell(\boldsymbol{r}) \cdot \delta \boldsymbol{u} (\delta \boldsymbol{u})^2, \tag{16}$$

does not depend on the choice of G. Onsager's assumption directly follows, and can even be weaken [20]. The key point is that in (15), $\mathscr{D}_I$ appears as the fraction of energy dissipated due to a lack of smoothness of the velocity field, and has nothing to do with viscosity. If $h = 1/3$ globally in space (like in Kolmogorov's theory), singularities dissipate energy independently from the viscosity, and we have Onsager's anomalous dissipation [17].

C. Connection with traditional turbulence notions

1. *Kármán-Howarth-Monin formula*

A corner stone of turbulence theory is provided by the Kármán-Howarth-Monin (KHM) relation [12, 31–33], valid for homogeneous turbulence, linking the energy dissipation per unit mass $\mathscr{D}$ and velocity increments via

$$\mathscr{D} = -\lim_{\ell \to 0} \frac{1}{4} \mathrm{div}_\ell \langle \delta \boldsymbol{u} (\delta \boldsymbol{u})^2 \rangle, \tag{17}$$

where $\langle \cdot \rangle$ denotes statistical averaging. The fraction of energy dissipated in singularities $\mathscr{D}_I$ (16) therefore appears as a weak formulation of the KHM relation which is valid when $\boldsymbol{u}$ is not differentiable, contrary to Eq. (17). The practical applicability of the KHM relation to turbulence relies on the fact that the statistical average of the third order structure function is smooth enough to be differentiable. If this is not the case, taking the divergence introduces noise. The weak formulation of Duchon and Robert ensures that the transfers can be computed locally and instantaneously, without introducing further noise: indeed, the derivative in scale is not applied directly to the velocity increments, but rather on the smoothing function, followed by a local angle averaging. This guarantees that no additional noise is introduced by the procedure. Even more, the noise coming from the estimate of the velocity is naturally averaged out by the angle smoothing. This makes the quantity $\mathscr{D}_I$ a very interesting tool to localize singularities in both space and time, as we discuss in Sec. III A.

2. Energy transfers

The fraction of energy dissipated in singularities $\mathscr{D}_I$ appears as the limit of a scale dependent quantity $\mathscr{D}_\ell(\boldsymbol{u})$. In their paper, Duchon and Robert prove that $\mathscr{D}_\ell$ has the same limit as $\ell \to 0$ as the classical energy transfer rate Π^ℓ, defined in Eq. (7). Moreover, they prove that at any finite ℓ, the statistical average $\langle \mathscr{D}_\ell(\boldsymbol{u}) \rangle$ coincides with the average over a ball of size ℓ of the energy dissipation per unit mass $\mathscr{D}$. We have indeed checked [34] in the case of an axisymmetric von Kármán flow that the space-time average of $\mathscr{D}_\ell$ over the whole volume of the experiment agrees with global direct torque measurements of the injected power within 2% at large Reynolds numbers, as long as the scale ℓ lies in the inertial range. The quantity $\mathscr{D}_\ell$ may therefore be interpreted as a local (in space and time) energy transfer through scale ℓ, and is related to the statistical energy dissipation rate which is at the base of the refined similarity hypothesis of Kolmogorov [12]. As long as ℓ lies in the inertial range, $\mathscr{D}_\ell$ coincides with the energy injection, while as $\ell \to 0$, it converges to the energy dissipation induced by singularities. In this picture, the classical Kolmogorov (dissipative) scale $\eta \sim Re^{-3/4}$ therefore appears as a natural border for the behavior of $\mathscr{D}_\ell(\boldsymbol{u})$

- when $\ell \geqslant \eta$, $\mathscr{D}_\ell$ describes some local energy transfers from injection scale.
- when $\ell \leqslant \eta$, $\mathscr{D}_\ell$ describes some local energy transfers towards scales smaller than the dissipative scale.

This is in agreement with the multi fractal picture of turbulence, in which a local singularity with exponent $h < 1/3$ transfers energy down to scale $\eta_h \sim Re^{-1/(1+h)} < \eta$. This kind of transfers may therefore be seen as local indicators of singularities with $h < 1/3$. Our method of detection of singularities relies on this remark. Note finally that the expression of $\mathscr{D}_\ell(\boldsymbol{u})$ is very suitable for its implementation starting from experimental PIV velocity fields: it involves only velocity increments, which are easily computed from the velocity field data obtained by such a technique.

III. SINGULARITY DETECTION THROUGH DUCHON-ROBERT FORMULA

A. Detection method

We saw in Sec. II A that if the velocity is locally characterized by a scaling exponent $h > 1/3$, then $\mathscr{D}_I = 0$. In this section, we will make use of the converse statement of this result, i.e. if locally $\mathscr{D}_I \neq 0$, then the flow in the region where this is observed is no more regular than Hölder continuous with some $h \leqslant 1/3$. If this is the case, then the velocity field is not differentiable, which necessarily comes from a blow-up of the velocity field itself [9–11]. However, there are several reasons why such singularities cannot be directly detected from experimental measurements. First of all, measurement systems inevitably have a coarsed space and time resolution while blow-ups occur instantaneously at one point [15]. Furthermore, post-processing techniques which provide the output velocity field smooth the data by performing local averages, and by considering very large velocities as spurious vectors which in the end are discarded. The key idea is therefore to track the singularities through the behaviour of $\mathscr{D}_\ell$ as one comes across the dissipative scale η. If $\mathscr{D}_\ell$ vanishes as one approaches or goes to smaller scales than η, then we have only seen local energy transfers through scales [34], which is ultimately converted into heat by viscous frictions, as in the traditional Taylor view of turbulence. If on the other hand, we see that $\mathscr{D}_\ell$ keeps a nonzero value larger than some threshold $\mathcal{Q}$, then we have detected a structure connected to a singularity with $h \leqslant 1/3$. This structure becomes fully singular in the exact limit $\ell \to 0$. Therefore, Eq. (16) will be used as a criterion (hereafter referred to as DR criterion) to detect singularity

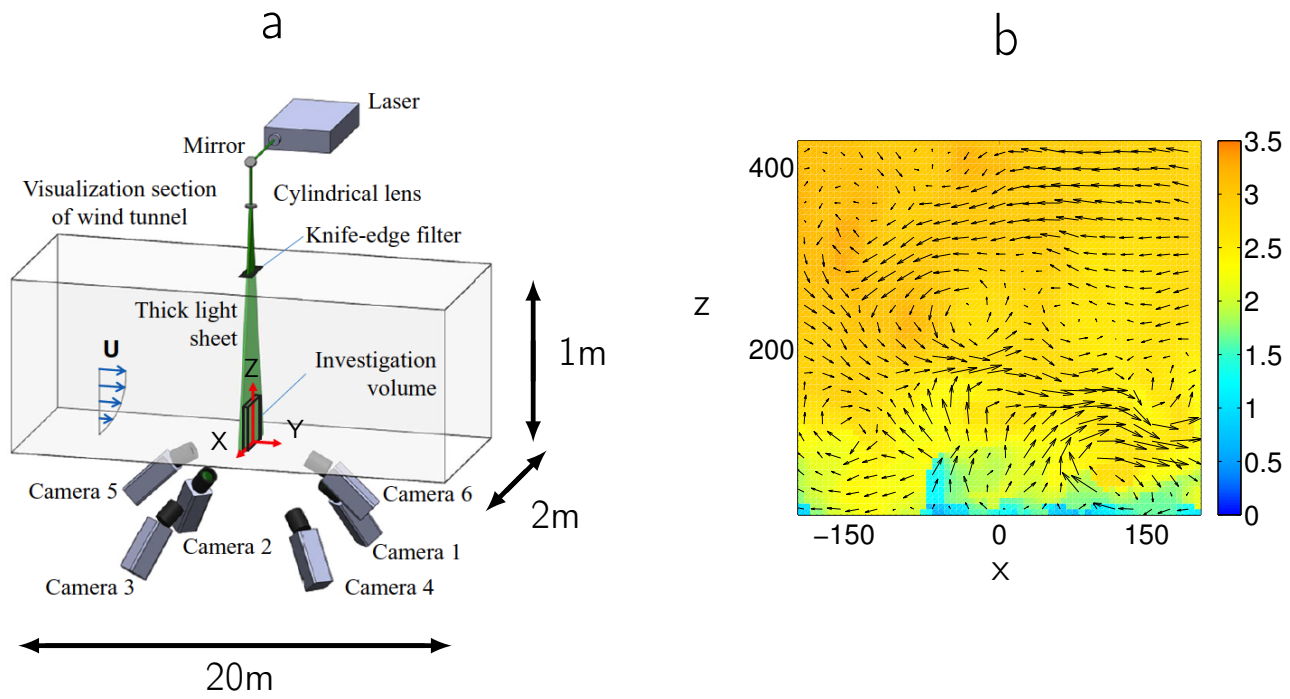

FIG. 1: (a) sketch of the experimental set-up and (b) typical instantaneous velocity field, obtained from TPIV measurements in a plane orthogonal to the mean flow. The arrows represent the in-plane component of the velocity field while the colors code the normal component.

candidates through scales. We shall call **"quasi-singularities"** structures with $h \leqslant 1/3$ located at a point where $\mathscr{D}_\ell \geqslant \mathcal{Q}$ for $0 < \ell < \eta$.
The only adjustable parameter in our detection method is the threshold $\mathcal{Q}$. A natural choice for $\mathcal{Q}$ is therefore to take

$$\mathcal{Q} = Q\overline{\mathscr{D}_\ell(\boldsymbol{u})}, \tag{18}$$

where the over line denotes spacetime averaging over the data set. That way, Q characterizes the quantile of the distribution of quasi-singularities. For example, if $Q = 10$, we select events with an amplitude 10 times over their mean. With $Q = 1000$, we select more extreme quasi-singularities, which represent in general very rare events.
In all our computations, we have used a spherically symmetric function of $\boldsymbol{r}$ given by

$$G(r) = \begin{cases} \frac{1}{N}\exp\left(-\frac{1}{1-r^2/4}\right) & \text{for } 0 \leqslant r \leqslant 1, \\ 0 & \text{otherwise,} \end{cases} \tag{19}$$

where N is a normalization constant such that $\int d\boldsymbol{r}\ G(r) = 1$. G has a compact support and satisfies the properties given in Sec. II A.

B. Implementation

We illustrate our detection method using experimental velocimetry measurements. The data are TPIV measurements performed inside a boundary layer of a wind tunnel located at the Laboratoire de Mécanique de Lille, France. A sketch of the experimental set-up is displayed in Fig. 1 along with a typical instantaneous frame in a plane orthogonal to the mean flow. The test section of the wind tunnel is 1m high, 2m wide and 20m long. The boundary layer thickness can reach up to 300mm and the Reynolds number R_θ based on the momentum thickness is $R_\theta = 8000$, with a wall region

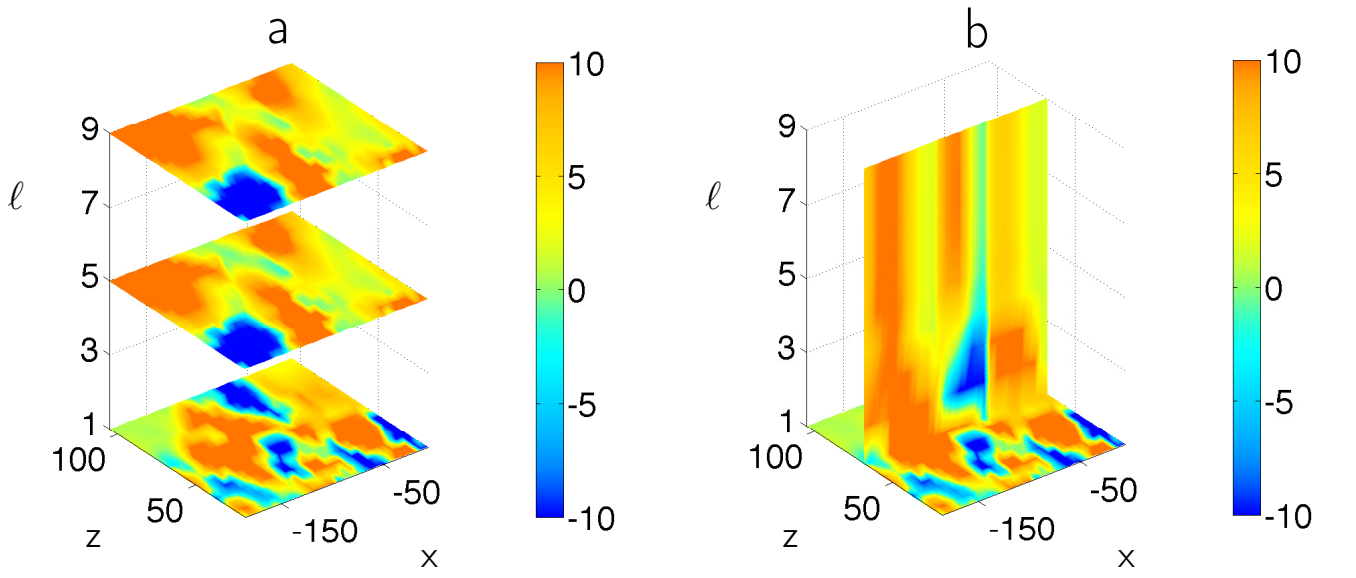

FIG. 2: Maps of the Duchon-Robert (DR) energy transfers as a function of scale ℓ. (a) map of $\mathscr{D}_\ell$ at three different scales and (b) map of $\mathscr{D}_\ell$ (normalized by their space-time averages) at different scales, along a line going through a potential singularity. The results are displayed in the plane $y = 0$ orthogonal to the streamwise direction, and the colors code $\mathscr{D}_\ell(\boldsymbol{u})$. The scale is expressed in units of the resolution scale (0.7mm).

of around 40mm. The TPIV system is composed of six high-speed cameras recording the flow into a volume normal to the wall (see Fig . 1). The investigation volume is $5 \times 45 \times 45$ mm^3 and, in the end, we get the three components of the velocity field on a grid of size $5 \times 67 \times 67$. Note that for these data, the resolution (grid spacing) is $\Delta x = 0.7$mm while the Kolmogorov scale is of the order of $\eta \approx 0.35$mm. Therefore, we will be able to test the DR criterion at scales close to the dissipative scale. More details about the experimental set-up can be found in [26].

An example of variation of $\mathscr{D}_\ell(\boldsymbol{u})/\overline{\mathscr{D}_\ell(\boldsymbol{u})}$ as a function of scale ℓ and position $\boldsymbol{x}$ in a plane orthogonal to the mean flow is provided in Fig. 2 (normalized by its space-time average). In these plots, the scale is expressed in units of the gridstep Δx. We see that for scales $\ell \gtrsim 4\Delta x$, the topology of the ratio $\mathscr{D}_\ell(\boldsymbol{u})/\overline{\mathscr{D}_\ell(\boldsymbol{u})}$ does not vary much. This is because at these scales, we are in the inertial range where the DR transfers capture the cascade of energy [34]. On the other hand, as we reach the dissipative range, i.e. $\ell \lesssim 4\Delta x$, $\mathscr{D}_\ell(\boldsymbol{u})/\overline{\mathscr{D}_\ell(\boldsymbol{u})}$ changes topology. We see that the DR transfers does not vanish, but instead remain larger than $Q = 10$ at localized areas which we identify as quasi-singularities with $h \leqslant 1/3$. It can be checked that overall, both quantities $\mathscr{D}_\ell(\boldsymbol{u})$ and $\overline{\mathscr{D}_\ell(\boldsymbol{u})}$ have an increasing magnitude as ℓ decreases, so that the energy transfers which we observe at the smallest scales in Fig. 2 are not just the fluctuations of a small quantity whose average is also very small.

C. Link with the Beale-Kato-Majda criterion

Contrary to Euler equations, the regularity of the solutions to the INSE is controlled by putting an upper bound on the norm of the velocity field [9–11]. As a consequence, our detection method based on the DR criterion is actually a detection of possible blow-ups of the velocity field. One might therefore wonder whether there are indicators of such blow-ups.

In the limit of zero viscosity, the Navier-Stokes equations become the Euler equations. In such a case, it can be proven [35] that if there exists a solution with a finite blow-up time T_*, then the vorticity $\omega(\boldsymbol{x}, t)$ satisfies

$$\int_0^{T_*} ||\omega(x,t)||_\infty dt = \infty. \tag{20}$$

Therefore, a necessary condition for the existence of singularities is the blowup of vorticity. This criterion (hereafter referred to as BKM criterion) is usually used in numerical detection of singularities in Euler equations. However, even though the authors of [35] only prove this result in the case of zero viscosity, they argue that their demonstration holds for nonzero viscosity, so that the theorem still applies to INSE. Therefore, in this section, we address the question of

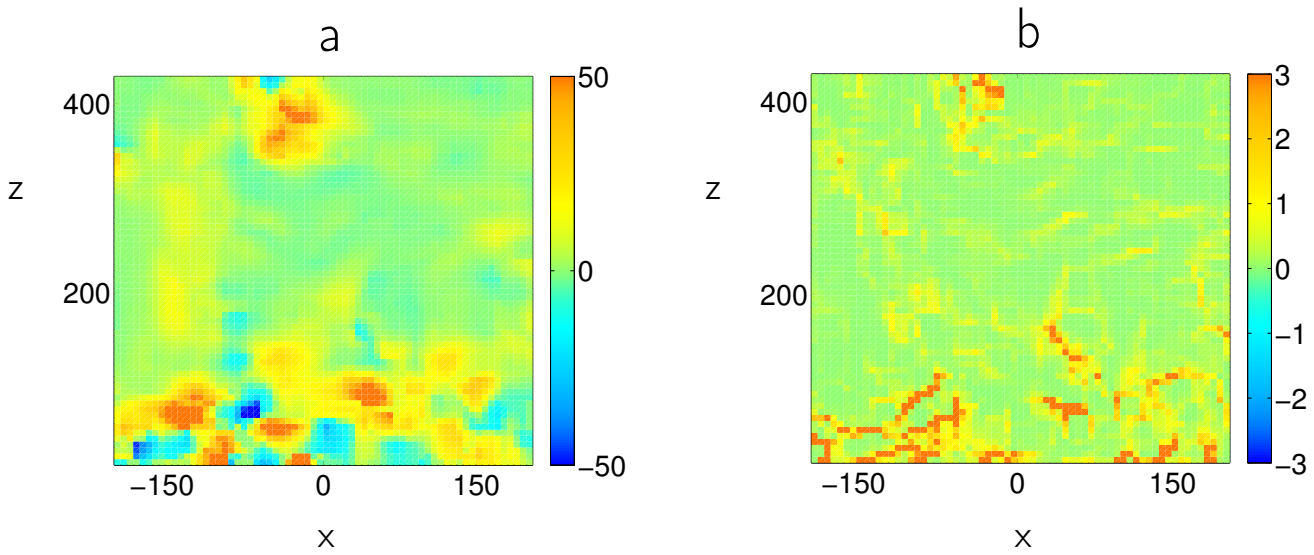

FIG. 3: Comparison between the Duchon-Robert (DR) and Beale-Kato-Majda criteria using TPIV data. (a) map of the DR energy transfers $\mathscr{D}_\ell$ and (b) map of the norm of the vorticity $|\boldsymbol{\omega}(x,z)|$ (normalized by their space-time averages) at the smallest resolved scale. The results are displayed in the plane $y=0$ orthogonal to the streamwise direction for the same data as in Fig. 2.

whether the DR and BKM criteria are correlated at large Reynolds numbers. Let us look at Fig. 3, where maps of Q and $|\boldsymbol{\omega}(x,z)|$ (normalized by its spacetime averages) are displayed.
First of all, we observe on Fig. 3b) that the vorticity is almost zero everywhere, except for some areas where vorticity is concentrated into thin filaments of high intensity which can be up to 60 times larger than its spacetime average. Moreover, comparing Fig. 3a) with Fig. 3b), it can be seen that areas where the structures of dissipation detected by the DR criterion are localized are also areas where the norm of the vorticity is high. In order to quantify how much both map are related, we compute the Pearson's coefficient R_N of linear correlation between areas where both criterion indicate quasi-singularities. We find $R_N = 0.59$, where the threshold of $Q = 10$ has been used to define quasi-singularities. Therefore, we deduce that areas of strong energy transfers in $\mathscr{D}_\ell(\boldsymbol{u})$ are well correlated with areas of strong vorticity. The BKM and DR criteria are thus in good agreement.

D. 2D vs 3D detection

In principle, our method of detection requires the input of the three components of the velocity field in a volume, i.e. requires data from TPIV. In practice, some PIV systems are only stereoscopic, giving access to the three components of the velocity field on a plane only, but allowing for very long statistics. Since velocity increments along one direction of space cannot be computed, this raises the question of whether the DR criterion is still able to detect quasi-singularities from SPIV data, or does the absence of the third direction leads to the detection of spurious structures which would disappear if the full 3D computation were to be performed. To answer this question, let us define a new quantity based on (16), which is built from the three components of the velocity increments on a two-dimensional plane

$$\mathscr{D}_I^{2D}(\boldsymbol{u}) \overset{def}{=} \lim_{\ell\to 0} \mathscr{D}_\ell^{2D}(\boldsymbol{u}) = \lim_{\ell\to 0} \frac{1}{4\ell} \int_{\mathcal{S}} d\boldsymbol{r}\ (\boldsymbol{\nabla} G_\ell)(\boldsymbol{r}) \cdot \delta^{2D}\boldsymbol{u}(\boldsymbol{r})\ |\delta^{2D}\boldsymbol{u}(\boldsymbol{r})|^2, \tag{21}$$

where $\delta^{2D}\boldsymbol{u}(\boldsymbol{r}) = \boldsymbol{u}(\boldsymbol{x}^{2D}+\boldsymbol{r}^{2D}) - \boldsymbol{u}(\boldsymbol{x}^{2D})$, $\boldsymbol{x}^{2D}$ and $\boldsymbol{r}^{2D}$ being the projection onto the plane of measurements of the 3D coordinates. We now argue that areas where $\mathscr{D}_I^{2D}(\boldsymbol{u})$ is nonzero are also areas where the full field $\mathscr{D}_I(\boldsymbol{u})$ is nonzero, thus proving that it is sufficient to look for singularities in SPIV data.
To prove this, we first consider a situation where the velocity field is regular in the direction perpendicular to the plane of measurement, that we call y. In such a case, as $\ell \to 0$ we may expand the velocity increments in Taylor series in the y-direction. Using the notations introduced in (21), we get

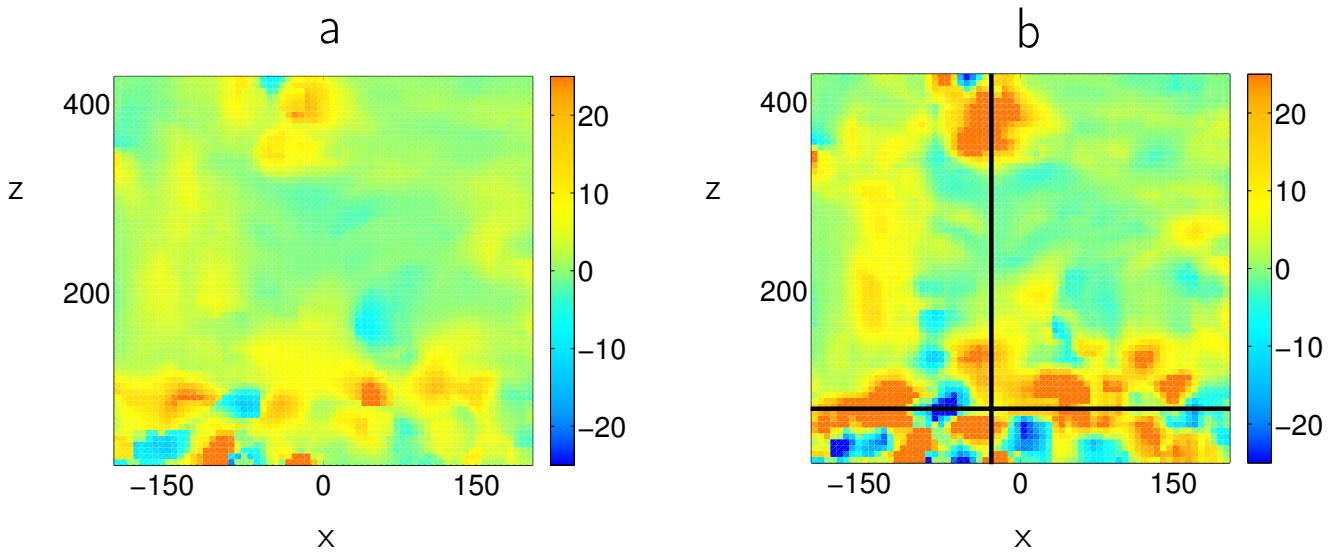

FIG. 4: Comparison between two instantaneous maps of the Duchon-Robert (DR) criterion computed from both SPIV and TPIV data. (a) map of the DR energy transfers $\mathscr{D}_\ell^{2D}$ and (b) map of the DR energy transfers $\mathscr{D}_\ell$ (normalized by their space-time averages) at the smallest resolved scale. The results are displayed in the plane $y = 0$ orthogonal to the streamwise direction for the same data as in Fig. 2. The two orthogonal lines on map (b) represent the two planar cuts displayed on Fig. 5.

$$\delta\boldsymbol{u}(\boldsymbol{r}) = \delta^{2D}\boldsymbol{u}(\boldsymbol{r}) + r_y\partial_y\boldsymbol{u} + \underset{r_y\to 0}{O}(r_y^2). \tag{22}$$

where r_y is the y-component of $\boldsymbol{r}$ and $\delta^{2D}\boldsymbol{u}(\boldsymbol{r})$ the velocity increments on the (XZ) plane. We then take the cube of this expression which leads to

$$[\delta^{2D}\boldsymbol{u}(\boldsymbol{r})]^3 = [\delta\boldsymbol{u}(\boldsymbol{r})]^3 + \underset{r_y\to 0}{O}([\delta\boldsymbol{u}(\boldsymbol{r})]^2 r_y). \tag{23}$$

As we said in section II A, $\mathscr{D}_\ell(\boldsymbol{u}) = O(\delta u(\ell)^3/\ell)$. So that if $\delta u(\ell) \sim \ell^h$, then

$$\mathscr{D}_\ell^{2D}(\boldsymbol{u}) = \mathscr{D}_\ell(\boldsymbol{u}) + \underset{\ell\to 0}{O}\left(\ell^{2h}\right), \tag{24}$$

where the first term is $O(\ell^{3h-1})$. So if the velocity field is regular with $h = 1$, then

$$\lim_{\ell\to 0}\mathscr{D}_\ell^{2D}(\boldsymbol{u}) = \lim_{\ell\to 0}\mathscr{D}_\ell(\boldsymbol{u}) = 0. \tag{25}$$

If the velocity field is singular with $h < 1$, the limit of $\mathscr{D}_\ell^{2D}(\boldsymbol{u})$ is controlled by the first term of (24) and so

$$\lim_{\ell\to 0}\mathscr{D}_\ell^{2D}(\boldsymbol{u}) = \lim_{\ell\to 0}\mathscr{D}_\ell(\boldsymbol{u}). \tag{26}$$

This means that if the flow is regular in the y direction, all areas where the flow is smooth in TPIV data is also smooth in SPIV data. Therefore, all singularities detected using SPIV measurements will correspond to singularities detected using TPIV. That is to say, computing the DR energy dissipation from SPIV measurements does not introduce any spurious structures which would disappear by performing the full 3D computation. However, we cannot detect singularities lying only on the y-direction by using SPIV data. Therefore, it is sufficient to use the criterion based on $\mathscr{D}^{2D}(\boldsymbol{u})$.

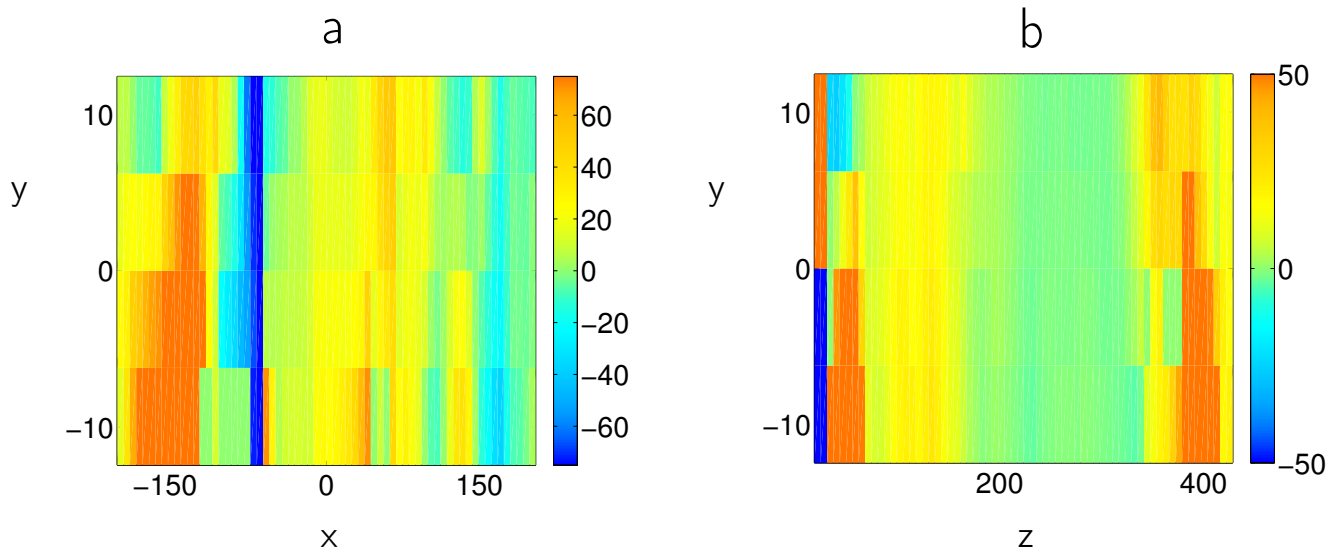

FIG. 5: Instantaneous maps of the Duchon-Robert (DR) energy transfers, in the two planes represented by black lines on Fig. 4, at the smallest resolved scale, and normalized by their space-time averages. (a) shows a planar cut in an (XY) plane and (b) shows a planar cut in a (ZY) plane for the same data as in Fig. 2. These maps allow us to see that singularities appear to have a three dimensional structure

An illustration of this result can be provided by an application to our experimental data. In such a case, there is a strong streamwise mean flow and singularities are more likely to occur in the direction orthogonal to this plane. We thus choose y as the streamwise direction and compare the DR criterion applied on SPIV and TPIV data via instantaneous maps of $\mathscr{D}_\ell^{2D}(\boldsymbol{u})$ (Fig. 4a)) and $\mathscr{D}_\ell(\boldsymbol{u})$ (Fig. 4b)) obtained from the same data as in Fig. 3. It can be seen that even though there are some differences between the two maps, both fields are qualitatively the same. This confirms what we showed previously, that all areas where $\mathscr{D}_\ell^{2D}(\boldsymbol{u}) \neq 0$ are also areas where $\mathscr{D}_\ell(\boldsymbol{u}) \neq 0$. Here again we have performed the computation of the Pearson's coefficient R of linear correlation between areas of high energy transfer in $\mathscr{D}_\ell^{2D}(\boldsymbol{u})$ and in $\mathscr{D}_\ell(\boldsymbol{u})$. We find $R = 0.92$ where the value $Q = 10$ has been kept. The two fields are very well correlated, as expected. However, if one is interested in the amount of energy dissipated on the plane of interest, taking into account increments along the streamwise direction appears necessary since the space-time averages of $\mathscr{D}_\ell^{2D}(\boldsymbol{u})$ is about 5 times larger than the space time-average of $\mathscr{D}_\ell(\boldsymbol{u})$ over the same plane. This may be due to contributions in the y direction that have not been taken into account. Indeed, the structures of energy dissipation appear stronger compared to their space-time average when increments along the streamwise direction are taken into account.

Fig. 5 displays two planar cuts at z constant (a) and x constant (b), as represented on Fig. 4b). As described in [26], the velocity field in only available in a few planes along the streamwise direction. Here, we have only access to five of them. Therefore, the resolution of the flow is not as good along the y direction as it is for x and z. However, we can see that singularities appear to have a three dimensional structure.

Let us now investigate whether the BKM and DR criteria are still in good agreement when computed from SPIV data. The maps are displayed in Fig. 6. In the case of SPIV data, the only component of the vorticity that we are able to reconstruct is the orthogonal component to the plane of measurement (here ω_y). Therefore, the question we ask is: does the link between the BKM and DR criteria still exist when using SPIV data? Or put another way, are areas of strong DR energy transfer also areas where ω_y is high? Comparing both maps on Fig. 6, there indeed seems to be a correlation between both maps. We can quantify this correlation by once again computing the correlation coefficient $R_y = 0.63$. As a consequence, the relation between the DR and BKM criteria seems to hold well for this geometry, whether for TPIV or for SPIV data. However, there is no guarantee that it is still the same in other geometries.

IV. SINGULARITY DETECTION THROUGH EYINK FORMULA

A few years after the publication of [20], Eyink noticed that singularities may also cause a breakdown of Kelvin's theorem [21–23], in the sense that in addition to a nonzero energy dissipation rate, they might also produce a nonzero rate of velocity circulation decay $\Gamma_\ell(\boldsymbol{u})$ given by

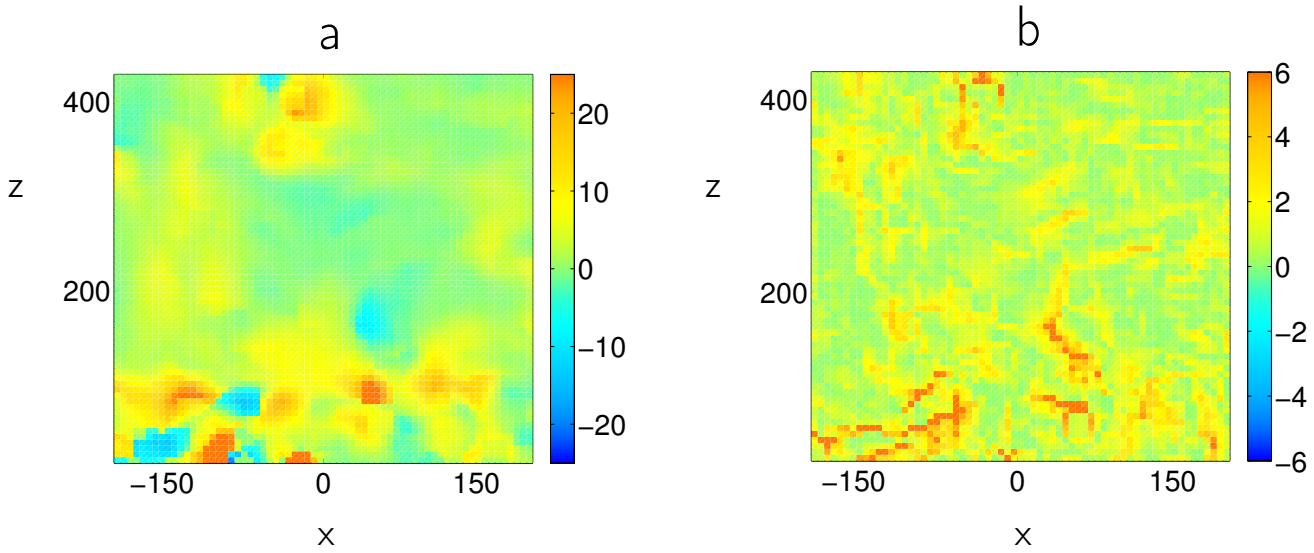

FIG. 6: Comparison between the Duchon-Robert (DR) and Beale-Kato-Majda criteria using SPIV data. (a) map of the 2D DR energy transfers $\mathscr{D}_\ell^{2D}$ and (b) map of the absolute value of the y-component of the vorticity $|\omega_y(x,z)|$ (normalized by their space-time averages) at the smallest resolved scale. The results are displayed in the plane $y=0$ orthogonal to the streamwise direction for the same data as in Fig. 2.

$$\frac{d}{dt}\Gamma_\ell(\boldsymbol{u}) = \oint_{\mathscr{C}} d\boldsymbol{s}\cdot\mathscr{F}_{\boldsymbol{\ell}}(\boldsymbol{u}), \tag{27}$$

where

$$\mathscr{F}_{\boldsymbol{\ell}}(\boldsymbol{u}) = \frac{1}{\ell}\int_{\mathcal{V}} d\boldsymbol{r}\ \left[\left(\delta\boldsymbol{u}(\boldsymbol{r}) - \int_{\mathcal{V}} d\boldsymbol{r}' G_\ell(\boldsymbol{r}')\delta\boldsymbol{u}(\boldsymbol{r}')\right)\cdot\boldsymbol{\nabla}G_\ell(\boldsymbol{r})\right]\ \delta\boldsymbol{u}(\boldsymbol{r}). \tag{28}$$

$\mathscr{C}$ being any contour advected by the fluid. $\mathscr{F}_{\boldsymbol{\ell}}(\boldsymbol{u})$ is called the turbulent vortex-force. This is an important remark since Kelvin's theorem plays an important role in Taylor's vortex stretching mechanism for energy dissipation [18, 19, 23].

A. Detection method

We saw in section II and III that the velocity field $\boldsymbol{u}$ of a flow might develop singularities due to some internal mechanisms of the INSE which are not fully understood. At the points in spacetime where this happens, $\boldsymbol{u}$ might however satisfy some Hölder continuity property with exponent h. At points where $h > 1/3$, no additional dissipation to viscosity occurs according to Onsager's arguments. However, if $h \leqslant 1/3$ an additional energy dissipation (or production) might appear [20, 23] causing kinetic energy to cascade through scales. Our detection method introduced in section III is based on the computation of this additional term to the energy balance and then track areas where it does not vanish with decreasing scale.

We introduce now a very similar detection method which is based on the observation that the turbulent vortex-force in (28) satisfies $\mathscr{F}_\ell(\boldsymbol{u}) = O(\delta u(\ell)^2/\ell) = O(\ell^{2h-1})$ if $\delta u(\ell) \sim \ell^h$ in the small scale limit, as discussed in [21–23]. Therefore, the computation of the turbulent vortex-force allows us to track singularities where $h \leqslant 1/2$, whereas the DR criterion only allows us to track the ones with $h \leqslant 1/3$. Moreover, just as for the DR term (16), this computation only involves velocity increments, which are easily accessible via PIV measurements. For the same reason mentioned in section III A, a detection criterion based on circulation production is only a necessary but not sufficient one (since our PIV set-up is not space resolved). Keeping the same test function G as in (19), we can implement a detection method very similar to the one described in section III, but based on another cascading quantity. Therefore, two questions arise. Starting from our TPIV data and computing maps of $\mathscr{D}_\ell(\boldsymbol{u})$ and $\frac{d}{dt}\Gamma_\ell(\boldsymbol{u})$, are intense events in both

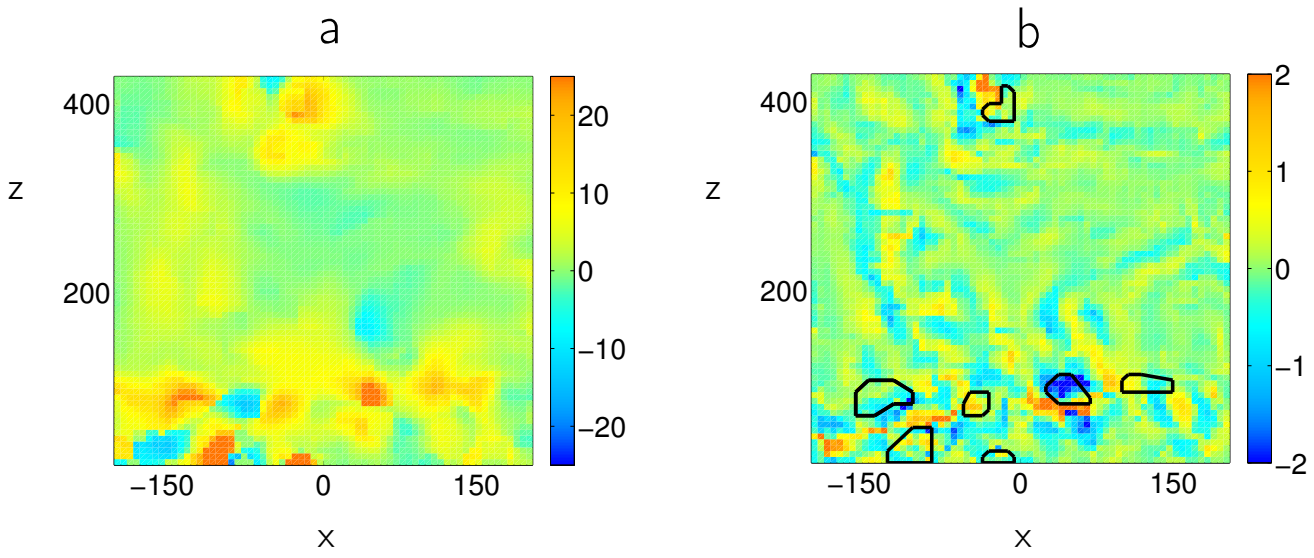

FIG. 7: Comparison between the Duchon-Robert (DR) and Eyink criteria using SPIV data. (a) map of the DR energy transfers $\mathscr{D}_\ell$ and (b) map of the velocity circulation production $\frac{d}{dt}\Gamma_\ell(\boldsymbol{u})$ (normalized by their space-time averages) at the smallest resolution scale accessbile. The results are displayed in the plane $y = 0$ orthogonal to the streamwise direction, and for the same data as in Fig. 2. For easier comparison, we have reported on the circulation map the contours of the areas where the DR dissipation is larger than 15 times its space-time average. We observe intense events in both maps.

cases well correlated? And, are we able to detect areas where a strong circulation production is observed while the DR term is weak? This would mean the detection of potential singularities with $1/3 < h \leqslant 1/2$.

B. Implementation of the method

The arguments which have been made in section III D to show that it is enough to look for singularities from SPIV via energy transfers can be once again made here. Therefore, in the following, we will focus on SPIV data.
Let us first compare maps of $\mathscr{D}_\ell(\boldsymbol{u})$ and $\frac{d}{dt}\Gamma_\ell(\boldsymbol{u})$ in order to answer the first question. On Fig. 7 are displayed maps of these two quantities (normalized by their space-time averages) for the same data set as in Fig. 4a).
First of all, it can be observed that areas where $\frac{d}{dt}\Gamma_\ell(\boldsymbol{u})$ is nonzero are organized as very thin filaments. Therefore, Fig. 7b) is more noisy than Fig. 7a) even though the same procedure is applied in both cases, i.e. a derivative in scale is applied on the smoothing function, followed by a local angle averaging. There is some correlation between the maps: in areas where the dissipation is strong, there always is some nonzero circulation. However, we observe that regions of largest rate of circulation are either shifted with respect to areas of strong dissipation, or exist in some areas where there is little dissipation (see contours on Fig. 7b)). Overall, the Pearson's coefficient of linear correlation R_Γ between regions of strong events in both fields is $R_\Gamma = 0.40$. This is consistent with the existence of singularities with local exponent $1/3 < h \leqslant 1/2$ that contribute mildly (or not all al) to the dissipation, but strongly to the circulation. Note that on Fig. 7b), areas of strong circulation production do not exceed ten times their space-time averages. Looking at other maps of $\frac{d}{dt}\Gamma_\ell(\boldsymbol{u})$, it seems to be a general observation that while $\mathscr{D}_\ell(\boldsymbol{u})$ can reach values up to 100 times its space-time average, intense events of $\frac{d}{dt}\Gamma_\ell(\boldsymbol{u})$ are weaker compared to their own space-time average. Therefore, the threshold we chose here to define "intense events" has been reduced to five times the space-time average. In addition, the fact that the maps of circulation are more noisy than the maps of dissipation renders their use less straightforward to detect singularities.

V. DISCUSSION

In this paper, we have introduced two new methods based on the work of Duchon, Robert and Eyink [20–23], which allow for the local detection of singularities in experimental flows. Both criteria assume the knowledge of spatial velocity increments only and are therefore easy to implement experimentally as well as numerically. The key idea

behind their implementation is that velocity field in turbulent flows might satisfy Hölder continuity conditions with an exponent $h \leqslant 1$ in the limit of small scales. If $h \leqslant 1/2$, a cascade of circulation might occur and Kelvin theorem breaks down. This cascade can be detected at larger scales provided that we are in the inertial range. In the same way, if $h \leqslant 1/3$, then a cascade of energy might occur which can also be detected in the inertial range. The first criterion that we introduced (DR criterion) focuses on these energy transfers.

Since Navier-Stokes singularities concern the blow-up of the velocity field, we compared the DR criterion to the well known Beale-Kato-Majda (BKM) criterion [35]. We found a good agreement between them, whether SPIV or TPIV data sets are considered.

We also showed analytically that to detect singularities, one does not need to have access to the whole velocity field inside a volume, but can instead look for them from stereoscopic particle image velocimetry (SPIV) data on a plane. This is confirmed by performing both 2D and 3D computations and comparing maps of the DR term $\mathscr{D}_\ell(\boldsymbol{u})$. In our case, the PIV data came from the measurements of the velocity field inside the boundary layer of a wind tunnel [26]. Clearly, being limited to SPIV data means the informations along a third direction are lacking meaning that singularities which only lies in this third direction cannot be detected. In this flow, we observe that the computation of the DR term actually shows areas where it is nonzero, some of them being characterized by very strong (extreme) energy transfers through scales.

Finally, we investigated a second new method for the detection of singularities based on the possibility of a breakdown of Kelvin theorem at very large Reynolds numbers [21–23]. We showed that this method seems correlated with the DR criterion even though areas of intense energy transfers are sometimes shifted compared to areas of high rate of circulation. However, due to higher noise, this method is less reliable than the DR method, but it may allow for the detection of a wider range of singularities.

In the present paper, our detection methods were applied inside a boundary layer geometry, the resolution of our data being close to, but not exactly reaching, the dissipative scale. The fact that we detect areas with negative $\mathscr{D}_\ell$ suggests that we observe energy transfers through scales [34], but not dissipation due to singularities. This is a strong indication that the Kolmogorov scale η is not the smallest relevant scale for energy dissipation and that there might actually exist smaller scales at which dissipation takes place, as suggested in the multifractal picture of turbulence. Therefore, we cannot yet conclude on the existence of singularities in experimental flows. This would require measurements with a resolution high enough to consider that the condition $\ell \to 0$ is experimentally satisfied with good approximation. This is still a challenge in measurement science. However, the results we showed are very promising, and applying our detection methods to other types of geometries with increased resolution to check whether the structures as well as the correlations we detect still exist appears to be the next step. We hope our work will help providing experimental constraints on the properties of Navier-Stokes singularities as well as on corresponding suitable weak solutions.

[1] J.L. Lions and G. Prodi. Un théorème d'existence et d'unicité dans les équations de navier-stokes en dimension 2. *Comptes rendus de l'Académie des Sciences*, 248:3519–3521, 1959.

[2] J.L. Lions. *Quelques Méthodes de Résolution des Problèmes aux Limites Non Linéaires*. 1969.

[3] O. A. Ladyzhenskaya. *The Mathematical Theory of Viscous Incompressible Flow*, volume 2 of *Mathematics and Its Applications*. Gordon and Breach, second edition, 1969.

[4] Y. Giga. Weak and strong solutions of the navier-stokes initial value problem. *Publications of the Research Institute for Mathematical Sciences*, 19:887–910, 1983.

[5] C.L. Fefferman. Existence and smoothness of the navier-stokes equation. The Millennium Prize Problems, 2006.

[6] J. Leray. Etude de diverses équations intégrales nonlinéaires et de quelques problèmes que pose l'hydrodynamique. *Journal de Mathématiques Pures et Appliquées*, 12(9):1–82, 1933.

[7] J. Leray. Sur le mouvement d'un liquide visqueux emplissant l'espace. *Acta Mathematica*, 63(1):193–248, July 1934.

[8] J. Leray. Essai sur les mouvements plans d'un liquide visqueux que limitent des parois. *Journal de Mathématiques Pures et Appliquées*, 13(9):331–418, 1934.

[9] J. Serrin. On the interior regularity of weak solutions of the Navier-Stokes equations. *Archive for Rational Mechanics and Analysis*, 9:187–195, January 1962.

[10] L. Escauriaza, G.A. Seregin, and V. Sverak. $l_{3,\infty}$ -solutions of the navier-stokes equations and backward uniqueness. *Russian Mathematical Surveys*, 58(2):211, 2003.

[11] P. Constantin. Euler and navier-stokes equations. *Publicacions Matemàtiques*, 52(2):235–265, 2008.

[12] U. Frisch. *Turbulence*. Cambridge University Press, 1995.

[13] P. Constantin and C. Fefferman. Scaling exponents in fluid turbulence: some analytic results. *Nonlinearity*, 7:41–57, January 1994.

[14] P. Constantin. Geometric statistics in turbulence. *SIAM Review*, 36(1):73–98, 1994.

[15] L. Caffarelli, R. Kohn, and L. Nirenberg. Partial regularity of suitable weak solutions of the Navier-Stokes equations. *Communications in Pure Applied Mathematics*, 35:771–831, November 1982.

[16] G. L. Eyink and K. R. Sreenivasan. Onsager and the theory of hydrodynamic turbulence. *Reviews of Modern Physics*, 78:87–135, January 2006.

[17] L. Onsager. Statistical hydrodynamics. *Nuovo Cimento (Suppl.)*, 6:279–287, 1949.

[18] G. I. Taylor and A. E. Green. Mechanism of the Production of Small Eddies from Large Ones. *Proceedings of the Royal Society of London Series A*, 158:499–521, February 1937.

[19] G. I. Taylor. Production and Dissipation of Vorticity in a Turbulent Fluid. *Proceedings of the Royal Society of London Series A*, 164:15–23, January 1938.

[20] J. Duchon and R. Robert. Inertial energy dissipation for weak solutions of incompressible Euler and Navier-Stokes equations. *Nonlinearity*, 13:249–255, January 2000.

[21] S. Chen, G. L. Eyink, M. Wan, and Z. Xiao. Is the Kelvin Theorem Valid for High Reynolds Number Turbulence? *Physical Review Letters*, 97(14):144505, October 2006.

[22] G. Eyink and H. Aluie. The Cascade of Circulations in Fluid Turbulence. In *APS Division of Fluid Dynamics Meeting Abstracts*, November 2006.

[23] G. L. Eyink. Dissipative anomalies in singular Euler flows. *Physica D Nonlinear Phenomena*, 237:1956–1968, August 2008.

[24] J. F. Muzy, E. Bacry, and A. Arneodo. Wavelets and multifractal formalism for singular signals: Application to turbulence data. *Physical Review Letters*, 67:3515–3518, 1991.

[25] P. Kestener and A. Arneodo. Generalizing the Wavelet-Based Multifractal Formalism to Random Vector Fields: Application to Three-Dimensional Turbulence Velocity and Vorticity Data. *Physical Review Letters*, 93(4):044501, July 2004.

[26] F.J.W.A. Martins, J.-M. Foucaut, L. Thomas, L.F.A. Azevedo, and M. Stanislas. Volume reconstruction optimization for tomo-piv algorithms applied to experimental data. *Measurement Science and Technology*, 26, 2015.

[27] A. N. Kolmogorov. The local structure of turbulence in incompressible viscous fluid for very large reynolds number. *Akademiia Nauk SSSR Doklady*, 30:9–13, 1941.

[28] A. N. Kolmogorov. On the degenreration of isotropic turbulence in an incompressible viscous fluid. *Akademiia Nauk SSSR Doklady*, 32:16–18, 1941.

[29] A. N. Kolmogorov. Dissipation of Energy in Locally Isotropic Turbulence. *Akademiia Nauk SSSR Doklady*, 32:16–18, 1941.

[30] A. N. Kolmogorov. On the logarithmically normal law of distibution of the size of particles under pulverization. *Akademiia Nauk SSSR Doklady*, 31:99–101, 1941.

[31] T. de Karman and L. Howarth. On the Statistical Theory of Isotropic Turbulence. *Proceedings of the Royal Society of London Series A*, 164:192–215, January 1938.

[32] A. S. Monin. The Theory of Locally Isotropic Turbulence. *Soviet Physics Doklady*, 4:271, October 1959.

[33] A. S. Monin and A. M. Yaglom. *Statistical Fluid Mechanics*, volume 2. J. Lumley, MIT Press, Cambridge, MA, 1975.

[34] D. Kuzzay, D. Faranda, and B. Dubrulle. Global vs local energy dissipation: The energy cycle of the turbulent von Kármán flow. *Physics of Fluids*, 27(7):075105, July 2015.

[35] J. T. Beale, T. Kato, and A. Majda. Remarks on the breakdown of smooth solutions for the 3- D Euler equations. *Communications in Mathematical Physics*, 94:61–66, March 1984.

Appendix D

Experimental characterization of extreme events of inertial dissipation in a turbulent swirling flow

nature COMMUNICATIONS

ARTICLE

Received 12 May 2016 | Accepted 6 Jul 2016 | Published 31 Aug 2016

DOI: 10.1038/ncomms12466 OPEN

Experimental characterization of extreme events of inertial dissipation in a turbulent swirling flow

E.-W. Saw[1], D. Kuzzay[1], D. Faranda[1,2], A. Guittonneau[1,3], F. Daviaud[1], C. Wiertel-Gasquet[1], V. Padilla[1] & B. Dubrulle[1]

The three-dimensional incompressible Navier–Stokes equations, which describe the motion of many fluids, are the cornerstones of many physical and engineering sciences. However, it is still unclear whether they are mathematically well posed, that is, whether their solutions remain regular over time or develop singularities. Even though it was shown that singularities, if exist, could only be rare events, they may induce additional energy dissipation by inertial means. Here, using measurements at the dissipative scale of an axisymmetric turbulent flow, we report estimates of such inertial energy dissipation and identify local events of extreme values. We characterize the topology of these extreme events and identify several main types. Most of them appear as fronts separating regions of distinct velocities, whereas events corresponding to focusing spirals, jets and cusps are also found. Our results highlight the non-triviality of turbulent flows at sub-Kolmogorov scales as possible footprints of singularities of the Navier–Stokes equation.

[1] SPEC, CEA, CNRS, Université Paris Saclay, CEA Saclay, 91191 Gif-sur-Yvette, France. [2] LSCE, IPSL, CEA-CNRS-UVSQ, Université Paris-Saclay, 91191 Gif-sur-Yvette, France. [3] ENS Lyon, 46 Allée d'Italie, F-69007 Lyon, France. Correspondence and requests for materials should be addressed to B.D. (email: berengere.dubrulle@cea.fr).

About 500 years ago, Leonardo Da Vinci published what appears to be one of the first detailed experimental account of vortices in water. It then took three centuries to establish the fundamental equations describing the dynamics of water, now known as the incompressible Navier–Stokes equations (INSE):

$$\partial_t \mathbf{u} + (\mathbf{u}\cdot\nabla)\mathbf{u} = -\nabla P + \nu\Delta\mathbf{u} + \mathbf{f}, \quad (1)$$

$$\nabla\cdot\mathbf{u} = 0, \quad (2)$$

where $\mathbf{u}$ is the d-dimensional velocity field, P the kinematic pressure, $\mathbf{f}$ a forcing and ν the kinematic viscosity. A natural control parameter of the INSE is the Reynolds number $Re = UL/\nu$, built using a characteristic length L and velocity U. The INSE are the cornerstones of many physical and engineering sciences, and are routinely used in numerical simulations[1–4]. From a mathematical point of view, however, it is still unclear whether the INSE are a well-posed problem in three dimensions, that is, whether their solutions remain regular over sufficient large time or develop singularities. This motivated their inclusion in the AMS Clay Millennium Prize list[5].

Historically, the search for singularities in INSE was initiated by Leray[6] who introduced the notion of weak solutions (that is, in the sense of distribution). This notion was used to prove that the mathematical singular set has a one-dimensional Haussdorff measure equals to zero in spacetime[7,8]. Therefore, if these singularities exist, they must be extremely localized events in space and time. This makes their direct detection an outstanding problem. For some times, the best evidence of their existence was provided by the observation that the energy dissipation rate in turbulent flows tends to a constant at large Reynolds numbers[9]. This observation is at the core of the 1941 Kolmogorov theory of turbulence[10] and was interpreted by Onsager[11] as the signature of singularities with local scaling exponent $h = 1/3$. Later, it was conjectured[12] that the singularities are organized into a multifractal set. Analysis of measurements of three-dimensional numerical or one-dimensional experimental velocity fields showed that the data are compatible with the multifractal picture, with a most probable h close to 1/3 (refs 13,14). However, this analysis could not reveal any information on the space-time statistics of possible singularities.

A major breakthrough was achieved when Duchon and Robert[15] derived a detailed energy balance for weak solutions of INSE and computed the contribution stemming from an eventual lack of smoothness. They show that it can be lumped into a single term $D(\mathbf{u})$, which quantifies the 'inertial' energy dissipation, that is, the energy dissipated by non-viscous means. They define dissipative weak solutions of Navier–Stokes equations as those with $D(\mathbf{u})\geq 0$, the equality being only achieved for smooth-enough solutions (corresponding to a local scaling exponent $h > 1/3$). Later, Eyink[16] proved the existence of a like-wise non-zero rate of velocity circulation decay $\frac{d}{dt}\Gamma(\mathbf{u})$, produced by singularities. These mathematical results are obtained in the limit of vanishing spatial scales, so that their direct application to experimental or numerical flows is problematic. In such cases, one can only expect to be able to measure coarse-grained quantities, $D_\ell(\mathbf{u})$ and $\frac{d}{dt}\Gamma_\ell(\mathbf{u})$, at a scale ℓ dictated by experimental or numerical constraints[17]. In that respect, a special role is played by the so-called dissipative scale $\ell = \eta$, as it is traditionally expected to be the scale at which all injected energy is converted into viscous dissipation, and the flow is regularized by viscosity. For example, it is at this scale that numerical simulations are usually truncated, or experimental velocity gradients estimated. On the road to the mathematical limit $\ell \to 0$, it seems interesting to study the properties of $D_\ell(\mathbf{u})$ and $\frac{d}{dt}\Gamma_\ell(\mathbf{u})$ down to the dissipative scale.

The purpose of the present study is to use high spatial resolution measurements of the velocity field in experiments of turbulent swirling flow (see 'Methods' for more on this choice) to compute $D_\ell(\mathbf{u})$ and $\frac{d}{dt}\Gamma_\ell(\mathbf{u})$ down to dissipative scales. We show that they are very intermittent in space and time, and provide the first experimental attempt at characterization of isolated extreme events of inertial dissipation. By characterizing the local topology of these events, we find that most of them appear as fronts separating regions of distinct velocities, whereas some correspond to focusing spirals, jets and cusps. Our results highlight the non-triviality of turbulent flows at sub-Kolmogorov scales as possible footprints of singularities of the Navier–Stokes equation.

Results

Relevant hydrodynamic parameters in von Kármán swirling flows. Details on the setup can be found in the Methods section. We vary the rotating frequency (F) of the impellers that drive the flow and use different mixture of glycerol/water, to vary the viscosity of the working fluid, and thus the Reynolds number $Re = 2\pi FR^2/\nu$, (where R is the radius of the impellers). Monitoring the torques C_1 and C_2 applied to each impeller, we obtain the energy injection rate (per unit mass of fluid) as:

$$\epsilon = \frac{2\pi F(C_1 + C_2)}{\rho\pi HR^2}. \quad (3)$$

where ρ is the fluid's mass density and H the distance between the impellers. From this, we can compute the Kolmogorov dissipative scale as $\eta = (\nu^3/\epsilon)^{1/4}$.

In a statistically stationary regime, the energy input must balance the rate of energy dissipated within the flow. This has been checked in a scale 4:1 version of our experiment in Helium, using precise calorimetric measurements[18]. Previous global dissipation measurements have shown that the dimensionless energy dissipation rate saturates at large Re towards a value that depends on the impellers and the mean flow geometry[19] (more details in Supplementary Note 1). This property allows us to determine the threshold for the onset of fully developed turbulence as $Re \approx 3{,}500$. This also corresponds to the threshold where non-dimensional velocity fluctuations become independent of the Reynolds number[20].

Here we present three cases of the experiments. Case A: 100% glycerol, where the flow is laminar; Case B: 59% glycerol by volume in water, where the flow is fully turbulent; and Case C:

Table 1 | Parameter space describing the 3 cases considered in this paper.

Case	F (Hz)	Re	η (mm)	δx (mm)	ϵ_1	$\langle D^{\nu}_{\delta x}\rangle$	$\langle D_{\delta x}\rangle$
A	2	149	4.3	3.4	0.088	0.007	<0.0001
B	1.2	6×10^3	0.32	0.24	0.049	0.07	0.007
C	5	3×10^5	0.02	0.24	0.046	0.008	0.03

δx is the grid spacing of our measurements and ϵ_1 is the dimensionless injected power (in units of $R^2(2\pi F)^3$), averaged over the whole volume of the experiment, measured using torque meter. $\langle D^{\nu}_{\delta x}\rangle$ is the space-time average of the viscous dissipation measured from stereoscopic particle image velocimetry system data in a region of 4×4 cm^2 localized at the centre of our experiment and $\langle D_{\delta x}\rangle$ is the dimensionless space-time average of the inertial dissipation in the same region (all in units of $R^2(2\pi F)^3$).

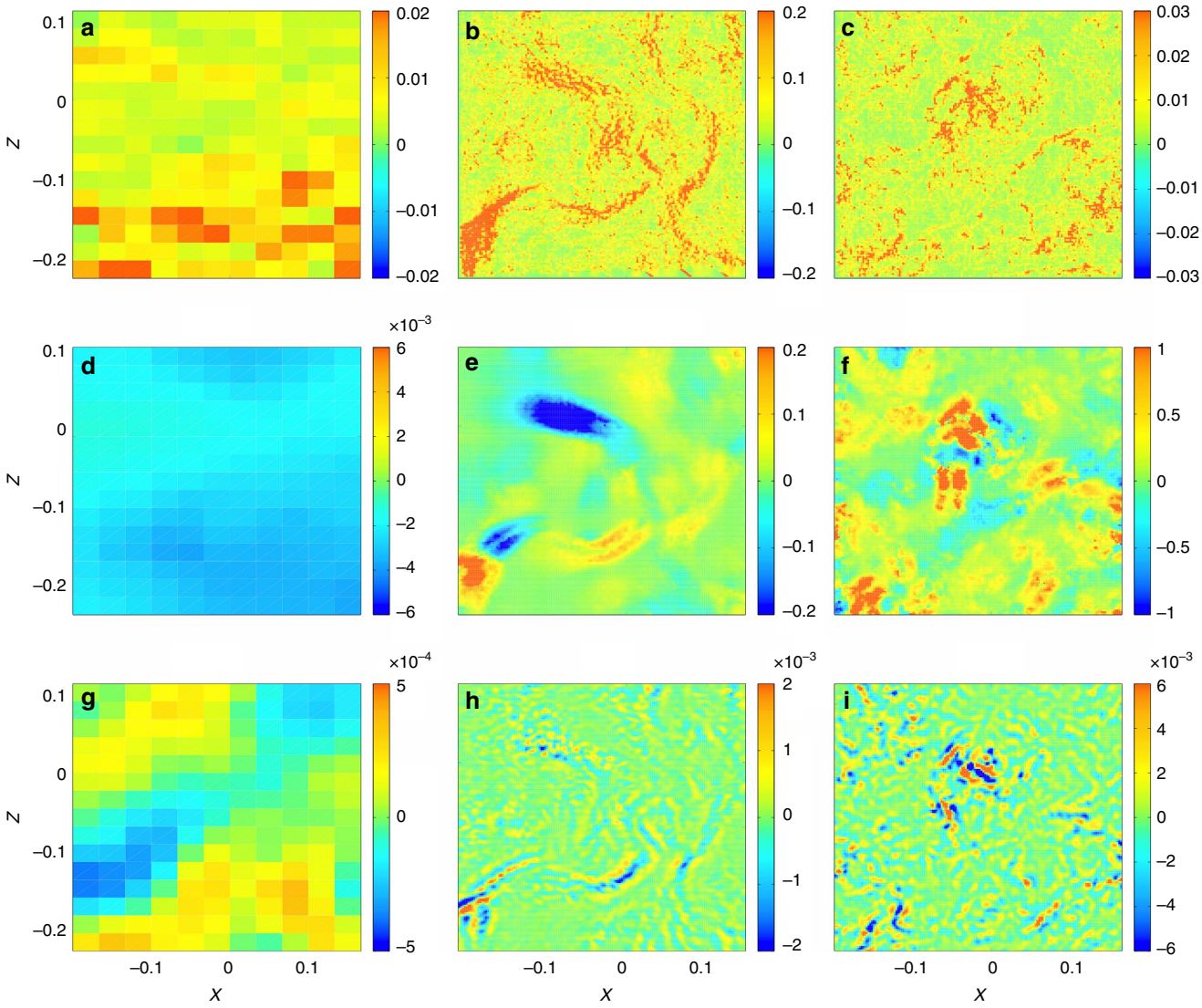

Figure 1 | Coarse-grained energy dissipation and velocity circulation decay. Maps of the coarse-grained viscous energy dissipation $D^{\nu}_{\delta x}(\mathbf{u})$ (**a** to **c**), the coarse-grained inertial energy dissipation $D_{\delta x}(\mathrm{u})$ (**d**–**f**) and the coarse-grained rate of velocity circulation decay $\frac{d}{dt}\Gamma_{\delta x}(\mathrm{u})$ (**g**–**i**) for the three cases described in Table 1. Figures for case A are on the left panels (**a**,**d**,**g**), B on the middle panels (**b**,**e**,**h**) and C on the right panels (**c**,**f**,**i**). All the quantities have been made dimensionless using the radius R of the cylinder and the angular velocity $(2\pi F)^{-1}$ of the impellers as units of length and time. We observe that the inertial dissipation remains strong in case B and C. (**g**–**i**) A non-zero circulation rate persists down to the dissipative scale. Finally, areas of high viscous dissipation seem correlated with the location of extreme events of inertial dissipation.

pure water (0% glycerol), where the flow is also fully turbulent. Table 1 lists the various parameters of the cases.

Velocity measurements and average quantities. Local velocity measurements are performed with a stereoscopic particle image velocimetry system (SPIV), providing the radial, axial and azimuthal velocity components on a meridional plane of the flow through a time series of 30,000 independent time samples. In the sequel, we work with dimensionless quantities, using R as the unit of length, and $(2\pi F)^{-1}$ as the unit of time. As shown in Kuzzay *et al.*[17], SPIV data are sufficient to detect events where $D_{\ell}(\mathbf{u})$ takes extreme values. Essentially, it was shown, through mathematical considerations and application on experimental data that SPIV is able to detect extreme events that have components intercepting the measurement plane, and that any such events detected via SPIV is also present when volumetric three-dimensional data are considered[17]. The detection method is based on evaluating two functions of $\delta\mathbf{u}(\ell)$, the velocity increment over a distance ℓ: (i) the inertial (non-viscous) energy dissipation rate $D_{\ell}(\mathbf{u})$ and (ii) the local circulation production rate $\frac{d}{dt}\Gamma_{\ell}(\mathbf{u})$ (see 'Methods' for detailed expression). If these events are connected to singularities in the flow, they can be characterized by a local exponent $h<1$ via $\delta\mathrm{u}\sim\ell^{h}$; these two functions should behave in the limit $\ell\to 0$ like $D_{\ell}(\mathbf{u}) = O(\ell^{3h-1})$ and $\frac{d}{dt}\Gamma_{\ell}(\mathbf{u}) = O(\ell^{2h-1})$ (see refs 11,16). Previous studies based on multifractal analysis indicate that the most probable exponent is close to $h=1/3$ (ref. 13). This corresponds to a constant bound for $D_{\ell}(\mathbf{u})$ as $Re\to\infty$. On the other hand, for stronger events with $h<1/3$, both $D_{\ell}(\mathbf{u})$ and $\frac{d}{dt}\Gamma_{\ell}(\mathbf{u})$ may diverge at small scales. Formally, the spatial resolution of PIV measurement is twice the grid spacing δx, which depends on the cameras resolution, the field of view and the size of the windows used for velocity reconstruction. In the sequel, we use 2 M-pixel cameras and two different zooms, to get measurements at $\delta x = 3.4$ mm, for a field of view covering the whole

experimental setup obtained through 32×32 pixel windows and $\delta x = 0.24$ mm for a field of view zoomed on a $4 \times 4\,\mathrm{cm}^2$ zone at the centre of the experiment, and reconstructed with 16×16 pixel windows. Table 1 summarizes the parameters corresponding to the three different cases. We see that the dissipative scale η is resolved for case A and B, but not for case C.

Energy dissipation and circulation production rates. To study the influence of the Reynolds number and to understand how the dissipated power is split between normal (viscous) and the estimates of inertial dissipation at various scales, we have computed the local viscous dissipation $D^{\nu}_{\delta x}(\mathbf{u})$, estimates of the inertial dissipation $D_{\delta x}(\mathbf{u})$ and the circulation production rate $\frac{d}{dt}\Gamma_{\delta x}(\mathbf{u})$ predicted by Eyink and Sreenivasan[21], at the resolution scale of our PIV system. Maps of these three quantities for instantaneous sets of data are displayed in Fig. 1 for a region of size $4 \times 3\,\mathrm{cm}^2$ located at the centre of our flow. All three cases described in Table 1 have been studied. For the three of them, we observe a smaller noise in the estimate of $D_{\delta x}(\mathbf{u})$ compared with $D^{\nu}_{\delta x}(\mathbf{u})$. As argued in Kuzzay *et al.*[17], this is due to the inherent smoothing procedure in the expression of $D_{\ell}(\mathbf{u})$.

As can be seen from Fig. 1, $D_{\delta x}(\mathbf{u})$ detects clear dissipation structures when the flow is fully turbulent and all scales down to the Kolmogorov scale are resolved (case B). One observes that the local inertial dissipation can be positive or negative, but on time average remains positive as reported in Table 1. This peculiar feature is parallel to the behaviour of entropy in non-equilibrium systems, where the entropy production can be positive or negative, but remains positive on time average, in accordance with generalized fluctuation–dissipation theorems[22–24]. The dissipation can also be locally very strong, sometimes over three orders of magnitude larger than the average injected power. The resulting distribution of dissipation intensity is strongly non-Gaussian, with very large tails (see Fig. 2).

Comparing with instantaneous maps of $\frac{d}{dt}\Gamma_{\ell}(\mathbf{u})$ at the same scale, we see that besides areas of large dissipation, there are also areas of non-zero local rate of velocity circulation decay, which could be the footprints of singularities providing local source of circulation/vorticity, as conjectured by Eyink[16]. If we turn to the laminar case (case A, Fig. 1a,d,g), the resolution of our measurements over the whole flow is smaller than the relevant scale; thus, all scales are resolved. There are no clear dissipation structures in the map of $D_{\delta x}(\mathbf{u})$, which appears to be negative over the whole observation window and, on average, 3.5 times smaller than the viscous dissipation. The latter is also very small in that area, over one order of magnitude smaller than the total energy injection. In a similar way, we observe on Fig. 1d,g that both $D_{\delta x}(\mathbf{u})$ and $\frac{d}{dt}\Gamma_{\delta x}(\mathbf{u})$ are very small at the centre compared with viscous dissipation and compared with their values for the two other (turbulent) flows. This is suggestive of the idea that the contribution of possible inertial dissipation plays a more important role at high Reynolds numbers, while viscous effects decrease. For case A, if the energy balance is performed over the whole experiment, the viscous dissipation accounts for all of the injected power and supersedes, by two order of magnitudes, the estimates of inertial dissipation. We also see by comparing Fig. 1b with Fig. 1e and Fig. 1c with Fig. 1f that areas of high viscous dissipation tend to be correlated with areas where strong inertial dissipation are localized.

To see whether the structures on Fig. 1d–f are located in areas of high vorticity, we may compare them with maps of vorticity magnitude[17]. In our case, we have only access to the y component of vorticity, $\omega_y = \partial_z u_x - \partial_x u_z$ at the resolution scale, whose magnitude is displayed in Fig. 3 for the three cases described in Table 1.

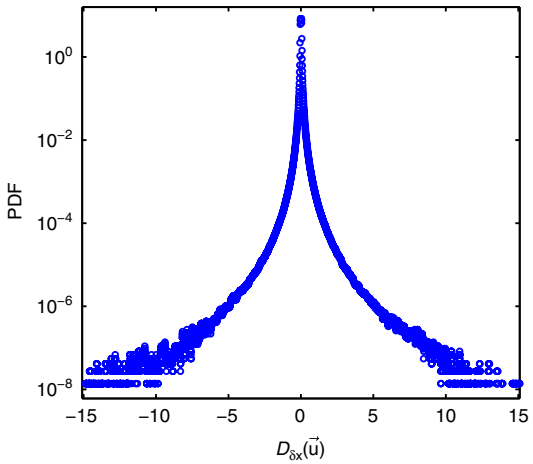

Figure 2 | Probability density function of the estimated inertial dissipation. Probability density function (PDF) of the coarse-grained inertial dissipation $D_{\delta x}(\mathbf{u})$ estimated at the dissipative scale (in units of $R^2(2\pi F)^3$, where R is the radius of the cylinder and F the rotation frequency of the impellers), evaluated from measurements in case B. The distribution is highly non-gaussian with many events at values larger than 1,000 times the mean value.

Comparing Fig. 3b with Fig. 1e we find an overall agreement between the vorticity and dissipation map. However, we see that some structures in the $D_{\delta x}(\mathbf{u})$ field are not mirrored in the vorticity field, and that the agreement is worse for case A and C, showing that the link between vorticity and inertial dissipation might be restricted only to turbulent flows, when dissipative scale is resolved.

Extreme events in the inertial dissipation estimates. To focus on the extreme events and to characterize them, we restrict our analysis to very intense events that are locally responsible for very large $D_{\delta x}(\mathbf{u})$. We harvest from case B (the turbulent resolved case) only those structures having $D_{\delta x}(\mathbf{u})$ of 1,000 times higher than its space-time average, corresponding to very rare extreme events. Out of 30,000 images, we found only 28 events, corresponding to probability of <1 in 50,000 (based on ratio of areas). Examples of these events are shown in Fig. 4. By observing the local velocity around these 28 events, we are able to classify them into 4 main types:

Fronts (Fig. 4a), where the velocity field shows two regions of very different velocities separated by a clear boundary along which the extreme event lies. In the frame of reference moving with the peak of the event, the in-plane velocities typically display a shock-like pattern. This type of structures is the result of two blobs of fluids, initially well-separated in space and velocity, being brought to close distance. In this sense, it is reminiscent of the fronts found in studies of turbulent mixing of passive scalar[25]. Similar patterns could also be found in weather patterns (for example, cold fronts). Many of these events also show velocity patterns such as in a saddle point (where fluid flows inwards on one axis while escaping on another) as can be seen in the periphery of Fig. 4a. In general, fronts and saddles belong to the same causal family in the sense that two blobs of fluid are mutually colliding and thus escape in other directions. These events are the most frequent, representing 21 events, that is, 75% of the cases. The inertial dissipation of most of these events (except two) increases without sign of saturation with decreasing scale, corresponding to a local exponent $h<1/3$ (otherwise $h=1/3$).

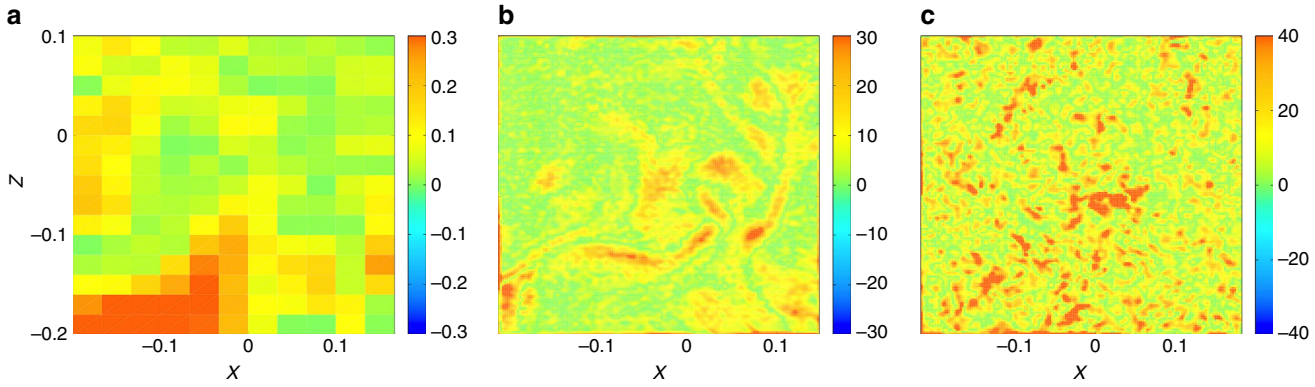

Figure 3 | Maps of vorticity. Maps of the norm of the dimensionless *y*-component of the vorticity, ω_y, computed on the plane of measurement of our SPIV setup. (**a**) Case A, (**b**) case B and (**c**) case C. All the quantities are made dimensionless using R and $(2\pi F)^{-1}$ as units of length and time.

Spirals (Fig. 4b), where the in-plane velocity has a spiral structure. The inertial dissipation increases without saturation, corresponding to a local exponent $h<1/3$. This type of events was found three times. All these events are converging spirals consistent with the scenario of vortex stretching in the out-of-plane direction.

Jets (Fig. 4c), where the in-plane velocity has a strong narrow jet and the peak is found near the edge where there is strong shear. Another common feature is the complex profile of the out-of-plane velocity. These are suggestive of further breakdown energy by instability at certain location of fronts in the flow. The inertial dissipation increases without saturation, while showing possible saturation in another case. This type of events was only found two times.

Cusps with helicity (Fig. 4d), where the velocity field in the in-plane displays a horse-shoe-like structure, whereas the out-of-plane velocity profile is clearly distinct across the hypothesized cusps. These are events that seem incompatible with the above categories. They have features suggestive of the velocity field generated by a vorticity line motion with a local cusp and axial motion (see Supplementary Note 3). Such vorticity pattern has been frequently observed in numerical simulation of vortex lines reconnection[26] and has even been suggested to be at the origin of the $k^{-5/3}$ turbulent spectrum[27]. On the other hand, as shown by Danchin[28], the velocity field generated by a cusp-like local vorticity patch is still regular, so that such a simple model might not be sufficient to explain our observations. The inertial dissipation around cusp events increases without saturation, corresponding to a local exponent $h<1/3$. They represent only two events.

Discussion

We characterize, in our experiments, the topology of extreme events of inertial dissipation estimated at the dissipative scales of turbulence. Our results provide a further indication of the non-trivial structures of sub-Kolmogorov flows, complementary to previous studies based on scaling studies of dissipative intermittency, for example, see Sreenivasan[29]. We show that extreme inertial dissipation events are associated with the existence of velocity fronts, saddle points, spirals, jets and, in some cases, suggestive of cusps. These kinds of topologies are typically associated with special configurations of eigenvalues of the velocity strain tensors around critical points of flow patterns. At such points, it is often the case that lagrangian trajectories cross[30], which would make these extreme events possible locations of shock-like singularities. In any case, the flow topology around the extreme inertial dissipation events is different from the usual flow topology associated with viscous dissipation. For instance, Moisy and Jimenez[31] used box counting to study the fractal structure of regions of intense vorticity and energy dissipation in a direct numerical simulation of isotropic turbulence. Their work suggests that the geometry of the regions of intense dissipation resemble sheets or ribbons. This suggests that inertial dissipation and viscous dissipation are two different processes, at least down to the dissipative scale.

Another interesting observation is that extreme events of inertial dissipation provide significant local contributions to energy balance at the Kolmogorov scale, regardless of whether the energy lost pertaining to these events is eventually dissipated by singularities or by viscosity at yet smaller scales. This suggests that Kolmogorov scale is not the only characteristic scale for dissipation. This seemingly surprising conjecture is in fact compatible with the multi-fractal picture of turbulence, which predicts that for a given flow singularity of exponent h, there is a specific dissipation scale[32] η_h scaling like $Re^{-1/(1+h)}$. For $h=1/3$, we recover the classical Kolmogorov scale η. For the case with $h<1/3$, we have $\eta_h<\eta$, so that the dissipation occurs at much smaller scale than the Kolmogorov one. Our findings are therefore compatible with the multi-fractal picture of turbulence, if the extreme events of inertial dissipation are the footprints of singularities of exponent $h<1/3$, as suggested in Kuzzay *et al.*[17].

Whether this interpretation is valid or not is still debatable, as we have no means to follow the inertial dissipation down to $\ell=0$, as required by the mathematical theorem[15]. To unambiguously distinguish between the possibilities of whether the energy contained in these extreme events is eventually dissipated by non-viscous mean or otherwise, one may need to resolve the flow down to the kinetic limit and track their evolution in time until they fully dissolve, which represents a experimental challenge for future works.

Perhaps a more immediate practical question one could ask is: knowing the significance of such extreme events even at the dissipative scales, how could one truncate models and simulations at tractable hydrodynamic scales with the correct physics reflecting their properties? In compressible fluid dynamics, these kinds of questions are usually addressed in relation with the building of a singularity through shock formation. In these cases, it has been common practice starting with von Neumann and Richtmyer[33], to select physically admissible solutions and ensure the stability of numerical schemes via the introduction of an appropriate numerical viscosity[34]. Our results suggest that the same kind of procedure should also be introduced in incompressible numerical simulations, to account for extreme events of inertial dissipation that are not captured at the model resolution scale.

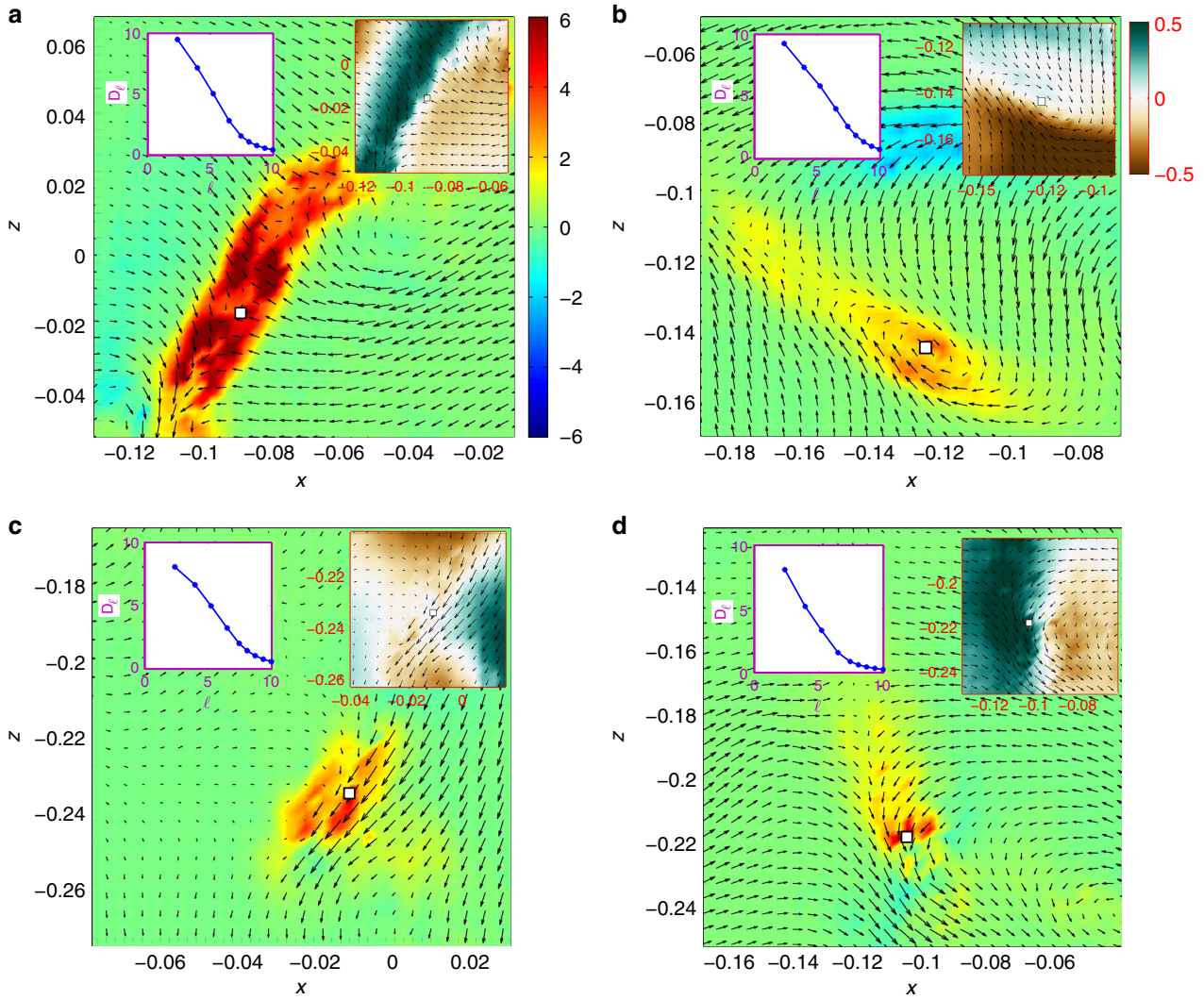

Figure 4 | Types of extreme events. Four types of structures found from the extreme events (1,000 times the mean) of inertial dissipation estimates $D_{\delta x}(\mathbf{u})$ in case B, where Kolmogorov scale is resolved. (**a**) Front, (**b**) spiral, (**c**) jet and (**d**) cusp. Main figures: spatial maps of dimensionless magnitude of $D_{\delta x}(\mathbf{u})$, with arrows showing in-plane velocities around each extreme event. Common colormap shown in **a**. $D_{\delta x}(\mathbf{u})$ is normalized by $R^2(2\pi F)^3$ and positions are normalized by R. Right insets: the three-component velocity fields (u_y in colours) around each event (in units of $2\pi RF$). All right insets share the colourmap in **b**. Coordinate axes are right handed. Left insets: $D_{\delta x}(\mathbf{u})$, averaged over a circle (of 21 points) around the peak (non-dimensionalized by $R^2(2\pi F)^3$) as a function of ℓ (non-dimensionalized by η) at the peak of each event.

Methods

The choice of von Kármán swirling flow. As inertial dissipation is expected to originate from flow singularities, we focus on a geometry where lack of smoothness is not forbidden by mathematical theorems. This motivates our choice of an experimental set-up providing a turbulent flow with statistical axisymmetry. This kind of geometry has attracted interest from many works on the regularity of INSE[35–41], where it was shown that the regularity properties of the axisymmetric Navier–Stokes equations heavily depend on the intensity of the swirl component of the flow υ_ϕ and its variation with respect to the distance from the rotation axis. When the swirl is zero, Ladyzhenskaya[35] proved that the flow is smooth at all times. When the swirl is non-zero, the regularity can also be proven for finite time, in a domain excluding the symmetry axis[38]. In our experiment, we therefore currently concentrate our measurements on a domain including the symmetry axis and generate turbulence in a vertical cylinder of height H and radius R filled with water, and stirred by two coaxial, counter-rotating impellers (von Kármán flow) providing energy and momentum flux at the upper and lower end of the cylinder. The resulting flow is statistically axisymmetric, with a time-averaged velocity consisting of a swirl (toroidal flow) $\upsilon_S(r,z)=\upsilon_\phi(r,z)e_\phi$ and a poloidal flow $\upsilon_P(r,z)=\upsilon_r(r,z)e_r+\upsilon_z(r,z)e_z$, where (r, ϕ, z) are the cylindrical coordinates and (e_r, e_ϕ, e_z) the corresponding unit vectors[42]. The ratio $\upsilon s/\upsilon p$ is controlled by the impellers geometry. In the sequel, we focus on impellers such that $\upsilon s/\upsilon p=2.5$. The impellers are driven by two independent motors rotating at a frequency F and the experiment is thermalized at a temperature $T\approx 20\,^\circ C$.

Torque and rotational frequency measurements. Torque (global) measurements at each impeller are performed with SCAIME technology and provide values over the kHz range of C_1 and C_2, being respectively the torque applied to the bottom and top shafts. They are calibrated using measurements at different mean frequencies, so as to remove spurious contributions from genuine offsets or mechanical frictions. From this, we compute the injected power necessary to maintain our turbulent flow in a statistical stationary state as $P=2\pi(C_1F_1+C_2F_2)$, where C_1 and F_1 are the torques and the frequencies at the two impellers, respectively. To get a meaningful comparison between different impellers, we further renormalize the injected power by $\rho R^5(2\pi F)^3$, where ρ is the fluid density, $F=F_1=F_2$ (exact counter-rotating regime) and R is the radius of the cylinder.

Particle image velocimetry. The typical size of the particles used in the PIV measurements is a few tens of micrometres and their density is 1.4. Two cameras take 30,000 successive pictures of the flow at a 15-Hz framerate. The resolution of our camera frame is 1,600 × 1200 pixels and the reconstruction is done using peak correlation performed over 50% overlapping windows of size 16 to 32. As a result, we get measurements of velocity field on a grid of approximate size 170 × 160 to 90 × 68 in a vertical plane containing the axis of symmetry (Oz), in a cylindrical system of coordinates. We performed two types of experiments: one with the cameras set at a distance such that their field of view covers the whole meridional plane. This set-up enables a global view of the flow and reaches a minimum grid

step of the order of $200/68 \approx 3$ mm. In the second, we adapt lenses on the camera, to focus on a five times smaller field of view, of the order of 40×30 mm. Increasing the number of particles in the flow and using overlapping windows of size 16×16, we are then able to reach a minimum grid step of the order of $40/160 \approx 0.25$ mm. The continuity between the two types of measurements can be checked by degrading the resolution of the zoomed picture using overlapping windows of 32×32 or 128×128 for the velocity reconstruction. This last case corresponds to the velocity field obtained without lenses, with a velocity field reconstructed using windows of size 16×16.

The total acquisition time is ~ 10 min to 2 h, that is, one or two orders of magnitude longer than the characteristic time of the slowest patterns of the turbulent flow. Fast scales are statistically sampled.

The velocity fields are non-dimensionalized using a typical velocity $V_0 = 2\pi R(F_1 + F_2)/2$ based on the radius of the cylinder and the rotation frequencies of the impellers. The resulting velocity fields are windowed so as to fit to the boundaries of the flow and remove spurious velocities measured in the impellers and at the boundaries. We apply a local filter (based on velocities of nearest neighbours) to remove isolated spurious vectors. Typically, $\sim 1\%$ of the data are changed by this processing.

Estimation of dissipation and circulation production rates. With our velocity fields, we can compute the velocity increments $\delta\mathbf{u}(\mathbf{r}) = \mathbf{u}(\mathbf{x}_{2D} + \mathbf{r}_{2D}) - \mathbf{u}(\mathbf{x}_{2D})$, From this, we define two scale dependent scalar functions: the local energy dissipation rate $D_\ell(\mathbf{u})$[15]:

$$D_\ell(\mathbf{u}) = \frac{1}{4}\int_v d^3r\ (\nabla G_\ell)(\mathbf{r}) \cdot \delta\mathbf{u}(\mathbf{r})\ |\delta\mathbf{u}(\mathbf{r})|^2, \tag{4}$$

where v is a full disk and the local rate of velocity circulation decay[16]:

$$\frac{d}{dt}\Gamma_\ell(\mathbf{u}) = \oint_{\mathscr{C}} d\mathbf{s} \cdot \mathscr{F}_\ell(\mathbf{u}), \tag{5}$$

where

$$\mathscr{F}_\ell(\mathbf{u}) = \int_v d^3r \left[\left(\delta\mathbf{u}(\mathbf{r}) - \int_v d^3r' G_\ell(\mathbf{r}')\delta\mathbf{u}(\mathbf{r}')\right) \cdot \nabla G_\ell(\mathrm{r})\right] \delta\mathbf{u}(\mathbf{r}), \tag{6}$$

$\mathscr{C}$ being any contour advected by the fluid and G_ℓ is a spherically symmetric function of r given by[17]:

$$G_\ell(r) = \frac{1}{N} exp\ (-1/(1-(r/2\ell)^2)), \tag{7}$$

where N is a normalization constant such that $\int d^3r G_\ell(r) = 1$.

In addition, we may also compute the local rate of viscous dissipation at the resolution scale, given by:

$$D^{\nu}_{\delta x}(\mathbf{u}) = \nu S_{ij} S_{ij}, \tag{8}$$

where $S_{ij} = \partial_j u_i$. In the present case, we are missing some components of the viscous dissipation. Incompressibility condition provides $S_{22} = -S_{11} - S_{33}$. We have also used statistical axisymmetry to replace S_{21} by S_{12} and S_{23} by S_{13}. We have checked that this last hypothesis does not change the topology of the local maps of dissipation, but changes the time-average, hopefully accounting for the missing dissipation due to plane projection.

Data availability. The data that support the findings of this study are available from the corresponding author upon request.

References

1. Bramwell, S. T., Holdsworth, P. C. W. & Pinton, J. F. Universality of rare fluctuations in turbulence and critical phenomena. *Nature* **396,** 552–554 (1998).
2. Hof, B., Westerweel, J., Schneider, T. M. & Eckhardt, B. Finite lifetime of turbulence in shear flows. *Nature* **443,** 59–62 (2006).
3. McKeon, B. J. Controlling turbulence. *Science* **327,** 1462–1463 (2010).
4. Kaneda, Y., Ishihara, T., Yokokawa, M., Itakura, K. & Uno, A. Energy dissipation rate and energy spectrum in high resolution direct numerical simulations of turbulence in a periodic box. *Phys. Fluids* **15,** L21–L24 (2003).
5. Fefferman, C. L. Existence and smoothness of the Navier-Stokes equation. *Millennium Prize Problems* 57–67 (2000).
6. Leray, J. Essai sur le mouvement d'un liquide visqueux emplissant l'espace. *Acta Math.* **63,** 193248 (1934).
7. Scheffer, V. Partial regularity of solutions to the Navier-Stokes equations. *Pacific J. Math.* **66,** 535552 (1976).
8. Caffarelli, L., Kohn, R. & Nirenberg, L. Partial regularity of suitable weak solutions of the Navier-Stokes equations. *Comm. Pure Appl. Math.* **35,** 771831 (1982).
9. Taylor, G. I. Statistical theory of turbulence. *Proc. R. Soc. A* **151,** 421–444 (1935).
10. Kolmogorov, A. N. Dissipation of energy in locally isotropic turbulence. *DAN SSSR* **32** (1941).
11. Onsager, L. Statistical hydrodynamics. *Nuovo Cimento* **6**(Suppl): 279287 (1949).
12. Parisi, G. & Frisch, U. in *Proceedings of the International School of Physics Enrico Fermi 1983* (eds Ghil, M., Benzi, R. & Parisi, G.) 8488 (North-Holland, 1985).
13. Muzy, J. F., Bacry, E. & Arneodo, A. Wavelets and multifractal formalism for singular signals: application to turbulence data. *Phys. Rev. Lett.* **67,** 35153518 (1991).
14. Kestener, P. & Arneodo, A. Generalizing the wavelet-based multifractal formalism to vector-valued random fields: application to turbulent velocity and vorticity 3D numerical data. *Phys. Rev. Lett.* **93,** 044501 (2004).
15. Duchon, J. & Robert, R. Inertial energy dissipation for weak solutions of incompressible Euler and Navier-Stokes equations. *Nonlinearity* **13,** 249255 (2000).
16. Eyink, G. L. Cascade of circulations in fluid turbulence. *Phys. Rev. E* **74,** 066302 (2006).
17. Kuzzay, D. *et al.* New criteria to detect singularities in experimental incompressible flows. *Nonlinearities*. preprint arXiv:1601.03922 (2016).
18. Rousset, B. *et al.* Superfluid high Reynolds von Kármán experiment. *Rev. Sci. Instrum.* **85,** 103908 (2014).
19. Saint-Michel, B., Daviaud, F. & Dubrulle, B. A zero-mode mechanism for spontaneous symmetry breaking in a turbulent von Kármán flow. *New J. Phys.* **16,** 013055 (2014).
20. Ravelet, F., Chiffaudel, A. & Daviaud, F. Supercritical transition to turbulence in an inertially-driven von Kármán closed flow. *J. Fluid Mech.* **601,** 339–364 (2008).
21. Eyink, G. L. & Sreenivasan, K. R. Onsager and the theory of hydrodynamic turbulence. *Rev. Modern Phys.* **78,** 87135 (2006).
22. Gallavotti, G. & Cohen, E. G. D. Dynamical ensembles in nonequilibrium statistical mechanics. *Phys.Rev. Lett.* **74,** 2694 (1995).
23. Jarzynski, C. Nonequilibrium equality for free energy differences. *Phys. Rev. Lett.* **78,** 2690 (1997).
24. Ciliberto, S., Joubaud, S. & Petrosyan, A. Fluctuations in out-of-equilibrium systems: from theory to experiment. *J. Stat. Mech. Theor. Exp.* **12,** P12003 (2010).
25. Shraiman, B. I. & Siggia, E. D. Scalar turbulence. *Nature* **405,** 639–646 (2000).
26. Melander, M. V. & Hussain, F. Cut-and-connect of two antiparallel vortex tubes. Research Proceedings of the Summer Program. 256–286 (1988).
27. Hunt, J. C. R. & Vassilicos, J. C. Kolmogorov's contributions to the physical understanding of small-scale turbulence and recent developments. *Proc. R. Soc. Lond. A* **434,** 183–210 (1991).
28. Danchin, R. Evolution d'une singularité de type cusp dans une poche de tourbillon. *Rev. Math. Iberoamericana* **16,** 281–329 (2000).
29. Sreenivasan, K. R. & Antonia, R. A. The phenomenology of small-scale turbulence. *Annu. Rev. Fluid Mech.* **29,** 435–472 (1997).
30. Perry, A. E. & Fairlie, B. D. Critical points in flow patterns. *Adv. Geophys.* **18B,** 299–315 (1974).
31. Moisy, F. & Jimenez, J. Geometry and intense clustering of structures in isotropic turbulence. *J. Fluid Mech.* **513,** 111–133 (2004).
32. Paladin, G. & Vulpiani, A. Degrees of freedom of turbulence. *Phys. Rev. A* **35,** 1971 (1987).
33. Von Neumann, J. & Richtmyer, R. D. A method for the numerical calculation of hydrodynamic shocks. *J. App. Phys.* **21,** 232–237 (1950).
34. Guermond, J. L., Pasquetti, R. & Popov, B. From suitable weak solutions to entropy viscosity. *J. Sci. Comp.* **49,** 35–50 (2011).
35. Ladyzhenskaya, O. A. Unique global solvability of the three-dimensional Cauchy problem for the Navier-Stokes equations in the presence of axial symmetry. *Zap. Nauécn. Sem. Leningrad. Otdel. Mat. Inst. Steklov* **7,** 155–177 (1968).
36. Chae, D. & Lee, J. On the regularity of the axisymmetric solutions of the Navier-Stokes equations. *Math. Z.* **239,** 645–671 (2002).
37. Chen, C.-C., Strain, R. M., Yau, H. & Tsai, T. Lower bound on the blow-up rate of the axisymmetric Navier-Stokes equations. *Int. Math. Res. Not.* **2008** (2008).
38. Hou, T. Y. & Li, C.-M. Dynamic stability of the 3D axisymmetric Navier-Stokes equations with swirl. *Comm. Pure Appl. Math.* **61,** 661–697 (2008).
39. Kubica, A., Pokorny, M. & Zajaczkowski, W. Remarks on regularity criteria for axially symmetric weak solutions to the Navier-Stokes equations. *Math. Methods Appl. Sci.* **35,** 360–371 (2012).
40. Abidi, H. & Zhang, P. Global smooth axisymmetric solutions of 3-D inhomogeneous incompressible Navier-Stokes system. *Calc. Var. Partial Differ. Equ.* **54,** 3251–3276 (2015).
41. Zhang, P. & Zhang, T. Global axisymmetric solutions to three-dimensional Navier-Stokes system. *Int. Math. Res. Not.* **2014,** 610–642 (2014).

42. Cortet, P.-P. *et al.* Normalized kinetic energy as a hydrodynamical global quantity for inhomogeneous anisotropic turbulence. *Phys. Fluids* **21,** 025104 (2009).

Acknowledgements
E.-W.S. acknowledges support from the EuHIT contract, FP7-INFRASTRUCTURE Collaborative Project number 312778. D.F. was supported by ERC grant number 338965-A2C2. All the authors thank H. Bercegol for fruitful discussions.

Author contributions
All the authors made significant contributions to this work. F.D., C.W.-G. and V.P. designed and built the experiment. A.G. and E.-W.S. made the measurements. E-W.S., D.F., B.D. and D.K. analysed the data. All authors discussed the results, wrote and commented on the paper.

Additional information
Supplementary Information accompanies this paper at http://www.nature.com/naturecommunications

Competing financial interests: The authors declare no competing financial interests.

How to cite this article: Saw, E.-W. *et al.* Experimental characterization of extreme events of inertial dissipation in a turbulent swirling flow. *Nat. Commun.* 7:12466 doi: 10.1038/ncomms12466 (2016).

1 Supplementary Figures

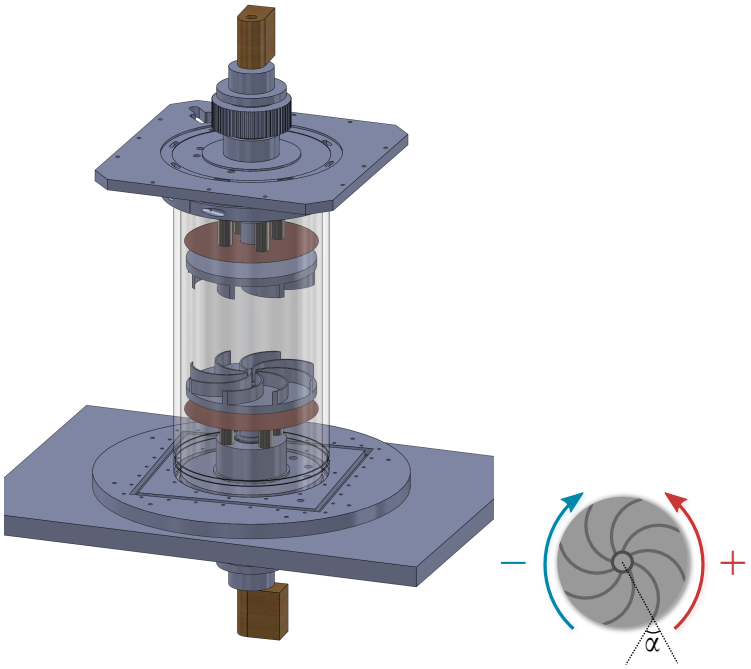

Supplementary figure 1: ***Experimental setup.*** *Picture of the experimental set-up and of an impeller. The notations for the two forcing conditions are defined along with the angle α characterizing the curvature of the blades.*

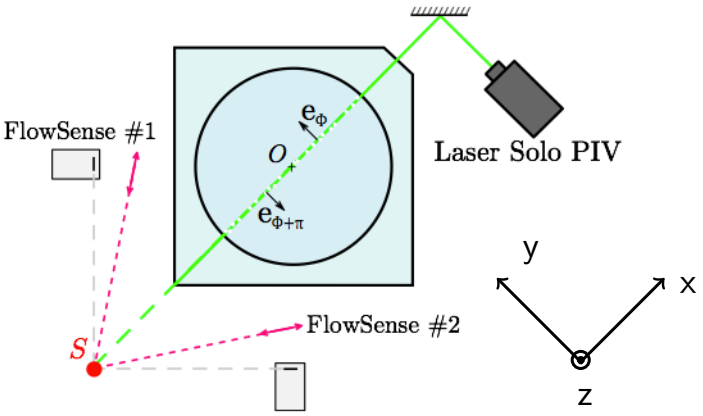

Supplementary figure 2: ***Imaging Setup.*** *Schematics of the PIV set-up viewed from above. A laser lights micrometer sized particles in a meridional plane, while two cameras take successive snapshots of the flow. This allows us to get the three components of the velocity field in the lit meridional plane.*

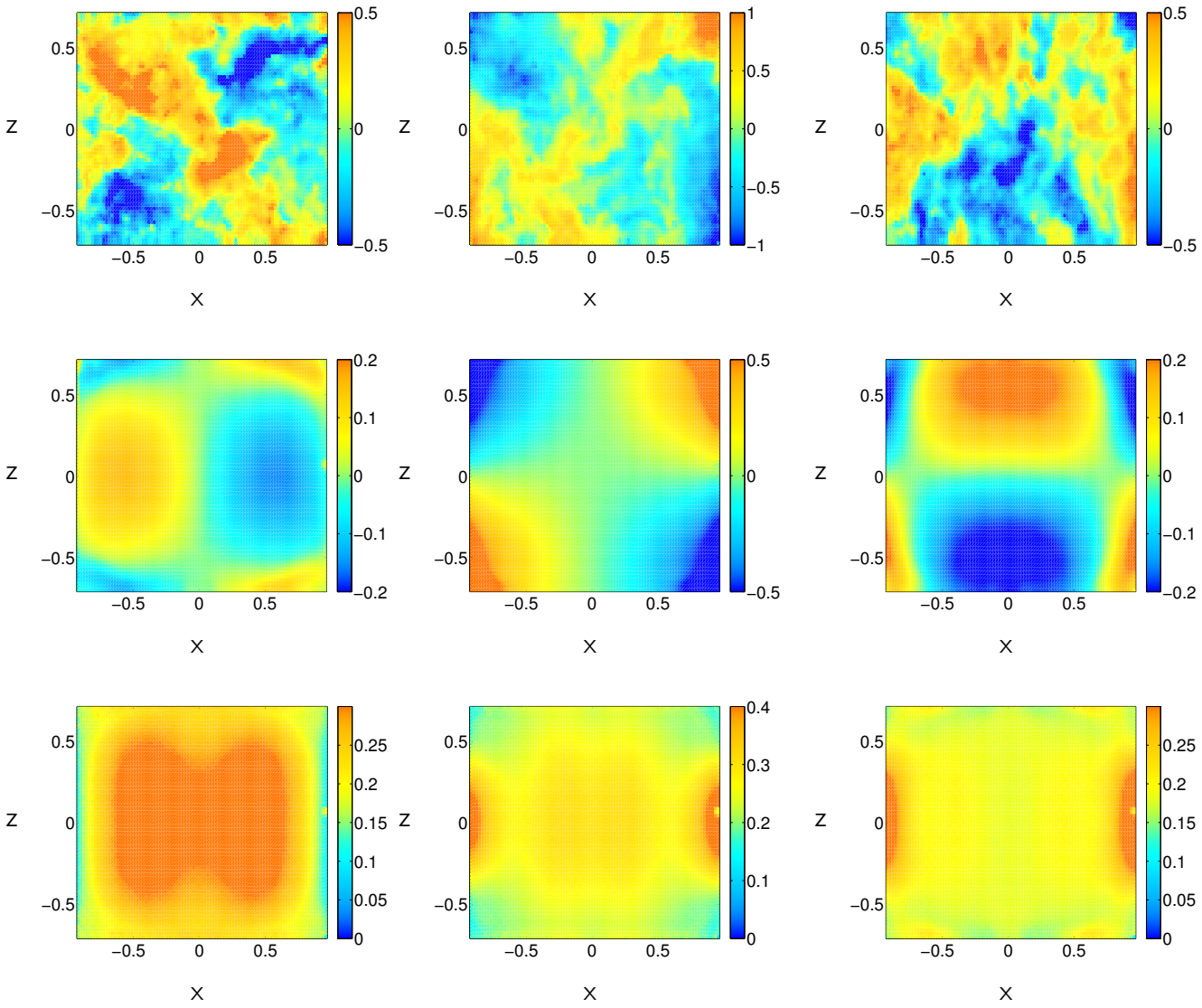

Supplementary figure 3: ***Mean flow and fluctuations.*** *Maps of the instantaneous (top panels) and mean (middle panels) flows along with the standard deviation (bottom panels) at each measurement points (same flow as in Fig. 1-4). Left column:* Vx*. Middle column:* Vy*. Right column:* Vz*. We see that the instantaneous flow is highly disordered, while the mean flow and the standard deviation have well defined structures. Mesurements made at* $Re \approx 3 \times 10^5$*.*

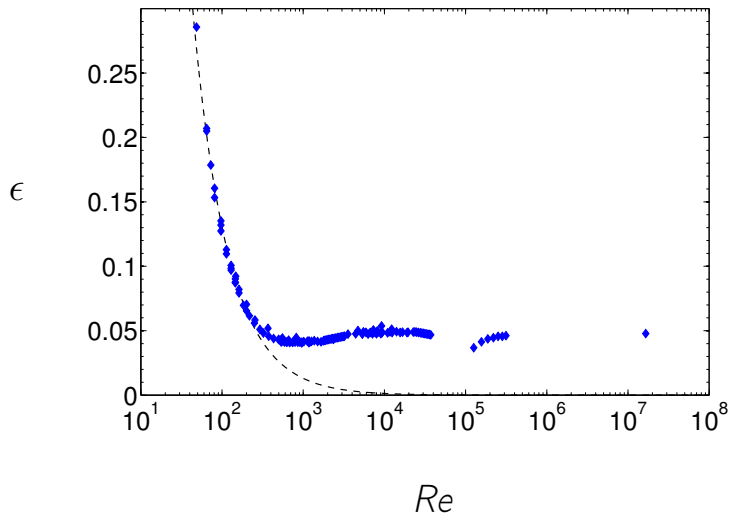

Supplementary figure 4: ***Mean injected kinetic power.*** *Global dimensionless injected power per unit mass ϵ (blue dots) in the stationary symmetric regime as a function of the Reynolds number Re. The dotted line represents the fit $\epsilon \propto Re^{-1}$. This figure has been adapted from Fig. 3 in [5]. The point at $Re \approx 10^7$ was measured using normal liquid helium in the SHREK experiment while all the other points have been obtained using water or glycerol.*

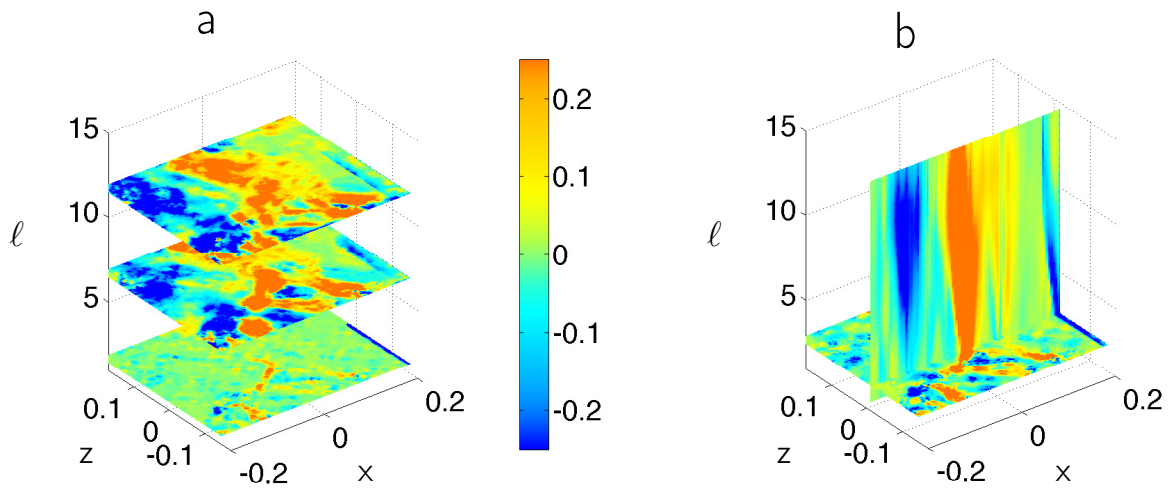

Supplementary figure 5: ***Variation of inertial energy dissipation with lenght-scale.*** *Maps of the instantaneous dimensionless coarse-grained inertial energy dissipation* $D_\ell(\mathbf{u})$ *as a function of scale* ℓ *for a flow at* $Re \approx 3 \times 10^5$. *a) Maps of* $D_\ell(\mathbf{u})$ *at three different scales. b) Maps of* $D_\ell(\mathbf{u})$ *at different scales, along a line going through a peak in inertial dissipation. The colors code* $D_\ell(\mathbf{u})$. *The scale is expressed in units of the grid step:* $0.25\ mm$.

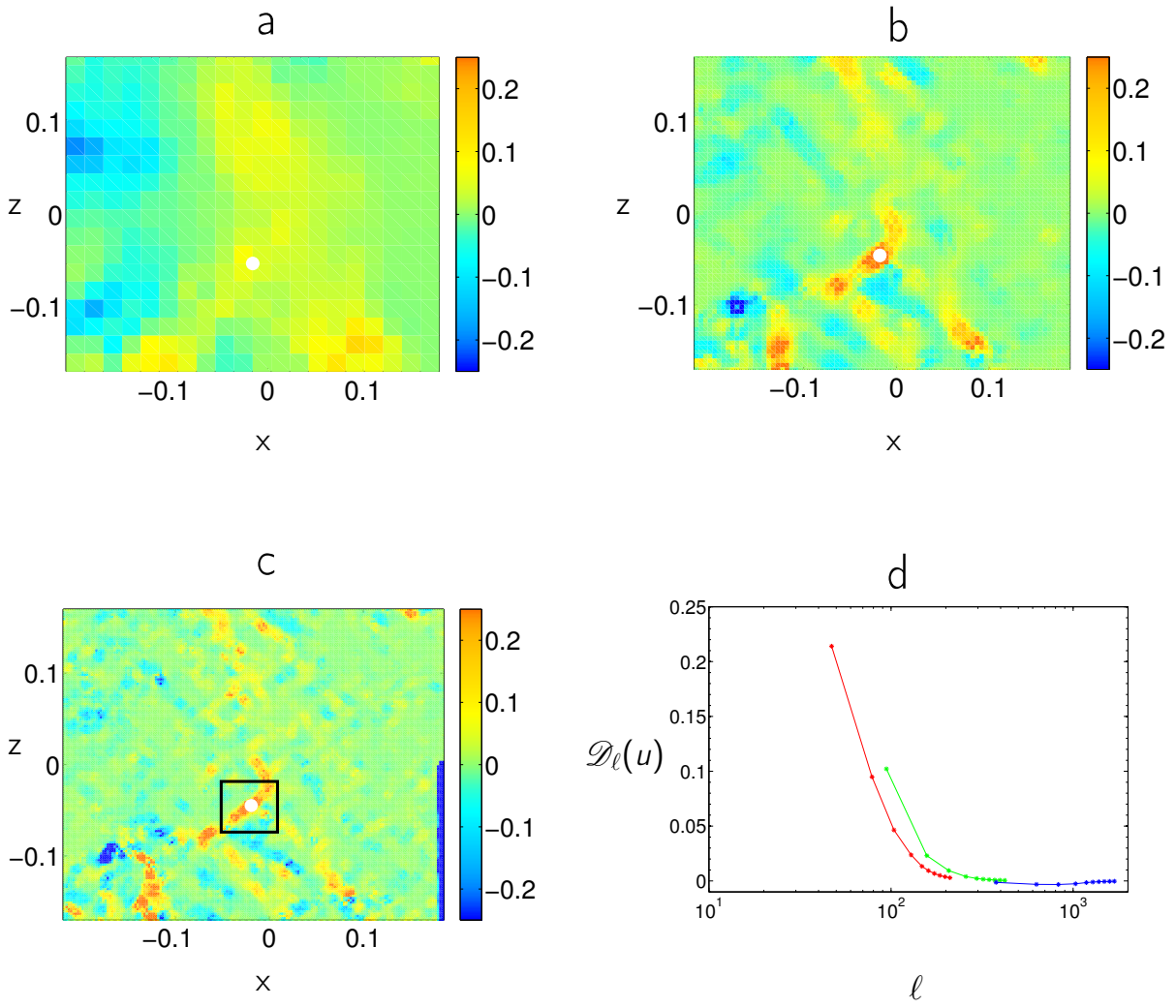

Supplementary figure 6: ***Inertial energy dissipation at different resolutions.*** *Maps of the instantaneous dimensionless coarse-grained inertial energy dissipation* $D_\ell(\mathbf{u})$ *at three different resolutions* ($2\delta x$)*: a) 4 mm (PIV window 128×128), b) 1 mm (PIV window 32×32) and c) 0.5 mm (PIV window 16×16). Figure d) shows* $D_\ell(\mathbf{u})$ *as a function of scale* ℓ*, at the "center" of the strong event identified by the white dot on the maps: blue: computed at the resolution* 4 *mm , green: computed at the resolution* 1 *mm; red: computed at the resolution* 0.5 *mm. The area inside the black square in figure c) is magnified in Fig. 7.*

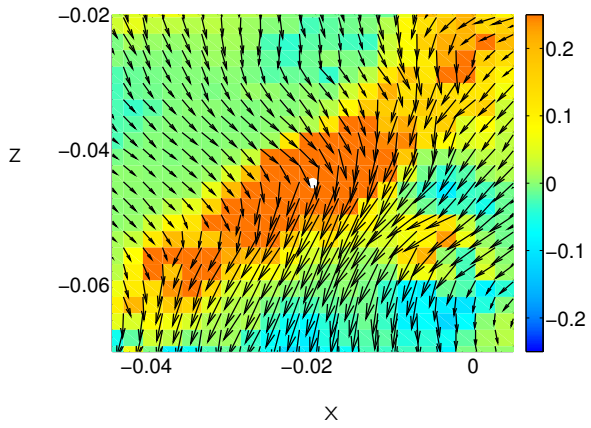

Supplementary figure 7: ***Local velocity around a strong event.*** *Local in-plane velocity around a strong inertial dissipation event*. The colors code the instantaneous dimensionless coarse-grained inertial energy dissipation $D_\ell(\mathbf{u})$, the arrows code the in-plane velocity. The region showed here corresponds to the area inside the black square of Fig. 6c). The white dot is at the same position as in Fig. 6. An abrupt change in the x-component of the velocity at this location can be observed.

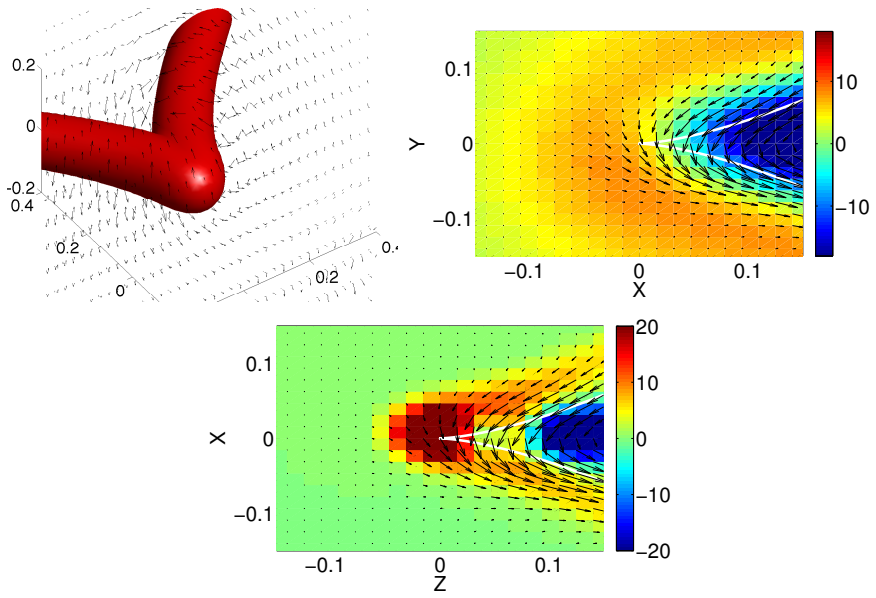

Supplementary figure 8: ***Simulated cusps.*** *(Color online) inertial dissipation near singularity generated by a vorticity cusp. Panel a: isocontour of vorticity showing the cusp at the origin. Panel b: velocity in the plane* $Z = 0$ *in the vicinity of the cusp. The white line is the location of maximum vorticity in that plane. The color code the out-of-plane velocity. The arrow codes the in-plane velocity. Panel c: inertial dissipation computed using the velocity field of Panel b. The color codes de inertial dissipation, while the arrow code the local in plane velocity. Units are arbitrary.*

2 Supplementary Notes

Supplementary Note 1: The experimental set-up Our von Kármán flow is generated by two counter-rotating impellers in a vertical cylinder (see Fig. 1). The radius of the cylinder is $R = 100\ mm$ and its height is $H = 240\ mm$. The impellers used in this paper are flat disks of diameter $185\ mm$, seperated by a distance $h = 180\ mm$ and fitted with 8 curved, radial blades of height $h_b = 20\ mm$. The curvature of the blades is characterized by an angle $|\alpha| = 72°$.

The impellers are driven by two independent motors which can rotate at frequencies up to typically $10\ Hz$. In our study, the motor frequencies have been set equal in order to get exact counter-rotating regime. The curvature of the blades allows to choose between two different forcing conditions in order to generate flows with different statistical properties. Here, we choose to rotate the impeller in the (-) direction defined on Fig. 1, to get $\alpha = -72°$

Our experimental set-up allows for both global and local flow diagnostics. Local velocity measurements are performed using Stereoscopic Particle Image Velocimetry (SPIV) in the stationary regime (see Fig. 2). The particles we have used have a size of a few tens of micrometers and their density is 1.4. A laser of wavelength 532 nm is used to light a meridional plane while two cameras of resolution 1600x1200 pixels, set at $45°$ with respect to that plane, take successive snapshots of the flow. Then, the velocity field is reconstructed using peak correlation performed over 50% overlapping windows of size 16 to 32 pixels. As a result, we get instantaneous snapshots of the three components of the velocity field on a grid of approximate size 90×70 (see Fig. 3).

Typical maps of the instantaneous (top panels) and time averaged (middle panels) velocity fields for the global experiments are provided on Fig. 3, along with maps of the standard deviation (bottom panels) of the three components of the velocity at each grid points at $Re \approx 3 \times 10^5$. The statistics for these maps have been obtained from 3×10^4 instantaneous snapshots. We observe that the instantaneous velocity fields are highly disordered contrary to the mean flow and the standard deviation which have well defined structures.

Along with local measurements, global diagnostics can be obtained. The torque applied to the top and bottom shafts are monitored using SCAIME technology, which allows us to measure the total power injected by the impellers into the flow (see Fig. 4). The calibration procedure, along with several other details on the experimental set-up may be found in [2,3] and references therein. Fig. 4 presents the global injected power per unit mass ϵ as a function of the Reynolds number Re (blue rhombi). It can be seen that at low Reynolds numbers (i.e $Re < 200$), ϵ decreases as Re^{-1} (dotted line). However, when Re becomes greater than 200, the flow becomes chaotic and a discrepancy between the experimental measurements and the Re^{-1} law appears. For very large Reynolds number, $Re > 10^5$, dissipation rate, ϵ, becomes constant [4] ($\epsilon \approx 0.046$).

Supplementary Note 2: Examples of measured inertial dissipation fields. An example of variation of $D_\ell(\mathbf{u})$ as a function of the scale ℓ and position $\mathbf{x}$ is provided in Fig. 5 for an instantaneous velocity field at $Re \approx 3 \times 10^5$. As the scale ℓ is decreased, the $D_{2D}(\mathbf{u})$ does not vanish, but instead points towards localized points which we identify as strong inertial dissipation event with $h \leq 1/3$.

For this computation, we have used a spherically symmetric function of x given by:

$$G_\ell(r) = \frac{1}{N} \exp(-1/(1-(r/(2\ell)^2)), \tag{1}$$

where N is a normalization constant such that $\int d^3r G_\ell(r) = 1$. According to [1], the results should not depend on the choice of this function, in the limit $\ell \to 0$.

To estimate the scaling range of the extreme event, we have performed the computation of $D_\ell(\mathbf{u})$ at different resolutions, using different averaging windows to reconstruct the velocity flow from the same image. An example is provided in Fig. 6. One sees that, as the resolution is increased, the region of elevated $D_\ell(\mathbf{u})$ becomes sharper and sharper, but globally remains at the same location (emphasized by the white dot). On the other hand, the plot of $D_\ell(\mathbf{u})$ at this location (Fig. 6d) as a function of ℓ shows that there is a continuity between the measurements. For this event, $D_\ell(\mathbf{u})$ is slowly varying at large scale, suggestive of a flow sturture with $h \approx 1/3$ and then increases at the smallest scales. This is corroborated by a local plot of the in-plane velocity field around the event (Fig. 3). One clearly observes a front-like structure of the velocity field at this location.

This study is however only performed at scales larger than about 10 times the dissipative scale. Similar structures at the resolution scale is provided in the main part of this paper.

Supplementary Note 3: Simulation of dissipation around a cusp singularity We have simulated an artificial vorticity line with a cusp $\boldsymbol{\omega}(\mathbf{x})$ on a 64^3 grid (Fig. 8-a). and computed the associated velocity field $\mathbf{v}_{BS}$ using Biot-Savart law. To obtain a non-zero velocity along the vortex

line, we then consider the velocity $\mathbf{v} = \mathbf{v}_{BS} + \alpha\boldsymbol{\omega}$ (where α is the helicity). Its structure near the cusp in a plane parallel to the vortex line is provided in Fig. 8-b. We then computed the function $D_{\delta x}(\mathbf{u})$ in the same plane, which is provided in Fig. 8-c. This singularity map is also similar to the singularity map we observe in our experiment.

3 Supplementary References

1. Duchon, J., Robert, R. Inertial energy dissipation for weak solutions of incompressible Euler and Navier-Stokes equations. *Nonlinearity* **13,** 249255 (2000).

2. Cortet, P.-P. et al., Normalized kinetic energy as a hydrodynamical global quantity for inhomogeneous anisotropic turbulence. *Phys. Fluids* **21,** 025104 (2009).

3. Saint-Michel, B., Daviaud, F., Dubrulle, B. A zero-mode mechanism for spontaneous symmetry breaking in a turbulent von Kármán flow. *New J. Phys.* **16,** 013055 (2014).

4. Ravelet, F., Chiffaudel, A., Daviaud, F., Supercritical transition to turbulence in an inertially-driven von Kármán closed flow. *J. Fluid Mech.* **601,** 339-364 (2008).

5. Saint-Michel, B. et al. Probing quantum and classical turbulence analogy in von Kármán liquid helium, nitrogen, and water experiments. *Phys. Fluids* **26,** 125109 (2014).

Bibliography

Abidi, H. (2008). Résultats de régularité de solutions axisymétriques pour le système de navier-stokes. *Bulletin des Sciences Mathématiques*, 132(7):592–624.

Agélas, L. (2013). Global Regularity of the 3D Axisymmetric Navier-Stokes Equations with swirl. 27 pages.

Arnold, V. (1986). The asymptotic hopf invariant and its applications. *Selecta Mathematica Sovietica*, 5:327–345.

Arnold, V. and Keshin, B. (1998). *Topological Methods in Hydrodynamics*, volume 125 of *Applied Mathematical Sciences*. Springer-Verlag, New York.

Aurell, E., Boffetta, G., Crisanti, A., Paladin, G., and Vulpiani, A. (1996). Growth of Noninfinitesimal Perturbations in Turbulence. *Physical Review Letters*, 77:1262–1265.

Aurell, E., Boffetta, G., Crisanti, A., Paladin, G., and Vulpiani, A. (1997). Predictability in the large: an extension of the concept of Lyapunov exponent. *Journal of Physics A Mathematical General*, 30:1–26.

Baldi, S. and Yianneskis, M. (2003). On the Direct Measurement of Turbulence Energy Dissipation in Stirred Vessels with PIV. *Industrial and Engineering Chemistry Research*, 42(26):7006–7016.

Batchelor, G. (1982). *The theory of homogeneous turbulence*. Cambridge University Press.

Beale, J. T., Kato, T., and Majda, A. (1984). Remarks on the breakdown of smooth solutions for the 3-D Euler equations. *Communications in Mathematical Physics*, 94:61–66.

Berhanu, M., Monchaux, R., Fauve, S., Mordant, N., Petrelis, F., Chiffaudel, A., Daviaud, F., Dubrulle, B., Marie, L., Ravelet, F., Bourgoin, M., Odier, P., Pinton, J. ., and Volk, R. (2007). Magnetic field reversals in an experimental turbulent dynamo. *Europhysics Letters*, 77(5):59001.

Betchov, R. (1961). Semi-Isotropic Turbulence and Helicoidal Flows. *Physics of Fluids*, 4:925–926.

Boffetta, G. (2007). Energy and enstrophy fluxes in the double cascade of two-dimensional turbulence. *Journal of Fluid Mechanics*, 589:253–260.

Boffetta, G., Giuliani, P., Paladin, G., and Vulpiani, A. (1998). An Extension of the Lyapunov Analysis for the Predictability Problem. *Journal of Atmospheric Sciences*, 55:3409–3416.

Bohm, D. (1961). *Causality & Chance in Modern Physics*. Harper & Row.

Borue, V. and Orszag, S. A. (1997). Spectra in helical three-dimensional homogeneous isotropic turbulence. *Physical Review E*, 55:7005–7009.

Bouchet, F. and Sommeria, J. (2002). Emergence of intense jets and Jupiter's Great Red Spot as maximum-entropy structures. *Journal of Fluid Mechanics*, 464:165–207.

Bourgoin, M., Moulin, M., Odier, P., Pinton, J.-F., Fauve, S., Pétrélis, F., Burguete, J., Chiffaudel, A., Daviaud, F., Ericher, D., Gasquet, C., Marié, L., Guigon, A., Pelisset, B., and Namer, F. (2000). The von Kármán Sodium (VKS) dynamo project. In *International Workshop on Homogeneous Dynamos*, KARLSRUHE, Germany.

Brissaud, A., Frisch, U., Leorat, J., Lesieur, M., and Mazure, A. (1973). Helicity cascades in fully developed isotropic turbulence. *Physics of Fluids*, 16:1366–1367.

Brossard, C., Monnier, J. C., Barricau, P., Vandernoot, F. X., Le Sant, Y., Champagnat, F., and Le Besnerais, G. (2009). Principles and applications of particle image velocimetry. *Aerospace Lab Journal*, 1.

Cadot, O., Couder, Y., Daerr, A., Douady, S., and Tsinober, A. (1997). Energy injection in closed turbulent flows: Stirring through boundary layers versus inertial stirring. *Physical Review E*, 56:427–433.

Caffarelli, L., Kohn, R., and Nirenberg, L. (1982). Partial regularity of suitable weak solutions of the Navier-Stokes equations. *Communications in Pure Applied Mathematics*, 35:771–831.

Cao, N., Chen, S., and Doolen, G. D. (1999). Statistics and structures of pressure in isotropic turbulence. *Physics of Fluids*, 11:2235–2250.

Cappanera, L. (2015). *Stabilisation non linéaire des équations de la magnétohydrodynamique et applications aux écoulements multiphasiques*. PhD thesis, Université Paris-Sud.

Castaing, B. (1996). The Temperature of Turbulent Flows. *Journal de Physique II*, 6:105–114.

Cencini, M. and Vulpiani, A. (2013). Finite size Lyapunov exponent: review on applications. *Journal of Physics A Mathematical General*, 46(25):254019.

Chae, D. and Lee, J. (2002). On the regularity of the axisymmetric solutions of the navier-stokes equations. *Mathematische Zeitschrift*, 239(4):645–671.

Chandrasekhar, S. (1961). *Hydrodynamic and Hydromagnetic Stability*. Clarendon Press.

Chavanis, P. H. (2004). Statistical mechanics of geophysical turbulence: application to jovian flows and jupiter's great red spot. *Physica D Nonlinear Phenomena*, 200:257–272.

Chavanis, P. H. and Sommeria, J. (1996). Classification of self-organized vortices in two-dimensional turbulence: the case of a bounded domain. *Journal of Fluid Mechanics*, 314:267–297.

Chavanis, P.-H. and Sommeria, J. (1997). Thermodynamical Approach for Small-Scale Parametrization in 2D Turbulence. *Physical Review Letters*, 78:3302–3305.

Chavanis, P. H. and Sommeria, J. (1998a). Classification of robust isolated vortices in two-dimensional hydrodynamics. *Journal of Fluid Mechanics*, 356:259–296.

Chavanis, P. H. and Sommeria, J. (1998b). Degenerate equilibrium states of collisionless stellar systems. *Monthly Notices of the Royal Astronomical Society*, 296:569–578.

Chavanis, P. H., Sommeria, J., and Robert, R. (1996). Statistical Mechanics of Two-dimensional Vortices and Collisionless Stellar Systems. *Astronomy Physics Journal*, 471:385.

Chen, H., Fang, D., and Zhang, T. (2015). Regularity of 3D axisymmetric Navier-Stokes equations. *ArXiv e-prints*.

Chen, Q. and Zhang, Z. (2007). Regularity criterion of axisymmetric weak solutions to the 3d navier-stokes equations. *Journal of Mathematical Analysis and Applications*, 331(2):1384–1395.

Chen, S., Eyink, G. L., Wan, M., and Xiao, Z. (2006). Is the Kelvin Theorem Valid for High Reynolds Number Turbulence? *Physical Review Letters*, 97(14):144505.

Chorin, A. (1994). *Vorticity and turbulence*, volume 103 of *Applied Mathematical Sciences*. Springer-Verlag.

Chossat, P. (1993). Forced reflectional symmetry breaking of an O(2)-symmetric homoclinic cycle. *Nonlinearity*, 6:723–731.

Ciliberto, S., Joubaud, S., and Petrosyan, A. (2010). Fluctuations in out-of-equilibrium systems: from theory to experiment. *Journal of Statistical Mechanics: Theory and Experiment*, 12:12003.

Clark, R. A., Ferziger, J. H., and Reynolds, W. C. (1979). Evaluation of subgrid-scale models using an accurately simulated turbulent flow. *Journal of Fluid Mechanics*, 91:1–16.

Comte-Bellot, G. and Corrsin, S. (1971). Simple Eulerian time correlation of full- and narrow-band velocity signals in grid-generated, 'isotropic' turbulence. *Journal of Fluid Mechanics*, 48:273–337.

Constantin, P. (1994). Geometric statistics in turbulence. *SIAM Review*, 36(1):73–98.

Constantin, P. (1995). A few results and open problems regarding incompressible fluids. *Notices of the American Mathematical Society*, 42:658–663.

Constantin, P. (2008). Euler and navier-stokes equations. *Publicacions Matemàtiques*, 52(2):235–265.

Constantin, P. and Fefferman, C. (1994). Scaling exponents in fluid turbulence: some analytic results. *Nonlinearity*, 7:41–57.

Constantin, P. and Majda, A. (1988). The Beltrami spectrum for incompressible fluid flows. *Communications in Mathematical Physics*, 115:435–456.

Constantin, P., Weinan, E., and Titi, E. S. (1994). Onsager's conjecture on the energy conservation for solutions of Euler's equation. *Communications in Mathematical Physics*, 165:207–209.

Cortet, P.-P., Chiffaudel, A., Daviaud, F., and Dubrulle, B. (2010). Experimental Evidence of a Phase Transition in a Closed Turbulent Flow. *Physical Review Letters*, 105(21):214501.

Cortet, P.-P., Diribarne, P., Monchaux, R., Chiffaudel, A., Daviaud, F., and Dubrulle, B. (2009). Normalized kinetic energy as a hydrodynamical global quantity for inhomogeneous anisotropic turbulence. *Physics of Fluids*, 21(2):025104.

Cortet, P.-P., Herbert, E., Chiffaudel, A., Daviaud, F., Dubrulle, B., and Padilla, V. (2011). Susceptibility divergence, phase transition and multistability of a highly turbulent closed flow. *Journal of Statistical Mechanics: Theory and Experiment*, 7:07012.

Crisanti, A., Jensen, M. H., Vulpiani, A., and Paladin, G. (1993). Intermittency and predictability in turbulence. *Physical Review Letters*, 70:166–169.

de La Torre, A. and Burguete, J. (2007). Slow Dynamics in a Turbulent von Kármán Swirling Flow. *Physical Review Letters*, 99(5):054101.

Delafosse, A., Collignon, M. L., Crine, M., and Toye, D. (2011). Estimation of the turbulent kinetic energy dissipation rate from 2d-piv measurements in a vessel stirred by an axial mixel ttp impeller. *Chemical Engineering Science*, 66:1728–1737.

Ditlevsen, P. D. and Giuliani, P. (2001). Cascades in helical turbulence. *Physical Review E*, 63(3):036304.

Diu, B., Lederer, D., and Roulet, B. (1997). *Physique Statistique*. Hermann.

Duchon, J. and Robert, R. (2000). Inertial energy dissipation for weak solutions of incompressible Euler and Navier-Stokes equations. *Nonlinearity*, 13:249–255.

Eckmann, J.-P. and Ruelle, D. (1985). Ergodic theory of chaos and strange attractors. *Reviews of Modern Physics*, 57:617–656.

Escauriaza, L., Seregin, G., and Sverak, V. (2003). $L_{3,\infty}$-solutions of the navier-stokes equations and backward uniqueness. *Russian Mathematical Surveys*, 58(2):211.

Eyink, G. and Aluie, H. (2006). The Cascade of Circulations in Fluid Turbulence. In *APS Division of Fluid Dynamics Meeting Abstracts*.

Eyink, G. L. (1994). Energy dissipation without viscosity in ideal hydrodynamics I. Fourier analysis and local energy transfer. *Physica D Nonlinear Phenomena*, 78:222–240.

Eyink, G. L. (2006). Multi-scale gradient expansion of the turbulent stress tensor. *Journal of Fluid Mechanics*, 549:159–190.

Eyink, G. L. (2007-2008b). Turbulence theory, lecture notes. http://www.ams.jhu.edu/ eyink/Turbulence/notes.html.

Eyink, G. L. (2008a). Dissipative anomalies in singular Euler flows. *Physica D Nonlinear Phenomena*, 237:1956–1968.

Eyink, G. L. and Sreenivasan, K. R. (2006). Onsager and the theory of hydrodynamic turbulence. *Reviews of Modern Physics*, 78:87–135.

Fefferman, C. (2006). Existence and smoothness of the navier-stokes equation. The Millennium Prize Problems.

Foias, C. and Témam, R. (1979). Some analytic and geometric properties of the solutions of the evolution navier-stokes equations. *Journal de Mathématiques Pures et Appliquées*, 58:339–368.

Forsee, A. (1963). *Albert Einstein, Theoretical Physicist*. Macmillan.

Frisch, U. (1995). *Turbulence*. Cambridge University Press.

Gallavotti, G. and Cohen, E. G. D. (1995). Dynamical Ensembles in Nonequilibrium Statistical Mechanics. *Physical Review Letters*, 74:2694–2697.

Gibson, C. H. and Schwarz, W. H. (1963). The universal equilibrium spectra of turbulent velocity and scalar fields. *Journal of Fluid Mechanics*, 16:365–384.

Giga, Y. (1983). Weak and strong solutions of the navier-stokes initial value problem. *Publications of the Research Institute for Mathematical Sciences*, 19:887–910.

Gotoh, T., Fukayama, D., and Nakano, T. (2002). Velocity field statistics in homogeneous steady turbulence obtained using a high-resolution direct numerical simulation. *Physics of Fluids*, 14:1065–1081.

Guermond, J.-L., Pasquetti, R., and Popov, B. (2011). *From suitable weak solutions to entropy viscosity*, volume 16 of *ERCOFTAC Series*, pages 373–390. Springer.

He, F., Wei, Z., and Zhu, W. (2016). On regularity for the axisymmetric navier-stokes equations. *Journal of Mathematical Analysis and Applications*, 436(2):1256–1265.

He, L. (2012). Smoothing estimates of 2d incompressible navier-stokes equations in bounded domains with applications. *Journal of Functional Analysis*, 262:3430–3464.

Heisenberg, W. (1948). Zur statistischen Theorie der Turbulenz. *Zeitschrift fur Physik*, 124:628–657.

Herbert, E., Daviaud, F., Dubrulle, B., Nazarenko, S., and Naso, A. (2012). Dual non-kolmogorov cascades in a von kármán flow. *EPL (Europhysics Letters)*, 100(4):44003.

Hinze, J. (1959). *Turbulence*. McGraw-Hill.

Hopf, E. (1951). Über die anfangswertaufgabe für die hydrodynamischen grundgleichungen. *Mathematische Nachrichten*, 4:213–231.

Jarzynski, C. (1997). Nonequilibrium Equality for Free Energy Differences. *Physical Review Letters*, 78:2690–2693.

Jimenez, J., Wray, A. A., Saffman, P. G., and Rogallo, R. S. (1993). The structure of intense vorticity in isotropic turbulence. *Journal of Fluid Mechanics*, 255:65–90.

Joseph, D. D. (1964). Incompatibility of Beltrami Flow with Viscous Adherence. *Physics of Fluids*, 7:648–651.

Kaneda, Y., Ishihara, T., Yokokawa, M., Itakura, K., and Uno, A. (2003). Energy dissipation rate and energy spectrum in high resolution direct numerical simulations of turbulence in a periodic box. *Physics of Fluids*, 15:L21–L24.

Kestener, P. and Arneodo, A. (2004). Generalizing the Wavelet-Based Multifractal Formalism to Random Vector Fields: Application to Three-Dimensional Turbulence Velocity and Vorticity Data. *Physical Review Letters*, 93(4):044501.

Kim, N. (2003). Remarks for the axisymmetric navier-stokes equations. *Journal of Differential Equations*, 187(2):226–239.

Kolmogorov, A. N. (1941a). Dissipation of Energy in Locally Isotropic Turbulence. *Akademiia Nauk SSSR Doklady*, 32:16–18.

Kolmogorov, A. N. (1941b). The local structure of turbulence in incompressible viscous fluid for very large reynolds number. *Akademiia Nauk SSSR Doklady*, 30:9–13.

Kolmogorov, A. N. (1941c). On the degenreration of isotropic turbulence in an incompressible viscous fluid. *Akademiia Nauk SSSR Doklady*, 32:16–18.

Kolmogorov, A. N. (1941d). On the logarithmically normal law of distibution of the size of particles under pulverization. *Akademiia Nauk SSSR Doklady*, 31:99–101.

Kolmogorov, A. N. (1962). A refinement of previous hypotheses concerning the local structure of turbulence in a viscous incompressible fluid at high Reynolds number. *Journal of Fluid Mechanics*, 13:82–85.

Kraichnan, R. H. (1967). Inertial Ranges in Two-Dimensional Turbulence. *Physics of Fluids*, 10:1417–1423.

Kraichnan, R. H. (1973). Helical turbulence and absolute equilibrium. *Journal of Fluid Mechanics*, 59:745–752.

Kuzzay, D., Faranda, D., and Dubrulle, B. (2015). Global vs local energy dissipation: The energy cycle of the turbulent von Kármán flow. *Physics of Fluids*, 27(7):075105.

Kuzzay, D., Saw, E.-W., Martins, F., Faranda, D., Foucaut, J.-M., Daviaud, F., and Dubrulle, B. (2016). New method for detecting singularities in experimental incompressible flows. *submitted to Nonlinearity*.

Ladyzhenskaya, O. A. (1958). Solution in the large to the boundary-value problem for the Navier–Stokes equations in two space variables. *Soviet Physics Doklady*, 123(3):1128–1131.

Ladyzhenskaya, O. A. (1968). Unique solvability in the large of a three-dimensional cauchy problem for the navier-stokes equations in the presence of axial symmetry. *Zapiski Nauchnych Seminarov LOMI*, 7:155–177.

Landau, L. and Lifshitz, E. (1987). *Fluid Mechanics*, volume 6 of *Course of Theoretical Physics*. Pergamon Press, second edition.

Lathrop, D. P., Fineberg, J., and Swinney, H. L. (1992). Transition to shear-driven turbulence in Couette-Taylor flow. *Physical Review A*, 46:6390–6405.

Leonard, A. (1974). Energy cascade in large-eddy simulations of turbulent fluid flows. In Frenkiel, F. and Munn, R., editors, *Turbulent Diffusion in Environmental Pollution*, volume 18 of *Advances in Geophysics*, pages 237–248. Academic Press, New York.

Leonardi, S., Málek, J., Necăs, J., and Pokorný, M. (1999). On axially symmetric flows in $\mathbb{R}^3$. *Zeitschrift für Analysis und ihre Anwendungen*, 18(3):639–649.

Leprovost, N., Dubrulle, B., and Chavanis, P.-H. (2006). Dynamics and thermodynamics of axisymmetric flows: Theory. *Physical Review E*, 73(4):046308.

Leray, J. (1933). Etude de diverses équations intégrales nonlinéaires et de quelques problèmes que pose l'hydrodynamique. *Journal de Mathématiques Pures et Appliquées*, 12(9):1–82.

Leray, J. (1934a). Essai sur les mouvements plans d'un liquide visqueux que limitent des parois. *Journal de Mathématiques Pures et Appliquées*, 13(9):331–418.

Leray, J. (1934b). Sur le mouvement d'un liquide visqueux emplissant l'espace. *Acta Mathematica*, 63(1):193–248.

Lions, J. (1969). *Quelques Methodes de Resolution des Problemes aux Limites Non Lineaires*. Gauthier-Villars.

Lions, J. and Prodi, G. (1959). Un théorème d'existence et d'unicité dans les équations de navier-stokes en dimension 2. *Comptes rendus de l'Académie des Sciences*, 248:3519–3521.

Lopez, J. M. (1990). Axisymmetric vortex breakdown. I - Confined swirling flow. *Journal of Fluid Mechanics*, 221:533–552.

Lorenz, E. N. (1963). Deterministic Nonperiodic Flow. *Journal of Atmospheric Sciences*, 20:130–148.

Luo, G. and Hou, T. Y. (2014). Potentially singular solutions of the 3d axisymmetric euler equations. *Proceedings of the National Academy of Sciences of the United States of America*, 111(36):12968–12973.

Marié, L. (2003). *Transport de moment cinétique et de champ magnétique par un écoulement tourbillonnaire turbulent: influence de la rotation*. PhD thesis, Université Paris 7.

Marié, L. and Daviaud, F. (2004). Experimental measurement of the scale-by-scale momentum transport budget in a turbulent shear flow. *Physics of Fluids*, 16:457–461.

Martins, F., Foucaut, J.-M., Thomas, L., Azevedo, L., and Stanislas, M. (2015). Volume reconstruction optimization for tomo-piv algorithms applied to experimental data. *Measurement Science and Technology*, 26.

Masuda, M. (1984). Weak solutions of navier-stokes equations. *Tôhoku Mathematical Journal*, 36:623–646.

Miller, J. (1990). Statistical mechanics of Euler equations in two dimensions. *Physical Review Letters*, 65:2137–2140.

Moffatt, H. (1969). The degree of knottedness of tangled vortex lines. *Journal of Fluid Mechanics*, 35:117–129.

Moisy, F. and Jiménez, J. (2004). Geometry and clustering of intense structures in isotropic turbulence. *Journal of Fluid Mechanics*, 513:111–133.

Moisy, F., Tabeling, P., and Willaime, H. (1999). Kolmogorov equation in a fully developed turbulence experiment. *Physical Review Letters*, 82(20):3994–3997.

Moisy, F., Willaime, H., Anderser, J., and Tabeling, P. (2001). Passive scalar intermittency in low temperature helium flows. *Physical Review Letters*, 86(21):4827.

Monchaux, R. (2007). *Mécanique statistique et effet dynamo dans un écoulement de von Kármán turbulent*. PhD thesis, Université Paris 7.

Monchaux, R., Berhanu, M., Bourgoin, M., Moulin, M., Odier, P., Pinton, J.-F., Volk, R., Fauve, S., Mordant, N., Pétrélis, F., Chiffaudel, A., Daviaud, F., Dubrulle, B., Gasquet, C., Marié, L., and Ravelet, F. (2007). Generation of a Magnetic Field by Dynamo Action in a Turbulent Flow of Liquid Sodium. *Physical Review Letters*, 98(4):044502.

Monchaux, R., Cortet, P.-P., Chavanis, P.-H., Chiffaudel, A., Daviaud, F., Diribarne, P., and Dubrulle, B. (2008). Fluctuation-Dissipation Relations and Statistical Temperatures in a Turbulent von Kármán Flow. *Physical Review Letters*, 101(17):174502.

Monchaux, R., Ravelet, F., Dubrulle, B., Chiffaudel, A., and Daviaud, F. (2006). Properties of Steady States in Turbulent Axisymmetric Flows. *Physical Review Letters*, 96(12):124502.

Monin, A. S. (1959). The Theory of Locally Isotropic Turbulence. *Soviet Physics Doklady*, 4:271.

Monin, A. S. and Yaglom, A. M. (1975). *Statistical Fluid Mechanics*, volume 2. J. Lumley, MIT Press, Cambridge, MA.

Moreau, J. (1961). Constantes d'un îlot tourbillonnaire en fluide parfait barotrope. *Comptes rendus de l'Académie des Sciences*, 252:2810–2812.

Moreau, J. (1977). Sur les intégrales premières de la dynamique d'un fluide parfait barotrope et le théorème de helmholtz-kelvin. *Travaux du Séminaire d'Analyse Convexe*, 7(1).

Muzy, J. F., Bacry, E., and Arneodo, A. (1991). Wavelets and multifractal formalism for singular signals: Application to turbulence data. *Physical Review Letters*, 67:3515–3518.

Nazarenko, S. (2014). *Wave Turbulence*. Springer.

Nelkin, M. (1974). Turbulence, critical fluctuations, and intermittency. *Physical Review A*, 9:388–395.

Nore, C., Tuckerman, L. S., Daube, O., and Xin, S. (2003). The 1:2 mode interaction in exactly counter-rotating von Kármán swirling flow. *Journal of Fluid Mechanics*, 477:51–88.

Obukhov, A. (1941a). On the distribution of energy in the spectrum of turbulent flow. *Akademiia Nauk SSSR Doklady*, 32(1):22–24.

Obukhov, A. (1941b). Spectral energy distribution in a turbulent flow. *Izvestiya Akademiia Nauk SSSR Doklady Seriya Geograficheskaya i Geofizicheskaya*, 5(4-5):453–466.

Onsager, L. (1949). Statistical hydrodynamics. *Nuovo Cimento (Suppl.)*, 6:279–287.

Orszag, S. (1973). Lectures on the statistical theory of turbulence. In *Proceedings of the Summer School in Theoretical Physics, Les Houches*.

Paladin, G. and Vulpiani, A. (1987a). Anomalous scaling laws in multifractal objects. *Physical Reports*, 156:147–225.

Paladin, G. and Vulpiani, A. (1987b). Degrees of freedom of turbulence. *Physical Review A*, 35:1971–1973.

Pan, X. (2016). Regularity of solutions to axisymmetric navier-stokes equations with a slightly supercritical condition. *Journal of Differential Equations*, 260(12):8485–8529.

Pelz, R. B., Yakhot, V., Orszag, S. A., Shtilman, L., and Levich, E. (1985). Velocity-vorticity patterns in turbulent flow. *Physical Review Letters*, 54:2505–2508.

Perry, A. E. and Fairlie, B. D. (1974). Critical points in flow patterns. In *Turbulent Diffusion in Environmental Pollution*, pages 299–315.

Poincaré, H. (1912). *Calcul des probabilités*. Gauthier-Villars, second edition.

Polyakov, A. M. (1993). The theory of turbulence in two dimensions. *Nuclear Physics B*, 396:367–385.

Porter, J. and Knobloch, E. (2005). Dynamics in the 1:2 spatial resonance with broken reflection symmetry. *Physica D Nonlinear Phenomena*, 201:318–344.

Ravelet, F. (2005). *Bifurcations globales hydrodynamiques et magnétohydrodynamiques dans un écoulement de von Kármán turbulent*. PhD thesis, Ecole doctorale de l'Ecole Polytechnique.

Ravelet, F., Chiffaudel, A., and Daviaud, F. (2008). Supercritical transition to turbulence in an inertially driven von Kármán closed flow. *Journal of Fluid Mechanics*, 601:339–364.

Ravelet, F., Chiffaudel, A., Daviaud, F., and Léorat, J. (2005). Toward an experimental von Kármán dynamo: Numerical studies for an optimized design. *Physics of Fluids*, 17(11):117104.

Ravelet, F., Marié, L., Chiffaudel, A., and Daviaud, F. (2004). Multistability and Memory Effect in a Highly Turbulent Flow: Experimental Evidence for a Global Bifurcation. *Physical Review Letters*, 93(16):164501.

Reynolds, O. (1883). An experimental investigation of the circumstances which determine whether the motion of water shall be direct or sinuous, and of the law of resistance in parallel channels. *Philosophical Transactions of the Royal Society*, 174(0):935–982.

Richardson, L. (1920). The supply of energy from and to atmospheric eddies. *Proceedings of the Royal Society A*, 97:354–373.

Riethmuller, M. L., editor (1994). *Particle Image Velocimetry: Principles, current applications and future prospects.*

Robert, R. (1990). Etat d'équilibre statistique pour l'écoulement bidimensionnel d'un fluide parfait. *Comptes rendus de l'Académie des Sciences*, 311:575–578.

Rousset, B., Bonnay, P., Diribarne, P., Girard, A., Poncet, J. M., Herbert, E., Salort, J., Baudet, C., Castaing, B., Chevillard, L., Daviaud, F., Dubrulle, B., Gagne, Y., Gibert, M., Hébral, B., Lehner, T., Roche, P.-E., Saint-Michel, B., and Bon Mardion, M. (2014). Superfluid high REynolds von Kármán experiment. *Review of Scientific Instruments*, 85(10):103908.

Saarenrinne, P. and Piirto, M. (2000). Turbulent kinetic energy dissipation rate estimation from PIV velocity vector fields. *Experiments in Fluids*, 29:300–307.

Saint-Michel, B. (2013). *L'écoulement de von Kármán comme paradigme de la physique statistique hors équilibre.* PhD thesis, Université Paris 6.

Saint-Michel, B., Daviaud, F., and Dubrulle, B. (2014a). A zero-mode mechanism for spontaneous symmetry breaking in a turbulent von Kármán flow. *New Journal of Physics*, 16(1):013055.

Saint-Michel, B., Herbert, E., Salort, J., Baudet, C., Bon Mardion, M., Bonnay, P., Bourgoin, M., Castaing, B., Chevillard, L., Daviaud, F., Diribarne, P., Dubrulle, B., Gagne, Y., Gibert, M., Girard, A., Hébral, B., Lehner, T., and Rousset, B. (2014b). Probing quantum and classical turbulence analogy in von Kármán liquid helium, nitrogen, and water experiments. *Physics of Fluids*, 26(12):125109.

Saw, E.-W., Kuzzay, D., Faranda, D., Guittonneau, A., Daviaud, F., Wiertel-Gasquet, C., Padilla, V., and Dubrulle, B. (2016). Experimental characterization of extreme events of inertial dissipation in a turbulent swirling flow. *Nature Communications*.

Scheffer, V. (1976a). Partial regularity of solutions to the navier-stokes equations. *Pacific Journal of Mathematics*, 66:535–552.

Scheffer, V. (1976b). Turbulence and hausdorff dimension. In *Turbulence and Navier-Stokes Equations*, number 565 in Lecture Notes in Mathematics, pages 94–112. Springer-Verlag.

Scheffer, V. (1977). Hausdorff measure and the Navier-Stokes equations. *Communications in Mathematical Physics*, 55:97–112.

Scheffer, V. (1980). The Navier-Stokes equations on a bounded domain. *Communications in Mathematical Physics*, 73:1–42.

Schwartz, L. (1997). *Théorie des distributions*. Hermann.

Schwinger, J. (1951). On Gauge Invariance and Vacuum Polarization. *Physical Review*, 82:664–679.

Serrin, J. (1962). On the interior regularity of weak solutions of the Navier-Stokes equations. *Archive for Rational Mechanics and Analysis*, 9:187–195.

Sheng, J., Meng, H., and Fox, R. O. (2000). A large eddy piv method for turbulence dissipation rate estimation. *Chemical Engineering Science*, 55:4423–4434.

Smagorinsky, J. (1963). General Circulation Experiments with the Primitive Equations. *Monthly Weather Review*, 91:99.

Sommeria, J., Nore, C., Dumont, T., and Robert, R. (1991). Statistical theory of the great red spot of jupiter. *Comptes rendus de l'Académie des Sciences*, 312(9):999–1005.

Sommeria, J. and Robert, R. (1991). Statistical equilibrium states for two-dimensional flows. *Journal of Fluid Mechanics*, 229:291–310.

Sreenivasan, K. R. and Antonia, R. A. (1997). The Phenomenology of Small-Scale Turbulence. *Annual Review of Fluid Mechanics*, 29:435–472.

Tabeling, P. (2002). Two-dimensional turbulence: a physicist approach. *Physics Report*, 362:1–62.

Tanaka, T. and Eaton, J. K. (2007). A correction method for measuring turbulence kinetic energy dissipation rate by PIV. *Experiments in Fluids*, 42:893–902.

Tao, T. (2014). Noether's theorem, and the conservation laws for the euler equations.

Taylor, G. I. (1935). Statistical Theory of Turbulence. *Royal Society of London Proceedings Series A*, 151:421–444.

Taylor, G. I. (1938). Production and Dissipation of Vorticity in a Turbulent Fluid. *Proceedings of the Royal Society of London Series A*, 164:15–23.

Taylor, G. I. and Green, A. E. (1937). Mechanism of the Production of Small Eddies from Large Ones. *Proceedings of the Royal Society of London Series A*, 158:499–521.

Thalabard, S. (2013). *Contributions to the statistical mechanics of ideal two-and-a-half dimensional flows*. PhD thesis, Université Paris-Sud 11.

Thalabard, S., Saint-Michel, B., Herbert, E., Daviaud, F., and Dubrulle, B. (2015). A statistical mechanics framework for the large-scale structure of turbulent von Kármán flows. *New Journal of Physics*, 17(6):063006.

Tokgoz, S., Elsinga, G. E., Delfos, R., and Westerweel, J. (2012). Spatial resolution and dissipation rate estimation in Taylor–Couette flow for tomographic PIV. *Experiments in Fluids*, 53:561–583.

Truesdell, C. (1954). *The kinematics of vorticity*. Indiana University Press.

Ukhovskii, M.-R. and Yudovich, V.-I. (1968). Axially symmetric flows of ideal and viscous fluids axially symmetric flows of ideal and viscous fluids filling the whole space. *Journal of Applied Mathematics and Mechanics*, 32(1):52–62.

von Kármán, T. and Howarth, L. (1938). On the Statistical Theory of Isotropic Turbulence. *Proceedings of the Royal Society of London Series A*, 164:192–215.

Von Neumann, J. and Richtmyer, R. D. (1950). A Method for the Numerical Calculation of Hydrodynamic Shocks. *Journal of Applied Physics*, 21:232–237.

von Weizsäcker, C. (1948). Das spektrum der turbulenz bei großen reynoldschen zahlen. *Zeitschrift für Physik*, 124:614–627.

Wang, L.-P., Shiyi, C., Brasseur, J., and Wyngaard, J. (1996). Examination of hypotheses in the kolmogorov refined turbulence theory through high-resolution simulations. part 1. velocity field. *Journal of Fluid Mechanics*, 309:113–156.

Weyl, H. (1950). *The theory of groups and quantum mechanics*. Dover Publications.

Williams, R. M. and Paulson, C. A. (1977). Microscale temperature and velocity spectra in the atmospheric boundary layer. *Journal of Fluid Mechanics*, 83:547–567.

Yakhot, V., Orszag, S. A., Yakhot, A., Panda, R., Frisch, U., and Kraichnan, R. H., editors (1987). *Weak interactions and local order in strong turbulence*, volume 4.

Yeung, P. K. and Zhou, Y. (1997). Universality of the Kolmogorov constant in numerical simulations of turbulence. *Physical Review E*, 56:1746–1752.

Résumé

En turbulence pleinement développée et incompressible, on constate que l'énergie cinétique d'un écoulement est dissipée à un taux indépendant du nombre de Reynolds. C'est la loi zéro de la turbulence. Cette loi, qui fut découverte en 1935 par Taylor, a eu de nombreuses confirmations expérimentales et numériques, et est au cœur de notre compréhension de la physique des régimes turbulents. Dans les années qui suivirent, Taylor proposa un mécanisme pour rendre compte de la loi zéro, basé sur la viscosité et sur l'idée d'une cascade d'énergie à travers les échelles. En 1949, Onsager se rend compte qu'une dissipation d'énergie peut aussi se produire sans l'assistance des forces visqueuses à petite échelle si le champ de vitesse devient suffisamment irrégulier, et propose une conjecture sur la régularité minimale que devrait satisfaire le champ de vitesse pour assurer la conversation de l'énergie en l'absence de viscosité. En 2000, deux mathématiciens français, Jean Duchon et Raoul Robert, formalise pour la première fois les idées d'Onsager dans un cadre mathématique rigoureux. Ils établissent la forme exacte de la dissipation d'énergie émanant de l'existence possible de singularités, et l'expriment en fonction des incréments de vitesse. Cependant, la pertinence de ces concepts en turbulence expérimentale reste à établir, et n'a jamais été étudiée.

Dans cette thèse, nous proposons les premiers tests des idées d'Onsager à partir de données expérimentales, en se basant sur le travail de Duchon et Robert. Pour cela, nous nous plaçons dans le cadre des écoulements de von Kármán où la régularité des équations de Navier-Stokes n'est pas connue. Nous utilisons des mesures de vélocimétrie par image de particules pour obtenir les trois composantes du champ de vitesse dans un plan méridien, et ainsi calculer ses incréments à l'échelle de résolution de notre système de mesure. Le résultat principal de ce travail est la mise en évidence du caractère non-trivial des écoulements turbulents à l'échelle de Kolmogorov, où l'on observe des topologies très irrégulières du champ de vitesse coïncidant avec des évènements extrêmes de transferts inertiels d'énergie.

Mots-clés: turbulence, dissipation, énergie, Onsager, singularités, Duchon-Robert, Navier-Stokes, von Kármán

Abstract

The zeroth law of turbulence states that fully developed turbulent incompressible flows dissipate their kinetic energy independently of the Reynolds number. Since its discovery by Taylor in 1935, this law has had many experimental and numerical confirmations, and is at the heart of our understanding of turbulence. In the following years, Taylor proposed a mechanism for the zeroth law, based on viscosity and the idea of a cascade of energy through scales. In 1949, Onsager realized that energy dissipation could occur without the final assistance by viscosity at small scales if the velocity field becomes sufficiently irregular, and conjectured the minimum regularity condition above which energy conservation is ensured in the absence of viscosity. In 2000, two french mathematicians, Jean Duchon and Raoul Robert, were able to derive the analytical expression for the inertial dissipation in terms of velocity increments, along with the corresponding energy balance. However, the relevance of these ideas for real turbulence has never been studied.

In this thesis, we present the first tests of Onsager's idea from experimental data, based on the work of Duchon and Robert. We enter the framework of von Kármán flows for which the regularity of Navier-Stokes equations is unknown. We use particle image velocimetry measurements which provide us with the three components of the velocity field on a meridional plane, and allows for the computation of velocity increments at the resolution scale of our measurement set-up. In this work, we point out the non-trivial character of turbulent flows at the Kolmogorov scale, where we observe irregular topologies in the velocity field at the location of extreme events of inertial energy transfers.

Keywords: turbulence, dissipation, energy, Onsager, singularities, Duchon-Robert, Navier-Stokes, von Kármán